JAN 2

PROCEEDINGS

CONF–8110101

Proceedings of the WorkshoRNF
QC 718.5.M36 U5x 1981
3 4456 0132657 7

US-JAPAN THEORY WORKSHOP on 3-D MHD STUDIES for TOROIDAL DEVICES

FUSION ENERGY DIVISION LIBRARY

OCTOBER 19–21, 1981

Oak Ridge, Tennessee

FUSION ENERGY DIVISION LIBRARY

QC
718.5
.M36
U5x
1981

SPONSORED B'
FUSION ENE ON
OAK RIDGE NATIONAL LABORATORY

Operated by Union Carbide Corporation
for the Department of Energy

OAK RIDGE NATIONAL LABORATORY
LIBRARY
U.S. PROPERTY

This report was prepared as an account of work sponsored by an agency of the United States Government. Neither the United States Government nor any agency thereof, nor any of their employees, makes any warranty, express or implied, or assumes any legal liability or responsibility for the accuracy, completeness, or usefulness of any information, apparatus, product, or process disclosed, or represents that its use would not infringe privately owned rights. Reference herein to any specific commercial product, process, or service by trade name, trademark, manufacturer, or otherwise, does not necessarily constitute or imply its endorsement, recommendation, or favoring by the United States Government or any agency thereof. The views and opinions of authors expressed herein do not necessarily state or reflect those of the United States Government or any agency thereof.

QC
718.5. M36
U5x
1981

CONF-8110101

PROCEEDINGS OF THE WORKSHOP

US-JAPAN THEORY WORKSHOP ON 3-D MHD STUDIES FOR TOROIDAL DEVICES

October 19-21, 1981

Oak Ridge, Tennessee

Contract No. W-7405-eng-26

B. A. Carreras
Editor

FUSION ENERGY DIVISION LIBRARY

Date Published: January 1982

Sponsored by

OAK RIDGE NATIONAL LABORATORY
FUSION ENERGY DIVISION
Oak Ridge, Tennessee 37830

Proceedings of the WorkshoRNF
QC 718.5.M36 U5x 1981
3 4456 0132657 7

PREFACE

The US-Japan theory workshop on 3-D MHD studies for toroidal devices was held at Oak Ridge, Tennessee on October 19-21, 1981. It was attended by more than 40 participants.

The main purpose of the workshop was to determine what important problems are ahead of us in 3-D MHD studies. In the meeting physics problems were addressed, as well as computational ones for different devices. The first day of the workshop was devoted to discussion of problems related to stellarators. The MHD properties of tokamaks were considered during the second day. Finally FRP, compact torus and EBT were discussed on the last day of the workshop. The discussions were held in a very informal fashion, which allowed a frank and open exchange of views between the participants.

These proceedings include the manuscripts that were presented at the workshop. They cover most of the oral presentations and are organized in the way they were delivered. An author index, attendance list, and the agenda are also included in the proceedings.

The Japanese delegation was led by Professor Ichiro Kawakami, Nihon University. His cooperation in the organization of the workshop is gratefully acknowledged.

The workshop was sponsored by the Fusion Energy Division, Oak Ridge National Laboratory and could not have been successful without the efforts of many dedicated individuals - Session chairmen, authors, participants, and last but not least, the workshop secretaries.

I would like to acknowledge special appreciation to: Caila Cox who handled all the problems of organization prior to the workshop in an efficient and professional manner; DeLena Akers and Gladys Warren, who acted as workshop secretaries during the workshop, taking care of all the details and problems which normally are associated with such meetings in an excellent way. I am particularly grateful to Gladys Warren for assembling the contributions of the proceedings, and handling much of the workshop paperwork.

Benjamin A. Carreras
Oak Ridge, Tennessee
November 1981

CONTENTS

THREE DIMENSIONAL MHD EQUILIBRIA
Harold Weitzner..... 1

BETA LIMITS FOR TORSATRONS
Octavio Betancourt..... 10

MHD EQUILIBRIUM AND STABILITY OF HELICAL SYSTEMS
K. Hanatani, S. Hamada, N. Hodoshima, M. Wakatani,
T. Amano and K. Uo..... 21

THE COMPUTATION OF INVERSE MAGNETIC CASCADES
David Montgomery..... 32

THEORETICAL OPTIMIZATION OF STELLARATORS
R. Chodura, W. Dommaschk, F. Herrnegger, W. Lotz,
J. Nührenberg, A. Schlüter..... 51

RESISTIVE MODES IN TOKAMAK-STELLARATOR CONFIGURATIONS
H. R. Hicks, B. Carreras, L. Garcia, J. A. Holmes, and
V. E. Lynch..... 59

STELLARATOR STABILITY AS A TWO-DIMENSIONAL PROBLEM
D. A. Monticello and H. R. Strauss..... 70

VARIATIONAL METHOD FOR THE THREE-DIMENSIONAL INVERSE EQUILIBRIUM PROBLEM IN TOROIDS
A. Bhattacharjee..... 82

A REVIEW OF TIME-DEPENDENT, THREE-DIMENSIONAL RESISTIVE MAGNETOHYDRODYNAMIC CALCULATIONS
John Killeen..... 98

TOKAMAK CURRENT DISRUPTIONS DUE TO IMPURITY RADIATION COOLING
Tsuneo Amano and Katsuhiro Shimizu..... 104

MAJOR DIRUPTION PROCESS IN TOKAMAK
T. Takeda, G. Kurita, M. Azumi, T. Tuda, T. Takizuka,
T. Tsunematsu, S. Tokuda, K. Itoh..... 116

THREE DIMENSIONAL NONLINEAR RESISTIVE STUDIES OF HIGH-BETA PDX DISCHARGES
W. Park, D. A. Monticello, R. B. White, K. McGuire, and
M. Reusch..... 129

INTERNAL DISRUPTION IN HIGH β_p TOKAMAK
T. Takeda, M. Azumi, S. Tokuda, G. Kurita, T. Tsunematsu,
T. Takizuka, T. Tuda, K. Itoh, Y. Tanaka..... 140

RESISTIVE MODES IN HIGH BETA TOKAMAK
J. A. Holmes, B. A. Carreras, L. A. Charlton, H. R. Hicks and V. E. Lynch..... 156

PROPERTIES OF THE IDEAL MHD m=1 MODE in TOKAMAKS
J. J. Ramos and G. B. Crew..... 168

THREE DIMENSIONAL SIMULATION OF SPHEROMAK FORMATION
Tetsuya Sato..... 170

MULTIDIMENSIONAL MHD COMPUTATIONS FOR THE FIELD-REVERSED THETA PINCH AND THE REVERSED-FIELD PINCH
D. D. Schnack..... 176

A SPECTRAL-FINITE DIFFERENCE ALGORITHM FOR THREE DIMENSIONAL INCOMPRESSIBLE MHD
A. Aydemir and D. C. Barnes..... 187

THREE-DIMENSIONAL TENSOR PRESSURE EQUILIBRIA FOR EBT
L. W. Owen and C. L. Hedrick..... 197

FINITE ELEMENT METHOD FOR 3-D MHD SIMULATIONS
Ichiro Kawakami..... 207

SETTING UP PHASE OF REVERSED FIELD PINCH
H. Matsuda, S. Ido and I. Kawakami..... 217

A 3-D MHD ALGORITHM FOR SIMULATION
Torkil H. Jensen and Ming S. Chu..... 227

AUTHOR INDEX..... 231

ATTENDANCE LIST..... 232

AGENDA..... 234

THREE DIMENSIONAL MHD EQUILIBRIA*

Harold Weitzner
New York University
New York, New York 10012

A survey of the current theoretical and computational effort.

A description of the problem of MHD equilibrium and its complexities.

Basic Models

1. Free boundary profiles.

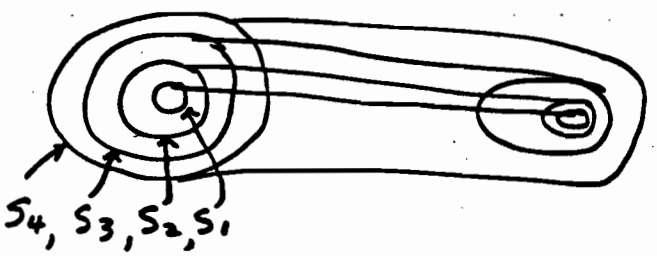

Let V be volume inside a surface

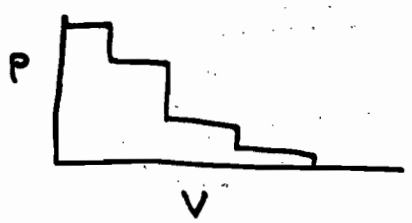

p_i constant between S_i, S_{i+1}

*Transcript of the viewgraphs used for the oral presentation at the workshop.

$\mathbf{B}_i$ is a vacuum field in domain between S_i, S_{i+1}

on S_i $\quad \mathbf{n}_i \cdot \mathbf{B}_i = 0$

on S_{i+1} $\quad \mathbf{n}_{i+1} \cdot \mathbf{B}_i = 0$

on S_i $\quad p_i + \frac{B_i^2}{2} = p_{i-1} + \frac{B_{i-1}^2}{2}$

Alternately (and little studied)

$\nabla \times \mathbf{B}_i = \lambda_i \mathbf{B}_i$ between S_i, S_{i+1}

with the same boundary conditions.

2. <u>Smooth pressure profiles</u>

$$\nabla p = \mathbf{J} \times \mathbf{B}$$

$$0 = \nabla \cdot \mathbf{B}$$

$$\mathbf{J} = \nabla \times \mathbf{B}$$

$$\mathbf{B} \cdot \nabla p = 0 = (\mathbf{J} \cdot \nabla p)$$

Thus, $\mathbf{B}$, $\mathbf{J}$ lie in the surface p = const.

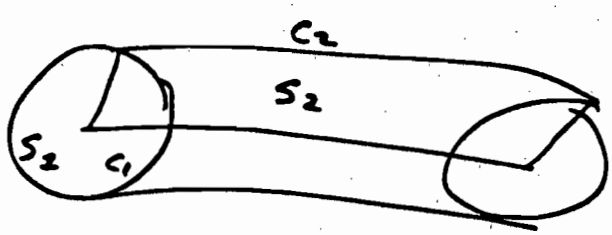

$$\psi_1 = \int_{S_1} \mathbf{B} \cdot d\mathbf{S} = \psi_1(p)$$

$$\psi_2 = \int_{S_2} \mathbf{B} \cdot d\mathbf{S} = \psi_2(p)$$

Clebsch Variables

$$\underset{\sim}{B} = \underset{\sim}{\nabla}\psi_1 \times \underset{\sim}{\nabla}\theta$$

$$\psi_1 = \int_{S_1} \underset{\sim}{B} \cdot \underset{\sim}{d}S = \int \underset{\sim}{d}\psi_1 \underset{\sim}{d}\theta$$

$$[\theta]_{c_1} = 1$$

$$\psi_2 = \int_{S_2} \underset{\sim}{B} \cdot dS = \int d\psi_1 \int_{C_2} d\theta$$

$$\frac{d\psi_2}{d\psi_1} = [\theta]_{c_2} = \iota$$

If ι = rational all lines on surface close

ι = irrational, line is ergodic on surface

By symmetry

$$\underset{\sim}{J} = \underset{\sim}{\nabla}\zeta \times \underset{\sim}{\nabla}p$$

$$I_1(p) = \int_{\underset{\sim}{S}_1} \underset{\sim}{J} \cdot d\underset{\sim}{S} \qquad \frac{dI_1(p)}{dp} = [\zeta]_{C_1}$$

$$I_2(p) = \int_{\underset{\sim}{S}_2} \underset{\sim}{J} \cdot d\underset{\sim}{S} \qquad \frac{dI_2(p)}{dp} = [\zeta]_{C_2}$$

$$\underset{\sim}{\nabla}p = \underset{\sim}{J} \times \underset{\sim}{B} = (\underset{\sim}{B}\cdot\underset{\sim}{\nabla})\zeta\, \underset{\sim}{\nabla}p$$

$$\therefore (\underset{\sim}{B}\cdot\underset{\sim}{\nabla})\zeta = 1$$

on a rational surface

$$[\zeta] = \oint \frac{d\ell}{B} = F(p)$$

$\oint \frac{d\ell}{B}$ is the same for all closed lines on a rational surface.

An alternate formulation (H. Grad)

$$\underset{\sim}{\nabla} \times \underset{\sim}{B} = \underset{\sim}{J} = \underset{\sim}{\nabla}\zeta \times \underset{\sim}{\nabla}p = \underset{\sim}{\nabla} \times \zeta\underset{\sim}{\nabla}p$$

$$\underset{\sim}{B} = \underset{\sim}{\nabla}\zeta + \zeta\underset{\sim}{\nabla}p$$

$$\underset{\sim}{B} \cdot \underset{\sim}{\nabla}p = 0$$

$$\underset{\sim}{B} \cdot \underset{\sim}{\nabla}\zeta = 1.$$

$$\underset{\sim}{\nabla} \cdot \underset{\sim}{B} = 0 = \Delta\phi + \underset{\sim}{\nabla}\cdot(\zeta\underset{\sim}{\nabla}p)$$

$$\underset{\sim}{\nabla}[\phi] + [\zeta]\underset{\sim}{\nabla}p = 0.$$

$$[\phi]_{c_i} = f_i(p)$$

$$i = 1,2.$$

$$[\zeta]_{c_i} = -f_i'(p)$$

For this problem what data do we give to expect a solution - a unique solution. We examine it two separate ways.

$\phi(x,y,z) = k$ is a characteristic surface

$(\underset{\sim}{B}\cdot\underset{\sim}{\nabla}\phi)^2\underset{\sim}{\nabla}\phi\cdot\underset{\sim}{\nabla}\phi = 0$

$\underset{\sim}{\nabla}\phi\cdot\underset{\sim}{\nabla}\phi = 0$ one elliptic second order equation

$(\underset{\sim}{B}\cdot\underset{\sim}{\nabla}\phi)^2 = 0$ one real characteristic counted twice, a hyperbolic system.

<u>Data</u>:

Elliptic: One piece of data on bounding surfaces.

Hyperbolic: Two characteristics imply two pieces of data on each magnetic line. <u>BUT</u>: repeated characteristic may reduce data and require consistency. We contemplate giving $\psi_1(p), \psi_2(p)$

Another formulation (H. Grad)

$$E = \int \left(\underset{\sim}{B}^2/2 - p\right) dV$$

$$\underset{\sim}{\nabla} \cdot \underset{\sim}{B} = 0$$

$$\underset{\sim}{B} \cdot \underset{\sim}{\nabla} p = 0$$

$$\int_{S_c} \underset{\sim}{B} \cdot \underset{\sim}{d}S = \psi_c(p) \qquad C = 1,2$$

$$\hat{n} \cdot \underset{\sim}{B} = 0 \quad \text{on outer boundary}$$

$(\underset{\sim}{B} = \underset{\sim}{\nabla} p \times \underset{\sim}{\nabla} \theta$ and get $\underset{\sim}{\nabla} p = (\underset{\sim}{\nabla} \times \underset{\sim}{B}) \times \underset{\sim}{B}$ as Euler equation)

Equivalently, (Basic energy principle)

$$E = \int \left(\underset{\sim}{B}^2/2 + \frac{p}{\gamma - 1}\right) dV$$

$$\underset{\sim}{\nabla} \cdot \underset{\sim}{B} = 0$$

$$\int_{S_c} \underset{\sim}{B} \cdot d\underset{\sim}{S} = \psi_c(v)$$

$$\int_{\text{interior } S_i} \rho \, d\underset{\sim}{x} = M(v)$$

$$p = \kappa \rho^{\gamma}$$

again counts correctly

In cylindrical symmetry, e.g.

$$\underset{\sim}{B} \cdot \underset{\sim}{\nabla} p = \underset{\sim}{J} \cdot \underset{\sim}{\nabla} p = 0 \qquad \underset{\sim}{\nabla} \cdot \underset{\sim}{B} = \underset{\sim}{\nabla} \cdot \underset{\sim}{J} = 0$$

$$B_r = \frac{1}{r} \frac{\partial \psi}{\partial z} \qquad J_r = \frac{1}{r} \frac{\partial \chi}{\partial z} = -\frac{\partial B_\theta}{\partial z}$$

$$B_z = \frac{1}{r} \frac{\partial \psi}{\partial r} \qquad J_z = \frac{1}{r} \frac{\partial \chi}{\partial r} = \frac{1}{r} \frac{\partial}{\partial r}\left(r B_\theta\right)$$

$$\chi = r B_\theta$$

$$p = p(\psi), \qquad \chi = \chi(\psi)$$

$$r \frac{\partial}{\partial r}\left(\frac{1}{r}\frac{\partial \psi}{\partial r}\right) + \frac{\partial^2 \psi}{\partial z^2} = -\left(r^2 p'(\psi) + \chi(\psi)\chi'(\psi)\right)$$

problems still in nonlinear elliptic equation

a) bifurcation

b) no solutions to nonlinear problem

c) free boundary problems.

Even with separated hyperbolic and elliptic parts, problems <u>may</u> appear.

What are three dimensional results?

First: KAM theory

Suppose we have area preserving mapping with surfaces

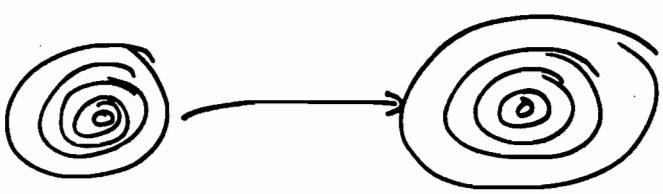

If $\iota \neq 0$ $\frac{\partial \iota}{\partial \psi} \neq 0$, both not too small or large, then in general perturbations of the mapping which are area preserving may destroy surfaces

Measure of surfaces > 0

Measure of ergodic region < A

What do we know?

1. <u>Free boundary</u>.

$p = 0$

Good - Solutions exists

Bad - Solutions found do not fill out space of data

Good - Hope to construct solutions of form

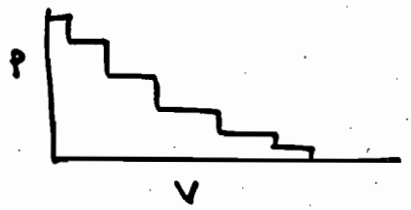

2. Closed lines.

With reflection symmetry (D. Lortz) solution exists with $\iota = 0$.

New results (D. Lortz)

perturb away from reflection symmetry solution exist

Plausible: still true if $\iota = m/n$, $\frac{\partial \iota}{\partial \psi} \equiv 0$

Need zero order equilibrium to start

3. Asymptotic expansions.

A) "Stellarator Expansion" Johnson and Greene

$$\underset{\sim}{B} = \underset{\sim}{B}_o + \delta \underset{\sim}{B}_k + \delta^2(\underset{\sim}{B}_T + \underset{\sim}{B}_\beta) + \ldots$$

$$\beta = O(\delta^2)$$

$$\kappa = O(\delta^2)$$

b) Mercier Expansion about axis curve $\underset{\sim}{x} = \underset{\sim}{X}(s)$

$$\underset{\sim}{x} = \underset{\sim}{X}(s) + \rho \cos\theta\, \hat{n} + \rho \sin\theta\, \hat{v}$$

expand about magnetic axis

C) Large aspect ratio

$$\underset{\sim}{x} = \frac{1}{\varepsilon}\,\underset{\sim}{X}(\varepsilon s) + \rho\cos\theta\,\hat{n}(\varepsilon s) + \rho\sin\theta\,\hat{v}(\varepsilon s)$$

Fills out full profile to $p = 0$.

4. <u>Numerical Calculation</u>

A) Betancourt - Garabedian with above variational principle equilibria with or without islands. No indication reported yet that as $\Delta x \to 0$ islands appear

B) Chodura - Schluter

$$\rho\frac{d\underset{\sim}{u}}{dt} + \kappa\underset{\sim}{u} + \underset{\sim}{\nabla}\rho = \underset{\sim}{J} \times \underset{\sim}{B}$$

gives equilibria

c) Barnes - Brackbill

3-D time dependent high beta code. gives equilibria.

D) Strauss - Monticello

Resistive reduced MHD

What is the situation

A) Some exact 3-D equilibria exist

Free boundary.

Lortz

B) K.A.M. says general perturbations destroy surfaces.

Q: Is equilibrium a general perturbation?

C) Resistive theory says islands may form and destroy surfaces

D) Many expansions exist

E) Numerical work appears to give good results.

F) Solutions may exist for restricted parameter ranges ($\mathcal{J} = 0$, hopefully $\frac{\partial \mathcal{J}}{\partial \psi} = 0$)

[Small domains in $\psi_1(p)$, $\psi_2(p)$]

G) Does it matter? MHD approximate and also error may produce slow changes in equilibrium only.

β Limits for Torsatrons

Octavio Betancourt
New York University

A fully three dimensional computer code based on an ideal magnetohydrodynamic model has been used to find stellarator configurations with finite critical values of the plasma parameter β. Description of the method [1], as well as results for some configurations like WISTOR-U and Heliotron E have been reported elsewhere [2,3].

In this abstract we discuss current free torsatron configurations which correspond to helical coils with a winding law given by

$$Q\phi = \ell(\theta - \alpha \sin \theta)$$

where ϕ and θ are the toroidal and poloidal angles respectively, Q the number of helical periods and α a modulation constant.

The equilibrium and stability properties of these configurations are found to depend on the Fourier components of the separatrix (last closed magnetic surface) which can be represented by an equation for its minor radius of the form

$$R = 1 + \sum_{\ell} \Delta_{\ell} \cos(\ell\theta - Q\phi) .$$

As β increases in a toroidal configuration, the magnetic axis drifts out towards the separatrix. This drift can be minimized by a large rotational transform as in Heliotron E, or it can be offset by combining ℓ and $\ell+1$ fields with opposite signs of Δ_{ℓ} and $\Delta_{\ell+1}$, which tend to shift the plasma inwards [4].

These multiple harmonics can be introduced by an appropriate choice of the modulation α in the winding law.

*This research was supported by the Department of Energy, Contract DE-AC02-76ER03077-VII.

Figures 1 and 2 show the dependence of Δ on α for $\ell = 2$ and 3 respectively. Here Δ_{10} denotes a shift of the separatrix given by the cos θ Fourier component, ε the inverse aspect ratio for the plasma, and V the vertical field.

It can be observed that Δ_ℓ is a slowly varying function of α, while $\Delta_{\ell-1}$ is rapidly varying and changes sign with α. It is also found that $\Delta_{\ell+1}$ as well as Δ_{10} are primarily controlled by the vertical field V, while Δ_ℓ and $\Delta_{\ell-1}$ vary slowly with this parameter [see Figure 4].

Among these configurations, we are most interested in the $\ell = 2,3$ torsatron, which is given by $\alpha = -0.5$ in the $\ell = 3$ winding law. In this case, $\Delta_2 = 0.15$ and $\Delta_3 = -0.15$ while Δ_4 can be decreased by increasing the vertical field. We have studied its properties extensively [3] and found no stability limitations, with the average critical β of 5% given by the axis shift for the equilibrium.

To attain a relatively high stability limit we find it is desirable to have adequate positive shear. In the case of Heliotron E this is achieved by a tight winding and a large number Q = 19 of field periods. For a moderate number of periods, it can be obtained from the $\ell = 1$ and $\ell = 3$ components of the field.

Figure 3 shows the dependence of the M = 2, N = 1 mode on Δ_1. Here $-\omega^2 > 0$ is the stable region. Curve B corresponds to $\Delta_2 = 0.2$ and $\Delta_3 = -0.1$. It should be noted that by lowering Δ_3 and increasing Δ_2 we have gone from the stable configuration mentioned above to one with critical β of 2%. Curves A and C show that a positive Δ_1 stabilizes this mode while a negative Δ_1 makes it more unstable. However, Δ_2 and Δ_1 of the same sign result on an outward shift of the magnetic axis, which in turn lowers the equilibrium limit. This is the case for curve A, corresponding to WISTOR U and for which the critical β is given by an equilibrium limit between 3% and 4%.

Therefore, we find that in order to obtain a high β limit for both stability and equilibrium we require a large Δ_3 of opposite sign from Δ_2. This we cannot achieve with an $\ell = 2$ winding law. Since Δ_3 is critical for stability, we want it to remain nearly constant for a reasonable range of vertical fields and β. For both of these reasons an $\ell = 3$ winding law with $\alpha = -0.5$ seems the best choice for a high critical β.

For this case the number of periods $Q = 10$ has been chosen so that the transform at the edge of the plasma is below 1. One may attempt to increase the equilibrium limit by increasing $\Delta_2 = 0.2$, $\Delta_3 = -0.15$, with $Q = 10$, or keeping $\Delta_2 = 0.15$, $\Delta_3 = -0.15$ and increasing Q. In both cases, the transform at the plasma edge is larger than one, and the $M = 1$, $N = 1$ mode becomes unstable with critical β below 2%.

Figures 4 through 7 show results obtained for the ISX-C torsatron design. Figure 4 shows Δ as a function of the vertical field V. Due to the small value of α, Δ_1 is negligible and the configuration is mainly $\ell = 2$ with a small $\ell = 3$ component. Notice that Δ_2 and Δ_3 are of the same sign, so at zero β the magnetic axis is shifted outwards relative to the separatrix.

The basic configuration is $\Delta_2 = -0.25$, $\Delta_3 = -0.07$, with the separatrix shifted inwards relative to the coils. If we decrease the vertical field, we obtain a configuration $\Delta_2 = -0.28$, $\Delta_3 = -0.14$ with the separatrix shifted outwards.

Figure 5 shows Δ as a function of β. As we increase β, the separatrix is slowly shifted outwards, with a corresponding change in Δ_3. This shift can be compensated for by a small increase in the vertical field.

Figure 6 shows the magnetic axis shift in units of the plasma radius. Figure 7 shows a parameter d which at zero β is proportional to island width, and for finite β also

measures the Pfirsch-Schluter current. From these we conclude that configuration A has an equilibrium limit around 3% while B is somewhat higher. Although we have not computed a stability limit, we expect A to have a low limit since Δ_3 is small. B has a large Δ_3, but of the same sign as Δ_2, and we do not know the critical β in this case.

References

[1] "Nonlinear magnetohydrodynamic stability," F. Bauer, O. Betancourt, and P. Garabedian, Phys. Fluids 24 (1), Jan. 1981.

[2] "Beta limits for torsatrons," F. Bauer, O. Betancourt, P. Garabedian, and J. L. Shohet, Proc. Natl. Acad. Sci. USA, Vol. 78, No. 1, pp. 1-3, Jan. 1981

[3] "Finite β Stellarators," F. Bauer, O. Betancourt, P. Garabedian, and J. L. Shohet, to appear; Trans. on Plasma Sci., Nov. 1981.

[4] "Numerical Studies of New Stellarator Concepts," F. Bauer, O. Betancourt, and P. Garabedian, J. Comp. Phys. 5, 341-355, 19 .

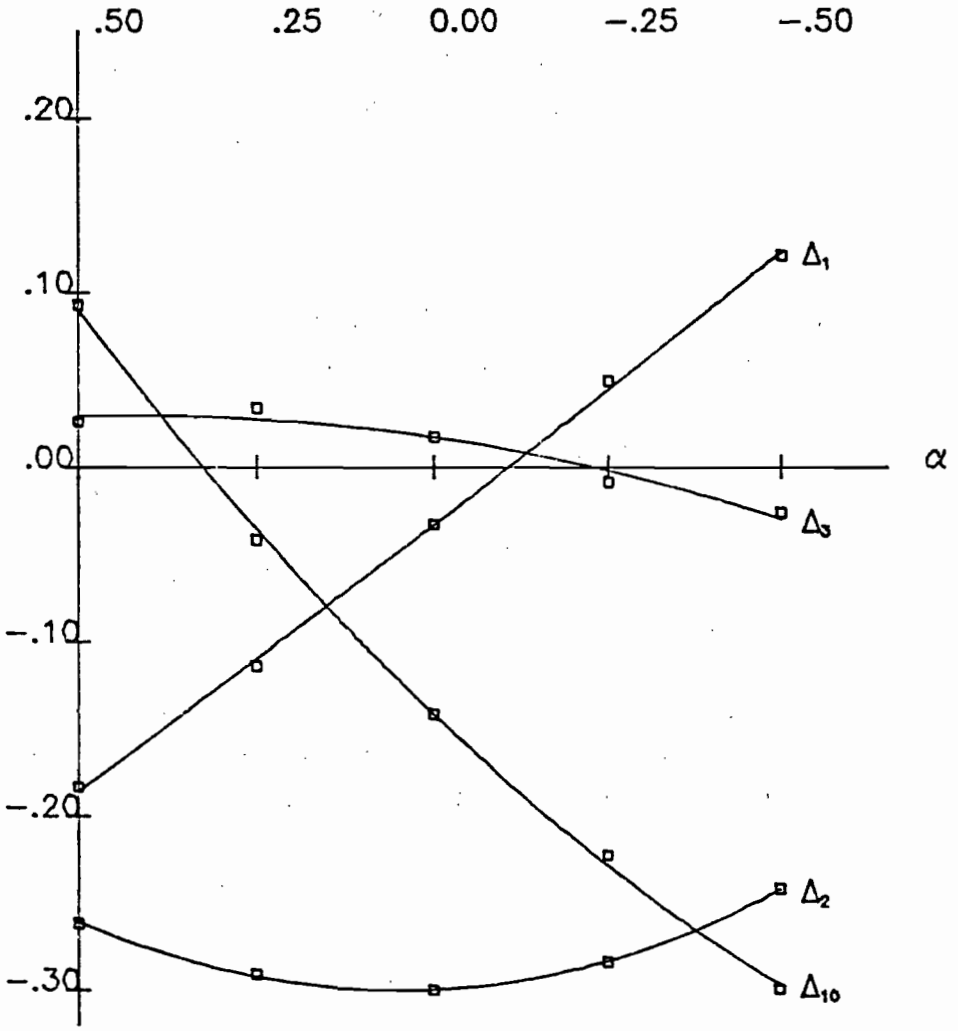

Δ AS A FUNCTION OF α

$\beta = 0.0$, $\varepsilon = 0.1$, $Q = 12$, FIXED V

$\theta \measuredangle Q = l(\varphi - \alpha \mathrm{SIN}\varphi)$; $l = 2$

Figure 1

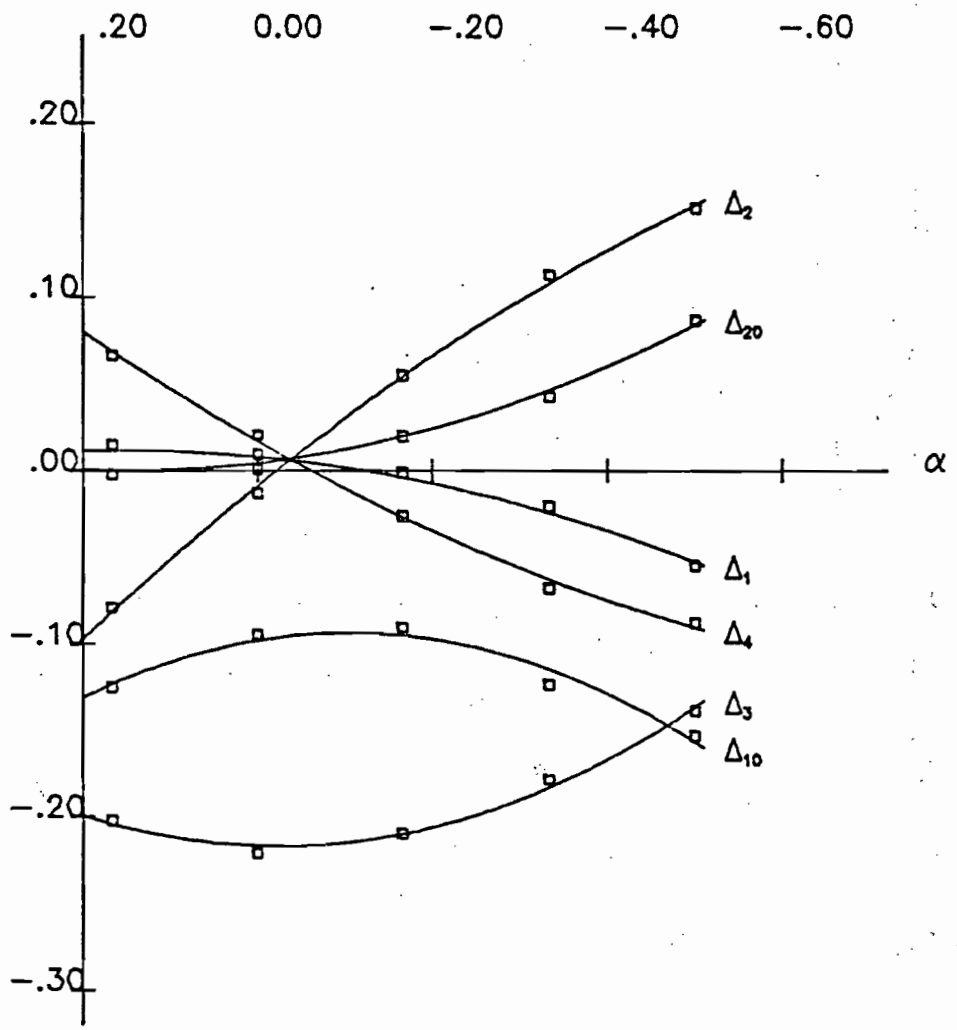

Δ AS A FUNCTION OF α

$\beta = 0.0$, $\varepsilon = 0.1$, $Q = 12$, FIXED V

$\theta \measuredangle Q = l(\varphi - \alpha \mathrm{SIN}\varphi)$, $l = 3$

Figure 2

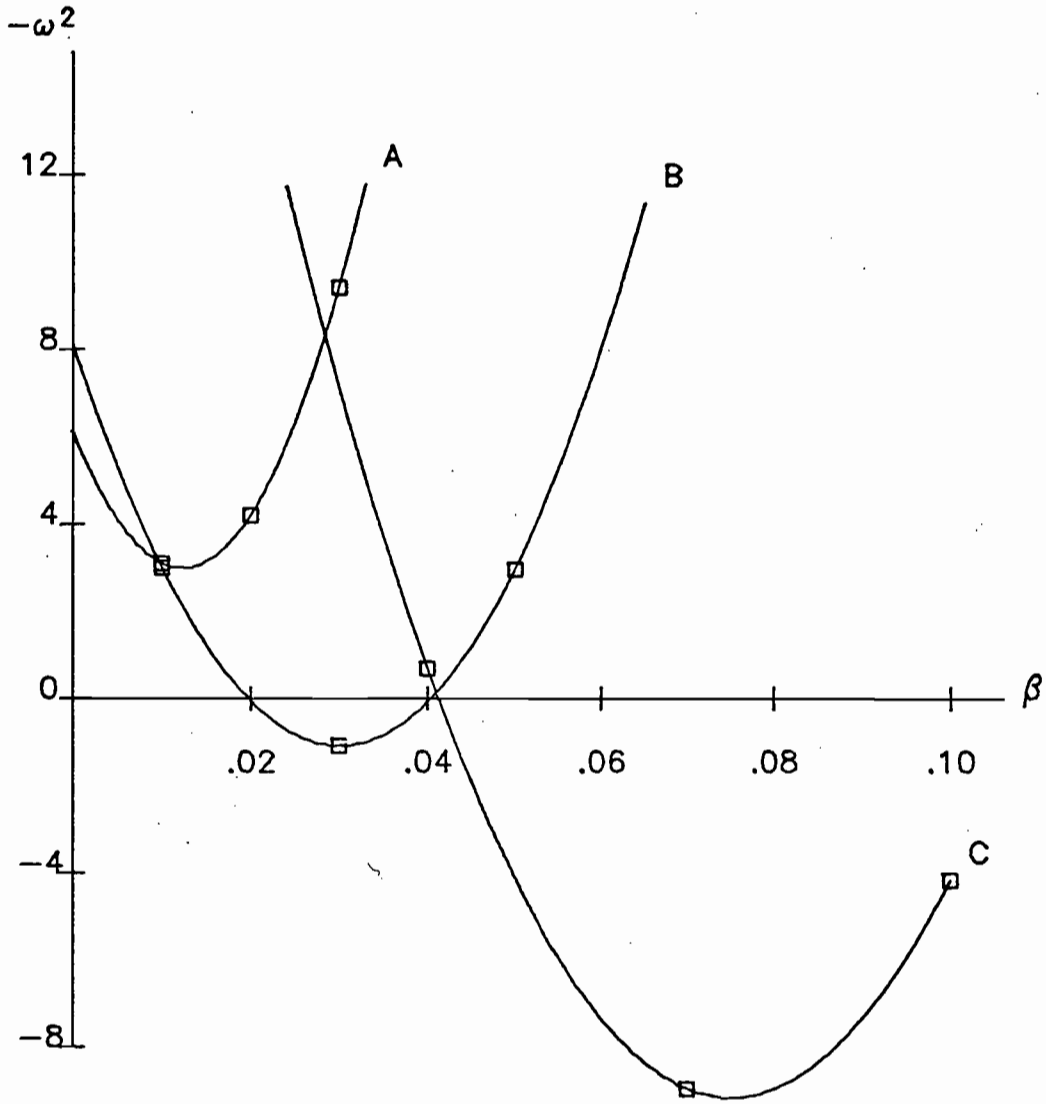

DEPENDENCE OF EIGENVALUE $-\omega^2$ ON β AND Δ_1 FOR M=2 , N=1 MODE WITH ε=0.1 , Q=12 , Δ_2=0.2 , Δ_3=−0.1

A. Δ_1= 0.2 (WISTOR U)

B. Δ_1= 0.0

C. Δ_1=−0.2

Figure 3

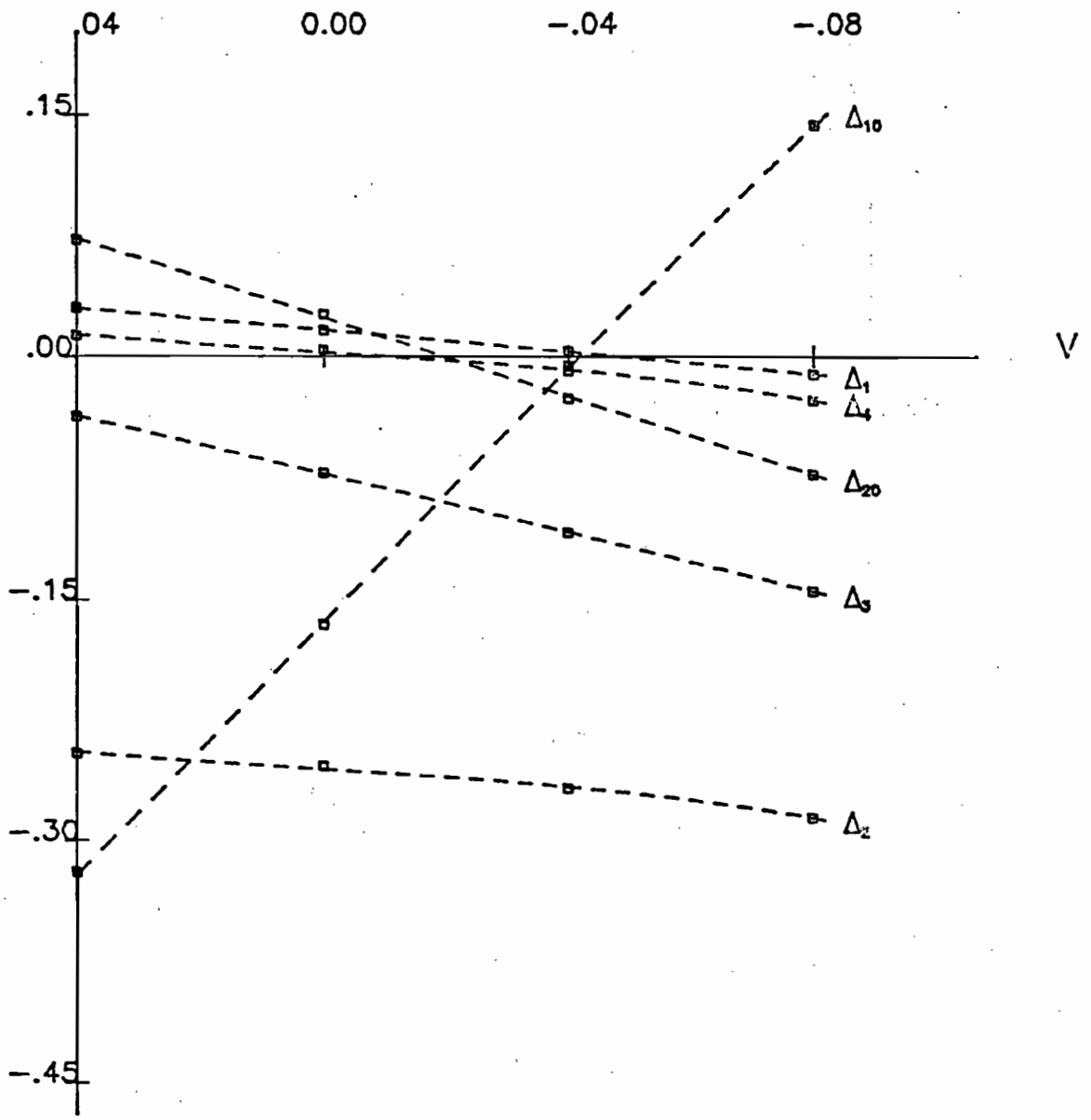

Δ AS A FUNCTION OF V

ISX−C DESIGN

$\alpha = -.2$, $\beta = 0.0$, $Q = 10$, $\varepsilon = .143$

Figure 4

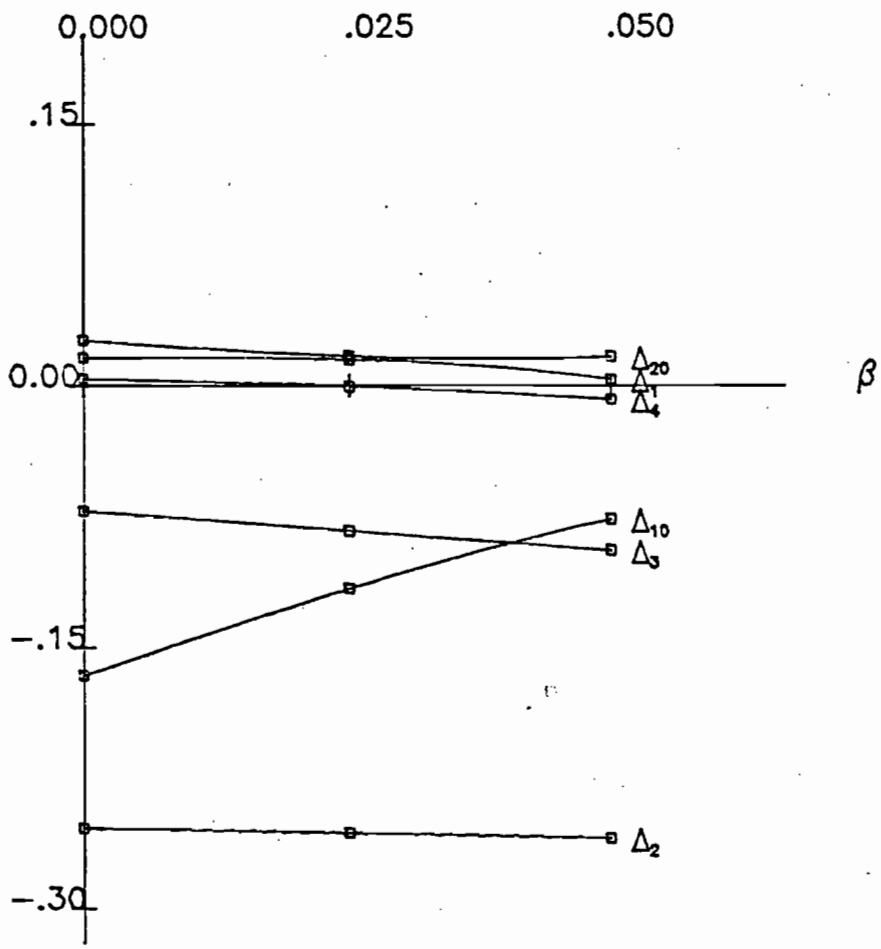

Δ AS A FUNCTION OF β

ISX−C DESIGN

$\alpha = -.2$, $Q = 10$, $\varepsilon = .143$, FIXED V

Figure 5

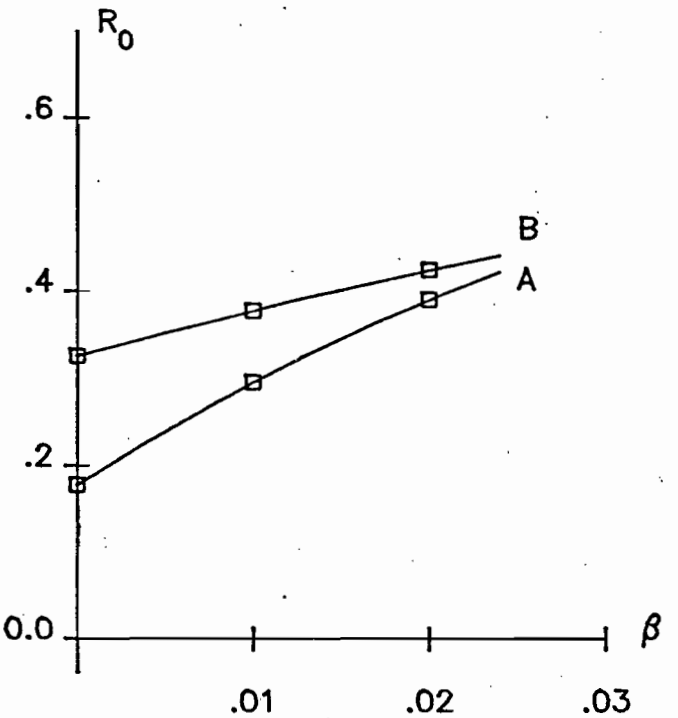

AXIS SHIFT AS A FUNCTION OF β

ISX–C DESIGN , $\alpha = -.2$, $\varepsilon = .143$, $Q = 10$

A. $\Delta_{10} = -.17$, $\Delta_2 = -.25$, $\Delta_3 = -.07$

B. $\Delta_{10} = +.14$, $\Delta_2 = -.28$, $\Delta_3 = -.14$

Figure 6

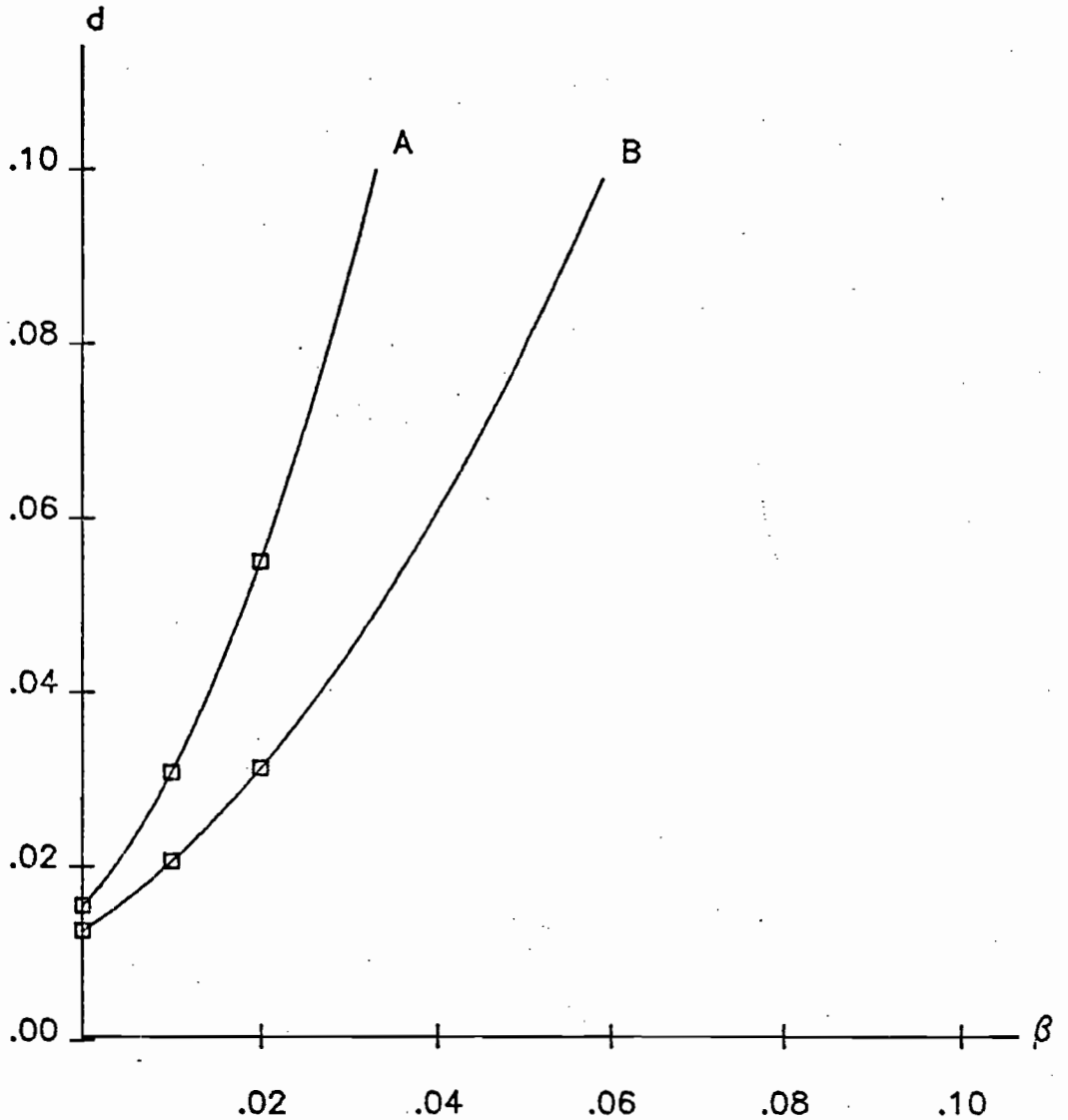

CONFINEMENT COEFFICIENT d (β)

ISX–C DESIGN , $\alpha = -.2$, $\varepsilon = .143$, Q = 10

A. $\Delta_{10} = -.17$, $\Delta_2 = -.25$, $\Delta_3 = -.07$

B. $\Delta_{10} = +.14$, $\Delta_2 = -.28$, $\Delta_3 = -.14$

Figure 7

US-JAPAN THEORY WORKSHOP ON 3-D MHD STUDIES FOR TOROIDAL DEVICES
Oak Ridge, Tennessee Oct. 19 - 21, 1981

MHD Equilibrium and Stability of Helical Systems

K. Hanatani, S. Hamada*, N. Hodoshima*,
M. Wakatani, T. Amano** and K. Uo

Plasma physics Laboratory, Kyoto University
College of Science and Technology, Nihon University*
Institute of Plasma Physics, Nagoya University**

[1] INTRODUCTION

This paper surveys recent computational studies concerning magnetohydrodynamic equilibrium and stability of a helical magnetic trap called 'heliotron', which was porposed and which has been extensively investigated experimentally at Kyoto university. This paper also describes 3D MHD code for multi-helicity tearing mode in current carrying stellarator.

Coil system of heliotron is much simpler than that of stellarator. All helical windings in heliotron carry uni-directional current. The helical windings, therefore, produce both poloidal and longitudinal field components by themselves. In heliotron, if one choose helical windings of relatively short pitch length L, one can obtain large closed magnetic surfaces without the aid of external solenoid which is, however, indispensable to stellarators. The elimination of solenoid yields several important magnetic surface properties that do not show up in conventional stellarators. For example, the Heliotron E device /1/ has large rotational transform, high magnetic shear and deep helical field ripple. On the other hand, Wendelstein VII-A stellarator has small transform, low shear and shallow helical ripple. In short, helical effects are dominant in heliotron while they are weak in stellarator.

[2] EQUILIBRIUM AND STABILITY OF STRAIGHT HELIOTRON

Equilibrium Code

Helically symmetric equilibria have usually been studied, both analytically and numerically, by assuming the normalized radius $\rho \equiv 2\pi r/L$ (Fig. 1) is to be a small expansion parameter. This ordering, which may be appropriate to conventional stellarator, is questionable to the heliotron equilibria because the heliotron device has short pitch helical windings $\rho_c \equiv 2\pi r_c/L > 1$.

To investigate the stability of the Heliotron E ($\rho_c \simeq 1.3$) plasma, we previously wrote a free-boundary helical equilibrium code /2/. This code, uses Correa-Lortz solutions for Grad-Shafranov type equation for magnetic flux function ψ

$$L(\psi) = 4h^2(\alpha + \eta) - 4(\alpha + \eta)\eta' - 2\beta'/h^2 - F \ , \tag{1}$$

$$L \equiv \nabla\cdot(h^2\nabla \quad), \qquad h^2 = 1/(1 + \rho^2),$$

$$F \ ; \text{ external helical windings,}$$

was applicable to only restricted class of equilibria. Namely, plasma pressure β and current flux function η were assumed to be linear functions of ψ, which implies quasi-parabolic pressure and quasi-uniform current distributions. To investigate more general classes of equilibria, we recently developed a new version of helical equilibrium code /4/, which enables us to calculate free-boundary equilibria with arbitrary pressure and current profiles. We now consider β and η appear in the RHS of Eq.(1) are not necessarily linear functions of ψ (Fig. 2).

In order to apply Green's function technique, we introduce a new function $\hat{\psi}$ by following relation

$$\psi = \psi_v + (\alpha - 1 + \eta_b)\rho^2 + \hat{\psi} \tag{2}$$

Here, ψ_v is vacuum ($\beta = \eta = 0$) solution of Eq.(1). An unknown constant α is the magnetic field strength on the axis devided by vacuum field strength on the axis. Substituting (2) into (1), we have

$$\nabla\cdot(h^2\nabla\hat{\psi}) = Q = Q_0 + \alpha Q_1 \ . \tag{3}$$

In the outside of the plasma ($\psi > \psi_b$), Q is equal to zero. $\hat{\psi}$ can be written using Green's function $\hat{\phi}$ of Eq.(3) as follows

$$\hat{\psi} = L^{-1}\, Q(\alpha,\psi) = \int \hat{\phi}\, Q\, ds. \tag{4}$$

Boundary conditions on $\hat{\psi}$ at the origin ($\rho = 0$) and at the infinity ($\rho \to \infty$) are $\hat{\psi} = 0$ and $\lim_{\rho\to\infty} \hat{\psi}/\rho^2 = 1 - \alpha - \eta_b$, respectively.

From these conditions, one can derive expression for α

$$\alpha = \ell(\psi) = \{1 - \eta_b - 1/4\pi\cdot\int Q_0\, ds\}/\{1 + 1/4\pi\cdot\int Q_1\, ds\} \qquad (5)$$

Two kinds of nonlinearities are involved in (3),(4) and (5); one from the free-boundary nature of the problem and the other from the nonlinear source terms. We use a simple iteration scheme to solve these coupled equations

$$\hat{\psi}^{(n)} = L^{-1}\, Q(\alpha^{(n-1)}, \psi^{(n-1)}), \qquad (6\text{-}1)$$

$$\alpha^{(n)} = \ell(\psi^{(n)}), \qquad (6\text{-}2)$$

$$\psi^{(n)} = \psi_v + (\alpha^{(n)} - 1 + \eta_b)\rho^2 + \hat{\psi}^{(n)}. \qquad (6\text{-}3)$$

As an initial guess, we take vacuum solution; $\psi^{(0)} = \psi_v$, $\hat{\psi}^{(0)} = 0$ and $\alpha^{(0)} = 1 - \eta_b$. To avoid time-consuming, repiticious integration (4), we first calculate $\hat{\psi}$ value on a circle of radius ρ_a ($> \rho_c$), which encircles both plasma and helical windings. Then, we solve finite-difference form of (6-1) inside this circle by SOR method

$$\nabla\cdot(h^2\hat{\psi}^{(n)}) = Q^{(n-1)} \qquad (7)$$

requiring the $\hat{\psi}$ value on $\rho = \rho_a$ as boundary condition. Figure 3 show the example of Heliotron E equilibrium calculated by the above scheme.

High m localized Mode

Straight helical equilibria are physically trivial, since no toroidal effects are included. We think, however, this kind of 2D equilibrium code has wide application to stability computation. First application of the equilibrium code is to estimate β limit of the straight heliotron plasma against localized mode using Mercier's criterion. This is done by introducing additional iteration loop exterior to the iteration scheme (6). At the end

of each inner iteration step, we calculate maximum possible β profile, which is marginally stable against Mercier's criterion. We repeat the outer iteration until all physical quantities can be regarded as converged. In the course of iteration, longitudinal current is adjusted so as to obtain net current free equilibrium.

Low m internal Mode

Second application of the equilibrium code is the stability of ideal low m internal mode. Although large rotational transform and high shear are favorable to attain large equilibrium critical β, they allow many rational surfaces inside the plasma column. It is, therefore, of interest to examine low m internal mode of heliotron plasma. Somewhat time-consuming but straightforward way to calculate m = 1, 2, 3 $\cdots$ mode is to solve linearlized MHD equations

$$
\begin{aligned}
\nu_0 \frac{\partial^2 \vec{\xi}}{\partial t^2} &= -\nabla P_1 + \vec{J}_0 x \vec{B}_1 + \vec{J}_1 x \vec{B}_0 \\
\vec{J}_1 &= \nabla x \vec{B}_1 \\
\vec{B}_1 &= \nabla x (\vec{\xi} x \vec{B}_0) \\
P_1 &= -\vec{\xi}\cdot\nabla P_0 - \gamma P_0 \nabla\cdot\vec{\xi}
\end{aligned}
\tag{8}
$$

as an initial-boundary value problem /5,6/. An explicit finite-difference scheme /7/ is applied to a non-orthogonal curvilinear coordinate system (f, u, ζ), which is convenient to treat helically symmetric geometry. Coordinates f, u and ζ are defined by the following transformation

$$
\begin{aligned}
x^* &= \kappa r \cos\theta = \rho(f, u) \cos(u + \zeta) \\
y^* &= \kappa r \sin\theta = \rho(f, u) \sin(u + \zeta) \\
z^* &= \kappa z \qquad = \zeta \\
f &= (\psi / \psi_b)^{1/2}, \qquad \kappa \equiv 2\pi/L,
\end{aligned}
\tag{9}
$$

where ψ_b is the value of ψ at the plasma boundary. Components of metric tensor of this coordinate system are then given by

$$g_{ff} = \left(\frac{\partial\rho}{\partial f}\right)^2, \qquad g_{fu} = \frac{\partial\rho}{\partial f}\cdot\frac{\partial\rho}{\partial u}, \qquad g_{f\zeta} = 0,$$

$$g_{uu} = \left(\frac{\partial\rho}{\partial u}\right)^2 + \rho^2, \qquad g_{u\zeta} = \rho^2, \tag{10}$$

$$g_{\zeta\zeta} = 1 + \rho^2, \qquad \sqrt{g} = \rho\cdot\frac{\partial\rho}{\partial f}.$$

Fourier analysis along the cyclic coordinate ζ reduces the problem to 2D. The growth rate of the dominant mode and its associated eigenfunction are obtained by the time evolution of initial perturbation.

Results for the Heliotron E equilibria, using Correa-Lortz solution, show that m = n = 1 internal kink mode is unstable (β = 10%), when the sum of rotational transform due to vacuum helical field and plasma current becomes unity inside the plasma column (Fig. 4). The growth rate tends to reduce when the m = n = 1 resonant surface is located near the peripheral region of the plasma, where the magnetic shear of heliotron is very high.

[3] 3D MHD CODE FOR MULTI-HELICITY TEARING MODES

It is recognized that disruptive instability is crucial for developing a tokamak reactor, since stored energy in plasmas is lost to a first wall instantaneously and this will give serious damage on it. Therefore, supression or control of the disruptive instability becomes an important subject in tokamak research.

Experiments in the Pulsator tokamak showed that the feed-back control by use of the resonant helical magnetic field was effective to control the disruption. On the other hand, stellarator experimint, especially in the W VII-A stellarator, showed that disruption can be supressed , when rotational transform exceed about 0.14.

The mechanism of the disruptive instability is given by Waddell, Carreras, Hicks and Holmes /8/. They demonstrated that behavior of magnetic field lines becomes ergodic and magnetic surfaces are destroyed in the whole plasma column, after the magnetic islands produced by the m = 2/n = 1 and m = 3/n = 2 tearing modes are overlapped. This might bring about rapid plasma losses and current termination or major disruption.

Our concern is to study the same phenomena in current carrying stellarators. By applying the ordering known as stellarator expansion, nonlinear reduced MHD equations can be obtained in stellarators /9/,

$$\frac{d}{dt}\nabla_\perp^2 U = \vec{B}\cdot A(\Delta_\perp A) + \frac{2}{R_0}\frac{\partial P}{\partial y} - \nabla\Omega\times\nabla P\cdot\hat{\zeta}$$

$$\frac{\partial A}{\partial t} = B\cdot\nabla U + \eta(\Delta_\perp A) \qquad (11)$$

$$\frac{\partial P}{\partial t} = -(\nabla U\times\hat{\zeta})\cdot\nabla P$$

where U denotes a stream fuction, A denotes a flux function and P is pressure. Ω means curvature due to stellarator fields. To study the disruptive instability, the pressure terms are not essential and a low beta approximation is used. Then the reduced equations become similar to tokamak case /10/.

First we solve these equations for cylindrical plasmas with fixed boundary. As a test q profile, we choose that studied in Ref /8/. We used 16 modes and 100 radial mesh points which might be minimum number to study nonlinear tearing mode of multi-helicity /11/. We have obtained the results showing the disruptive instability. Figure 5 show the overlapping of magnetic islands due to the m = 3/n = 2 and m = 2/n = 1 tearing mode. Figure 6 shows evolution of plasma current profile. After T $\sim$ 220, the current profile deforms and spikes develop. After the overlapping between magnetic islands begin (T > 230), behavior

of the magnetic field lines becomes stochastic near the separatrix of magnetic islands. At T ≃ 260, the magnetic field lines become ergodic except the central region as shown in Fig.7. We can check the degree of ergodic behavior by calculating K-S entropy. Figure 8 shows K-S entropy at r = 0.5. The lower curve corresponds to T = 20 and K-S entropy decreases exponentially as the magnetic field line goes around the torus. But at T = 250, K-S entropy Predicts ergodic behavior.

We consider our numerical code works well for tokamaks and we have started to apply it to stellarator cases. First we study the difference the case assuming the averaging or stellarator expansion and the case including additional mode couplings due to the stellarator field.

REFERENCES

/1/ K. Uo, et al, in "Plasma Physics ans Controlled Nuclear Fusion Research 1980", Vol I, IAEA, Vienna (1981) 217.

/2/ K. Uo, et al, ibid, Vol II, (1979) 323.

/3/ D. Correa and D. Lortz, Nucl. Fusion 13 (1972) 127.

/4/ S. Hamada, K. Hanatani, N. Hodoshima, Equilibrium of Straight Heliotron, Japan/US Workshop on Heliotron Experiment and New Stellarator (Oct. 1980).

/5/ G. Batemann, W. Schneider, W. Grossmann, Nucl. Fusion 14 (1974) 669.

/6/ A. Sykes and J.A. Wesson, Nucl. Fusion 14 (1974) 645.

/7/ G. Kurita and T. Amano, JEARI-M 6774 (1976).

/8/ B. Waddell, B.Carreras, H.R. Hicks and J.A. Holmes, Physics Fluids 22 (1979) 896.

/9/ H.R. Strauss, Plasma Physics 22 (1980) 733.

/10/ M. Wakatani, Nucl. Fusion 18 (1978) 1499.

/11/ H.R. Hicks, J.A. Holmes, D.K. Lee, B. Carreras and B.V. Waddell. ORNL/TM-7132 (1981).

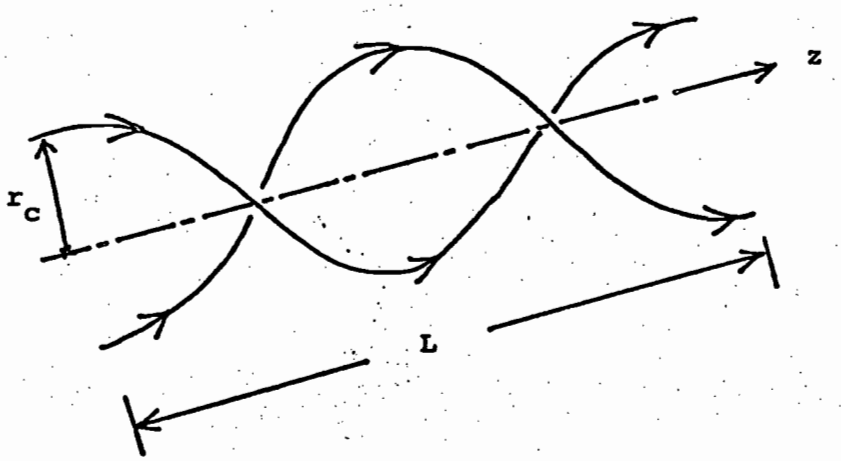

Fig. 1 : Helical Winding of $\ell = 2$ Straight Heliotron.

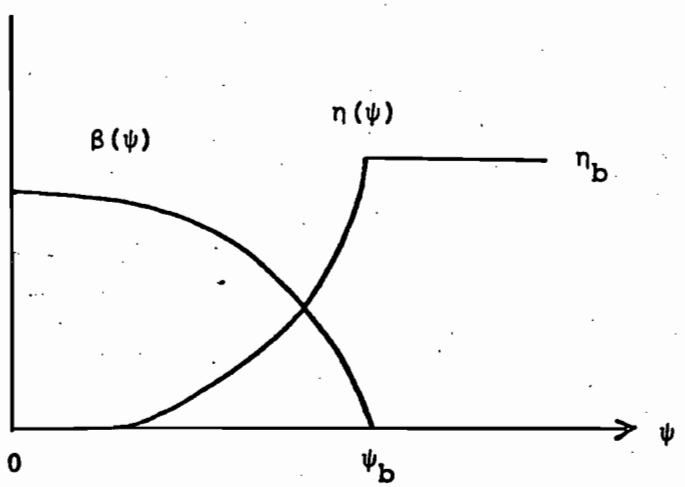

Fig. 2 : Beta and Current Flux Function Profile.

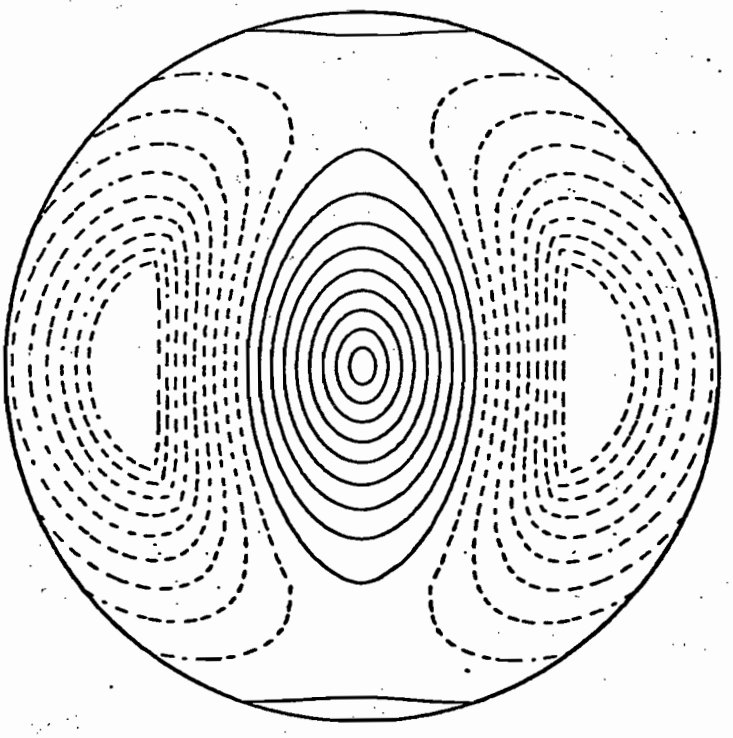

Fig. 3 : Equilibrium Flux Surface of Straight Heliotron.

Fig. 4

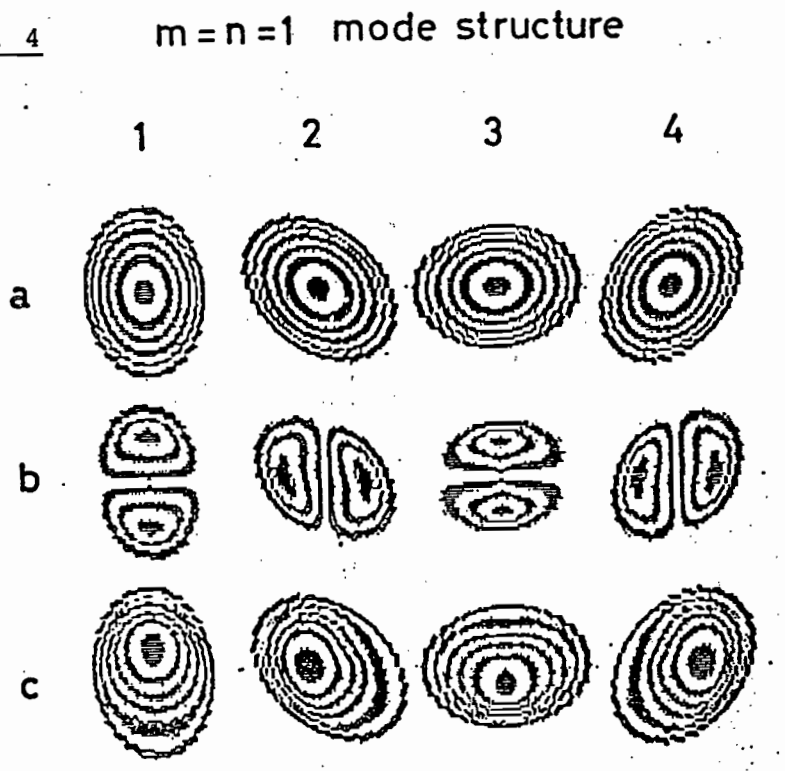

Fig. 5 : Island Width

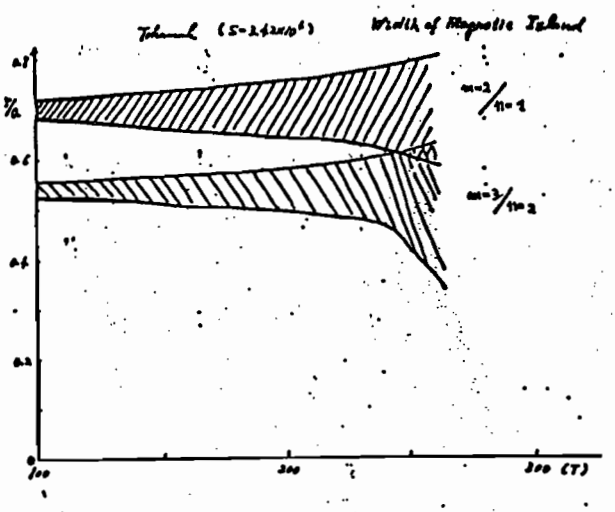

Fig. 6

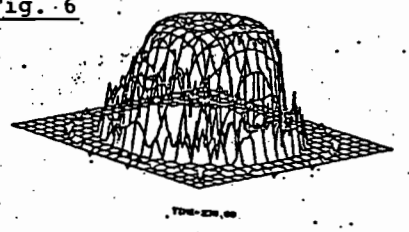

Current profile

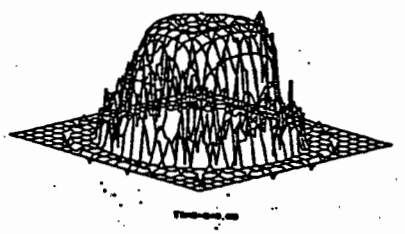

Fig. 7 : Mapping of Field Lines

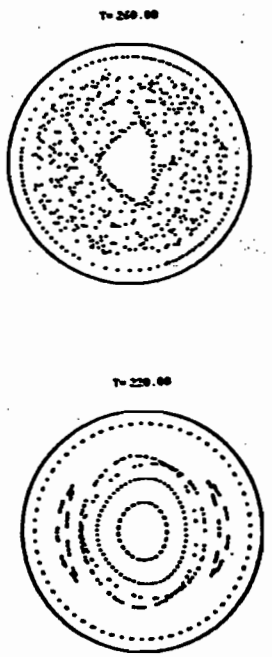

Fig. 8 : K-S Entropy

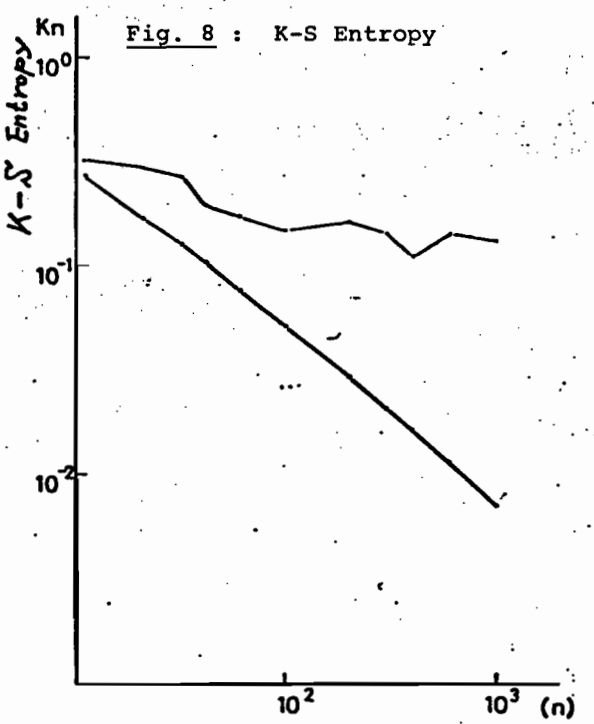

THE COMPUTATION OF INVERSE MAGNETIC CASCADES*

David Montgomery
Physics Department
College of William and Mary
Williamsburg, Virginia 23185

October, 1981

ABSTRACT

Inverse cascades of magnetic quantities for turbulent incompressible magnetohydrodynamics are reviewed, for two and three dimensions. The theory is extended to the Strauss equations, a description intermediate between two and three dimensions appropriate to tokamak magnetofluids. Consideration of the absolute equilibrium Gibbs ensemble for the system leads to a prediction of an inverse cascade of magnetic helicity, which may manifest itself as a major disruption. An agenda for computational investigation of this conjecture is proposed.

*Presented at the US-Japan Workshop on 3D MHD Studies for Toroidal Devices, Oak Ridge National Laboratory, October 19, 1981.

I. INTRODUCTION

A. Background

Over the last fifteen years, the term "inverse cascade" has been applied to a class of turbulent processes in which the small spatial scales (high wavenumbers) feed some quantity, by nonlinear processes, to the large spatial scales (low wavenumbers). A variety of quantities can be inversely cascaded, depending upon the medium and upon the geometry: the process can look quite different in different cases. Inverse cascades have been most intensively studied in Navier-Stokes fluids and incompressible magnetofluids. Most progress has been numerical, and the accurate computation of an inverse cascade is a strenuous numerical challenge because of the high spatial resolution required. This needed high spatial resolution considerably restricts the range of allowable Reynolds numbers, and the implications of these restrictions have yet to be felt in the plasma simulation community, though the hydrodynamicists are painfully aware of them.

The idea of an inverse cascade first appeared in connection with flows in two-dimensional[1,2,3,4,5] Navier-Stokes fluids, then in magnetofluids, first in three dimensions[6,7,8,9] and then in two.[10,11,12] Most of the work has assumed the simplest and most highly idealized boundary conditions: rectangular periodic ones. But now, possible relevance to the "magnetic dynamo" and to magnetic fusion confinement is exerting pressure for computations with fewer idealizations and more realism. Computations are crucial for demonstrating most of the theoretical consequences. Analytical indicators can be used to anticipate the existence of inverse cascades, but accurate prediction of any of their details seems inherently to require sophisticated numerics. No one has had much success proceeding solely with pencil and paper. The intention here is to clarify the implications of certain classes of possible computations.

The mechanism underlying an inverse cascade is essentially simple.[3,13] Two things seem to be necessary: (1) a dissipation which only becomes effective at small spatial scales, such as viscous or Ohmic dissipation; and (2) two or more non-dissipative integral invariants of the motion which are representable as sums which emphasize differently the large and small scales.

Take an example: two-dimensional Navier-Stokes flow at high Reynolds numbers (the same mathematics does as well for electrostatic guiding center plasmas). The two non-dissipative invariants, expressed in terms of the Fourier coefficients of the velocity field $\underset{\sim}{v}(\underset{\sim}{k},t)$, are the energy per unit mass E and the mean-square vorticity or "enstrophy" Ω:

$$E = \Sigma_{\underset{\sim}{k}} \, |\underset{\sim}{v}(\underset{\sim}{k},t)|^2, \qquad \Omega = \Sigma_{\underset{\sim}{k}} \, k^2 |\underset{\sim}{v}(\underset{\sim}{k},t)|^2 \, .$$

The non-dissipative terms in the equations of motion are the nonlinear ones, and if they transfer excitations to the high $|\underset{\sim}{k}|$ part of the spectrum (as they surely must), the only way the simultaneous constancy of both E and Ω can be preserved is for there to be an accompanying transfer to low $|\underset{\sim}{k}|$. The additional constant of the non-dissipative motion Ω (which is not conserved in three dimensions) demands that the non-dissipative (i.e., non-linear) terms in the Navier-Stokes equation must transfer excitations in <u>both</u> directions in wavenumber space, if there is any transfer at all. The <u>paths</u> in $\underset{\sim}{k}$ space by which the transfer occurs are a secondary issue, but there is nothing simple about them.

Subtleties arise when one begins to ask sharper questions, such as which quantity gets transferred in which direction and how fast. These questions have been earnestly addressed in the literature and do not lead to short, graphic answers, only to long, contingent ones. Relatively simple and persuasive answers can be given for the quasi-steady state, when a source of excitations, band-limited in wavenumber space, is regarded as injecting the excitations at a statistically steady rate and attention is directed toward the spectra and the transfer rates of the cascaded quantities. The word "source" can mean lots of things, from an externally-applied forcing field (such as an electric field or current field, in magneto-hydrodynamics) to some microscopic instability which might be present.

Computationally, one often works initial value problems starting from smooth initial conditions, and in that case, it may be useful to identify a particular unstable normal mode as associated with the onset of the turbulent fluctuations. In the laboratory one usually does <u>not</u> work an initial value problem starting from smooth initial conditions; rather, unstable systems are often created only with some level of excitations already in place. It may then be a less interesting question as to which "mode" is the "most unstable" one,

because the fully developed and observed state may bear little relation to the kind of smooth profiles on which any kind of stability calculations can be done. A hydrodynamic analogy is pipe flow far above the critical Reynolds number: there is hardly even an academic relation between the details of the flow and any stability calculation that can be done. Particularly in plasma confinement experiments, there may be many simultaneous sources of excitation: a gradient in virtually any mean field variable (pressure, magnetic field, electric current, flow velocity, density, temperature) is potentially a source of excitations. Many sources may act simultaneously. They may interfere with or reinforce each other.

What happens to the excitations once they are launched on their journey through $\underset{\sim}{k}$-space may be the more interesting and the more physically significant question. There is a clear difference between turbulent processes that transfer their disturbances to small rather than large scales from the point of view of thermonuclear confinement. In the former case, the worst that can happen is an enhanced transport, a disadvantage which may well be offset by an enhanced heating. (A tokamak which had no "directly cascaded" turbulence of this kind might not heat at all!) Transfer toward large scales can clearly be more serious: macroscopic bulk deformations can redistribute and disrupt the plasma variables and perhaps terminate the confinement. Disruptions in tokamaks have some of the flavor of what one might expect from an inverse cascade, though experiments with highly resolved enough diagnostics to study the small scales of what happens in a major disruption appear not to have been carried out. (A respectable beginning on the problem was made some time ago by Hutchinson[14] and Morton.[15]) For the near-term future, connections between tokamak disruptions and possible inverse cascades are likely to continue to be primarily a numerical subject.

B. Numerical Examples

We briefly remark upon three examples of attempted computations of inverse magnetic cascades. The quantities expected to be inversely cascaded are mean square vector potential in two dimensions and magnetic helicity in three.

Figure 1, due to Pouquet,[16] displays the results of a closure calculation of an inversely cascading magnetic vector potential spectrum in two dimensions. The mechanical and magnetic Reynolds numbers are of the order of 4500. The excitations are injected at a wave number indicated by an arrow, and everything at lower wave numbers is the result of back transfer in wave number space. The computation is not a direct solution of the dynamical equations themselves, but rather a statistical, eddy-damped "closure" approximation to them which permits higher values of the Reynolds numbers than a direct computation could possibly permit with present-day computers.

Figure 2, due to Fyfe et al.,[12] shows a direct numerical solution of the two-dimensional magnetohydrodynamic equations, driven by a random magnetic forcing confined to the indicated wavenumber band. All the points below $k^2 = 55$ correspond to inverse magnetic transfer to long wavelengths. This, incidentally, is a calculation in which spatial resolution was inadequate to the Reynolds number chosen, and as a consequence there is no "dissipation range", or region of precipitous fall-off at increasing k, apparent at the upper end.

Figure 3 is taken from Meneguzzi et al.,[17] and illustrates the results of a direct computation from the three-dimensional incompressible magnetohydrodynamic equations, again with a random forcing, but this time with a helical, mechanical one. A weak "seed" magnetic field amplifies with time as the injected kinetic energy converts into magnetic energy through dynamo action. The back transfer of magnetic helicity is apparent.

Additional direct inverse cascade computations which may be mentioned are those of Lilly[18] and Fyfe et al.,[12] for the two-dimensional Navier Stokes case; see also Pouquet et al.[19] for the corresponding closure computation. Pouquet and Patterson[7] have displayed three-dimensional magnetohydrodynamic direct computations. Pouquet et al.[8] have given three-dimensional inverse cascade closure computations for incompressible magnetohydrodynamics.

All the computations cited assume rectangular periodic boundary conditions with no net flux of any quantity through any cross section of the system.

II. THE STRAUSS EQUATIONS; ABSOLUTE EQUILIBRIUM ENSEMBLE THEORY

Rectangular periodic boundary conditions, which characterize most of the computational efforts to study inverse cascades, idealize away several key features of real systems. In particular, they preclude net fluxes of such quantities as electric current through a cross-section of the region of computation. They also rule out all true boundary effects, which undoubtedly play a role in real situations. It is desirable to state the ideas associated with inverse cascades in a mathematics that corresponds to more realistic representations of actual plasmas.

The Strauss equations[20] are a set of magnetohydrodynamic equations that are close to those of incompressible two-dimensional magnetohydrodynamics, but which include some important three-dimensional effects. They are far more tractable than the full set of three-dimensional magnetohydrodynamic equations. What appears to the writer to be a more transparent derivation than Strauss's can be given, ending with the same equations; the derivation is not simple, however. Their most important feature is that of their near two-dimensionality: the variable magnetic fields and velocity fields are perpendicular to the z-direction (say), but the field variables are functions of all three spatial coordinates. The variable part of the magnetic field is $\underset{\sim}{B}$ and is expressed in terms of a vector potential A as $\underset{\sim}{B} = \nabla_\perp \times \hat{e}_z A$. (The subscript "$\perp$" will always mean perpendicular to $\hat{e}_z$.) The velocity field $\underset{\sim}{v}$ is expressed in terms of a stream function U as $\underset{\sim}{v} = \nabla_\perp \times \hat{e}_z U$. There is a constant, uniform dc magnetic field in the z direction, of magnitude $B_0 \gg |\underset{\sim}{B}|$. The vorticity $\underset{\sim}{\omega}$ and the current density $\underset{\sim}{j}$ are in the z direction and are given by $\nabla_\perp^2 U = -\omega$ and $\nabla_\perp^2 A = -j$, in terms of A and U.

The Strauss equations[20] are, in a familiar set of dimensionless variables in which flow velocities are measured in units of the Alfvén speed,

$$\frac{\partial A}{\partial t} + \underset{\sim}{v}\cdot\nabla_\perp A - \mu\nabla_\perp^2 A = B_0 \frac{\partial U}{\partial z} \tag{1}$$

$$\rho\left(\frac{\partial \omega}{\partial t} + \underset{\sim}{v}\cdot\nabla_\perp \omega\right) - \underset{\sim}{B}\cdot\nabla_\perp j - \rho\nu\nabla_\perp^2 \omega = B_0 \frac{\partial j}{\partial z} \tag{2}$$

The uniform dimensionless mass density ρ can be consistently set equal to unity. The quantities μ^{-1} and ν^{-1} are essentially the magnetic and mechanical Reynolds numbers, respectively.

Except for the terms on the right hand sides of Eqs. (1) and (2) and the z-dependences, Eqs. (1) and (2) are identical with the equations of two-dimensional incompressible magnetohydrodynamics,[10-12] a system which is now getting to be rather well understood. Many interesting questions can be asked of Eqs. (1) and (2). For example, the question of possible stability thresholds for quiescent, slowly-decaying equilibria as μ and ν decrease towards zero is an analogue of the question of the stability of hydrodynamic pipe flow or Couette flow as the Reynolds number increases. Computational studies of Eqs. (1) and (2) have been initiated by Carreras, Hicks and others[21,22,23,24] in connection with tokamak confinement.

The following considerations are intended to facilitate this enterprise by sharpening the mathematical framework in which the interpretation of a major disruption as an inverse magnetic cascade may be numerically tested. In a paper published in 1977, we put forward the suggestion[12] that the inverse cascade of magnetic helicity might be responsible for major tokamak disruptions, and a test of this hypothesis seems now to be within reach. Related considerations are discussed in a forthcoming paper by Tetreault.[25]

All inverse cascade computations to date have been motivated by considering first a model problem in which the non-dissipative dynamical equations have been expanded in a set of orthogonal functions.[3,13] The expansion is then truncated at a large but finite number of terms. Statistical mechanical procedures are then performed in the phase space defined by the expansion coefficients. Somewhat surprisingly, absolute equilibrium canonical ensembles (Gibbs distributions) have proved to be accurate predictors of time averages of phase functions of the expansion coefficients. Considering the limiting behavior, as the number of expansion coefficients becomes infinite, highlights any tendencies which may exist for some invariant to migrate to long wavelengths.

The Gibbs distributions are constructed from those non-dissipative invariants which remain invariant after the truncation: i.e., are "rugged". For the Strauss equations there are apparently three such rugged invariants. They are the energy E, the "cross helicity" H_c, and the magnetic helicity H_m:

$$E = \int r dr d\theta dz \, [\underset{\sim}{B}^2 + \underset{\sim}{v}^2] \tag{3}$$

$$H_c = \int r dr d\theta dz \, \omega A \tag{4}$$

$$H_m = B_0 \int r dr d\theta dz \, A. \tag{5}$$

The integrations are over the three dimensional region $0 \leq \theta < 2\pi$, $0 \leq r < a$,

$0 \leq z < L_z$, where periodicity in z with period L_z is assumed. Free-slip boundary conditions $\underset{\sim}{v}\cdot\hat{e}_r = 0$, $\underset{\sim}{B}\cdot\hat{e}_r = 0$ are assumed at r = a, the wall of the rigid cylinder. For added realism (but added complexity), we might add the "no slip" boundary conditions on the tangential components: $(\nabla_\perp \times \underset{\sim}{B}) \times \hat{e}_r = 0$ and $\underset{\sim}{v} \times \hat{e}_r = 0$. These are superfluous, however, for the model problem at hand, and greatly complicate the mathematics.

Usually, only quadratic invariants are easily proved to be "rugged", and this can be achieved by the somewhat formal device of treating B_0 itself as a phase space coordinate whose equation of motion just happens to be $dB_0/dt = 0$. B_0 itself is then a rugged invariant, and all the terms in Eqs. (1) and (2) as well as the expressions (3)-(5) can be considered as quadratic. The ensemble chosen can be chosen to be sharp in B_0: i.e., microcanonical in B_0 but canonical in the other invariants.

A and U are expanded in the complete orthonormal set of eigenfunctions of the Laplacian,[26]

$$A_{nmq} \equiv C_{nmq} J_m(\gamma_{nmq} r)\exp(im\theta + ik_n z), \tag{6}$$

where $k_n = 2\pi n/L_z$, m and n are integers, and $\gamma_{nmq} a$ is the qth zero of $J_m(x)$. The normalization constant C_{nmq} is

$$C_{nmq} = (\pi L_z a^2)^{-1/2}/J_{m+1}(\gamma_{nmq} a). \tag{7}$$

If we define $\lambda^2_{nmq} = \gamma^2_{nmq} + k_n^2$, $\nabla^2 A_{nmq} = -\lambda^2_{nmq} A_{nmq}$, and $\nabla_\perp^2 A_{nmq} = -\gamma^2_{nmq} A_{nmq}$. The A_{nmq} are eigenfunctions of both $\nabla_\perp^2$ and ∇^2.

We may write the infinite sums

$$U = \sum_{nmq} \eta_{nmq} A_{nmq} \tag{8}$$

$$A = \sum_{nmq} \xi_{nmq} A_{nmq} \tag{9}$$

and

$$E = \sum_{nmq} \gamma^2_{nmq}(|\xi_{nmq}|^2 + |\eta_{nmq}|^2) \tag{10}$$

$$2H_c = \sum_{nmq} \gamma^2_{nmq} \xi^*_{nmq} \eta_{nmq} + \left(\begin{matrix}\text{complex}\\ \text{conjugate}\end{matrix}\right) \tag{11}$$

$$H_m = 2B_0 \left(\frac{\pi}{L_z}\right)^{1/2} \sum_q \frac{\xi_{00q}}{\gamma_{00q}} \equiv \Lambda \sum_q \frac{\xi_{00q}}{\gamma_{00q}} \quad , \tag{12}$$

where for economy of notation, $\Lambda \equiv 2B_0(\pi/L_z)^{1/2}$. The sums are over large but finite sets of terms once the truncation is performed. Also to be truncated is the set of ordinary first-order differential equations for $d\xi_{nmq}/dt$ and $d\eta_{nmq}/dt$ that result when Eqs. (8) and (9) are inserted in Eqs. (1) and (2).

The Gibbs ensemble which is appropriate to the case of no initial correlation between $\underset{\sim}{v}$ and $\underset{\sim}{B}$ is the multivariate probability distribution

$$D_{eq.} = \text{const. x exp } \{-\alpha E - \beta H_m\} , \tag{13}$$

with reciprocal temperatures α^{-1}, β^{-1} chosen to match desired ensemble expectations $\langle E\rangle$, $\langle H_m\rangle$.

Inserting Eqs. (10) and (12) into (13), the modal expectations are readily calculated. First $\langle\xi_{nmq}\rangle = \langle\eta_{nmq}\rangle = 0$, $m^2 + n^2 \neq 0$, and

$$\langle|\xi_{nmq}|^2\rangle = \langle|\eta_{nmq}|^2\rangle = \frac{2}{\alpha\gamma_{nmq}^2} , \quad m^2 + n^2 \neq 0 . \tag{14}$$

Also

$$\langle\xi_{00q}\rangle = -\frac{\beta\Lambda}{2\alpha}\frac{1}{\gamma_{00q}^3} \tag{15}$$

$$\langle(\xi_{00q} - \langle\xi_{00q}\rangle)^2\rangle = \frac{1}{\alpha\gamma_{00q}^2} . \tag{16}$$

α and β are determined as the roots of

$$\langle E\rangle = \sum_{\substack{nmq \\ n^2+m^2\neq 0}} \frac{4}{\alpha} + \sum_q \left\{\frac{1}{\alpha} + \frac{\beta^2\Lambda^2}{4\alpha^2\gamma_{00q}^4}\right\} , \tag{17}$$

and

$$\langle H_m\rangle = -\frac{\Lambda^2\beta}{2\alpha}\sum_q \frac{1}{\gamma_{00q}^4} , \tag{18}$$

which keep all the $\langle|\xi_{nmq}|^2\rangle$ and $\langle|\eta_{nmq}|^2\rangle$ positive.

If $\langle E\rangle$ and $\langle H_m\rangle$ are held fixed and the number of nmq modes is allowed to increase without limit, it is easy to show that $\alpha \to \infty$, $|\beta| \to \infty$ with $|\alpha/\beta|$ a finite ratio. The sum in Eq. (18) is convergent as the maximum $q \to \infty$. Except for the excess energy distributed in infinitessimal increments over the $m^2 + n^2 \neq 0$ modes, the fluid excitations freeze into the 00q magnetic modes. The vector potential $\langle A\rangle$ approaches a function

$$\begin{aligned}\langle A\rangle &\to \sum_{q=1}^{\infty} \langle\xi_{00q}\rangle A_{00q} \\ &= -\frac{\beta\Lambda}{2\alpha}(\pi L_z a^2)^{-1/2}\sum_{q=1}^{\infty}\frac{J_0(\gamma_{00q}r)}{\gamma_{00q}^3 J_1(\gamma_{00q}a)} ,\end{aligned} \tag{19}$$

a universal function whose defining expression is manifestly convergent. For all $m^2 + n^2 \neq 0$,

$$\frac{\langle|\xi_{nmq}|^2\rangle}{\langle\xi_{00q}\rangle^2} \to 0$$

as the number of terms approaches infinity.

This behavior is slightly different from the corresponding inverse cascade behaviors found in previously examined cases, insofar as the helicity does not condense into the 001 mode alone but into the rapidly converging series defined by Eq. (19). The state (19) is in fact a uniform current density state, with <A> varying proportionately to r^2. Nevertheless, the earmarks are there, and to anyone familiar with the previous history of the theory of inverse cascades, provide a basis for conjecturing that in the presence of dissipation and forcing, there would be an inverse cascade of H_m to long wavelengths, headed for the state defined by Eq. (19).

The uniform-current state (19) has the additional significance of being either the state of minimum energy for given helicity, or the state of maximal helicity for given energy. This can readily be seen from the Euler equation for the variational problem of minimizing E subject to a fixed value of H_m: $\nabla_\perp^2 A =$ a constant. For the dissipative initial value problem, it has been previously demonstrated that under many circumstances, the directly cascadable invariants will "selectively decay" relative to the inversely cascadable ones, and their ratios will approach their theoretical lower bounds for large times.[9,27] For the Strauss equations, it appears that this uniform current state is the "selectively decayed" state, analogous to the "Taylor state"[28] or force-free state of the full set of magnetohydrodynamic equations.

If the more realistic "no slip" boundary conditions are invoked, requiring $j = 0$ at $r = a$, the uniform current state is not attainable. At the least, a sharp current gradient must develop somewhere across the cross-section of the cylinder as the selective decay progresses, perhaps in the form of a boundary layer near $r = a$. (Something similar was seen in a recent selective decay calculation inside a compact toroid.[29]) This current gradient, which necessarily exists at the edge of a current-carrying plasma bounded by a conducting wall, looms as a rather universal and difficult-to-avoid source of "tearing mode turbulence."

This gradient in the current near the walls is one among many potential sources for the helicity which might be inversely cascaded. There is probably no single mechanism for supplying small-scale helicity. A second likely possibility is current filamentation[12] that may develop along local hot spots in the magnetofluid; the resistivity falls off with increasing temperature,

and may thus channel the current along hot tubes of force, resulting in still higher local heating. There is probably no single mechanism for supplying small-scale helicity, which basically results any time current flows along a field line in the presence of resistivity. Arguing in favor of particular drivers or sources may prove as fruitless an activity as the generation of debates that has surrounded linear instability theory. It appears imperative to produce major disruptions in the presence of as many parameter variations as possible, to begin to acquire discrimination among the variety of sources that may be operative.

III. A POSSIBLE COMPUTATIONAL AGENDA

Numerical demonstration of the possible inverse cascade properties of Strauss's equations will be facilitated by taking advantage of earlier experience and conceptualizations gained in studying inverse cascades, and by resistance to letting the conceptual framework be circumscribed by linear stability analysis. The first limitation that will have to be confronted will be the limitation on the Reynolds numbers ν^{-1}, μ^{-1}. A currently popular rule of thumb for fluid computations is that for every unit of Reynolds number, one grid point (or finite element, or expansion coefficient) is required in each spatial dimension. Thus a three-dimensional simulation at a Reynolds number of 30 requires about $(30)^3$ grid points to resolve the smallest spatial scales. This limitation might be violated by a factor of two, but probably not by an order of magnitude. At present the smallest μ and ν that are feasible to compute with are between about 10^{-2} and 10^{-3} for two dimensions and 10^{-1} to 10^{-2} for three. The desired physical values, for real experiments, are likely to be considerably smaller than that (particularly μ). There is no simple way around this difficulty.

Progress can be made in perhaps only one of two ways. (1) It may be attempted to escape the connection between the aforementioned necessary spatial resolution and wave number requirements by introducing an artificial enhanced dissipation which only becomes effective at high wave numbers.[17] The hope is that small scale dissipation only provides a sink anyway, and that the large scale dynamics will become independent of the details of the sink. (2) Alternatively, one may settle for the qualitative demonstration of the physics and extrapolate crudely to the behavior at the very high Reynolds numbers. In the former choice, the ultimate validation can only be a comparison with the results of very high-resolution codes in which no anomalous dissipation is introduced. In the second choice, the ultimate recourse is most probably to experiments.

The most single important possibility, as far as major disruptions are concerned, has to do with the possible existence of thresholds in Reynolds numbers. Such thresholds, at sometimes surprisingly low values, have characterized[17] the three-dimensional computations on the dynamo problem: above certain critical Reynolds numbers, a given stirring mechanism will initiate an inverse cascade,

otherwise it will not.[17] Of particular interest to tokamaks is the possibility that because of the drop of resistivity with increasing temperature, critical Lundquist numbers (Alfvén speed x length scale/magnetic diffusivity) or magnetic Reynolds numbers (flow speed x length scale/magnetic diffusivity) will be crossed as the magnetofluid heats up, and an inverse cascade will start dramatically.

A spectral-method numerical solution in search of inverse helicity cascades might proceed as follows, for Eqs. (1) and (2). Pick μ, $\nu \sim 1/50$ or so, with a resolution of the order of, say, 100 in the radial and azimuthal coordinates and perhaps 15 to 20 in the z coordinate. (It is unknown as to how rapidly small scales in z will multiply themselves, but if they develop as readily as the small scales in θ and r, the Strauss equations probably are not useful, anyway.) There is no reason to believe less spatial resolution is required in θ than in r. Invariance of the results to increased resolution in θ, r, and z is a necessary check on their accuracy. An initial current profile which is thought to be close to experimental reality should be chosen and an external forcing term (probably from a random number generator) should be permitted to drive the magnetofluid at the small scales, either locally or randomly in space as well. This can be most effectively accomplished by adding a small random term to the right hand sides of Eqs. (1) and (2), in the manner of Lilly,[18] or Fyfe *et al.*[12]

The purpose of this first exercise would be simply to see if an inverse cascade with the features of a major disruption can be induced, either by lowering the dissipation coefficients or raising the strength of the random forcing. Once such an event has been shown to exist, an infinite variety of refinements of the calculation, such as eliminating the random forcing in favor of a resistivity which depends upon the local temperature T, are imaginable. T, for example, might be convected and grow locally due to Ohmic dissipation:

$$\left(\frac{\partial}{\partial t} + \underset{\sim}{v}\cdot\underset{\sim}{\nabla}_{\perp}\right) T = K\nabla_{\perp}^{2}T + \eta j^{2},$$

where η is a heating rate, and K is a thermal conductivity.

Finally, the most important question connected with major disruptions is not so much can they occur as what can be done about them. If their interpretation as an inverse cascade of helicity is correct, then at a formal level,

the remedy is apparent: feed the magnetofluid some helicity of opposite sign. This means in effect inducing in the plasma some current flowing in the opposite direction from the main toroidal current. Where and how to do this seems like a delicate matter. Not much help is to be expected from attempts at suppression by static external helical windings, which supply a vacuum helicity at a particular n,m mode, but do little to the bulk distribution over modes that provides the basis for an inverse helicity cascade.

The clear-cut demonstration of an example of inverse cascade behavior for the Strauss equations would undoubtedly stimulate many additional refinements and insights that are now hard to foresee. The time is overdue, also, when the plasma simulation community should begin to seek a conceptual framework for its computations in their hydrodynamic antecedents, and cease to expect that linear stability analyses will provide adequate insight into processes in which nonlinear transfer is the dominant effect.

IV. ACKNOWLEDGMENTS

Useful discussions with Drs. U. Frisch, A. Pouquet, W. H. Matthaeus, and P.-L. Sulem are gratefully acknowledged.

This work was supported in part by the U. S. Department of Energy and in part by the National Aeronautics and Space Administration, under Grant NSG-7416.

FIGURE CAPTIONS

Fig. 1. Magnetic potential spectrum as a function of wave number for successive times, in two dimensions. Magnetic fluctuations and kinetic energy are injected at the wave number indicated by the arrow, and their transfer is approximated by an eddy-damped "closure" calculation. (Taken from Pouquet.[16])

Fig. 2. Magnetic modal energies, averaged over angle, as function of $|\underset{\sim}{k}|$, for a direct solution of the two-dimensional magnetohydrodynamic equations in two dimensions (taken from Fyfe et al.[12]). Magnetic fluctuations are randomly injected in the band between the arrows, and the spectrum is allowed to fill up. Initially, it is empty.

Fig. 3. Omni-direction magnetic energy spectrum for the three-dimensional case (taken from Meneguzzi et al.[17]). A small seed magnetic field is amplified by a driven velocity field which contains mechanical helicity, $\int \underset{\sim}{v} \cdot \underset{\sim}{\omega}\, d^2x$. The spectra are labeled by the appropriate values of the time. This is the most clear-cut computation of "dynamo" action to date.

REFERENCES

1. L. Onsager, Nuovo Cimento Suppl. 6, 279 (1949).
2. R. Fjortoft, Tellus 5, 225 (1953).
3. R. H. Kraichnan, Phys. Fluids 10, 1417 (1967).
4. C. E. Leith, Phys. Fluids 11, 671 (1968).
5. G. K. Batchelor, Phys. Fluids Suppl. 12, II: 233 (1969).
6. U. Frisch, A. Pouquet, J. Leorat, and A. Mazure, J. Fluid Mech. 68, 769 (1975).
7. A. Pouquet and G. S. Patterson, J. Fluid Mech. 85, 305 (1978).
8. A. Pouquet, U. Frisch, and L. Leorat, J. Fluid Mech. 77, 321 (1976).
9. D. Montgomery, L. Turner, and G. Vahala, Phys. Fluids 21, 757 (1978).
10. D. Fyfe and D. Montgomery, J. Plasma Phys. 16, 181 (1976).
11. D. Fyfe, G. Joyce, and D. Montgomery, J. Plasma Phys. 17, 317 (1977).
12. D. Fyfe, D. Montgomery, and G. Joyce, J. Plasma Phys. 17, 369 (1977).
13. R. H. Kraichnan and D. Montgomery, Rep. Prog. Phys. 43, 547 (1980).
14. I. H. Hutchinson, Phys. Rev. Lett. 37, 338 (1976).
15. A. H. Morton, Nucl. Fusion 16, 571 (1976).
16. A. Pouquet, J. Fluid Mech. 88, 1 (1978).
17. M. Meneguzzi, U. Frisch, and A. Pouquet, "Helical and Non-Helical Turbulent Dynamos", pre-print, Observatoire de Nice, 1981.
18. D. K. Lilly, Phys. Fluids Suppl. 12, II: 233 (1971).
19. A. Pouquet, M. Lesieur, J. C. Andre, and C. Basdevant, J. Fluid Mech. 72, 305 (1975).
20. H. Strauss, Phys. Fluids 19, 134 (1976).
21. B. Carreras, B. V. Waddell, and H. R. Hicks, Nucl. Fusion 19, 1423 (1979).
22. B. Carreras, H. R. Hicks, J. A. Holmes, and B. V. Waddell, Phys. Fluids 23, 1811 (1980).
23. B. Carreras, H. R. Hicks, and D. K. Lee, Phys. Fluids 24, 66 (1981).
24. H. R. Hicks, J. A. Holmes, V. E. Lynch, and B. A. Carreras, "Nonlinear Analysis of Disruptions in the JIPP T-II Tokamak", Oak Ridge National Laboratory Preprint ORNL/TM-7733 (1981).
25. D. J. Tetreault, "MHD Coupling and Anomalous Dissipation in MHD Turbulence", M.I.T. Preprint, 1981 (to appear in Phys. Fluids).
26. D. Montgomery and G. Vahala, J. Plasma Phys. 21, 71 (1979).

27. W. H. Matthaeus and D. Montgomery, Ann. N.Y. Acad. Sci. 357, 203 (1980).

28. J. B. Taylor, in Pulsed High Beta Plasmas, D. E. Evans, Ed., (Pergamon Press, Oxford, 1976).

29. A. Bondeson, S. Riyopoulis, and D. Montgomery, "Relaxation Toward States of Minimum Energy in a Compact Torus", University of Maryland Preprint #81-039 (1981), submitted to Phys. Fluids.

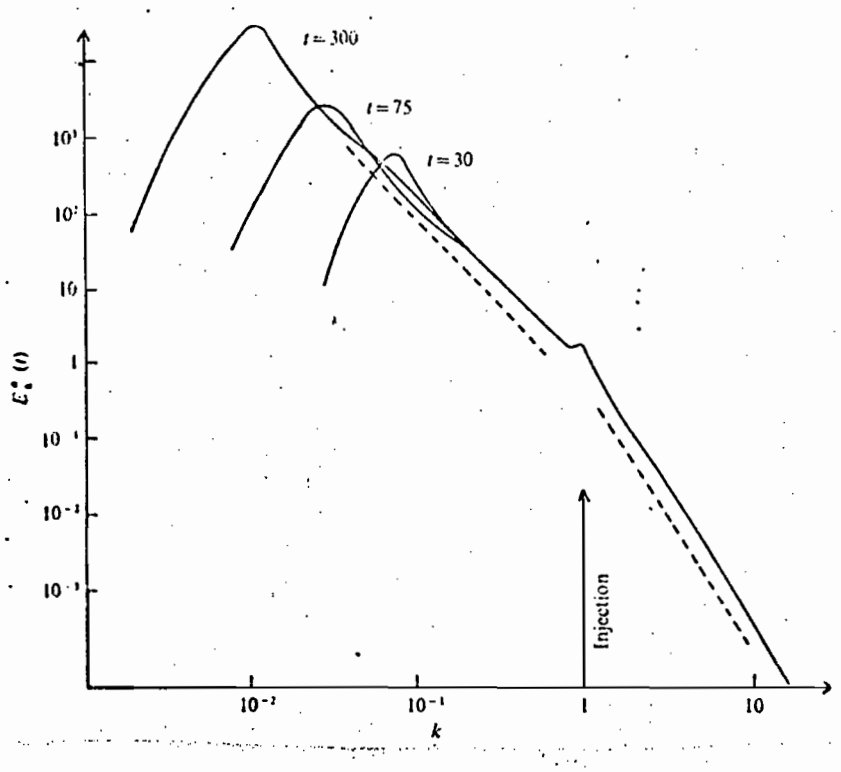

FIG. 1

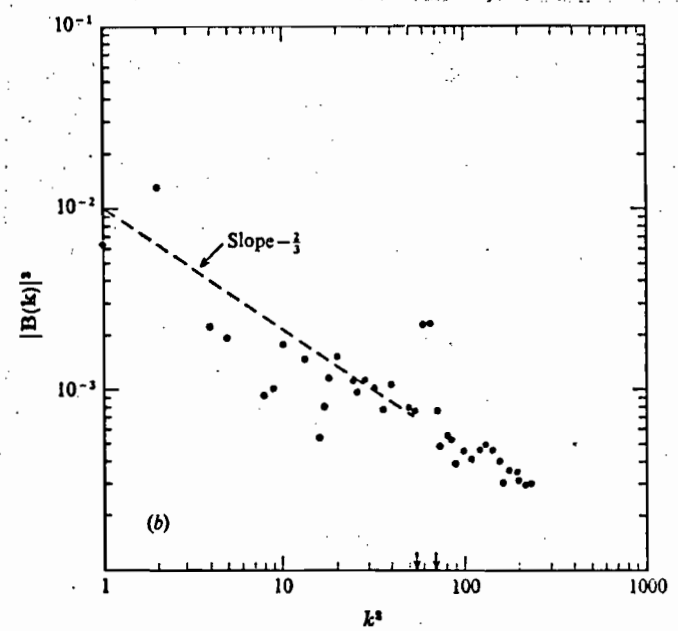

FIG. 2

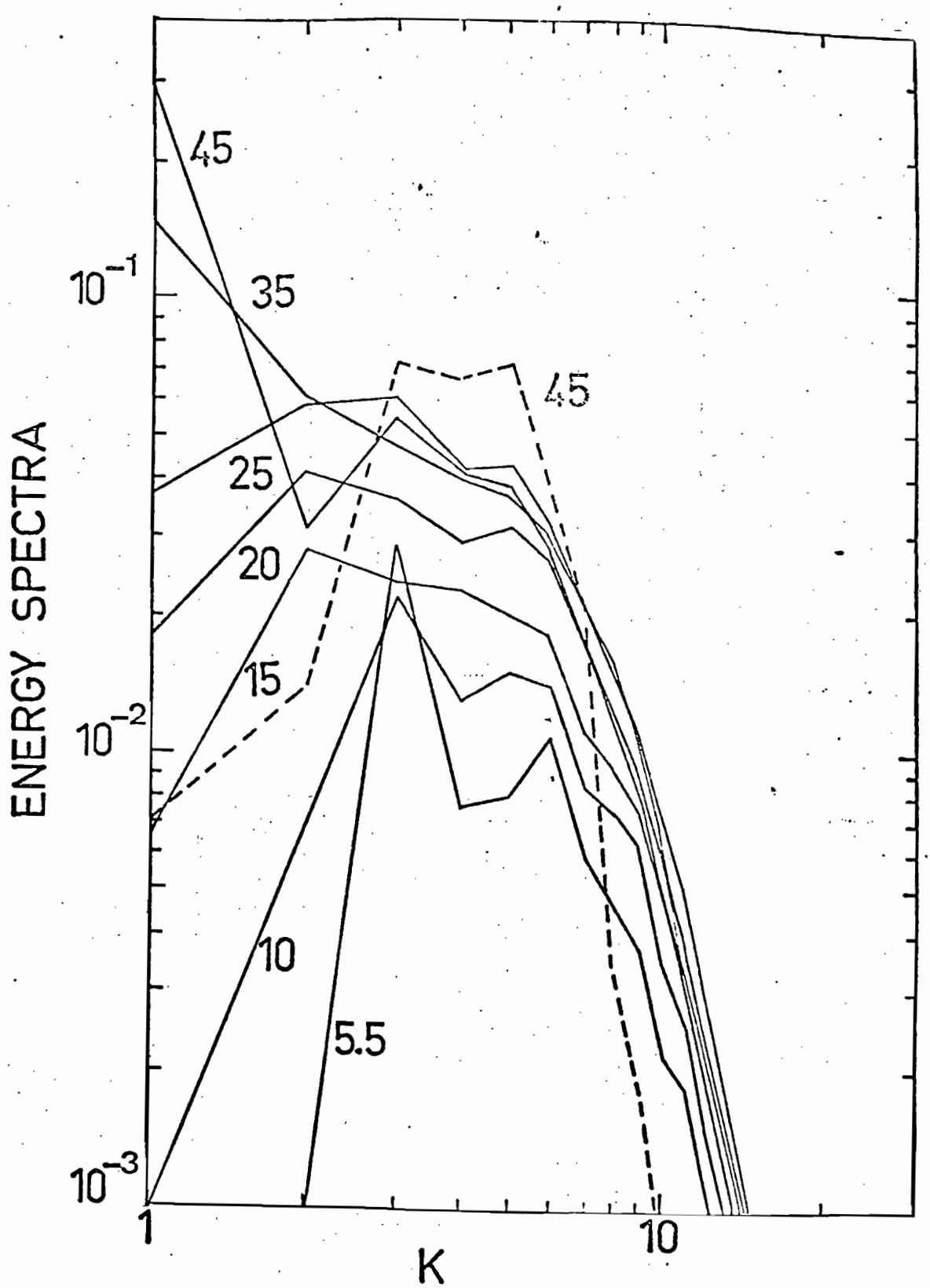

FIG. 3

Theoretical Optimization of Stellarators

R. Chodura, W. Dommaschk, F. Herrnegger,
W. Lotz, J. Nührenberg, A. Schlüter,

Max-Planck-Institut für Plasmaphysik
EURATOM-Association, D-8046 Garching

Abstract

Net current free toroidal ("stellarator") confinement is studied with a combination of several methods.

1) A complete set of explicit harmonic fields [1] is used to compose vacuum field configurations with prescribed properties like the number of field periods N, the aspect ratio A of the outermost magnetic surface, the twist number ι (rotational transform divided by 2π), the shear, the magnetic well, the variation of $\int d\ell/B$ on magnetic surfaces (where the integral is performed along a field line over one field period), a surface minimum of $|\vec{B}|$ which only weakly decreases outwardly as a prerequisite for improvement of trapped particle confinement at finite β.

2) Adding finite plasma pressure these configurations are then studied with 3D-MHD codes [2, 3] to assess the achievable equilibrium-β limit. The expansion of a general toroidal equilibrium around its magnetic axis [4] is used as a help for the computational search in configurational space and for finite-β MHD stability.

3) Monte-Carlo simulations of ion transport are performed using guiding centre orbits in given magnetic fields [5]. For a first comparative study of configurations with different magnetic properties the limit of small ratio of gyroradius to plasma radius is considered, so that the problem of lost orbits is avoided while computing the transport coefficient for given mean-free path.

4) Continuous [6] and line current modular coil systems are calculated which generate the configurations considered.

Some results have already been reported [7] and can be summarized as follows.

A) Vacuum field configurations with sizeable $\ell = 0, 1, 2, 3$ fields have been found which posses simultaneously substantial twist ($\iota \gtrsim \frac{1}{2}$), either shear or no shear, significant reduction of the parallel current as compared to the diamagnetic current, a vacuum magnetic well, and a toroidal aspect ratio of 15 - 20.

B) Any given field configuration can be generated by a surface current density on an arbitrary enclosing surface. In addition, the current lines can be chosen to be poloidally closed loops ("modular coils"). A qualitative adjustment of the surface on which the coils are placed to the shape of the outermost magnetic surface leads to a large reduction of the excursions from meridional planes as compared to a circular axisymmetric enclosing surface. For an aspect ratio as low as $\frac{1}{2}$ of that of the magnetic configuration, the geometrical form of the current lines seems still to be acceptable for the configurations characterized in A) if the enclosing surface is adjusted.

C) The finite-β equilibrium results for these configurations show that the finite-β toroidal shift is indeed reduced, so that a larger β-value (factor 2 - 4) than in the equivalent $\ell = 2$ stellarator can be achieved. (Finite-β equilibrium calculations for $\ell = 2$ configurations with strong shear hitherto seem not to support the result obtained by asymptotic analysis [8], namely that $\langle\beta\rangle = \frac{1}{2}\,\iota_b^{\,2}/A$ can be achieved, ι_b = twist number at the boundary.)

D) The 3D codes now in use at IPP do not allow a definite conclusion with respect to MHD stability. (However, improvement appears to be possible [9]). Summarizing the evidence from i) magnetic well creation by the residual finite-β shift, ii) numerical 3D code results, iii) results obtained from the expansion around the magnetic axis [10], and iv) evaluation of ballooning modes and low-n internal as well as external modes for helically symmetric equilibria [11], we want to repeat our previous statement [7] that stable equilibria with $\langle\beta\rangle \sim 0.05 - 0.1$ still appear to be possible.

E) Ion transport calculations lead to results in the form $D^*(\lambda^*)$ where $\lambda^* = \lambda/L_c$, λ mean free path, $L_c = \pi R_T/\iota$ half the connection length and

$$D^* = D\iota^2/r_i^2\nu_i(\lambda = L_c)$$

where D is the computed diffusion coefficient, r_i gyroradius, ν_i collision frequency. It shows that the transport is improved in the collisional and the plateau regimes and is not worse in the long-mean-free path regime, if the configurations with magnetic well of A) are compared to an $\ell = 2$ stellarator with correspondingly lower aspect ratio (as to allow a comparable equilibrium-β value).

To exemplify this summary, some more recent results are given which concern the equilibrium-β value and the ion transport of two configurations which are being studied as successors to the IPP W VII-A device.

Fig.1 shows vacuum field magnetic surfaces and variation of $\int d\ell/B$. Fig.2 shows the corresponding finite-β results with $\langle\beta\rangle = 0.025$ and $\langle\beta\rangle = 0.04$, respectively. In Fig.3, $D^*(\lambda^*)$ is plotted and compared to corresponding tokamak and $\ell = 2$ stellarator cases.

References

[1] Dommaschk, W., IPP-Report 0/38 (1978)

[2] Bauer, F., Betancourt, O., Garabedian, P., A Computational Method in Plasma Physics, Springer Verlag (1978)

[3] Chodura, R., Schlüter, A., J.Comput.Phys.41 (1981) 68

[4] Lortz, D., Nührenberg, J., Z.Naturforsch.31a (1976) 1277

[5] Lotz, W., Nührenberg, J., Proc.of the Annual Meeting on Theoretical Aspects of Contr.Thermonucl.Res., Austin 1981, paper 3B41

[6] Dommaschk, W., Z.Naturforsch.36a (1981) 251

[7] Chodura, R., Dommaschk, W., Herrnegger, F., Lotz, W., Nührenberg, J., Schlüter, A., IEEE Transactions of Plasma Science, December 1981; Stellarators, Joint US-EURATOM Report (1981), Report IPP 2/254, Sec.V.2

[8] Danilkin, I.S., Kovriznykh, L.M., Shchepetov, S.V., Proc.of the 10th Eur.Conf.on Controlled Fus.and Plasma Physics, Moscow (1981) E10

[9] Bauer, F., Betancourt, O., Garabedian, P., Phys.Fluids 24 (1981) 48

[10] Nührenberg, J., Proc.of the Annual Meeting on Theoretical Aspects of Contr.Thermonucl.Res., Mount Pocono, Pa., IC20 (1979), and Proc.of Int.Symposium on Stellarators with Three Dimensional Magnetic Axis, Sendai (1979) 1

[11] Gruber, R., Kerner, W., Merkel, P., Nührenberg, J., Schneider, W., Troyon, F., European Workshop on Comput.Models of the Behaviour of Magnetically Confined Plasmas, Wildhaus (Switzerland) (1981)

Figure Captions

Fig.1 Magnetic surfaces of vacuum fields. Columns 1 and 2 belong to two different field configurations (1, WAD428A: N = 10, ι_o = 0.54, ι_E = 0.80, marginal well; 2, ASC742: N = 5, ι = 0.54, small shear, marginal well). Left sides of abscissas in row 4 correspond to radially outward directed parts of surfaces. Ordinates show Q/Q_{axis}, $Q = \int d\ell/B$, for a surface with the indicated aspect ratio (solid curves). Curves for ℓ = 2 surface (with the same value of ι, A) are shown for comparison (dotted).

Fig.2 Flux surfaces of the finite-β equilibria corresponding to the vacuum field configurations of Fig.1 obtained with the NYU-Code for which the shape of the perfectly conducting boundary was here described by

$$r - R_o = r_w(U,V) = (1 + \Delta_o)\cos U + \Delta_1 \cos V - \Sigma\Delta_{\ell m} \cos[(\ell-1)U - mV]$$

$$z = z_w(U,V) = (1 + \Delta_o)\sin U + \delta_1 \sin V + \Sigma\Delta_{\ell m} \sin[(\ell-1)U - mV]$$

$$0 \le U \le 2\pi, \quad 0 \le V \le 2\pi, \quad V = N\theta$$

where r, θ, z are cylindrical coordinates, N is the number of field periods and U the poloidal parameter. For case 1, N = 10, A $\sim$ 20, and the nonvanishing coefficient are $\Delta_1 = \delta_1 = 0.39$, $\Delta_{20} = 0.11$, $\Delta_{21} = 0.22$, $\Delta_{22} = -0.01$, $\Delta_{23} = 0.03$, $\Delta_{30} = 0.02$, $\Delta_{32} = -0.06$, $\Delta_{40} = -0.02$, $\Delta_{41} = 0.02$, $\Delta_{42} = -0.01$, $\Delta_{43} = 0.03$. For case 2, N = 5 A $\sim$ 14, $\Delta_o = -0.03$, $\Delta_1 = 0.60$, $\Delta_{20} = 0.23$, $\Delta_{21} = 0.35$, $\Delta_{22} = 0.01$, $\Delta_{23} = -0.02$, $\Delta_{30} = -0.02$, $\Delta_{32} = -0.02$, $\Delta_{33} = -0.01$. The β-values are $\langle\beta\rangle = 0.04$ and $\langle\beta\rangle = 0.025$, respectively.

Fig.3 Curves $D^*(\lambda^*)$ (explained in the main text) for various stellarator and tokamak cases. Upper part. Solid curve: WAD428A (column 1 of Fig.1) A = 33, ι = 0.61; dashed curves: tokamak with A = 40, and ℓ = 2 stellarator (N = 10) with A = 40 ι = 0.50, and stellarator (N = 10) with A = 10, ι = 0.50. Lower part. Solid curve: ASC742 (column 2 of Fig.1) A = 20, ι = 0.54; dashed curves: tokamak with A = 20, and ℓ = 2 stellarator (N = 5) with A = 20, ι = 0.50, and stellarator (N = 5) with A = 10, ι = 0.51.

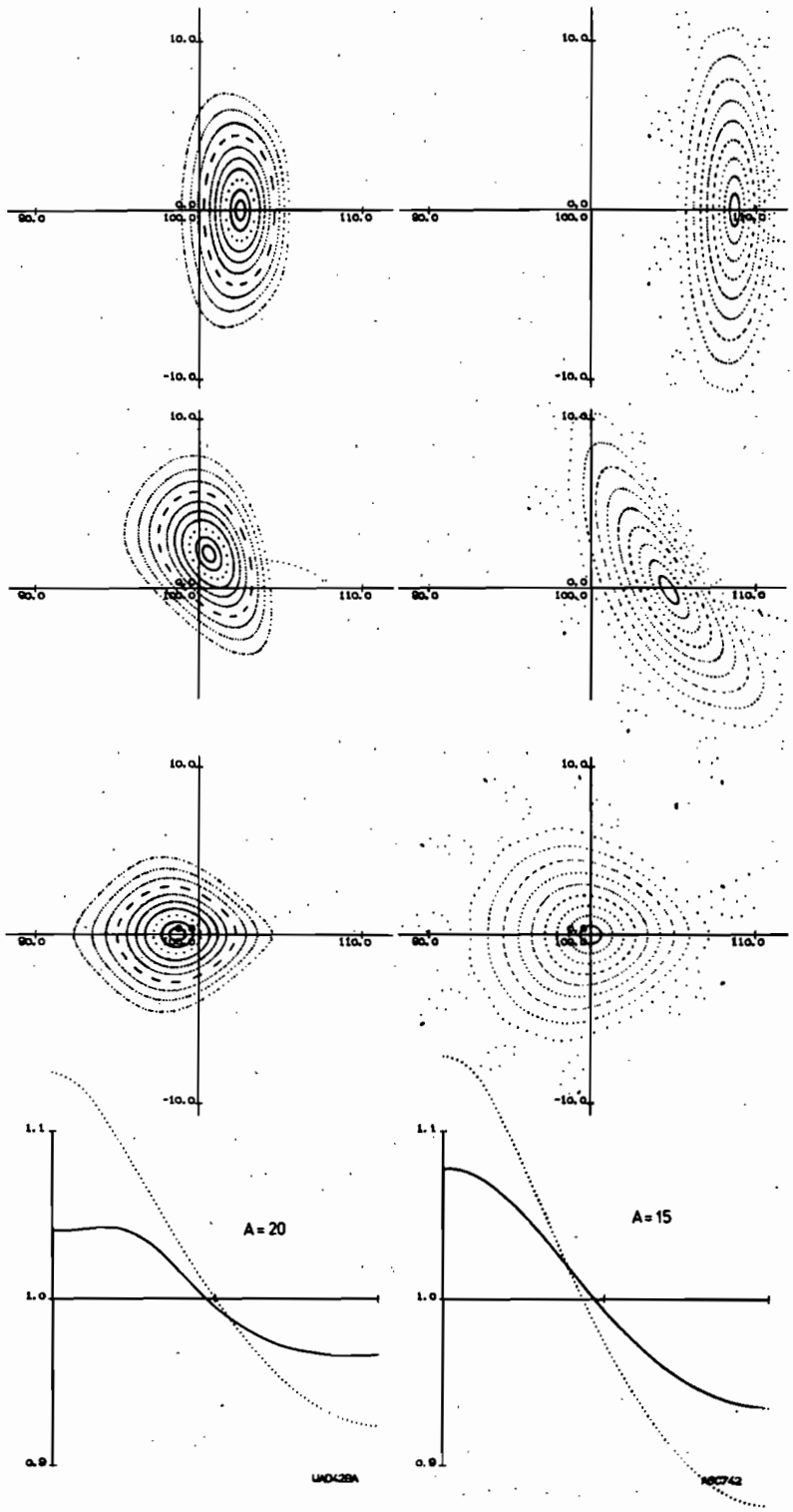
10.0
0.0
-10.0
90.0
100.0
110.0
1.1
1.0
0.9
A = 20
A = 15
UAD428A
NSC742

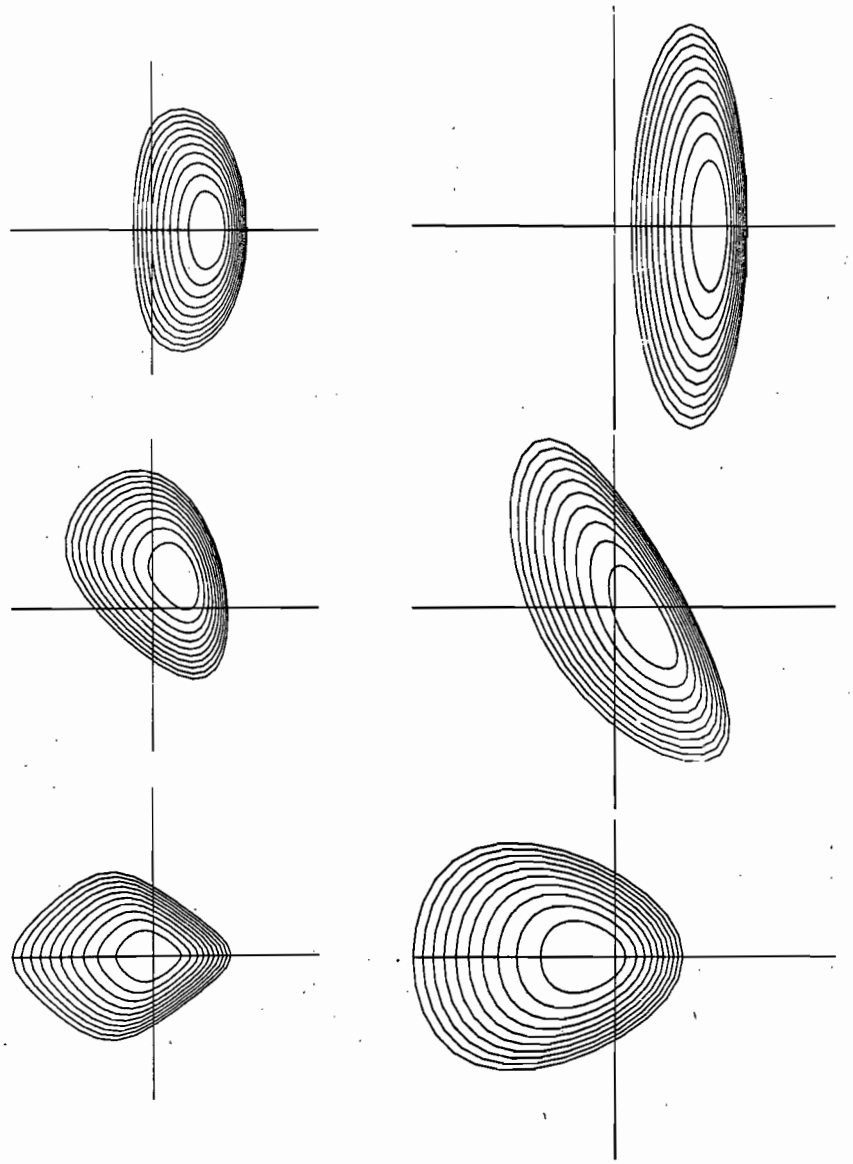

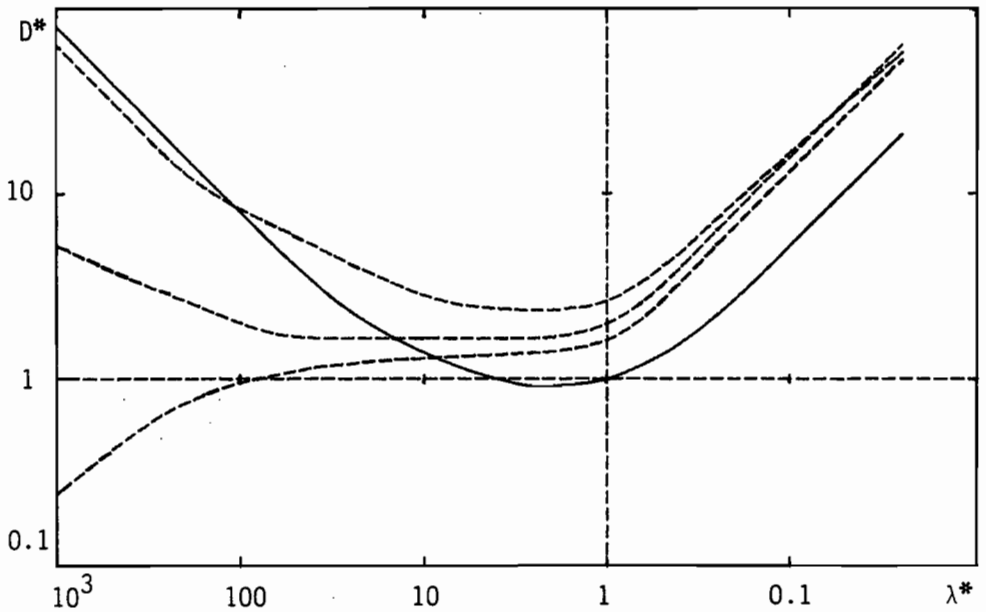
D*
10
1
0.1
10^3
100
10
1
0.1
λ*

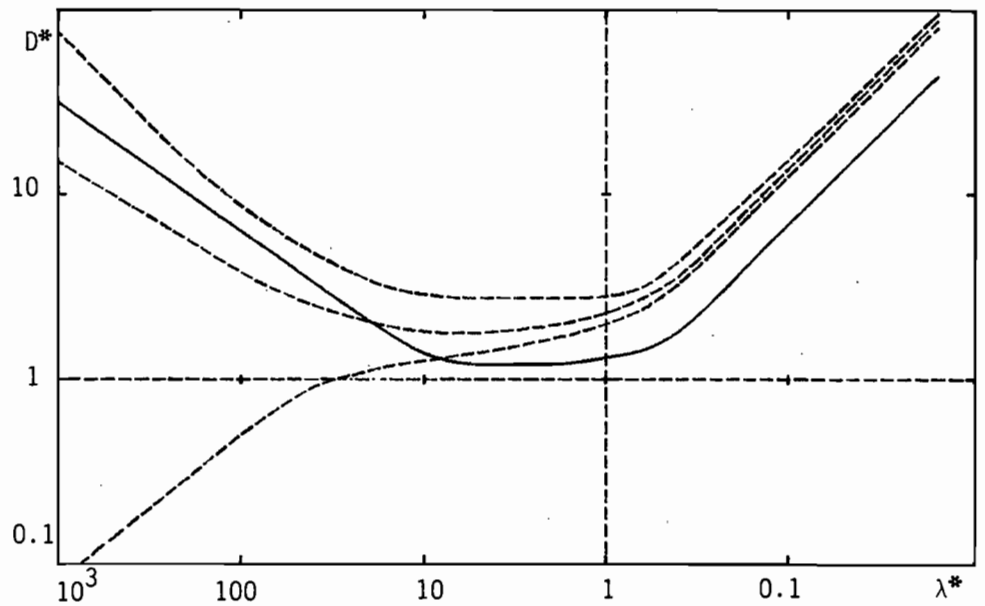
D*
10
1
0.1
10^3
100
10
1
0.1
λ*

RESISTIVE MODES IN TOKAMAK-STELLARATOR CONFIGURATIONS*

H. R. Hicks,† B. Carreras, L. Garcia,
J. A. Holmes,† and V. E. Lynch†

Oak Ridge National Laboratory
Oak Ridge, Tennessee 37830 U.S.A.

ABSTRACT

The stability and nonlinear evolution of MHD tearing modes is studied for tokamaks with stellarator windings. The approach builds on techniques used for tokamak calculations. However, there are several significant complications that are absent in the pure tokamak problem.

Introduction

A standard procedure for studying tearing modes in tokamaks is first to calculate an axisymmetric MHD equilibrium. In general, this is done by solving the Grad-Shafranov equation on the poloidal plane, although in certain limits analytic equilibria exist. For an unstable equilibrium, the linear growth rate and eigenfunction of the fastest growing tearing mode instability can be determined by a linear initial value calculation using the reduced MHD equations.[1] The nonlinear evolution of such instabilities can be studied with a nonlinear initial value code.[2] We shall investigate how these methods, and the techniques used to accomplish them, can be employed for tokamaks with stellarator windings.

Several lessons can be drawn from the tokamak initial value calculations. Linear stability analysis is not completely adequate. Nonlinear evolution is needed to determine both the time scale and the extent of damage of unstable modes. Correct geometry is necessary in order to get a level of detail sufficient to compare with experiment. In three-dimensional (3-D) calculations with resistivity, not only can the flux topology change, but flux surfaces can be destroyed. Finally, there are two rather technical points: it is desirable to have an equilibrium solver which is compatible with the initial value code to be used, and a Fourier

* Research sponsored by the Office of Fusion Energy, U.S. Department of Energy, under contract W-7405-eng-26 with the Union Carbide Corporation.

† Computer Sciences at ORNL.

series representation in toroidal and poloidal angles is usually more economical than finite difference grids in these directions.[3]

For the numerical experiments presented here, the strategy conforms with these lessons, except that circular cylinder geometry is used. The equations to be solved are the low-β, reduced, resistive MHD equations. Although considerable work has been done by others on stellarator equilibrium and stability, it is hoped that our somewhat different strategy will yield results that will complement such work.

Three techniques for adding external helical (stellarator) fields will be considered. In each case, one must first determine a tokamak equilibrium. For the low-β, circular cylinder case this can be done analytically. The procedure is to algebraically define a q profile for the plasma [Fig. 1b (upper curve)]. The equilibrium poloidal flux function is given by

$$\frac{\partial}{\partial r}\psi_{eq}(r)=\frac{-r}{q_p} \ , \tag{1}$$

From this the toroidal plasma current density can be derived (Fig. 1a),

$$J_{eq}=\frac{1}{r}\frac{\partial}{\partial r}\left[r\frac{\partial}{\partial r}\psi_{eq}(r)\right] \ .$$

These profiles will be used in the remainder of this work.

Now, consider the vacuum field generated by a helical coil with toroidal winding number n_c and poloidal winding number l. The poloidal flux function due to this coil is given by

$$\psi_{l,n_c}(r,\theta,\zeta)=rb_l I_l(nr/R)\cos(l\theta+n_c\zeta) \ ,$$

which is well approximated by

$$\psi_{l,n_c}(r,\theta,\zeta)=\left(\phi_{l,n_c}\frac{n_c}{l-1}\right)1/2\,\frac{r^l}{l}\cos(l\theta+n_c\zeta) \ , \tag{2}$$

where ϕ_{l,n_c} is a constant related to the coil current.

It is possible to calculate an average $\phi_{l,n_c}(r)$ by averaging the vacuum field over the $n_c\zeta$ oscillations.[4] The result is

$$\iota_{ext} = \frac{l}{2n_c r}\frac{\partial}{\partial r}\left(\frac{\psi_{l,n_c}}{r}\frac{\partial}{\partial r}\psi_{l,n_c}\right) \approx \iota_{l,n_c} r^{2l-4} \quad . \tag{3}$$

So, the parameter ι_{l,n_c} chosen in Eq. (2) is actually the average rotational transform at the plasma edge (r = 1) due to the coil with winding numbers l,n_c.

Average Method (or Stellarator Expansion)

If the toroidal winding number of the helical coil n_c is large compared with the toroidal mode numbers to be considered, then it is appropriate to consider only the toroidally averaged helical field. In this model, the tokamak equilibrium is modified by adding ι_{ext} from Eq. (3),

$$\iota_{tot}(r) = \iota_p(r) + \iota_{ext}(r) \quad . \tag{4}$$

This can be accomplished with

$$\frac{\partial}{\partial r}\psi_{eq}(r) = -\frac{r}{q_p(r)} - \iota_{ext} r^{2l-3} \quad . \tag{5}$$

The added term produces zero toroidal current; so, the current density profile is unchanged.

This new equilibrium is axisymmetric, since the toroidal variable has been averaged over. The effect on the total q profile is shown in Fig. 1b. This method is important because of its simplicity and historical role.

Vacuum Coil Field Method

In order to see the effects of toroidal dependence of the helical field, for this method we use a tokamak equilibrium field plus the poloidal flux function of a helical coil [Eq. (2)] as an initial condition. The field components with the symmetry of the coil (l,n_c) are not allowed to evolve in time. This initial condition is not a self-consistent equilibrium. Moreover, the stability results obtained from this initial condition are contrary to those obtained with the following more complete model.

Calculated Equilibrium

Using the reduced MHD equations plus some dissipation, relax from the helical initial state (above) to an equilibrium which has the symmetry of the system. All components, including the one corresponding to the helical coil, are allowed to evolve. The boundary flux values are held fixed in time, thus retaining the effects from the external helical coil.

Three dissipative procedures have been tested and are listed as follows:

(1) removing velocity at each iteration (Fig. 2a),

(2) ion viscosity, and

(3) resistivity (Fig. 2b).

When only one helical coil is present, the equilibrium solution is required to have helical symmetry. In this case, for a wide range of q_p and ψ_{ext}, these relaxation methods successfully carry the equations to equilibrium solutions. These solutions depend somewhat on the method of relaxation, but they strongly resemble the initial state and are dominated by its characteristics (Fig. 3).

When the initial state consists of a tokamak equilibrium plus the vacuum field from two helical coils of different pitch, then helical symmetry is broken and one has a true 3-D solution. We still demand that the equilibrium solutions have the symmetry of the device. For example, if we combine ($l = 2; n_c = 4$) and ($l = 3; n_c = 4$) coils, then we require that the solution contain only n = 4, 8, 12, ... components. Such initial states generally contain flux surfaces surrounded by stochastic magnetic field. The volume containing flux surfaces gets larger when either one of the external helical currents is reduced (Fig. 4a,b,c) or the plasma current is reduced (Fig. 4b,d). We have shown that when the helical fields are not too strong, even the 3-D case can be relaxed (Fig. 5a) to an equilibrium (Fig. 5b) using this technique.

Nonlinear Stability

Taking an initial condition determined in one of these three ways, we add a small perturbation of m = 2, n = 1 mode. This test mode, when it is unstable, will grow to saturation. We characterize its final state by the saturated island width. This is indicated in Fig. 6a as a function of ψ_{ext} due to a single helical coil ($l = 2; n_c = 4$). For comparison the average method result is seen to be slightly more optimistic (more stable). The field line configuration for the final, saturated magnetic island, state is shown in Fig. 6b for $\psi_{ext} = 0.9$.

Numerical Representation

For both the relaxation to equilibrium and the subsequent nonlinear evolution, the solution functions are written as expansions in θ and ζ

$$\psi(r,\theta,\zeta) = \sum_{m,n} \psi_{mn}(r)\cos(m\theta + n\zeta) \quad . \tag{6}$$

For the tokamak case, this is a much more economical representation than a finite difference grid in θ and ζ would be because the tokamak solutions can be well represented by a fairly small number of terms in Eq. 6. The tokamak-stellarator cases studied so far indicate that such a geometry will generally require more terms in Eq. (6), but this representation is still probably more economical than a 3-D finite difference grid would be. For the special case of relaxation to a helical equilibrium, the series representation is very economical, requiring generally less than seven modes. Evolution of the (m = 2;n = 1) mode in a helical equilibrium can be studied with as few as 16 terms. Relaxation to a 3-D equilibrium dominated by two helical coils can be performed accurately with 21 modes.

REFERENCES

1. H. R. Strauss, Phys. Fluids *19*, 134 (1976).

2. B. Carreras, H. R. Hicks, J. A. Holmes, and B. V. Waddell, Phys. Fluids *23*, 1811 (1980).

3. H. R. Hicks, B. Carreras, J. A. Holmes, D. K. Lee, and B. V. Waddell, to be published in J. Comput. Phys.

4. J. L. Johnson, C. R. Oberman, R. M. Kulsrud, and E. A. Frieman, Phys. Fluids *1*, 281 (1958).

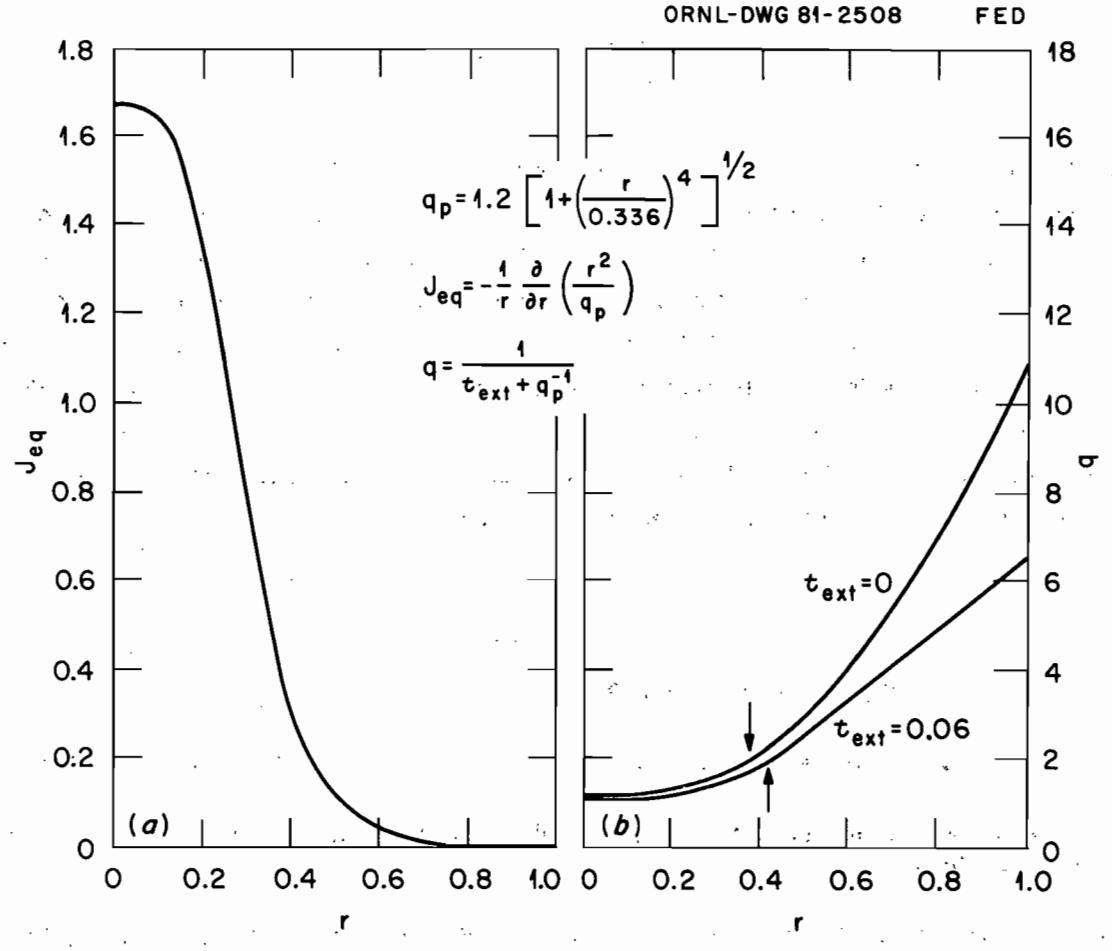

Fig. 1. Plasma toroidal current density profile (a) and q profile (b) are shown. In the stellarator expansion model, the addition of an $l = 2, \iota_{ext} = 0.06$ helical field leaves the current unchanged but lowers the q profile.

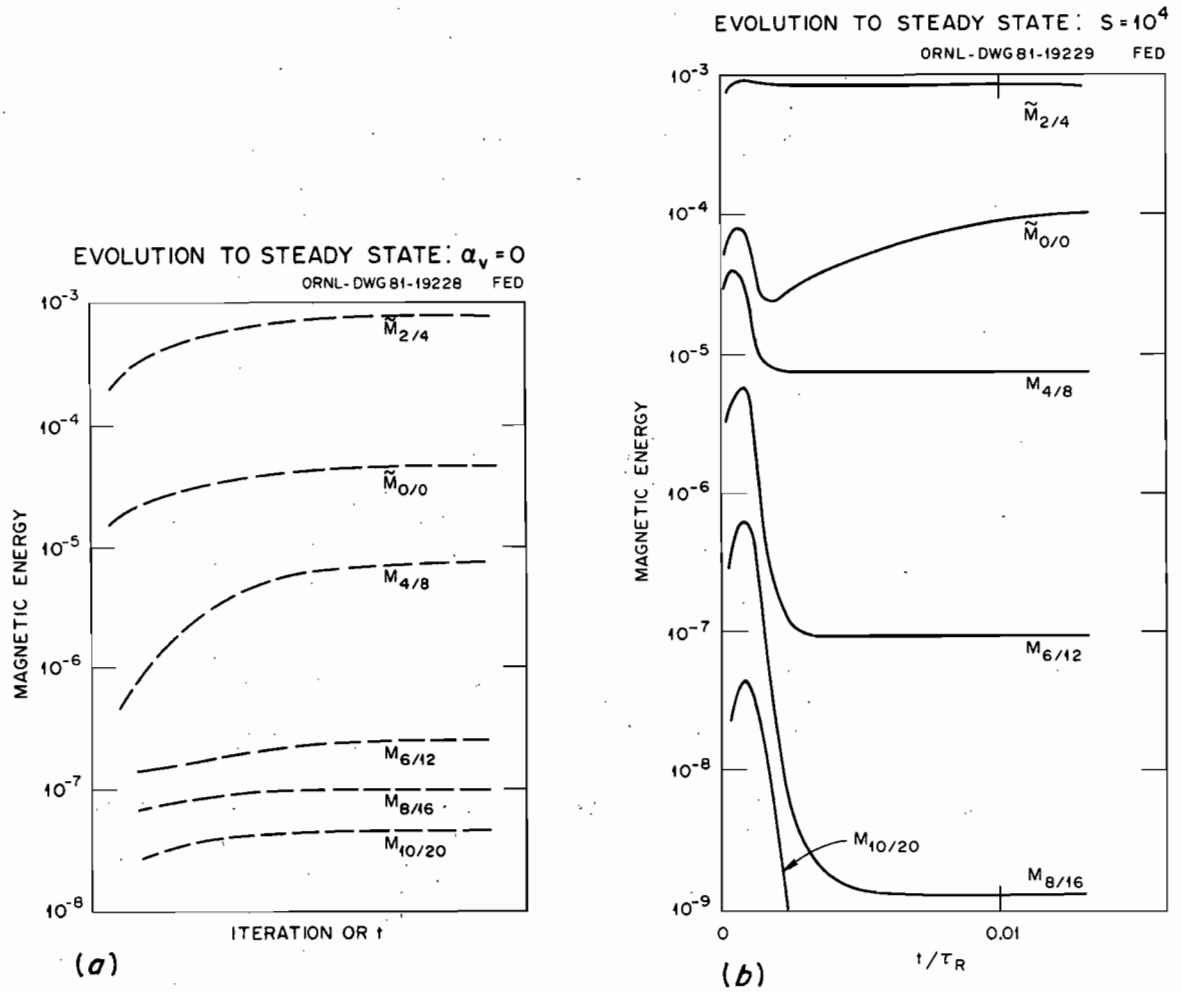

Fig. 2. Magnetic energy evolution of all components in the iteration to a single-helicity equilibrium. Two relaxation methods are shown: (a) zeroing the velocity every step and (b) using large resistivity.

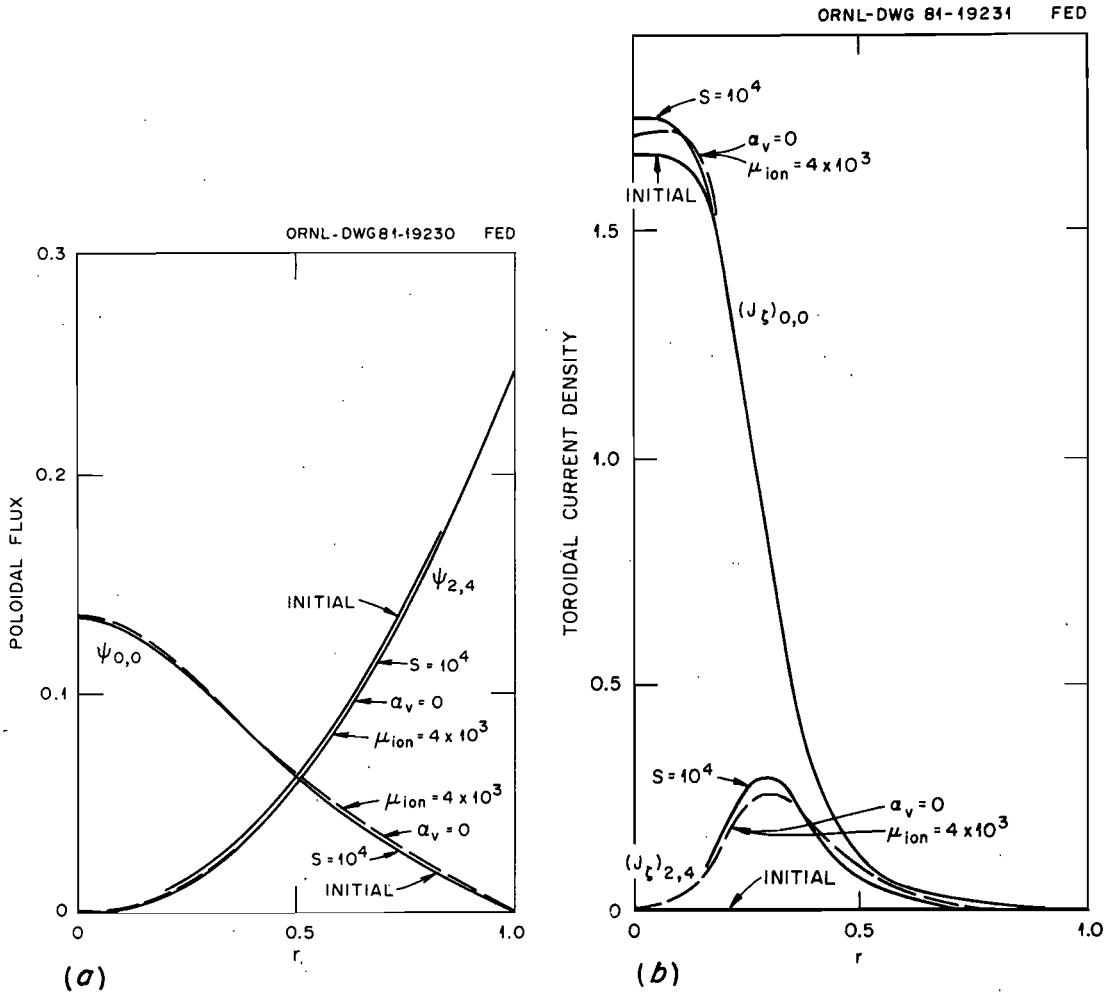

Fig. 3. Comparison of the (nonequilibrium) initial condition with the (equilibrium) relaxed states resulting from the three methods of relaxation used. The two largest components of poloidal flux (a) and toroidal current density (b) are shown.

ORNL-DWG. 82-8514

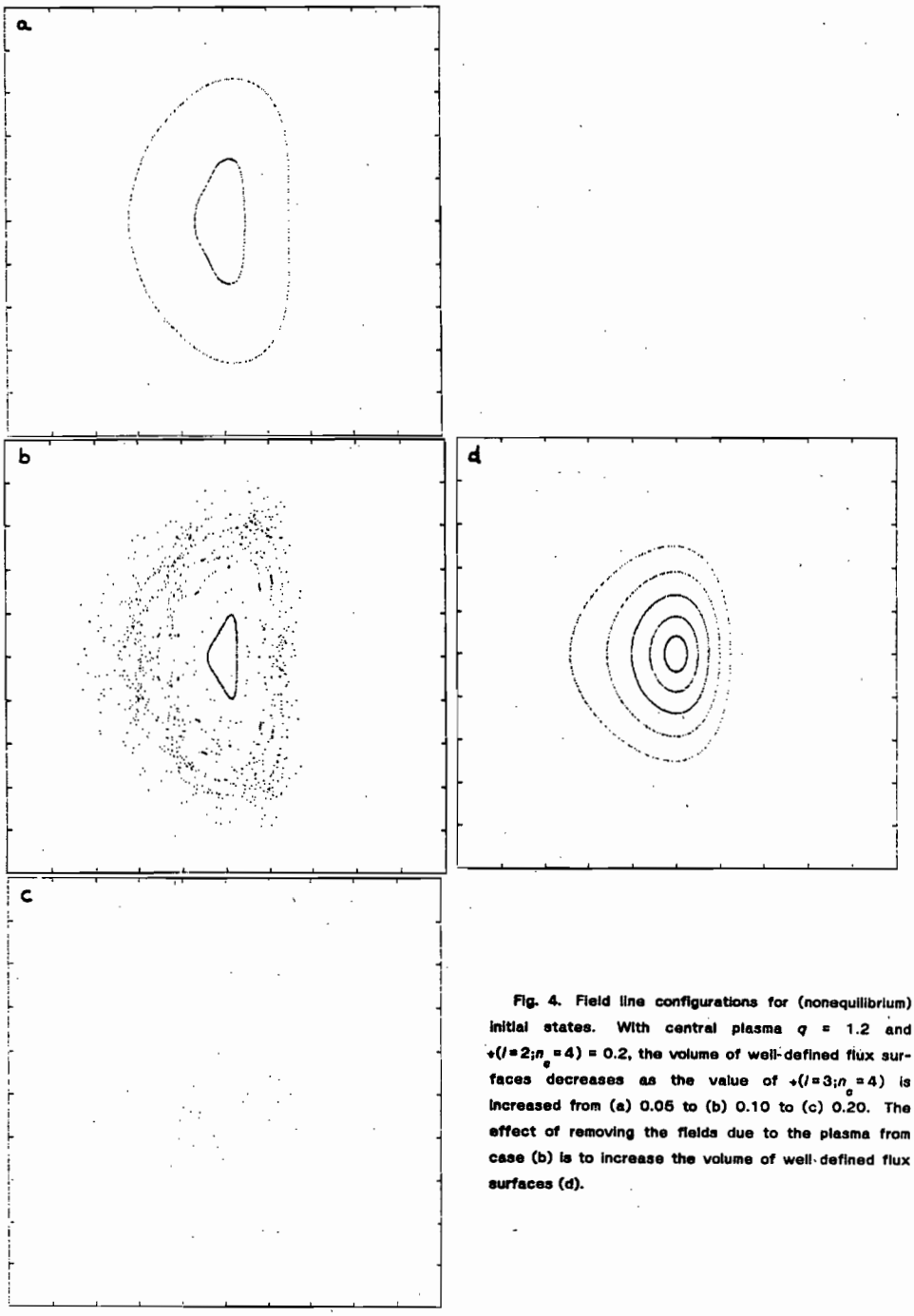

Fig. 4. Field line configurations for (nonequilibrium) initial states. With central plasma q = 1.2 and $\psi(l=2;n_\theta=4)$ = 0.2, the volume of well-defined flux surfaces decreases as the value of $\psi(l=3;n_\theta=4)$ is increased from (a) 0.05 to (b) 0.10 to (c) 0.20. The effect of removing the fields due to the plasma from case (b) is to increase the volume of well-defined flux surfaces (d).

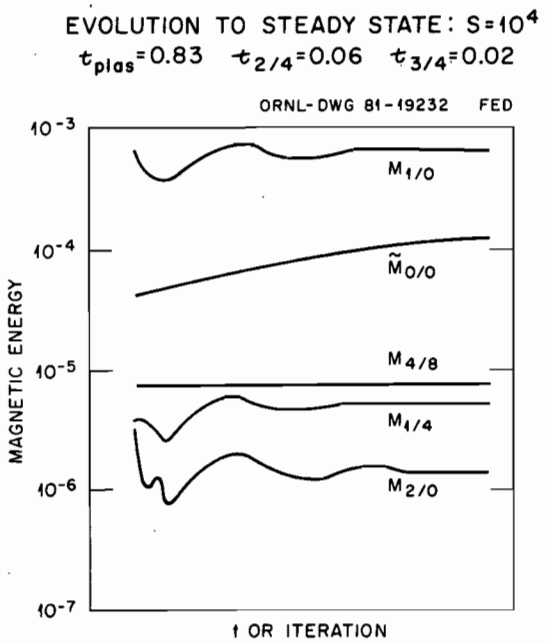

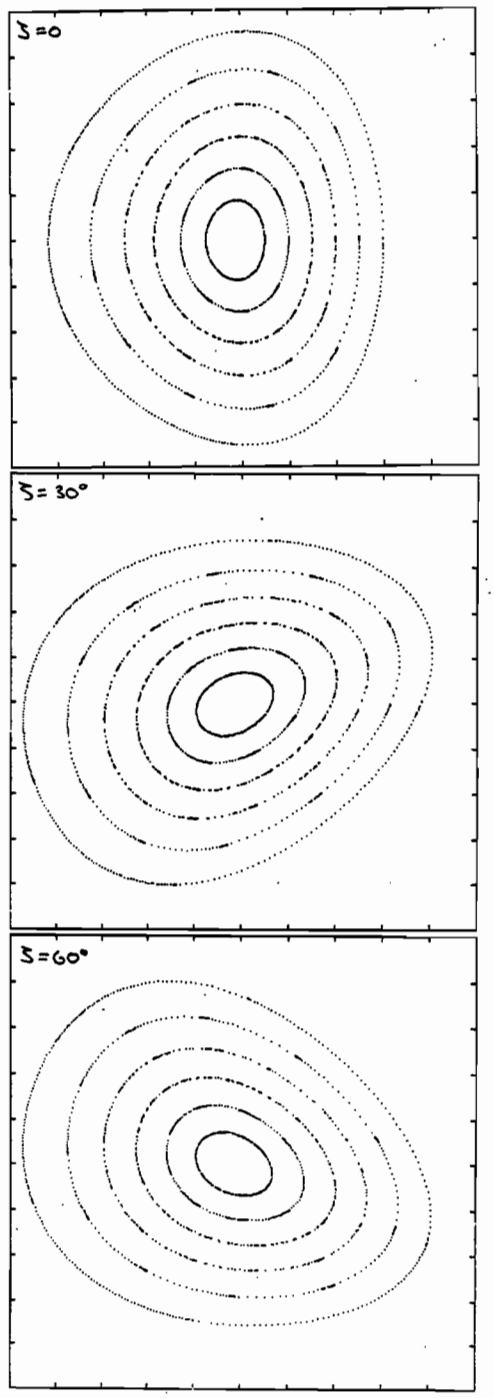

Fig. 5. Relaxation to equilibrium of a case with two small helical perturbations. The result is a 3-D equilibrium.

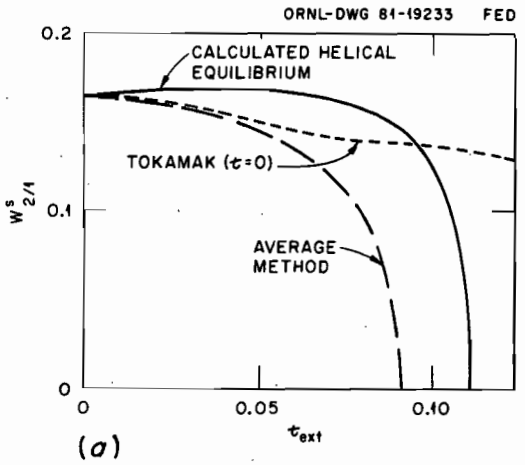

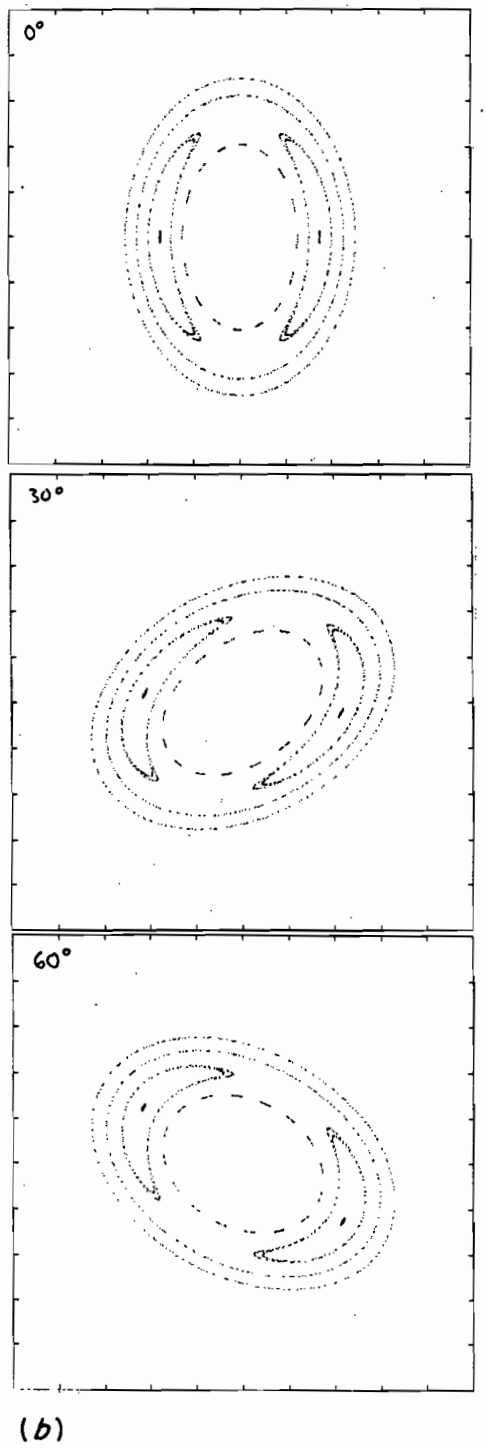

Fig. 6. The saturated width of the (m = 2;n = 1) tearing mode is shown (a) for a sequence of helical equilibria with increasing $\iota(l = 2; n_c = 4)$. The field line configuration is shown (b) on three poloidal planes for $\iota(l = 2; n_c = 4)$ = 0.9.

Stellarator Stability as a Two-Dimensional Problem

D. A. Monticello and H. R. Strauss*

Plasma Physics Laboratory, Princeton University

Princeton, New Jersey 08544

We report here on a method of solving the 3-dimensional stability problem of stellarators by an averaging method that reduces the problem to two 2-dimensional problems. We use the usual reduced MHD equations appropriate for large aspect ratio, $q \sim 1$ devices generalized to include helical fields that are of the order of the $\sqrt{\varepsilon}\, B_o$. Here, ε is the inverse aspect ratio of the device and B_o is the large toroidal field. The reduction to a 2-dimensional problem is made by taking N, the number of helical periods to be large, i.e., $N \sim \frac{1}{\varepsilon}$, and to look for long wave length modes i.e. $\lambda \sim R$. This procedure is effected by using the techniques of the multiple scale length expansion. The two disparate length being R and R/N. The resulting averaged reduced equations differ from the high β toroidal equations only in that the flux now contains a contribution from the external helical current, as well as contribution from the plasma currents. In addition the curvature term is also modified by the average curvature of the external helical fields.

For this report we have studied two stellarator devices W-VII with parameters $\ell = 2$, $ha = .25$, $q(a) = 1.8$, $\varepsilon = \frac{1}{20}$, $N = 5$. Here, ℓ is the poloidal harmonic number of the helical field coils, $h = N/R$, and q is the safety factor. Heliotron E has values $\ell = 2$, $ha = 1.8$, $q(a) = .55$, $\varepsilon = \frac{1}{10}$ and $N = 19$.

The equilibrium is solved for by constraining the net current through each flux surface to vanish, i.e., a true resistive equilibrium for the case of no ohmic driving voltage.

Figure (1) shows the flux contours, Fig. (2) the current profile across the midplane, and Fig. (3) the current contours for the W-VII device. The corresponding figures for Heliotron E are quite similar. We stress that these are plots of averaged quantities. For example the outer flux surface is not really circular but is given by $r/a = 1 + \left[\varepsilon\iota/ha(\ell-1)\right]^{1/2}\cos(\ell\theta - N\zeta)$ to order $\sqrt{\varepsilon}$. Here we are using toroidal coordinates r, θ, ζ. The fact that the shear is much larger in Heliotron E than in W-VII is illustrated in Fig. (4) and (5).

Figure (6) shows a $\langle\beta\rangle_c \sim .5\%$ for W-VII for $q(a) = 1.85$. However, Figs. (7) and (8) show that complete stability of the W-VII device is possible for toroidal mode numbers up to 3, if $q(a) = 1.7$. These results can be achieved because the low shear in W-VII make it possible to keep any singular surfaces from being inside the plasma.

It is not possible to achieve complete stabilization in Heliotron E, however, because of its large shear the critical beta is quite high, of the order of 1.5%, Fig. (9). Also in contrast to W-VII there does not appear to be any second region of stability in Heliotron E. This is probably due to the fact that the bad helical curvature is about 8 times larger than that for W-VII.

We remark here on the applicability of our results by considering how well each device satisfies our approximations. ε is small in both devices, however, the expansion is in $\sqrt{\varepsilon}$, meaning terms of the order of 20% have been neglected for W-VII and terms of the order of 30% have been neglected for Heliotron E. The number of helical periods in heliotron is quite large,

giving good separation between the two length scales, where as this separation is not as good in W-VII.

Details of these calculations may be found in Phys. Fluids 24, 6 (June 1981).

*Permanent address: Courant Institute of Mathematical Sciences, New York University, New York, N.Y. 10012.

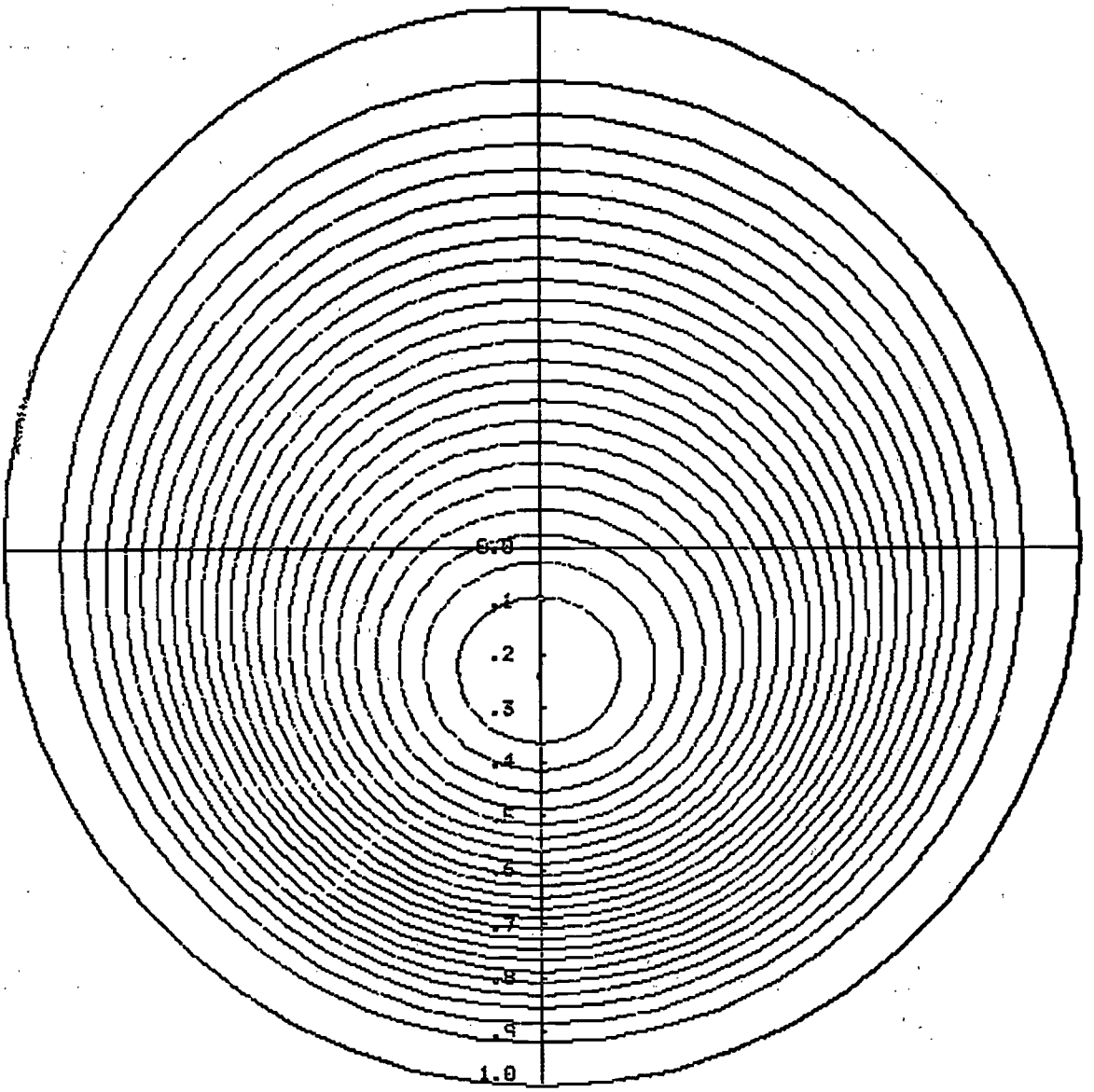
0.0
.1
.2
.3
.4
.5
.6
.7
.8
.9
1.0

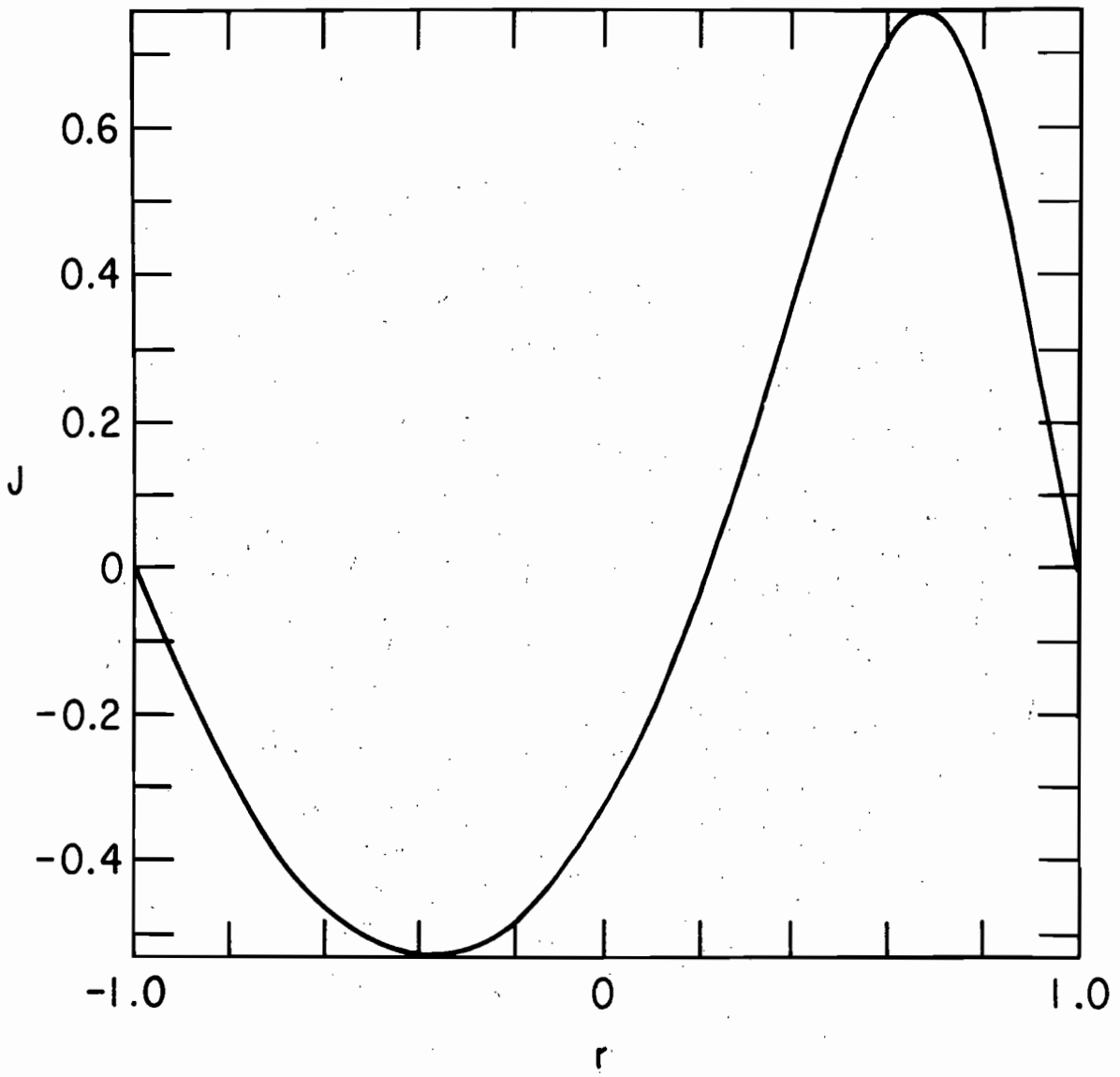
0.6
0.4
0.2
J
0
-0.2
-0.4
-1.0
0
1.0
r

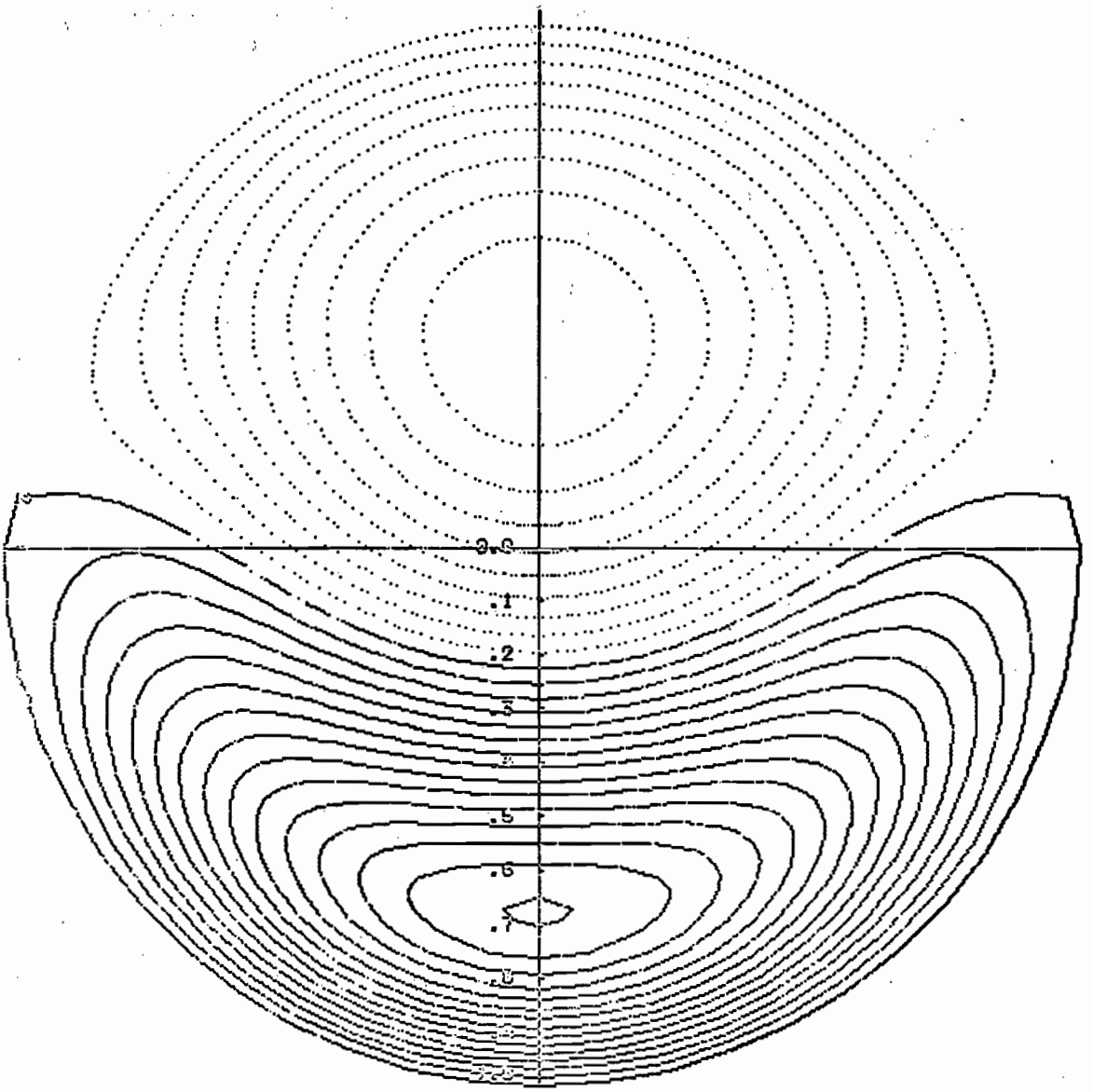
0.0
.1
.2
.3
.4
.5
.6
.7
.8

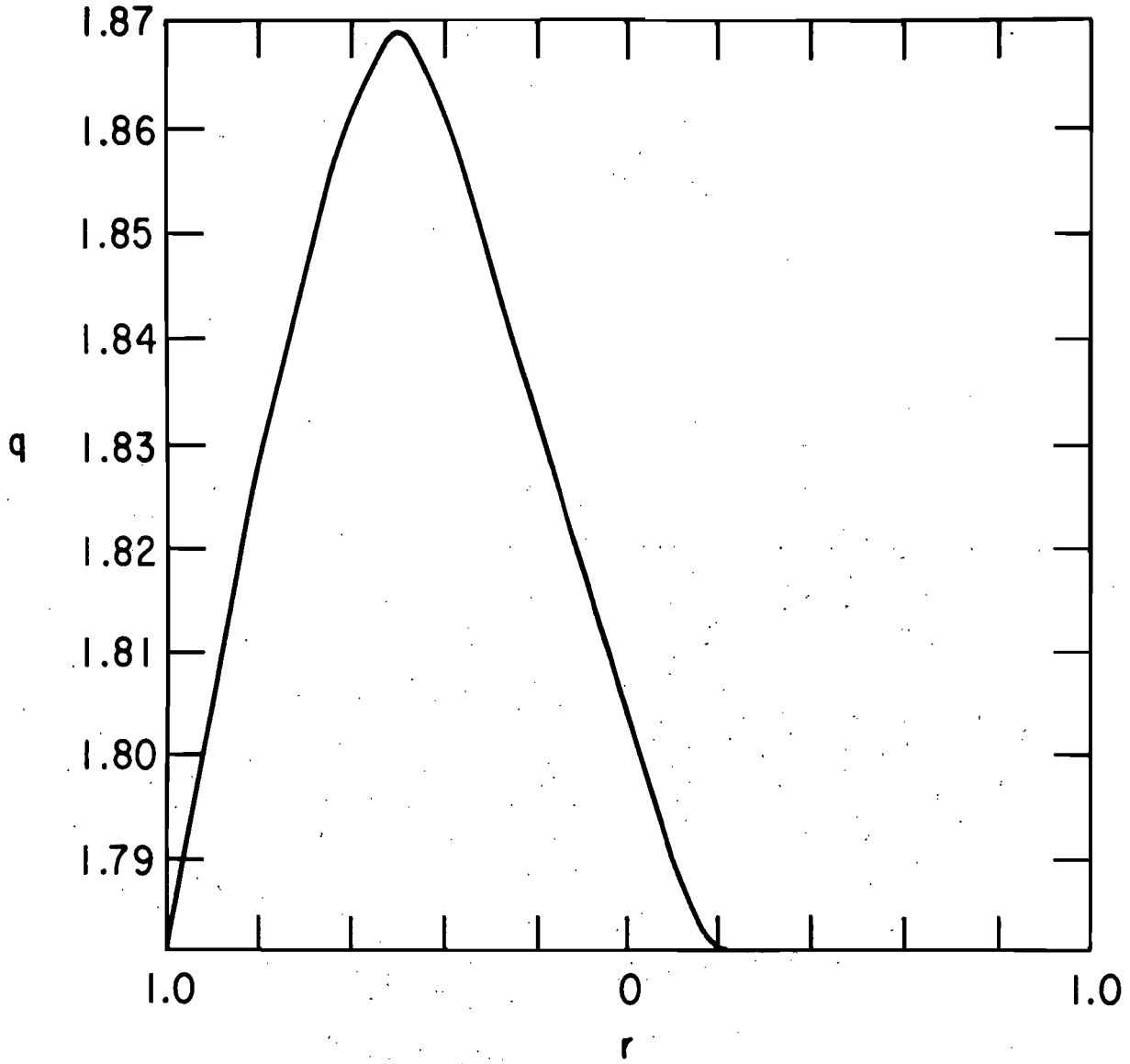
1.87
1.86
1.85
1.84
q
1.83
1.82
1.81
1.80
1.79
1.0
0
1.0
r

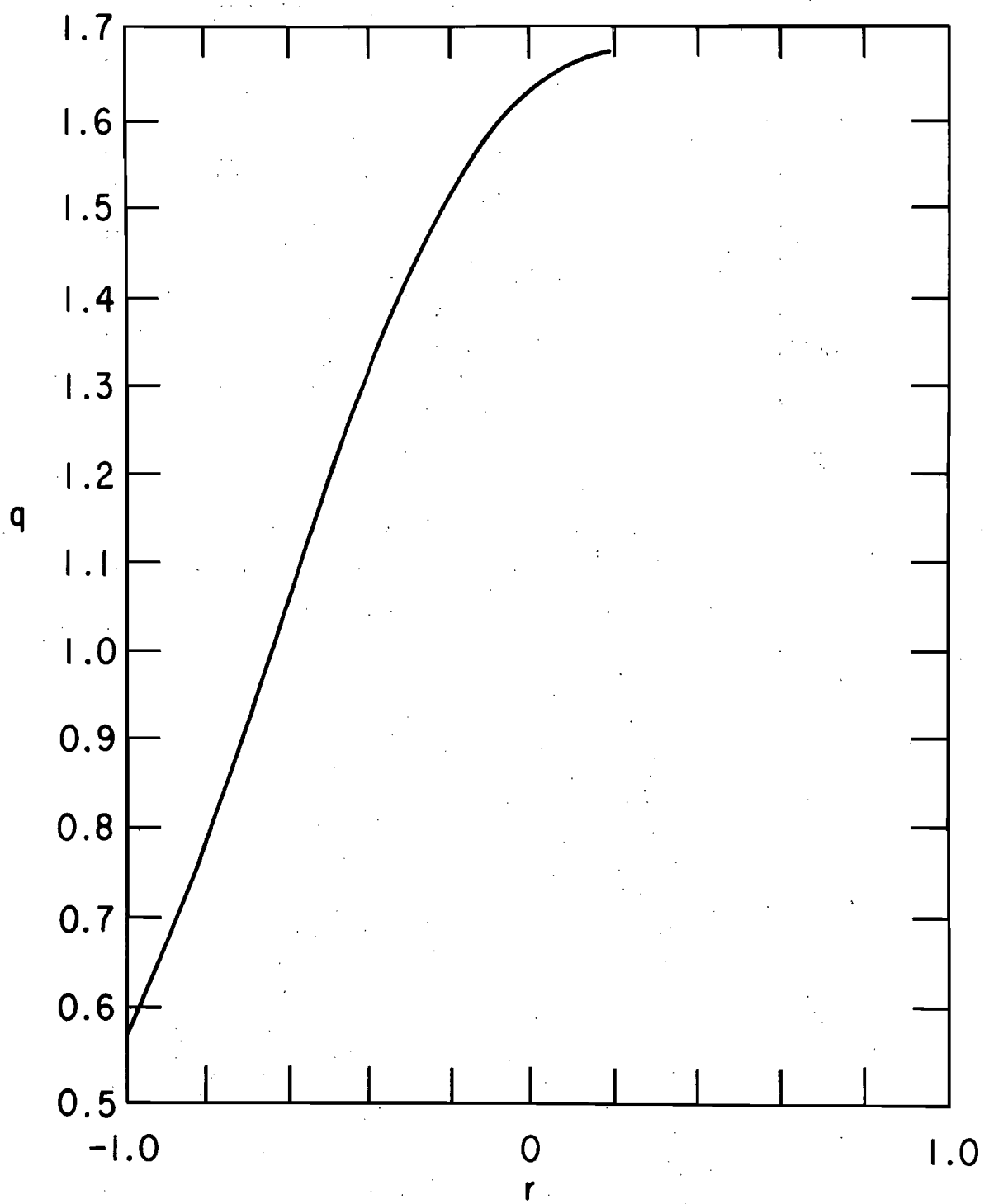
1.7
1.6
1.5
1.4
1.3
1.2
q
1.1
1.0
0.9
0.8
0.7
0.6
0.5
-1.0
0
1.0
r

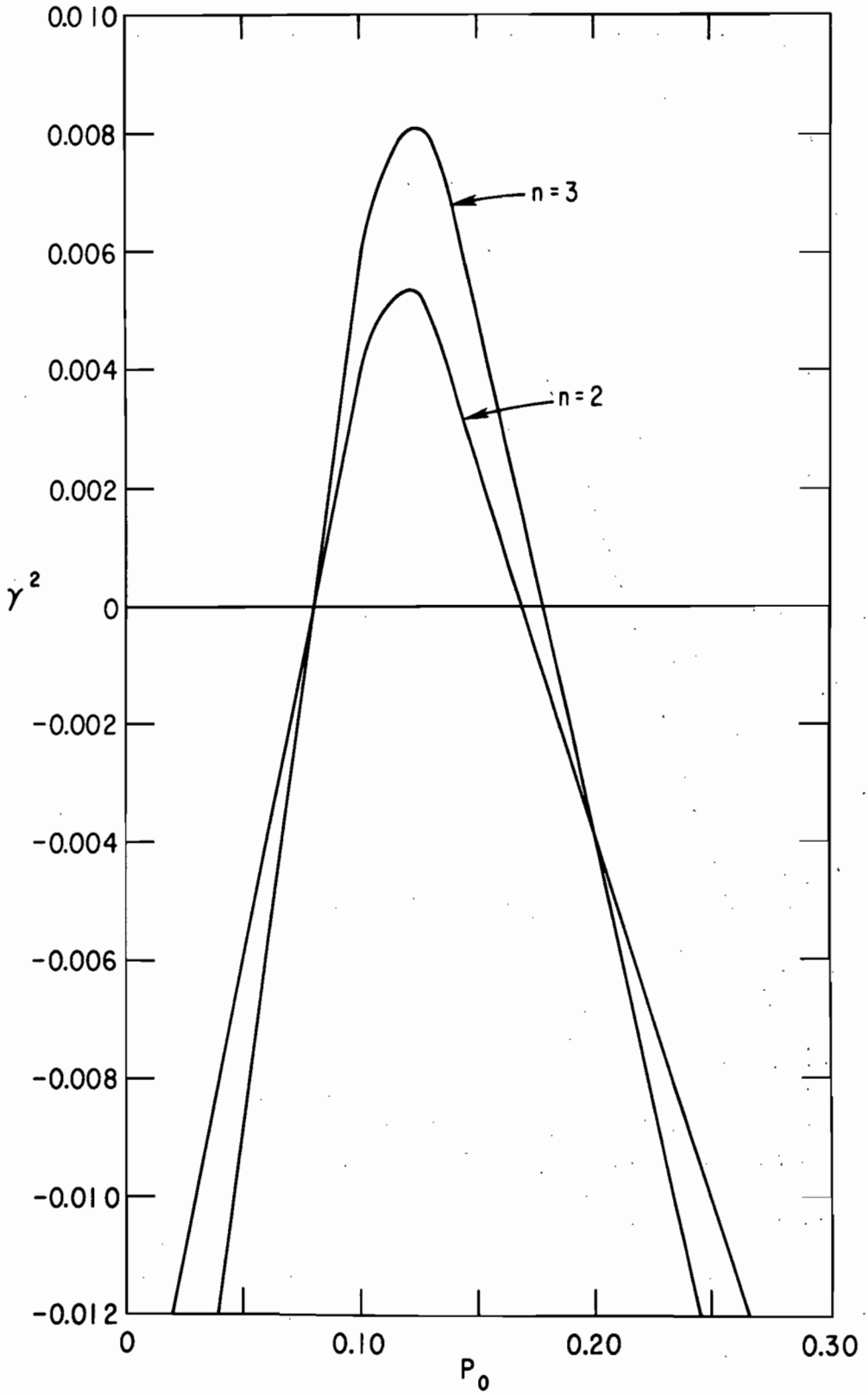
0.010
0.008
0.006
0.004
0.002
0
-0.002
-0.004
-0.006
-0.008
-0.010
-0.012
γ^2
n = 3
n = 2
0
0.10
0.20
0.30
P_0

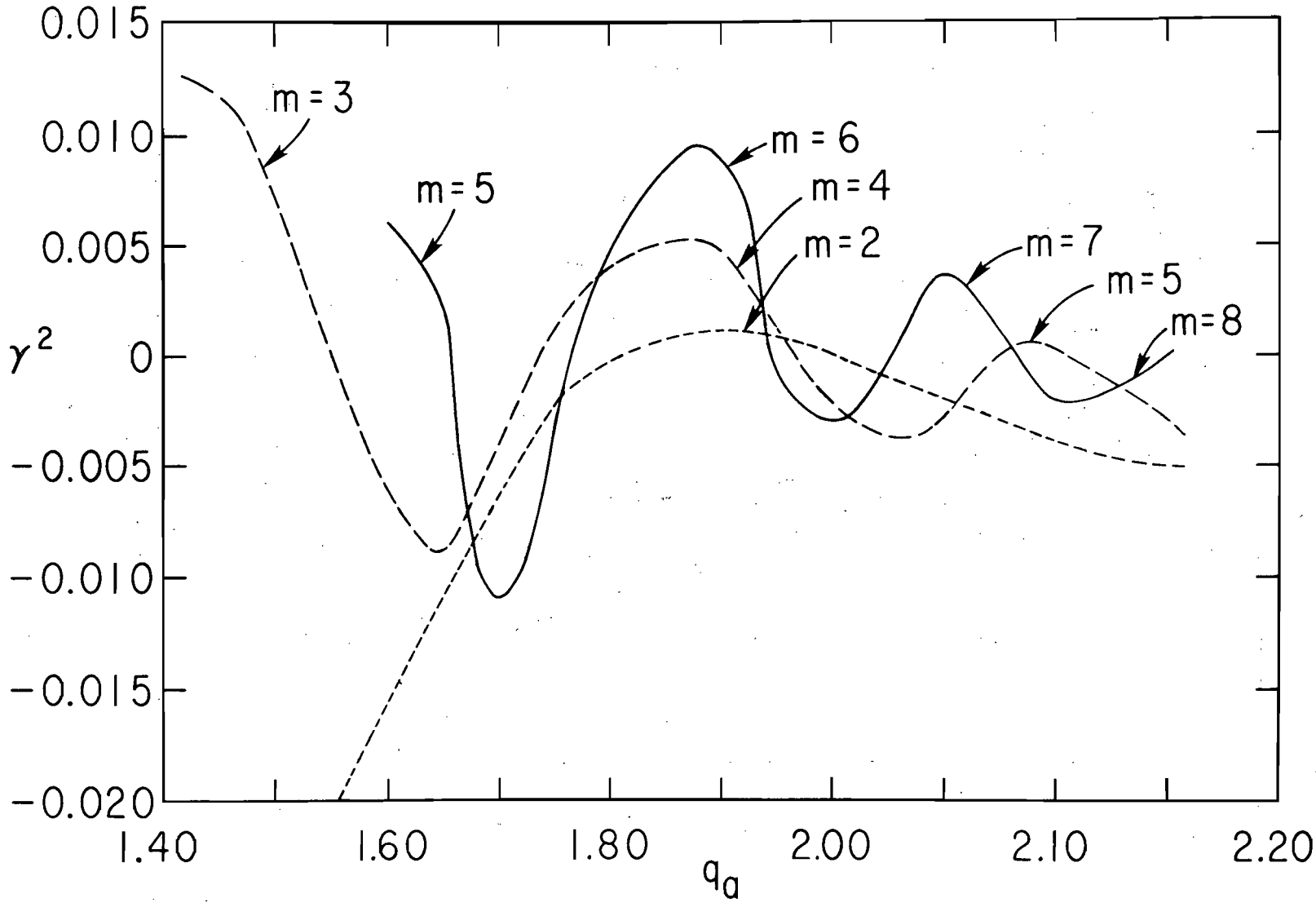
0.015
0.010
0.005
0
-0.005
-0.010
-0.015
-0.020
γ^2
1.40
1.60
1.80
2.00
2.10
2.20
q_a
m = 3
m = 5
m = 6
m = 4
m = 2
m = 7
m = 5
m = 8

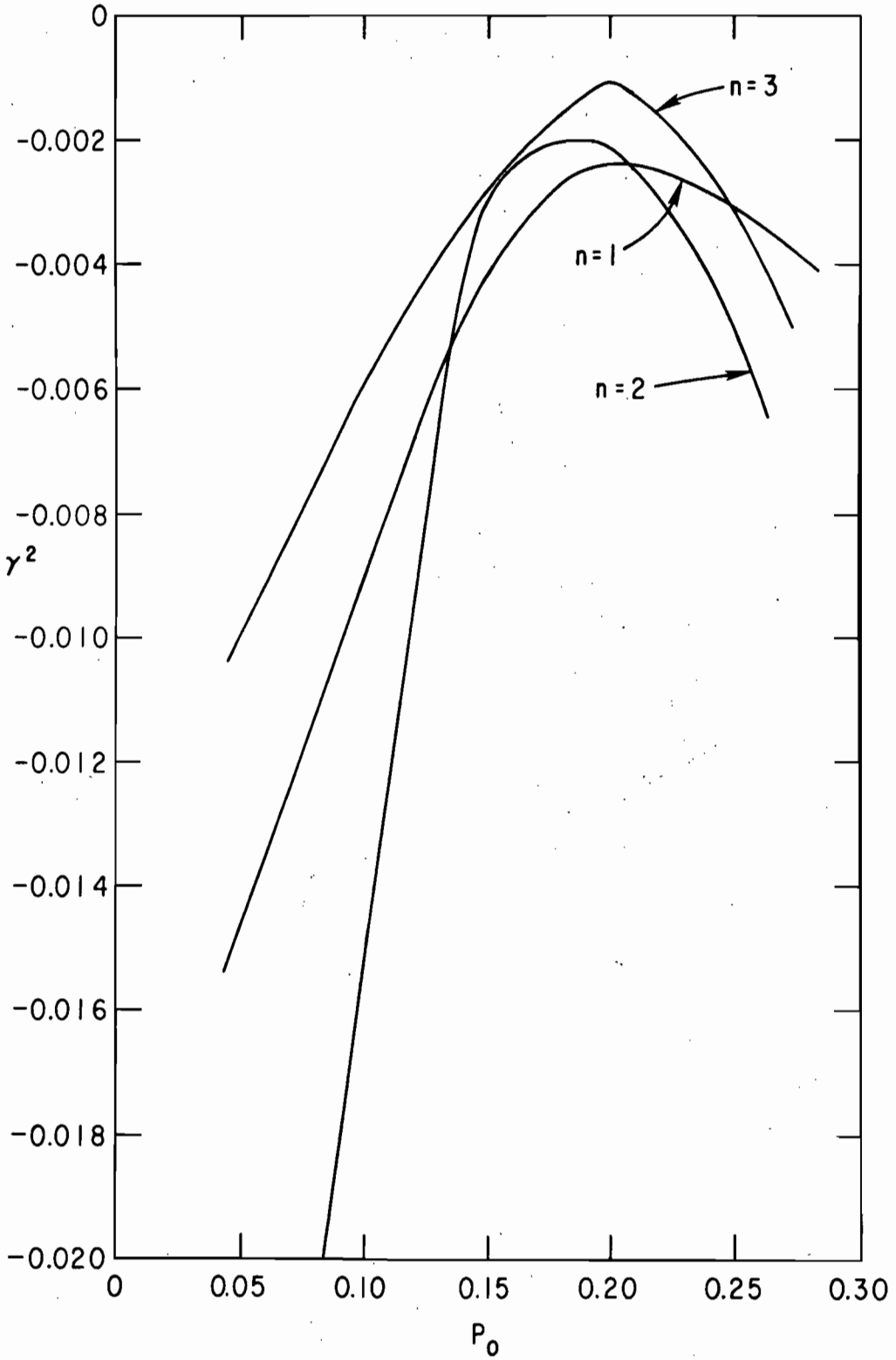
0
-0.002
-0.004
-0.006
-0.008
-0.010
-0.012
-0.014
-0.016
-0.018
-0.020
γ^2
0
0.05
0.10
0.15
0.20
0.25
0.30
P_0
n = 3
n = 1
n = 2

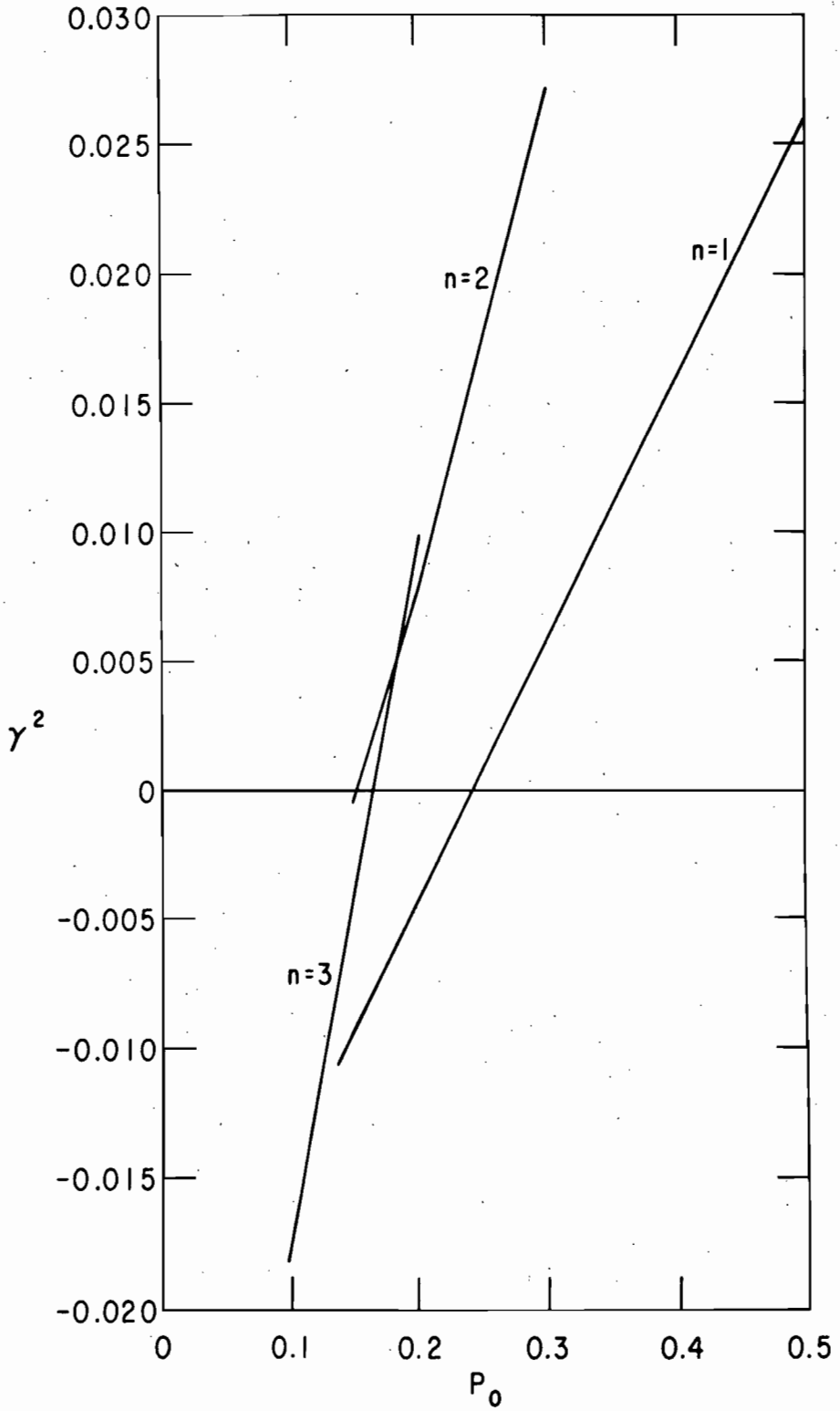
0.030
0.025
0.020
0.015
0.010
0.005
0
-0.005
-0.010
-0.015
-0.020
γ^2
n=1
n=2
n=3
0
0.1
0.2
0.3
0.4
0.5
P_0

VARIATIONAL METHOD FOR THE THREE-DIMENSIONAL INVERSE EQUILIBRIUM PROBLEM IN TOROIDS

A. Bhattacharjee*, Institute for Fusion Studies, The University of Texas at Austin, Austin, Texas 78712.

I. Introduction

The computation of magnetostatic equilibria in toroids is crucial to the study of plasma stability and transport in toroidal devices such as the tokamak and the stellarator. In axisymmetric devices like the tokamak, these equilibria are described by the Grad-Shafranov equation

$$\vec{\nabla} \cdot \left(\frac{\vec{\nabla}\Psi}{R^2}\right) + p'(\Psi) + \frac{FF'(\Psi)}{R^2} = 0 \quad , \tag{1}$$

which is commonly solved in cylindrical coordinates (R,ϕ,Z) with ϕ as the ignorable coordinate. In the work of Greene, Johnson and Weimer[1] on tokamak equilibria, it has been indicated, however, that a very useful set of coordinates is the magnetic flux surface coordinates (v,θ,ζ), where v is a radial flux surface label, and θ and ζ are respectively the poloidal and toroidal angles parameterizing a flux surface. Indeed, since the magnetic surface coordinates have built into themselves the properties characterizing any toroidal equilibrium, they define the most natural coordinate system in which an equation, such as equation (1), may be studied. With this point of view, we will attempt to determine the mapping

$$R = R(v,\theta,\zeta) \quad , \tag{2a}$$

$$\phi = \phi(v,\theta,\zeta) \quad , \tag{2b}$$

$$Z = Z(v,\theta,\zeta) \quad , \tag{2c}$$

for toroidal equilibria, a problem we have called the three-dimensional inverse equilibrium problem in toroids. Figure 1 depicts the two coordinate systems (R,ϕ,Z) and (v,θ,ζ); both are right-handed.

In a recent paper, Lao, Hirshman and Wieland[2] have constructed a variational principle for the Grad-Shafranov equation (1). For the axisymmetric case, which is their concern, they have considered the mapping

$$R = R(v,\theta) \quad , \tag{3a}$$

*This work is the result of a collaboration with J. C. Wiley (Fusion Research Center, University of Texas at Austin) and R. L. Dewar (Plasma Physics Laboratory, Princeton University).

$$\phi = \zeta , \tag{3b}$$

$$Z = Z(v,\theta) , \tag{3c}$$

which is a particular case of equations (2).

In this paper, we develop a variational method for three-dimensional equilibria in toroids. The method generalizes the approach of Lao, Hirshman and Wieland to embrace all mappings of the form given by equations (2). Needless to say, the variational principle of Lao, Hirshman and Wieland is too restrictive to be of use in the general case. The crucial point is to begin with a variational principle for the magnetostatic equations

$$\vec{J} \times \vec{B} = (\vec{\nabla} \times \vec{B}) \times \vec{B} = \vec{\nabla} p , \tag{4a}$$

$$\vec{\nabla} \cdot \vec{B} = 0 , \tag{4b}$$

where p is the scalar pressure of a plasma confined by a magnetic field $\vec{B}$, and $\vec{J}$ is the current density. The variational principle we use is described in Section II and is originally due to Grad.[3]

II. Variational Principle for Magnetostatic Equilibria

It has been demonstrated by Kruskal and Kulsrud[4] that solutions of the magnetostatic equations (4) for plasmas bounded spatially have the property that the magnetic field lines lie on nested surfaces which are topologically toroids. Greene and Johnson[5] have shown that under these conditions the magnetic field $\vec{B}$ may be represented as

$$\begin{aligned} \vec{B} &= \vec{\nabla}\zeta \times \vec{\nabla}\Psi(v) + \vec{\nabla}\Phi(v) \times \vec{\nabla}\theta , \\ &\equiv \vec{\nabla}v \times (\Phi_v \vec{\nabla}\theta - \Psi_v \vec{\nabla}\zeta) , \end{aligned} \tag{5}$$

in the magnetic coordinate system (v,θ,ζ), where $\Psi(v)$ and $\Phi(v)$ are respectively the poloidal and the toroidal flux functions. We will now show that the first variation of the functional

$$L = \int_{V_0} d\tau \left[\frac{B^2}{2} - p \right] , \tag{6}$$

defined over the total volume V_0 of a toroidal plasma bounded by a perfectly conducting wall, subject to the constraint,

$$p = p(v) , \tag{7}$$

vanishes if and only if the magnetostatic equations are satisfied. Since equation (4b) is satisfied identically by the representation of $\vec{B}$ given by equation (5), it will suffice to show that a necessary and sufficient condition for extrema of L is given by equation (4a).

The first variation of L is given by

$$\delta L = \int_{V_0} d\tau [\delta v\{\Phi_v \vec{J}\cdot\vec{\nabla}\theta - \Psi_v \vec{J}\cdot\vec{\nabla}\zeta - p_v\} - \delta\theta\Phi_v \vec{J}\cdot\vec{\nabla}v + \delta\zeta\Psi_v \vec{J}\cdot\vec{\nabla}v] , \tag{8}$$

using the boundary conditions

$$\hat{n} \times \vec{\nabla}\Psi = \hat{n} \times \vec{\nabla}\Phi = 0 , \tag{9a}$$

$$\delta\Psi = \delta\Phi = 0 , \tag{9b}$$

on the conducting wall. Since $\delta L = 0 \; \forall \; \delta v, \delta\theta, \delta\zeta$, the Euler-Lagrange equations are

$$\vec{J}\cdot(\Phi_v \vec{\nabla}\theta - \Psi_v \vec{\nabla}\zeta) - p_v = 0 , \tag{10a}$$

$$\vec{J}\cdot\vec{\nabla}v = 0 , \tag{10b}$$

$$\vec{J}\cdot\vec{\nabla}v = 0 , \tag{10c}$$

Equations (10b) and (10c) are identical, and require that the current $\vec{J}$ lies on the flux surfaces in equilibrium. It is now easily seen from equations (5), (10a) and (10b) that

$$\vec{J} \times \vec{B} = \vec{\nabla}p , \tag{11}$$

which proves that if L is stationary under arbitrary variations subject to the constraints (7) and (9), the Euler-Lagrange equations satisfy the equations of magnetostatics. It is obvious that the argument may be reversed to show that the equation (11), along with the constraint (7), implies that $\delta L = 0$ for arbitrary variations.

III. Variable Inversion

Since L is a scalar, it is independent of the coordinate system in which it is expressed. We now transform from the cylindrical coordinate system (R,ϕ,Z) to the magnetic coordinate system (v,θ,ζ) whereupon $R(v,\theta,\zeta)$, $\phi(v,\theta,\zeta)$ and $Z(v,\theta,\zeta)$ are the new dependent variables in the functional L. The elements of the metric tensor $g_{ij} \equiv \vec{e}_i\cdot\vec{e}_j$, where $\vec{e}_i = \partial\vec{r}/\partial x_i$, for the transformation from (x,y,z) coordinates to (v,θ,ζ) coordinates are

$$g_{vv} = R_v^2 + R^2\phi_v^2 + Z_v^2 , \tag{12a}$$

$$g_{v\theta} = R_v R_\theta + R^2\phi_v\phi_\theta + Z_v Z_\theta = g_{\theta v} , \tag{12b}$$

$$g_{v\zeta} = R_v R_\zeta + R^2\phi_v\phi_\zeta + Z_v Z_\zeta = g_{\zeta v} , \tag{12c}$$

$$g_{\theta\theta} = R_\theta^2 + R^2\phi_\theta^2 + Z_\theta^2 , \tag{12d}$$

$$g_{\theta\zeta} = R_\theta R_\zeta + R^2\phi_\theta\phi_\zeta + Z_\theta Z_\zeta = g_{\zeta\theta} , \tag{12e}$$

$$g_{\zeta\zeta} = R_\zeta^2 + R^2\phi_\zeta^2 + Z_\zeta^2 . \tag{12f}$$

The infinitesimal volume element $d\tau$ is given by

$$d\tau = dxdydz = RdRd\phi dz = \sqrt{\|g\|}\, dvd\theta d\zeta , \tag{13}$$

where

$$\sqrt{\|g\|} \equiv \sqrt{\mathrm{Det}g_{ij}} = R[R_v(\phi_\theta Z_\zeta - Z_\theta\phi_\zeta) + R_\theta(\phi_\zeta Z_v - \phi_v Z_\zeta) + R_\zeta(\phi_v Z_\theta - Z_v\phi_\theta)] . \tag{14}$$

By straightforward manipulations, we get

$$L \equiv \int_0^a dv \int_0^{2\pi} d\theta \int_0^{2\pi} d\zeta \mathcal{L}(R,R_v,R_\theta,R_\zeta,\phi_v,\phi_\theta,\phi_\zeta,Z_v,Z_\theta,Z_\zeta)$$

$$= \int_0^a dv \int_0^{2\pi} d\theta \int_0^{2\pi} d\zeta \sqrt{\|g\|}\left[\frac{\Psi_v^2}{2}\frac{g_{\theta\theta}}{\|g\|} + \frac{\Phi_v^2}{2}\frac{g_{\zeta\zeta}}{\|g\|} + \Psi_v\Phi_v\frac{g_{\theta\zeta}}{\|g\|} - p(v)\right] , \tag{15}$$

where $v = a$ is the radial label for the conducting wall, assumed to be fixed. A necessary and sufficient condition for extrema of L is then given by the Euler-Lagrange equations,

$$Q_1 \equiv \frac{\partial}{\partial v}\frac{\partial\mathcal{L}}{\partial f_v^i} + \frac{\partial}{\partial\theta}\frac{\partial\mathcal{L}}{\partial f_\theta^i} + \frac{\partial}{\partial\zeta}\frac{\partial\mathcal{L}}{\partial f_\zeta^i} - \frac{\partial\mathcal{L}}{\partial f^i} = 0, \tag{16}$$

where $i = 1,2,3$ and $f^1 = R$, $f^2 = \phi$, $f^3 = Z$.
Using now the definition of $\mathcal{L}$ given by equation (15), we obtain the following equations for variations with respect to R, ϕ, and Z respectively:

$$Q_1 \equiv R\left[(Z_\theta\phi_\zeta - \phi_\theta Z_\zeta)\frac{\partial}{\partial v} + (Z_\zeta\phi_v - \phi_\zeta Z_v)\frac{\partial}{\partial\theta} + (Z_v\phi_\theta - \phi_v Z_\theta)\frac{\partial}{\partial\zeta}\right]$$
$$\times\left[\frac{\Psi_v^2}{2}\frac{g_{\theta\theta}}{\|g\|} + \frac{\Phi_v^2}{2}\frac{g_{\zeta\zeta}}{\|g\|} + \Psi_v\Phi_v\frac{g_{\theta\zeta}}{\|g\|} + p\right] + \Psi_v^2\left[\frac{\partial}{\partial\theta}\frac{R_\theta}{\sqrt{\|g\|}} - \frac{R\phi_\theta^2}{\sqrt{\|g\|}}\right]$$
$$+ \Phi_v^2\left[\frac{\partial}{\partial\zeta}\frac{R_\zeta}{\sqrt{\|g\|}} - \frac{R\phi_\zeta^2}{\sqrt{\|g\|}}\right] + \Psi_v\Phi_v\left[\frac{\partial}{\partial\theta}\frac{R_\zeta}{\sqrt{\|g\|}} + \frac{\partial}{\partial\zeta}\frac{R_\theta}{\sqrt{\|g\|}} - \frac{\phi_\theta\phi_\zeta}{\sqrt{\|g\|}}\right]$$
$$= 0 , \tag{17}$$

$$Q_2 \equiv R\left[(R_\theta Z_\zeta - Z_\theta R_\zeta)\frac{\partial}{\partial v} + (R_\zeta Z_v - Z_\zeta R_v)\frac{\partial}{\partial\theta} + (R_v Z_\theta - Z_v R_\theta)\frac{\partial}{\partial\zeta}\right]$$
$$\times\left[\frac{\Psi_v^2}{2}\frac{g_{\theta\theta}}{\|g\|} + \frac{\Phi_v^2}{2}\frac{g_{\zeta\zeta}}{\|g\|} + \Psi_v\Phi_v\frac{g_{\theta\zeta}}{\|g\|} + p\right] + \Psi_v^2\frac{\partial}{\partial\theta}\frac{R^2\phi_\theta}{\sqrt{\|g\|}}$$
$$+ \phi_v^2\frac{\partial}{\partial\zeta}\frac{R^2\phi_\zeta}{\sqrt{\|g\|}} + \Psi_v\Phi_v\left[\frac{\partial}{\partial\theta}\frac{R^2\phi_\zeta}{\sqrt{\|g\|}} + \frac{\partial}{\partial\zeta}\frac{R^2\phi_\theta}{\sqrt{\|g\|}}\right] = 0 , \tag{18}$$

and

$$Q_3 \equiv R\left[(\phi_\theta R_\zeta - R_\theta\phi_\zeta)\frac{\partial}{\partial v} + (\phi_\zeta R_v - R_\zeta\phi_v)\frac{\partial}{\partial\theta} + (\phi_v R_\theta - R_v\phi_\theta)\frac{\partial}{\partial\zeta}\right]$$

$$\times\left[\frac{\Psi_v^2}{2}\frac{g_{\theta\theta}}{\|g\|} + \frac{\Phi_v^2}{2}\frac{g_{\zeta\zeta}}{\|g\|} + \Psi_v\Phi_v\frac{g_{\theta\zeta}}{\|g\|} + p\right] + \Psi_v^2\frac{\partial}{\partial\theta}\frac{Z_\theta}{\sqrt{\|g\|}}$$

$$+ \Phi_v^2\frac{\partial}{\partial\zeta}\frac{Z_\zeta}{\sqrt{\|g\|}} + \Psi_v\Phi_v\left[\frac{\partial}{\partial\theta}\frac{Z_\zeta}{\sqrt{\|g\|}} + \frac{\partial}{\partial\zeta}\frac{Z_\theta}{\sqrt{\|g\|}}\right] = 0 \; . \tag{19}$$

It is easy to identify equations (17), (18) and (19) as the covariant components of equation (4a) in the coordinate system (R,ϕ,Z). This is best done by writing equation (4a) in the form

$$\vec{\nabla}\left(p + \frac{B^2}{2}\right) - \vec{B}\cdot\vec{\nabla}\vec{B} = 0 \; , \tag{20}$$

and taking its dot product with $\vec{\nabla}R$, $R\vec{\nabla}\phi$ and $\vec{\nabla}Z$ respectively. We get

$$\vec{\nabla}R\cdot\vec{\nabla}\left(p + \frac{B^2}{2}\right) - \vec{B}\cdot\vec{\nabla}B_R - \frac{B_\phi^2}{R} = 0 \; , \tag{21}$$

$$R\vec{\nabla}\phi\cdot\vec{\nabla}\left(p + \frac{B^2}{2}\right) - \vec{B}\cdot\vec{\nabla}(RB_\phi) = 0 \; , \tag{22}$$

$$\vec{\nabla}Z\cdot\vec{\nabla}\left(p + \frac{B^2}{2}\right) - \vec{B}\cdot\vec{\nabla}B_Z = 0 \; , \tag{23}$$

where

$$B_R \equiv \vec{B}\cdot\vec{\nabla}R \tag{24}$$

$$B_\phi \equiv R\vec{B}\cdot\vec{\nabla}\phi \tag{25}$$

and

$$B_Z \equiv \vec{B}\cdot\vec{\nabla}Z \; . \tag{26}$$

If we now use the (operator) equation

$$\vec{B}\cdot\vec{\nabla} = \frac{1}{\sqrt{\|g\|}}\left[\Psi_v\frac{\partial}{\partial\theta} + \Phi_v\frac{\partial}{\partial\zeta}\right] \tag{27}$$

and the identity

$$\frac{\partial(v,\theta,\zeta)}{\partial(R,\phi,Z)}\;\frac{\partial(R,\phi,Z)}{\partial(v,\theta,\zeta)} = 1 \; , \tag{28}$$

it is straightforward to show that equations (17), (18) and (19) are respectively identical to equations (21), (22) and (23) written in inverse variables.

IV. Choice for the Toroidal Angle

For many cases of interest, a convenient choice for the toroidal angle is

$$\phi = \zeta \quad . \tag{29}$$

We may not then vary ϕ in computing δL. For the two independent variations δR and δZ, the Euler-Lagrange equations are obtained by formally substituting

$$\phi_v = 0 , \qquad \phi_\theta = 0 , \qquad \phi_\zeta = 1 , \tag{30}$$

in equations (17) and (19). It may be shown that the remaining equation (18) can be obtained by linear combination of equations (17) and (19). By straightforward algebraic manipulations, we now cast equations (17) and (19) in the form

$$\begin{aligned} RZ_\theta \Bigg[& \frac{\Psi_v}{\sqrt{\|g\|}} \left\{ \frac{\partial}{\partial v} \left(\frac{g_{\theta\theta}\Psi_v}{\sqrt{\|g\|}} + \frac{g_{\theta\zeta}\Phi_v}{\sqrt{\|g\|}} \right) - \frac{\partial}{\partial \theta} \left(\frac{g_{v\theta}\Psi_v}{\sqrt{\|g\|}} \right) \right\} + p_v \\ & + \frac{\Phi_v}{\sqrt{\|g\|}} \left\{ \frac{\partial}{\partial v} \left(\frac{g_{\zeta\zeta}\Phi_v}{\sqrt{\|g\|}} + \frac{g_{\zeta\theta}\Psi_v}{\sqrt{\|g\|}} \right) - \frac{\Phi_v}{2\sqrt{\|g\|}} \frac{\partial}{\partial v} g_{\zeta\zeta} \right. \\ & \left. - \frac{\Psi_v}{\sqrt{\|g\|}} \frac{\partial}{\partial v} g_{\theta\zeta} \right\} \Bigg] - RZ_v\Phi_v \left[\frac{\Phi_v}{2} \frac{\partial}{\partial \theta} \frac{g_{\zeta\zeta}}{\|g\|} + \Psi_v \frac{\partial}{\partial \theta} \frac{g_{\theta\zeta}}{\|g\|} \right] \\ & + \Psi_v\Phi_v \left[\frac{\partial}{\partial \theta} \frac{R_\zeta}{\sqrt{\|g\|}} + \frac{\partial}{\partial \zeta} \frac{R_\theta}{\sqrt{\|g\|}} \right] + \Phi_v^2 \left[\frac{\partial}{\partial \zeta} \frac{R_\zeta}{\sqrt{\|g\|}} - \frac{R}{\sqrt{\|g\|}} \right] = 0, \end{aligned} \tag{31}$$

and

$$\begin{aligned} RR_\theta \Bigg[& \frac{\Psi_v}{\sqrt{\|g\|}} \left\{ \frac{\partial}{\partial v} \left(\frac{g_{\theta\theta}\Psi_v}{\sqrt{\|g\|}} + \frac{g_{\theta\zeta}\Phi_v}{\sqrt{\|g\|}} \right) - \frac{\partial}{\partial \theta} \left(\frac{g_{v\theta}\Psi_v}{\sqrt{\|g\|}} \right) \right\} + p_v \\ & + \frac{\Phi_v}{\sqrt{\|g\|}} \left\{ \frac{\partial}{\partial v} \left(\frac{g_{\zeta\zeta}\Phi_v}{\sqrt{\|g\|}} + \frac{g_{\zeta\theta}\Psi_v}{\sqrt{\|g\|}} \right) - \frac{\Phi_v}{2\sqrt{\|g\|}} \frac{\partial}{\partial v} g_{\zeta\zeta} - \frac{\Psi_v}{\sqrt{\|g\|}} \frac{\partial}{\partial v} g_{\theta\zeta} \right\} \Bigg] \\ & - RR_v\Phi_v \left[\frac{\Phi_v}{2} \frac{\partial}{\partial \theta} \frac{g_{\zeta\zeta}}{\|g\|} + \Psi_v \frac{\partial}{\partial \theta} \frac{g_{\theta\zeta}}{\|g\|} \right] \\ & - \Psi_v\Phi_v \left[\frac{\partial}{\partial \theta} \frac{Z_\zeta}{\sqrt{\|g\|}} + \frac{\partial}{\partial \zeta} \frac{Z_\theta}{\sqrt{\|g\|}} \right] - \Phi_v^2 \frac{\partial}{\partial \zeta} \frac{Z_\zeta}{\sqrt{\|g\|}} = 0 . \end{aligned} \tag{32}$$

Dividing equation (31) by RZ_θ, equation (32) by RR_θ, and subtracting the resultant equations from one another we get

$$\Phi_v \left[\frac{1}{\sqrt{\|g\|}} \left\{ \frac{\partial}{\partial\theta} \frac{g_{\zeta\zeta}}{\sqrt{\|g\|}} - \frac{\partial}{\partial\zeta} \frac{g_{\zeta\theta}}{\sqrt{\|g\|}} \right\} \right] + \Psi_v \left[\frac{1}{\sqrt{\|g\|}} \left\{ \frac{\partial}{\partial\theta} \frac{g_{\zeta\theta}}{\sqrt{\|g\|}} - \frac{\partial}{\partial\zeta} \frac{g_{\theta\theta}}{\sqrt{\|g\|}} \right\} \right]$$

$$= 0 . \tag{33}$$

Equation (33) may be identified to be the condition

$$\vec{J}\cdot\vec{\nabla}v = \vec{\nabla}\cdot(B \times \vec{\nabla}v) =$$

$$\Phi_v \vec{\nabla}\cdot[|\vec{\nabla}v|^2\vec{\nabla}\theta - \vec{\nabla}v(\vec{\nabla}v\cdot\vec{\nabla}\theta)] - \Psi_v \vec{\nabla}\cdot[|\vec{\nabla}v|^2\vec{\nabla}\zeta - \vec{\nabla}v(\vec{\nabla}v\cdot\vec{\nabla}\zeta)] = 0 , \tag{34}$$

derived earlier as an Euler-Lagrange equation [(10b) or (10c)] from the variational principle.

Once equations (31) and (32) are given, equation (34) is not an independent equation. However, if we take equation (34) as given, both of the equations (31) and (32) become

$$\frac{\Psi_v}{\sqrt{\|g\|}} \left\{ \frac{\partial}{\partial v} \left(\frac{g_{\theta\theta}\Psi_v}{\sqrt{\|g\|}} + \frac{g_{\theta\zeta}\Phi_v}{\sqrt{\|g\|}} \right) - \frac{\partial}{\partial\theta} \left(\frac{g_{v\theta}\Psi_v}{\sqrt{\|g\|}} \right) \right\} + p_v$$

$$+ \frac{\Phi_v}{\sqrt{\|g\|}} \left\{ \frac{\partial}{\partial v} \left(\frac{g_{\zeta\zeta}\Phi_v}{\sqrt{\|g\|}} + \frac{g_{\zeta\theta}\Psi_v}{\sqrt{\|g\|}} \right) - \frac{\partial}{\partial\zeta} \left(\frac{g_{\zeta v}\Phi_v}{\sqrt{\|g\|}} \right) \right\} = 0, \tag{35}$$

which is $\vec{J} \times \vec{B} = p_v\vec{\nabla}v$ in inverse variables.

V. Euler-Lagrange Equations for Fourier Amplitudes of the Inverse Mapping

Exploiting the periodicity of $R(v,\theta,\zeta)$ and $Z(v,\theta,\zeta)$ in θ and ζ, we expand them in Fourier series.

$$R(v,\theta,\zeta) = \sum \Big[R_{m_1,m_2}(v) \cos(m_1\theta - m_2\zeta) + R_{n_1,n_2}(v) \sin(n_1\theta - n_2\zeta) \Big] \tag{36}$$

$$Z(v,\theta,\zeta) = \sum \Big[Z_{p_1,p_2}(v) \cos(p_1\theta - p_2\zeta) + Z_{q_1,q_2}(v) \sin(q_1\theta - q_2\zeta) \Big] , \tag{37}$$

where, unless stated otherwise, the sums extend from $-\infty$ to $+\infty$ over all integers m_1, m_2, etc. The first variation of L becomes

$$\delta L = -\sum \int_0^a dv \int_0^{2\pi} d\theta \int_0^{2\pi} d\zeta \Big[\{ \delta R_{m_1,m_2}(v) \cos(m_1\theta - m_2\zeta) + \delta R_{n_1,n_2}(v) \sin(n_1\theta - n_2\zeta) \} Q_1 + \{ \delta Z_{p_1,p_2}(v) \cos(p_1\theta - p_2\zeta) + \delta Z_{q_1,q_2}(v) \sin(q_1\theta - q_2\zeta) \} Q_3 \Big] \quad . \tag{38}$$

We may now treat $\delta R_{m_1,m_2}$, $\delta R_{n_1,n_2}$, $\delta Z_{p_1,p_2}$, and $\delta Z_{q_1,q_2}$ as independent variations to obtain an Euler-Lagrange equation for each Fourier amplitude. These ordinary differential equations, which constitute an infinite set and determine stationary values of L , are

$$\langle\langle \cos(m_1\theta - m_2\zeta) Q_1 \rangle\rangle = 0, \quad m_1, m_2 \epsilon (-\infty, +\infty) \quad , \tag{39}$$

$$\langle\langle \sin(n_1\theta - n_2\zeta) Q_2 \rangle\rangle = 0, \quad n_1, n_2 \epsilon (-\infty, +\infty) \quad , \tag{40}$$

$$\langle\langle \cos(p_1\theta - p_2\zeta) Q_3 \rangle\rangle = 0, \quad p_1, p_2 \epsilon (-\infty, +\infty) \quad , \tag{41}$$

$$\langle\langle \sin(q_1\theta - q_2\zeta) Q_3 \rangle\rangle = 0, \quad q_1, q_2 \epsilon (-\infty, +\infty) \quad , \tag{42}$$

where $\langle\langle \ \rangle\rangle$ is a double-averaging operator defined by

$$\langle\langle A \rangle\rangle \equiv \frac{1}{(2\pi)^2} \int_0^{2\pi} d\theta \int_0^{2\pi} d\zeta A(v,\theta,\zeta) \quad . \tag{43}$$

Equations (39) through (42) are the three-dimensional generalization of the variational moment equations derived by Lao, Hirshman and Wieland for the Grad-Shafranov equation (1). For numerical computations, we truncate this infinite set by retaining only a few terms in the infinite expansions (36) and (37). We will now illustrate the power of this method by applying it to axisymmetric toroidal configurations.

VI. Axisymmetric Toroidal Equilibrium

For axisymmetric equilibria, $\partial/\partial\zeta = 0$ equations (31) and (32) reduce to

$$G_R \equiv RZ_\theta \left[\frac{\Psi_v}{\sqrt{\|g\|}} \left\{ \frac{\partial}{\partial v} \left(\frac{g_{\theta\theta}\Psi_v}{\sqrt{\|g\|}} \right) - \frac{\partial}{\partial\theta} \left(\frac{g_{v\theta}\Psi_v}{\sqrt{\|g\|}} \right) \right\} + \frac{\Phi_v}{\sqrt{\|g\|}} \left\{ \frac{\partial}{\partial v} \left(\frac{g_{\zeta\zeta}\Phi_v}{\sqrt{\|g\|}} \right) \right\} + p_v - \frac{\Phi_v^2}{2\|g\|} \frac{\partial}{\partial v} g_{\zeta\zeta} \right] - \frac{\Phi_v^2}{2} RZ_v \frac{\partial}{\partial\theta} \frac{g_{\zeta\zeta}}{\|g\|} - \frac{\Phi_v^2 R}{\sqrt{\|g\|}} = 0 \tag{44}$$

and

$$G_z \equiv$$

$$RR_\theta \left[\frac{\Psi_v}{\sqrt{\|g\|}} \left\{ \frac{\partial}{\partial v} \left(\frac{g_{\theta\theta}\Psi_v}{\sqrt{\|g\|}} \right) - \frac{\partial}{\partial \theta} \left(\frac{g_{v\theta}\Psi_v}{\sqrt{\|g\|}} \right) \right\} + \frac{\Phi_v}{\sqrt{\|g\|}} \left\{ \frac{\partial}{\partial v} \left(\frac{g_{\zeta\zeta}\Phi_v}{\sqrt{\|g\|}} \right) \right\} \right.$$

$$\left. + p_v - \frac{\Phi_v^2}{2\|g\|} \frac{\partial}{\partial v} g_{\zeta\zeta} \right] - \frac{\Phi_v^2}{2} RR_v \frac{\partial}{\partial \theta} \frac{g_{\zeta\zeta}}{\|g\|} = 0 . \qquad (45)$$

Equation (23) yields the condition

$$\frac{\partial}{\partial \theta} \frac{g_{\zeta\zeta}}{\sqrt{\|g\|}} = 0 , \qquad (46)$$

which is not an independent equation once equations (44) and (45) are given, but may be incorporated in the (axisymmetric) variational form at the outset by defining the toroidal field function

$$F(v) \equiv \frac{g_{\zeta\zeta}}{\sqrt{\|g\|}} \Phi_v . \qquad (47)$$

If we do so, the two Euler-Lagrange equations, (44) and (45) become each identical to

$$G \equiv \frac{1}{\sqrt{\|g\|}} \left[\frac{\partial}{\partial v} \left(\frac{g_{\theta\theta}\Psi_v}{\sqrt{\|g\|}} \right) - \frac{\partial}{\partial \theta} \left(\frac{g_{v\theta}\Psi_v}{\sqrt{\|g\|}} \right) \right] + \frac{FF_\Psi}{R^2} + p_\Psi = 0 , \qquad (48)$$

which is the Grad-Shafranov equation in inverse variables, derived first by Greene, Johnson and Weimar, and used extensively by Lao, Hirshman and Wieland. We propose, however, to work with equations (44) and (45) because equation (34) is not generally reducible to a form as simple as equation (46) [which, in turn, suggests the definition of the new dependent variable $F(v)$] for three-dimensional equilibria, and it is therefore best to work with a set of equations easily amenable to further generalization.

In the study of axisymmetric equilibria, it is often customary to specify $F(v)$ and $p(v)$. Alternatively, as is done in the study of flux conserving equilibria, one may specify $q(v)$ and $p(v)$, where $q(v)$ is the q-profile, defined by the equation

$$\Phi_v - q(v)\Psi_v = 0 . \qquad (49)$$

For axisymmetric equilibria with up-down symmetry, we must have

$$R(v,\theta) = R(v,-\theta) , \qquad (50a)$$

$$Z(v,\theta) = -Z(v,-\theta) , \qquad (50b)$$

The appropriate Fourier expansions for $R(v,\theta)$ and $Z(v,\theta)$ are

$$R(v,\theta) = \sum_{m=0}^{\infty} R_m(v) \cos m\theta \ , \tag{51}$$

$$Z(v,\theta) = \sum_{p=1}^{\infty} Z_p(v) \sin p\theta \ , \tag{52}$$

and the Euler-Lagrange equations for the Fourier amplitudes are

$$\langle \cos m\theta G_R \rangle = 0 \qquad m \epsilon (0,\ldots,\infty) \ , \tag{53}$$

$$\langle \sin p\theta G_Z \rangle = 0 \qquad p \epsilon (1,\ldots,\infty) \ , \tag{54}$$

where $\langle\ \rangle$ is now defined to be

$$\langle A \rangle \equiv \frac{1}{2\pi} \int_0^{2\pi} d\theta A(v,\theta) \ . \tag{55}$$

VII. Choice of the Radial Flux Surface Label and Boundary Conditions

The radial flux surface label v is, as yet, unspecified. Any one of the Fourier amplitudes may be used for labelling flux surfaces. However, we may not then vary the chosen amplitude while calculating the first variation of L. Instead, the variation of L with respect to Ψ, with $\Phi(\Psi)$ fixed, provides an independent Euler-Lagrange equation

$$\left\langle\!\!\left\langle \frac{\partial}{\partial v} \frac{\partial}{\partial \Psi_v} - \frac{\partial \mathcal{L}}{\partial \Psi} \right\rangle\!\!\right\rangle = 0 \ , \tag{56}$$

which gives

$$\left\langle\!\!\left\langle \sqrt{\|g\|} \left[\frac{\Psi_v}{\sqrt{\|g\|}} \left\{ \frac{\partial}{\partial v} \left(\frac{g_{\theta\theta}\Psi_v}{\sqrt{\|g\|}} + \frac{g_{\theta\zeta}\Phi_v}{\sqrt{\|g\|}} \right) \right\} + p_v \right.\right.$$
$$\left.\left. + \frac{\Phi_v}{\sqrt{\|g\|}} \left\{ \frac{\partial}{\partial v} \left(\frac{g_{\zeta\zeta}\Phi_v}{\sqrt{\|g\|}} + \frac{g_{\zeta\theta}\Psi_v}{\sqrt{\|g\|}} \right) \right\} \right] \right\rangle\!\!\right\rangle = 0 \ . \tag{57}$$

We identify at once equation (57) as the surface-averaged form of equation (35). In the special case of axisymmetry, equation (57) becomes

$$\left\langle \Psi_v \frac{\partial}{\partial v} \left(\frac{g_{\theta\theta}\Psi_v}{\sqrt{\|g\|}} \right) + \Phi_v \frac{\partial}{\partial v} \left(\frac{g_{\zeta\zeta}\Phi_v}{\sqrt{\|g\|}} \right) + \sqrt{\|g\|}\ p_v \right\rangle \equiv G = 0 \ . \tag{58}$$

We have found it convenient to choose $-R_1$ as the flux surface label v for the study of axisymmetric equilibria. The boundary conditions on the Fourier amplitudes for this choice of the flux surface label have been obtained by Lao, Hirshman and Wieland. By performing expansions near the magnetic axis $v=0$, they obtain

$$R_{mv}(0) = 0 , \qquad m = 0 , \tag{59a}$$

$$R_m(0) = 0 , \qquad m = 2,3,\ldots, \tag{59b}$$

$$Z_p(0) = 0 , \qquad p = 1,2,\ldots . \tag{59c}$$

The shape of the outer boundary at $v=a$ is specified as an input for this method and provides us with the additional boundary conditions

$$R_m(a) \equiv R_{ma} \qquad m = 0,2,3,\ldots, \tag{60a}$$

$$Z_p(a) \equiv Z_{pa} \qquad p = 1,2,3,\ldots . \tag{60b}$$

We thus have two boundary conditions for each Fourier amplitude obeying the second-order ordinary differential equations (53) and (54). For the poloidal flux function Ψ, the two boundary conditions are

$$\Psi_v(0) = 0 , \tag{61a}$$

and

$$\Psi(a) \equiv \Psi_a . \tag{61b}$$

For the toroidal flux function Φ, we require that

$$\Phi(0) = 0 , \tag{62}$$

and solve the first order differential equation (47) [or equation (49)] for Φ if $F(v)$ [or $q(v)$] is specified.

VIII. Comparison with Analytic Solovév Equilibria

To solve the two-point boundary-value system of equations referred to in the last section, we use the Method of Collocation at Gaussian points due to DeBoor and Swartz.[6] Details will be given elsewhere. We compare the numerical results from the axisymmetric version of the three-dimensional algorithm described earlier, with analytic Solovév equilibria[7] which are exact solutions of the Grad-Shafranov equation (1). It may be shown by direct substitution that equation (1) has the solution

$$\Psi(R,Z) = F_0^2 \ell_0^2 Z^2 + \frac{p_0}{8}\left(R^2 - \ell_0^2\right)^2 \tag{63}$$

if

$$F^2 = 4F_0^2 \ell_0^2 (\Psi_a - \Psi)^2 , \tag{64}$$

and

$$p = p_0(\Psi_a - \Psi) \tag{65}$$

where F_0 is a constant. We note that $\Psi = 0$ at the magnetic axis $R = \ell_0$, $Z = 0$.

We now consider a model equilibrium for which $p_0 = .125$, $F_0 = 0.25$ and $\ell_0 = 4$, a case also studied in Reference 8. In order to represent reasonably accurately the outermost flux surface for the stated parameters, it is found necessary to include three Fourier coefficients each for R and Z. In other words, the parametric equations for the out flux surface are taken to be

$$R = R_{0a} - a\cos\theta + R_{2a}\cos 2\theta + R_{3a}\cos 3\theta \quad , \tag{66a}$$

and

$$Z = Z_{1a}\sin\theta + Z_{2a}\sin 2\theta + Z_{3a}\sin 3\theta \ . \tag{66b}$$

The coefficients R_{0a}, R_{2a}, Z_{1a}, Z_{2a}, and Z_{3a} are determined by a least-squares fit to the equation for the outermost flux surface,

$$1 = F_0^2\ell_0^2 Z^2 + \frac{p_0}{8}\left(R^2 - \ell_0^2\right)^2 \ , \tag{67}$$

where we have assumed $\Psi_a = 1$. In Figure 2, we compare the analytical and numerically determined flux surface contours for this particular test case. It is worth noting that remarkable accuracy is achieved by solving the variational moment equations at only eight collocation points within the radial interval $\epsilon(0,1)$.

In Figure 3, we have plotted the Fourier amplitudes as a function of v. In the graph, each of the Fourier amplitudes is normalized to its maximum magnitude, which is displayed on the top. We note that for axisymmetric equilibria of the kind considered here, the Fourier amplitudes decrease in magnitude rapidly. This accounts for the accuracy obtainable in the variational method by retaining only a few Fourier amplitudes.

IX. Concluding Remarks

The variational method described in this paper may be used for the study of three-dimensional magnetostatic equilibria. In this paper, we have presented numerical results for axisymmetric equilibria in order to establish the validity of the method and to make contact with existing numerical codes. The computation of three-dimensional equilibria will be the subject of a future publication.

The rigorous validity of the method is predicated on the existence of a flux surface quantity v such that $\vec{B}\cdot\vec{\nabla}v = 0$. The existence of a well-defined symmetry direction is a sufficient condition for the existence of such flux

surfaces. In that case, as we have seen for the axisymmetric equilibrium considered here, the Fourier series for the inverse variables R and Z converge rapidly. However, even in the absence of a well-defined symmetry direction, as may indeed be the case for toroidal stellarators, the present algorithm may be expected to yield "asymptotic equilibria" for which the Fourier series is asymptotic, provided the equilibria are not characterized by the presence of large magnetic islands at resonant surfaces inside the plasma.

References

1. J. M. Greene, J. L. Johnson, and K. E. Weimar, Phys. Fluids 14, 671 (1971).
2. L. L. Lao, S. P. Hirshman, and R. M. Wieland, Phys. Fluids 24, 1431 (1981).
3. H. Grad, Phys. Fluids 7, 1283 (1964).
4. M. D. Kruskal and R. M. Kulsrud, Phys. Fluids 1, 265 (1958).
5. J. M. Greene and J. L. Johnson, Phys. Fluids 5, 510 (1962).
6. C. DeBoor and B. Swartz, SIAM J. Numer. Anal. 14, 441 (1977).
7. L. S. Solovév, Zh. Eksp. Teor. Fiz. 53, 626, (1967).
8. F. Bauer, O. Betancourt, and P. Garabedian, A Computational Method in Plasma Physics, (Springer-Verlag New York, Inc., New York) 1978.

Figure Captions

Fig. 1 Two coordinate systems; the cylindrical coordinate system (R, ϕ, Z) and the magnetic coordinate system (v, θ, ζ).

Fig. 2 Comparison of exact (indicated by dots) and numerically determined (indicated by solid lines) flux surfaces for a Solovév equilibrium.

Fig. 3 Radial plots of the Fourier amplitudes for the equilibrium shown in Figure 2 (Key: $u1 = R_0$, $u2 \equiv Z_1$, $u3 \equiv R_2$, $u4 \equiv Z_2$, $u5 \equiv R_3$, $u6 \equiv Z_3$).

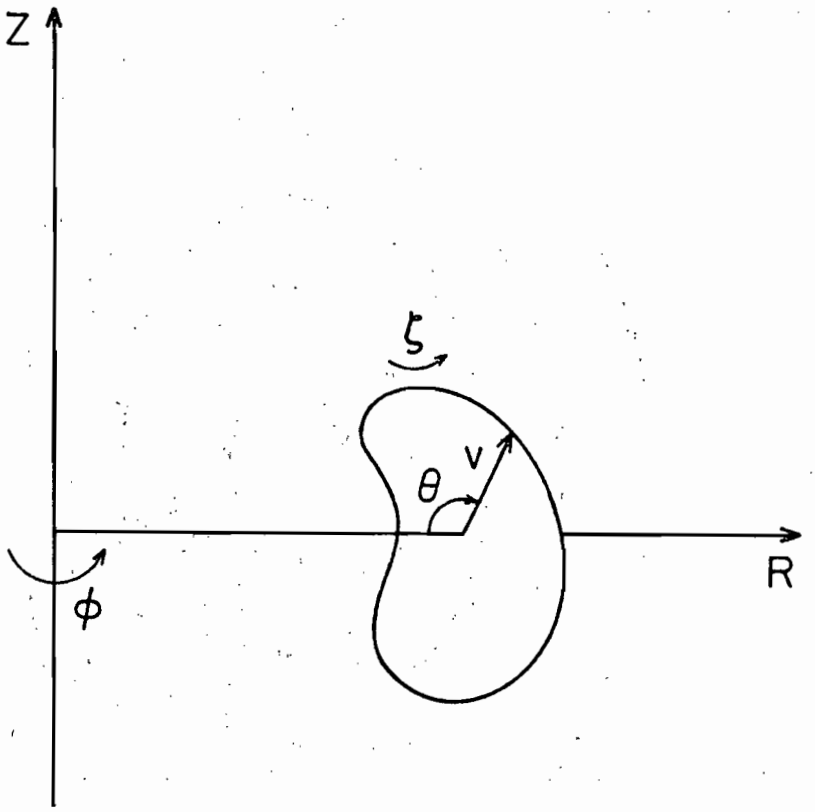

Fig. 1

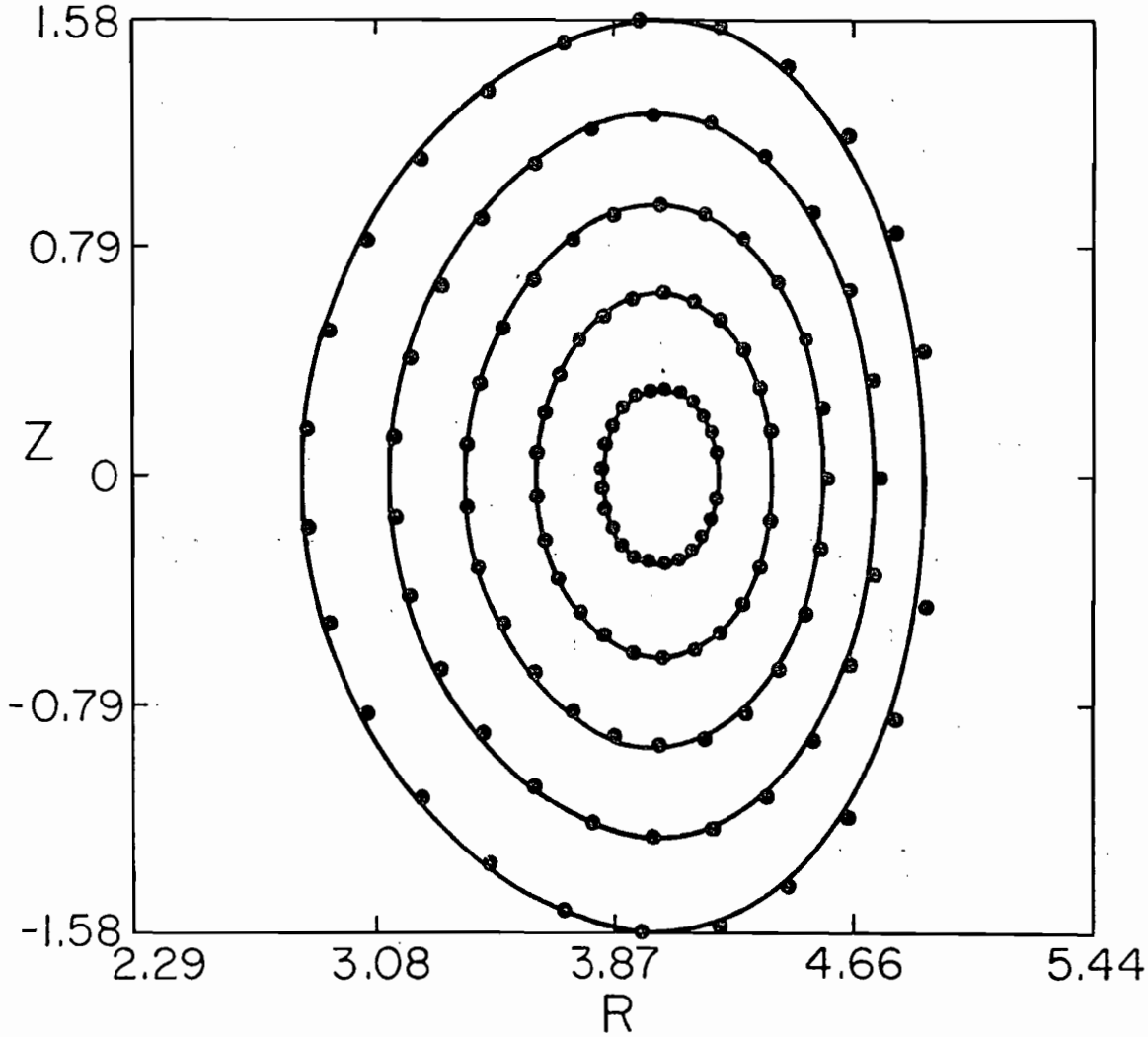

Fig. 2

Maximum of

U1 4.025E+00 U2 1.621E+00 U3 6.127E-02

U4 1.572E-01 U5 3.443E-02 U6 4.236E-02

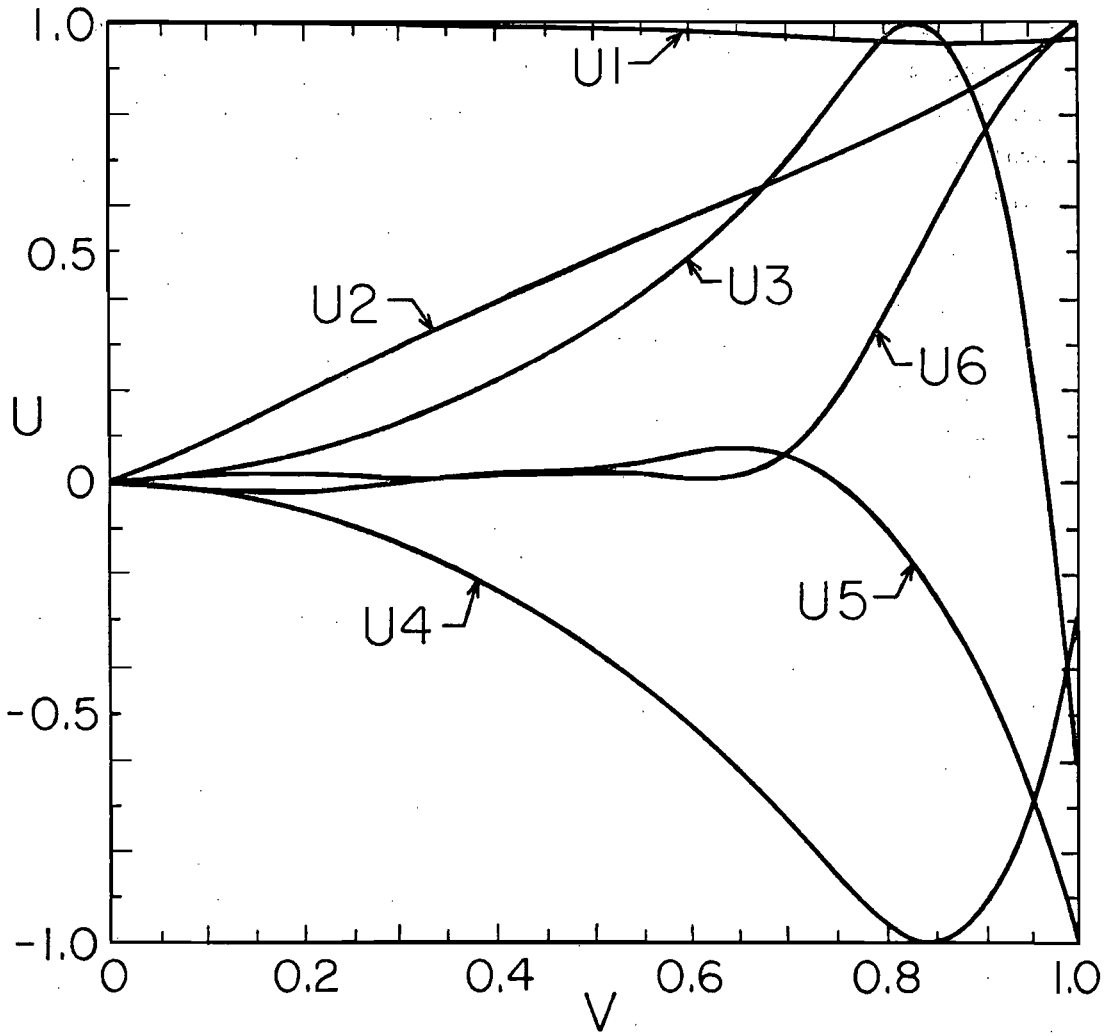

Fig. 3

A REVIEW OF TIME-DEPENDENT, THREE-DIMENSIONAL RESISTIVE MAGNETOHYDRODYNAMIC CALCULATIONS*

John Killeen

National Magnetic Fusion Energy Computer Center
Lawrence Livermore National Laboratory
Livermore, California 94550

ABSTRACT

The development of three-dimensional, initial-value codes for the solution of MHD equations has evolved from a few exploratory studies in the 1970's to several production type codes, which at the present time are making important contributions to the understanding of resistive instabilities in toroidal plasmas. This evolution is examined from several points of view. It is useful to consider the following options for initial-value MHD code development:

- primitive MHD equations, reduced MHD equations
- compressible, incompressible
- ideal MHD, dissipative MHD
- one, two, three dimensions
- linear, nonlinear
- Eulerian, Lagrangian, ALE, dynamical grid
- finite differences, finite elements, expansions
- explicit difference equations, implicit difference equations

The codes considered in this review will be categorized according to the above options. In addition the applications of the codes will be discussed, as these usually explain the choice of options. It is important to note that all of the models and techniques listed above have been used and are appropriate for certain types of problems.

Primitive MHD Equations

The numerical study of linear MHD stability has followed two paths. In the first, the linearized MHD equations (either resistive or ideal) are treated as an initial value problem. [1-9] The equilibrium state of the system is specified and is given a perturbation. The MHD equations are advanced forward in time to trace the evolution of the plasma. The fastest growing instability eventually dominates over all other motions. The second approach which has been used very successfully is to utilize the energy

*Work performed under the auspices of the U.S.D.O.E. by Lawrence Livermore National Laboratory under contract W-7405-ENG-48.

principle [10,11] to gain information on the full spectrum of ideal MHD instabilities.

After the linear modes have been determined, the resultant eigenmodes may be used to start a nonlinear calculation which can then follow their growth to some final state. These nonlinear calculations have all been with initial-value codes in two and three space dimensions.

One of the earliest 3D resistive MHD codes was TRINITY developed by Roberts and Boris [12]. It was an Eulerian code using an explicit leapfrog difference scheme with the resistive diffusion terms employing the DuFort and Frankel algorithm. Similar 3D codes subsequently developed were those of Wooten et al (ideal) [13], Cochran et al [14], and Pritchett et al (ideal) [15].

Sykes and Wesson have also developed a 3D Eulerian code which includes a tensor resistivity and thermal conductivity [16-18]. Their code employs a Lax-Wendroff scheme and the diffusion terms are also treated by an explicit method. Ogino had developed a similar code at Nagoya. [19]

All of the above codes must satisfy a Courant time-step condition. Generally this is much smaller than one imposed by the time scale of the physical instability being studied. To avoid this limitation Finan [20,21] developed a 3D Eulerian code which uses the Douglas-Gunn algorithm for Alternating-Direction Implicit temporal advancement. The eight equations are solved simultaneously to avoid syncronization errors. The resulting finite difference equations are a coupled system of nonlinear algebraic equations which are solved by the Newton-Raphson iteration technique. Time steps 10-50 times the Courant condition are used in long time simulations. The Finan code, IMP, generalizes to three dimensions techniques that have proved successful in two dimensional resistive MHD calculations . [22-25]

All of the above 3D nonlinear codes use finite differences in all three directions. In order to obtain the required spatial resolution for high S resistive instabilities, and simultaneously to decrease the computer time for the simulation of these instabilities, recent 3D MHD code developments have used expansions in one or two directions with finite differences in the remaining direction(s).

Hender [26] has developed a 3D Eulerian code to study resistive "g" modes in reversed field pinches. It assumes cylindrical geometry and starts

with an equilibrium which is a function of r only. The linear codes RIPPLE 4a [2,3] or RESTAB [4] are used to calculate unstable modes which are parametrized by m and k_z. The 3D nonlinear code uses finite differences in the r direction and a Fourier expansion in θ and z. The finite difference method is a mixture of implicit and explicit algorithms.

Mirin [27] has developed a 3D Eulerian code to study the nonlinear growth of MHD instabilities in axisymmetric toroidal equilibria which are functions of r and z. The linear code RIPPLE VI [7] calculates unstable modes, periodic in ϕ, which can be used as initial values for the 3D nonlinear code. The nonlinear code uses an explicit Lax-Wendroff method in r and z with a Fourier expansion in ϕ.

Turner and Wesson are developing a similar code [28] for 3D MHD simulations of JET. Wesson will discuss this code at the workshop.

Another approach for achieving better accuracy is the method of finite-elements. Kawakami, at this workshop, will describe a finite element ALE code for solving 3D resistive MHD equations.

Reduced MHD Equations

In order to study resistive instabilities in Tokamaks a set of reduced equations has been derived [29] and solved in two dimensions by several groups. Strauss [30,31] has extended the reduced model of White el al [29] to three dimensions. He uses an Eulerian mesh with a leap-frog time advancement algorithm. The diffusion terms are differenced via the DuFort-Frankel method.

The Oak Ridge code RS3 [32] solves reduced equations using differences in all three directions with a mixed explicit-implicit scheme. This code has been superceded by RSF [33] which uses finite differences in r and expansions in the two periodic directions, and runs considerably faster for the same accuracy. Applications of this code to Tokamaks has been reported in a series of papers. [34-41]

Another 3D reduced MHD code which makes use of an expansion in the two periodic directions is that of Edery et al. [42,43]

A 3D reduced MHD code which makes use of finite differences in all three directions is that of Schmalz. [44]

Summary

A number of codes which solve either the primitive or reduced equations of resistive magnetohydrodynamics in three dimensions, as initial-value problems, have been examined. Because of the nature of resistive

instabilities e.g., tearing and reconnection, the Eulerian representation is generally used. Recent developments favor the use of expansions in one or two directions because of increased speed and accuracy, as long as the number of modes considered is not too large. The codes which employ expansions are also more compatible with the linear codes [1-9] which solve each mode separately. These modes can be combined to start the nonlinear problems.

REFERENCES

1. J. Killeen and H. P. Furth, *Bull. Am. Phys. Soc.* 6 (1961), 193.
2. J. Killeen *in* "Physics of Hot Plasmas" (B. J. Rye and J. C. Taylor, Eds.), Plenum, New York, 1970, P. 202.
3. J. E. Crow, J. Killeen and D. C. Robinson, "Sixth European Conference on Controlled Fusion and Plasma Physics," Moscow (1973), 269.
4. J. A. Dibiase, J. Killeen, D. C. Robinson, D. Schnack, *in* "Third Topical Conference on Pulsed High Beta Plasmas," (Culham 1975) Pergammon Press, Oxford 1976, 283-289.
5. J. Dibiase and J. Killeen, *J. Comp. Phys.* 24 (1977), 158.
6. J. Killeen and A. I. Shestakov, *Phys. Fluids* 21, (1978), 1746.
7. A. I. Shestakov, J. Killeen and D. D. Schnack, *J. Comp. Phys.* (Accepted) UCRL-86493.
8. G. Batemen, W. Schneider, and W. Grossmann, *Nucl. Fusion* 14 (1974), 669.
9. A. Sykes and J. Wesson, *Nucl. Fusion* 14 (1974), 645.
10. R. C. Grimm, J. M. Greene, and J. L. Johnson *in* "Methods in Computational Physics" (J. Killeen, Ed.), Vol. 16, p. 253, Academic Press, New York, 1976.
11. R. Gruber, F. Troyon, D. Berger, L. C. Bernard, S. Rousset, R. Schreiber, W. Kerner, W. Schneider and K. V. Roberts, *Comput. Phys. Comm.* 21 (1981) 323-371.
12. K. V. Roberts and J. P. Boris, *in* "Proceedings of the Culham Conference on Computational Physics" 2 (1969) 44.
13. J. Wooten, H. R. Hicks, G. Bateman and R. A. Dory, ORNL/TM-4784 (1974).
14. F. L. Cochran, P. C. Liewer and G. Bateman *in* "Proceedings of the Eighth Conf. on Numer. Simulation of Plasmas," Paper PB-3, LLNL Report CONF-780614 (1978).
15. P. L. Pritchett, C. C. Wu, and J. M. Dawson, *Phys. Fluids* 21 (1978), 1543.
16. A. Sykes and J. A. Wesson, *Phys. Rev. Letters* 37 (1976), 140.
17. A. Sykes and J. A. Wesson, "8th Europ. Conf. on Controlled Fusion and Plasma Physics, Prague (1977).
18. A. Sykes *in* "Proceedings of the 1981 Wildhaus Workshop on Computational MHD Models of the Behavior of Magnetically Confined Plasmas" to be published in *Comput. Phys. Comm.*
19. T. Ogino, paper presented at the "1980 U.S.-Japan Workshop on Computational Theory," Nagoya.
20. C. H. Finan III, "The Alternating-direction Implicit Numerical Solution of the Time-dependent, Three-dimensional, Single Fluid, Resistive Magnetohydrodynamic Equations," Ph.D. Thesis, UCRL-53086, December 1980.
21. C. H. Finan III and J. Killeen *in* "Proceedings of the 1981 Wildhaus Workshop on Computational MHD Models of the Behavior of Magnetically Confined Plasmas" to be published in *Comput. Phys. Comm.*

22. I. Lindemuth and J. Killeen, *J. Comp. Phys.* 13 (1973), 181.

23. D. Schnack and J. Killeen *in* "Theoretical and Computational Plasma Physics," p. 337, IAEA Vienna (1978).

24. D. Schnack and J. Killeen, *Nucl. Fusion* 19 (1979), 877.

25. D. Schnack and J. Killeen, *J. Comp. Phys.* 35 (1980), 110.

26. T. C. Hender and D. C. Robinson *in* "Proceedings of the 1981 Wildhaus Workshop on Computational MHD Models of the Behavior of Magnetically Confined Plasmas" to be published in *Comput. Phys. Comm.*

27. A. A. Mirin and A. I. Shestakov, *Bull. Am. Phys. Soc.* 26 (1981) 956.

28. M. F. Turner and J. A. Wesson, *in* "Proceedings of the 1981 Wildhaus Workshop on Computational MHD Models of the Behavior of Magnetically Confined Plasmas" to be published in *Comput. Phys. Comm.*

29. R. White, D. Monticello, M. N. Rosenbluth, H. Strauss and B. B. Kadomtsev, "Plasma Physics and Controlled Nucl. Fusion," Tokyo, IAEA, Vienna (1975) Vol I, 495.

30. H. R. Strauss, *Phys. Fluids* 19 (1976), 134.

31. H. R. Strauss, *Phys. Fluids* 20 (1977), 1354.

32. H. R. Hicks, B. Carreras, J. A. Holmes, D. K. Lee, S. J. Lynch, and B. V. Waddell, *in* "Proc. Eighth Conf. on Numerical Simulation Plasma," Paper PA-7, Monterey, CA., LLNL Report CONF-780614 (1978).

33. H. R. Hicks, J. A. Holmes, D. K. Lee, B. Carreras and B. V. Waddell, "3-D Nonlinear Calculations of Resistive Tearing Modes," ORNL/TM/7132, 1981. Accepted in *J. Comp. Phys.*

34. J. D. Callen et al, in *Plasma Physics and Controlled Nuclear Fusion Research*, IAEA Vienna (1979), Vol. I, 415.

35. J. A. Holmes, B. Carreras, H. R. Hicks, S. J. Lynch, B. V. Waddell, *Nucl. Fusion* 19 (1979), 1333.

36. B. Carreras, B. V. Waddell, H. R. Hicks, *Nucl. Fusion* 19 (1979), 1423.

37. H. R. Hicks, J. A. Holmes, B. A. Carreras, D. J. Tetreault, G. Berge, J. P. Freidberg, P. A. Politzer, D. Sherwell, "8th International Conf. on Plasma Physics and Controlled Nuclear Fusion Research," IAEA Vienna (1981), Vol I, 259.

38. B. Carreras, H. R. Hicks, J. A. Holmes, B. V. Waddell, *Phys. Fluids* 23 (1980), 1811.

39. B. Carreras, J. A. Holmes, H. R. Hicks, V. E. Lynch, *Nucl. Fusion* 21 (1981), 511.

40. B. Carreras, H. R. Hicks D. K. Lee, *Phys. Fluids* 24, (1981), 66.

41. H. R. Hicks, J. A. Holmes, V. E. Lynch, B. Carreras, "Nonlinear Analysis of Disruptions in the JIPP T-11 Tokamak," ORNL/TM-7733, (1981).

42. D. Edery et al in *Plasma Physics and Controlled Nuclear Fusion Research*, IAEA Vienna (1981) Vol I, 269.

43. D. Edery, R. Pellat, J. L. Soulé "Proceedings of the 1981 Wildhaus Workshop on Computational MHD Models of the Behavior of Magnetically Confined Plasmas" to be published in *Comput. Phys. Comm.*

44. R. Schmalz, "Proceedings of the 1981 Wildhaus Workshop on Computational MHD Models of the Behavior of Magnetically Confined Plasmas" to be published in *Comput. Phys. Comm.*

Tokamak Current Disruptions due to Impurity Radiation Cooling

Tsuneo Amano and Katsuhiro Shimizu

Institute of Plasma Physics
Nagoya University
Nagoya 464, Japan

Abstract

Major disruptions in the JIPP T-II and "R" tokamak are investigated. The plasma and impurity transport equations are solved and the resulting current profiles are used to estimate the growth of island width of m/n=2/1 and 2/3 tearing modes. Nonlinear delta prime analysis code and a single-helicity 2D tearing instability code are employed to obtain the saturated island width. A 3-D multi-helicity tearing code is now under development and its possible use is discussed.

§1. Introduction

The major disruption limits plasma density and current in tokamak experiments. The thoeretical and computational approaches suggest two plausible causes of the disruptions. One is the contact of m/n=2/1 (m : poloidal mode number, n : toroidal mode number) island with a limiter.[1] The other is the overlapping of m/n=2/1 island with m/n=3/2 island.[2]

In near future larger tokamaks with high plasma current, the effect of the major disruption will be very serious, since the abrupt decay of the plasma current will cause eddy currents to flow in the surrounding conductors inducing formidable mechanical loads.
At IPPJ, we are now planning to construct a new tokamak called "R tokamak".[3] Here "R" stands for the "reacting" D-T plasma. The dimensions and physical parameters are listed in Table I. In this device, neutral beam power of 15 MW will be injected to heat a plasma up to 10 keV. Axisymmetric bumper limiters surround the plasma to absorb the major plasma heat load on the order of 15 MW. During a long pulse operation of one second, it is possible that the sputtered impurities from the limiters will enter the plasma and cool the periphery region thereby causing a current distribution vulnerable to the major disruption.

In order to investigate possible implications of the major disruption on the "R" tokamak, we attempt to predict the onset of the disruption by utilizing a 1-D tokamak plasma and impurity transport code coupled with the non-linear Δ' analysis. To check the validity of Δ' analysis, we use a 2D single helicity tearing code to calculate saturated island widths. We are now also developing a 3-D tearing code similar to the Oak Ridge code.[4] This code will give a more accurate onset time of the disruption as well as the time scale of the current decay.

In §2, we will consider the major disruptions observed in JIPP T-II tokamak.[5,6] The cause of the disruption in this experiment has been well understood as a overlapping process of 2/1 and 3/2 islands.[5,6,7] We use this experiment as a bench mark test to our analysis of the major disruption. We solve the oxygen impurity transport equations

and include the radiation cooling effect in the plasma transport equations. The current profiles thus obtained can well explain the JIPP T-II disruptions.

In §3, we use the same approach for the analysis of the "R" tokamak. Here we inject 15 MW neutral beams and consider the carbon and titanium impurities sputtered from the limiters. The resulting current profiles are used to estimate the stability against the tearing modes.

§4 is devoted to discussion.

§2. Current Disruptions in JIPP T-II Tokamak

The JIPP T-II is a circular cross-section tokamak whose major and minor radii are 91 cm and 15 cm, respectively. In an experiment, three typical discharges with different conditions of gas puffing and current rise are compared as shown in Fig. 1.[5] The discharge of case I is produced by applying a strong gas puffing from 80 ms without a second current-rise to the medium q(a) ($\simeq$4~5) plasma. In case II, a second current-rise is applied at 90 ms to the relatively low density discharge. In case III, both strong gas puffing and second current-rise are used, where the start time of the current-rise is delayed by 10 ms from that of the gas puffing. In case I, the m/n=2/1 mode with 3/2 mode component rapidly grows up just before the major disruption. Toi has termed this disruption as a "soft" disruption, since the plasma current does not decay appreciably. In case II, the m/n=4/1, 3/1 and 2/1 modes successively observed in the second rising phase of the plasma current and the relative amplitude of 2/1 mode fluctuations attaines 0.8%. In case III, the m/n=4/1 and 3/1 modes are completely suppressed and the relative amplitude of m/n=1/2 mode is reduced less than 0.1%. To explain these results by tearing instability theory, Toi et al. determined the current profiles through magnetic diffusion equation by adjusting the $Z_{eff}(r)$ profile iteratively so that the calculated loop voltage and location of q(r)=1 surface should be the best-fit to the experimentaly observed ones. He used the current profiles thus obtained as inputs to a non-linear Δ' code to calculate island width and poloidal field fluctuations. As a result he has obtained a good correlation between the experiments and the theory.

Recently, Toi has analyzed the other high density discharges case IV to VI.[6] In these, cases V and VI are characterized by low q values with q_a=2.3 and 2.2, respectively. These two cases are shown in Figs. (2) and (3). In the experiment, these high density discharges occasionaly lead to the "hard" major disruption (the right hand side of Figs. (2) and (3)) in which the currents are terminated abruptly. From the Δ' analysis, Toi has suggested that the almost simultaneous interaction of the 2/1 island with 3/2 one and the limiter plays an essential role for triggering the hard major disruption in these discharges.

Hicks et al. analyzed the case I, II and III of the JIPP T-II experiment by use of their nonlinear 3D tearing code and obtained a good agreement between the observations and the computations.[7]

We will take another approach. We solve the following transport equations for the JIPP T-II parameters :

$$\frac{\partial n_e}{\partial t} = -\frac{1}{r}\frac{\partial}{\partial r} r\Gamma + S_I \tag{2.1}$$

$$\frac{3}{2}\frac{\partial}{\partial t} n_e T_e = -\frac{1}{r}\frac{\partial}{\partial r}(rQ_e) + E_z j_z - \frac{3m_e}{m_i}\frac{n_e}{\tau_e}(T_e - T_i) - W_I - W_R \tag{2.2}$$

$$\frac{3}{2}\frac{\partial}{\partial t} n_i T_i = -\frac{1}{r}\frac{\partial}{\partial r}(rQ_i) + \frac{3m_e}{m_i}\frac{n_e}{\tau_e}(T_e - T_i) - W_{cx} \tag{2.3}$$

$$\frac{\partial B_\theta}{\partial t} = c\frac{\partial E_z}{\partial r} \tag{2.4}$$

$$E_z = \eta j_z = \frac{c\eta}{4\pi}\frac{1}{r}\frac{\partial}{\partial r}(rB_\theta) \tag{2.5}$$

$$\Gamma = -D\frac{\partial n_e}{\partial r} - n_e\frac{cE_z}{B_\theta}L_{14} \tag{2.6}$$

$$Q_e = -X_e\frac{\partial T_e}{\partial r} - \frac{3}{2}DT_e\frac{\partial n_e}{\partial r} - n_e T_e\frac{cE_z}{B_\theta}L_{24} \tag{2.7}$$

$$Q_i = -X_i\frac{\partial T_i}{\partial r} - \frac{3}{2}DT_i\frac{\partial n_i}{\partial r}, \tag{2.8}$$

where W_R, W_I, W_{cx} are radiation, ionization and charge exchange losses, respectively. Terms with L_{14}, L_{24} represent the Ware pinch effects. The other variables have their usual meanings. For the anomalous coefficients D and X_e, we use

$$D = 4.7 \times 10^{16} \frac{1}{n_e \sqrt{q}} \tag{2.9}$$

$$X_e = 4.0 \times n_e D$$

$$X_e^{MHD} = 0.12\ n_e D_B \quad (\text{for } q(r)<1),$$

which have been obtained to fit the density and temperature evolution of the case III.

The impurity transport equations (or diffusion-rate eqs.) are given by

$$\frac{\partial n_k}{\partial t} = -\frac{1}{r}\frac{\partial}{\partial r} r\,\Gamma_k + n_e(n_{k-1}S_{k-1} - n_k S_k + n_{k+1}\alpha_{k+1} - n_k\alpha_k) \tag{2.10}$$

where n_k and Γ_k are the number density and radial diffusion flux of the k-th ion, and S_k and α_k are the ionization and recombination rate coefficients, respectively.[8] For Γ_k, we assume the form

$$\Gamma_k = \Gamma_k^N + \Gamma_k^A \tag{2.11}$$

where Γ_k^N is the neoclassical diffusion flux given by Hirshman[9] and Γ_k^A is an empirical diffusion flux,

$$\Gamma_k^A = -D_A \frac{dn_k}{dr}. \tag{2.12}$$

For D_A, we take the same form as Eq. (2.9). From n_k, we can calculate the ionization and line radiation losses W_I and W_R in Eq. (2.2).

The stability of a cylindrical tokamak plasma against tearing modes is examined by solving the following equation for the poloidal flux function ψ:[10]

$$\frac{1}{r}\frac{d}{dr}\left(r\frac{d\psi}{dr}\right) = \left(\frac{m^2}{r^2} + \frac{mq}{r(m - nq)}\frac{dj_z}{dr}\right)\psi. \tag{2.13}$$

When a singular surface $r=r_s$ exists in the plasma, the linear stability against the tearing mode is discussed in terms of $\Delta'(o)$ defined by,

$$\Delta'(o) = \lim_{\varepsilon\to 0} \left(\frac{\partial\psi}{\partial r}\Big|_{r_s+\varepsilon} - \frac{\partial\psi}{\partial r}\Big|_{r_s-\varepsilon}\right)/\psi(r_s), \tag{2.14}$$

$$q(r_s) = \frac{m}{n}.$$

Now the concept of the nonlinear $\Delta'(W)$ is introduced as

$$\Delta'(W) = \left(\frac{\partial\psi}{\partial r}\Big|_{r_s+\frac{W}{2}} - \frac{\partial\psi}{\partial r}\Big|_{r_s-\frac{W}{2}}\right)/\psi(r_s). \tag{2.15}$$

The saturated width W_s is estimated from $\Delta'(W_s)=0$, since $\Delta'(W)$ is proportional to the potential energy of the instability for the tearing modes.[11,12]

The current density distribution j_z which is obtained by solving Eqs. (2.1)∿(2.8) numerically is substituted in Eqs. (2.13) and (2.15) to evaluate the saturated island width W_s. Figure (4) shows the computed time evolution of the island width of m/n=2/1 and m/n=3/2 tearing modes for cases I, II and III of the JIPP T-II experiment. In case I, a strong gas puffing cools the periphery of the plasma together with enhanced oxygen radiations. The current channel shrinks producing a sharp current density gradient and the 2/1 and 3/2 singular surfaces move outward. From 20 msec after the start of the strong gas puffing, both 2/1 and 2/3 islands begin to grow and finally lead to a soft major disruption by overlapping. In case II, a rapid second current-rise moves the q=2 surface outward and enhance the current density gradient there at the same time. Therefore, the m=2 island is shifted outward while growing and presumably touches the limiter. In case III, the occurrence of the disruption has been avoided by an appropriate combination of the strong gas puffing and the second current-rise. In this case, q=2 surface comes to near r=12 cm close to the limiter at r=15 cm. The current density gradient near r=12 cm which is responsible for the 2/1 tearing mode instability is determined from a delicate balance between heating and cooling due to the increased current and gas puffing. Computationaly, it is difficult to reproduce such a delicate balance and the calculated $\tilde{B}_\theta$ fluctuation level is much larger than the measured one. It should be noted that the electron temperature in the region r=12∿15 cm has not been measured.

The Δ' analysis by use of experimental measurement of T_e profile needed a trial and error guess for the T_e profile in this region.

In Figs. (5), (6) are shown time evolutions of island width computed by use of a 2-D single helicity code for case I and case II. The computed island widths agree well with those obtained from Eq. (2.15).

To understand Murakami scaling law[13] for the density limit of tokamaks in terms of the edge cooling of the plasma, we tried the following simulation for the JIPP T-II parameters. We fix q_a=3.5 and Z_{eff}=3.0 (oxygen) and change B_z, I_p and the electron density. The edge region is cooled mainly by the oxygen impurity radiation in the simulation. The major disruption caused by the overlapping of 2/1 and 3/2 islands is assumed to be responsible for the density limit. In Fig. (7) is shown the density limit thus obtained in comparison with the original Murakami scaling law.

§3. Tearing Mode Analysis for "R" Tokamak

To simulate the neutral beam heating of the "R" tokamak, we solve the equations given in §2, supplemented with the neutral beam and α heating Fokker Planck codes. We also include a scrape-off region in the shadow of the limiters. In this region, particles move along the magnetic field lines and hit the limiters. We consider bumper limiters made of TiC tiles. The sputtering processes taken into account are D→TiC, T→TiC, Ti→TiC. We assume a fraction α of sputtered atoms enter the plasma as neutrals. In simulations, the neutral beam heating is switched on at t=0.1 sec and switched off at t=1 second. We used Intror scaling for X_e and D_A : $X_e=5\times10^{17}/n_e$, $D_A=1.25\ 10^{17}/n_e$. α is assumed 0.4. In Fig. (8) is shown a time history of the central electron density and temperature and ion temperature. After the onset of neutral beam injection, the impurity radiation increases almost linearly with time from 1 MW at t=0.1 sec and 7 MW at t=1 sec. The radiation mainly consists of line radiations from titanium impurity and is concentrated in the periphery of the plasma. In Fig. (9), we plot the calculated island widths of 2/1 and 3/2 modes from Eq. (2.15). Safety factor q at the plasma surface is 2.7. The 3/2 island gradually

grows with time approaching the 2/1 island around t=0.3 sec. The two islands do not overlap, however, they come very close to each other. It is surmised that the presence of 2/1 island actually enhances the growth of 3/2 mode through a modification of the current distribution and leads to the overlapping of the islands. In order to examine such a surmise, a 3-D multi-helicity code simulation is being prepared.

§4. Discussion

In §2, we have shown that the nonlinear Δ' analysis combined with plasma and impurity transport calculations is useful to explain the major disruption observed in the JIPP T-II.

In §3, an intense neutral beam heating of "R" tokamak has been simulated. The edge cooling due to the sputtered impurities has not led to the major disruption as far as Δ' analysis is concerned. Since m/n=2/1 and m/n=3/2 islands have come very close to each other, however, we need a 3-D tearing code analysis to obtain a definite conclusion.

In "R" tokamak, we are considering a possibility to wind helical coils to form a kind of helical divertor. There is a danger, however, that such helical perturbations will induce a disruption by forming resonant islands inside the plasma. This problem also awaits the 3-D tearing analysis.

Table I

R Tokamak Parameters

Major radius	R	2.1 m
Minor radius	a	0.6 m
Plasma current	I_p	1.5∿1.8 MA
Maximum toroidal field	B_T	5 Tesla
Injected beam power	W_B	15 MW
Injected beam energy	E_B	120 keV

References

1) R. B. White, D. A. Monticello, M. N. Rosenbluth:
Phys. Rev. Lett. 39 (1977) 1681.

2) B. V. Waddel, B. Carreras, H. R. Hicks, J. A. Holmes:
Phys. Fluids 22 (1979) 896.

3) A. Miyahara, H. Momota, Y. Hamada, K. Kawamura et al.:
IPPJ-500 (1981).

4) H. R. Hicks, J. A. Holmes, D. K. Lee, B. Carreras, B. V. Waddel:
ORNL/TM-7132 (1981).

5) K. Toi, S. Itoh, K. Kadota, K. Kawahata et al.:
Nucl. Fusion 19 (1979) 1643.

6) K. Toi, K. Sakurai, S. Tanahashi, S. Yasue:
IPPJ to be published.

7) H. R. Hicks, J. A. Holmes, V. E. Lynch and B. A. Carreras:
ORNL/TM 7733 (1981).

8) T. Amano, E. C. Crume:
ORNL/TM-6363 (1978).
M. Sato, T. Amano, K. Sato, K. Miyamoto:
J. Phys. Soc. Jpn. 50 (1981) 2114.

9) S. P. Hirshman :
Phys. Fluids 20 (1977) 589.
R. J. Hawryluk, S. Suckewer, S. P. Hirshman:
Nucl. Fusion 19 (1979) 607.

10) J. A. Wesson:
Nucl. Fusion 18 87 (1978).

11) R. B. White, D. A. Monticello, M. N. Rosenbluth, B. V. Waddel:
Phys. Fluids 20 800 (1977).

12) B. Carreras, B. V. Waddel, H. R. Hicks:
Nucl. Fusion 19 1423 (1979).

13) M. Murakami, J. D. Callen, L. A. Berry:
Nucl. Fusion 16 (1976) 347.

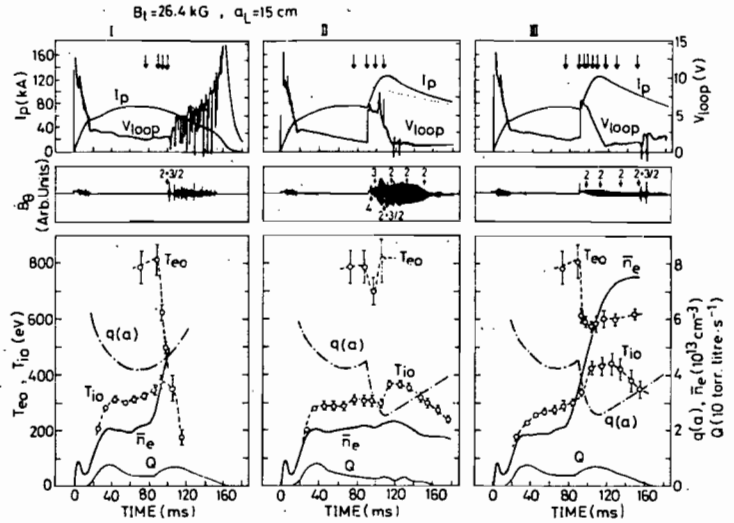

Fig. 1

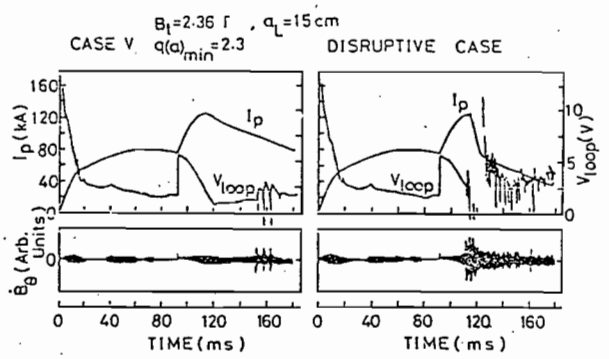

Fig. 2

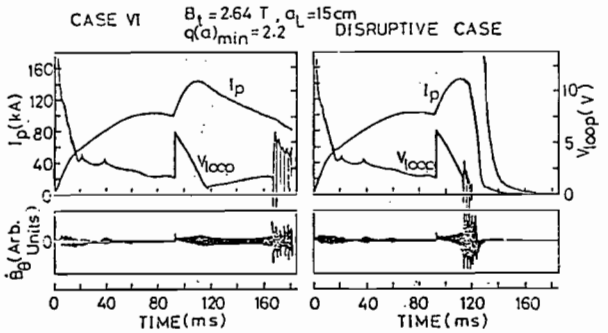

Fig. 3

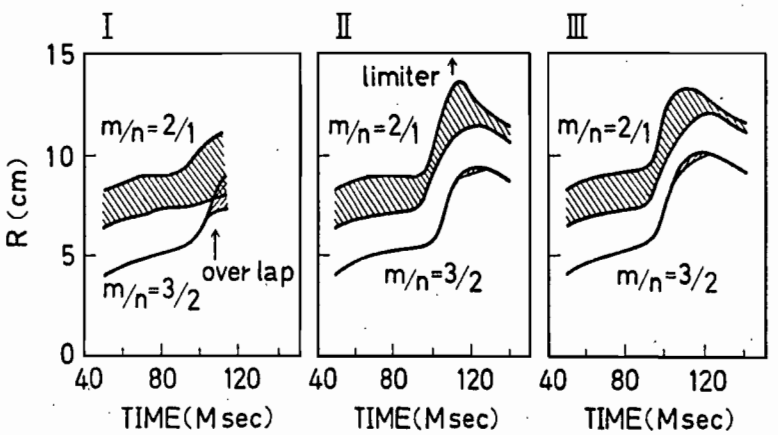

Fig. 4

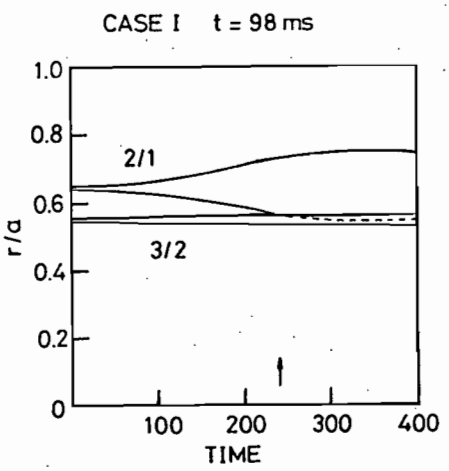

Fig. 5

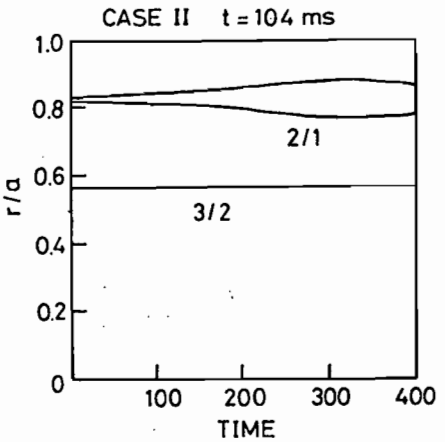

Fig. 6

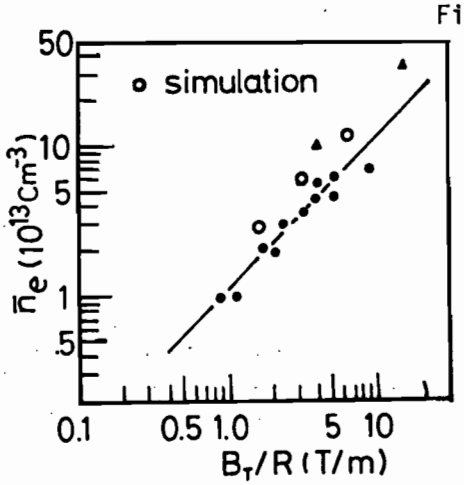

Fig. 7

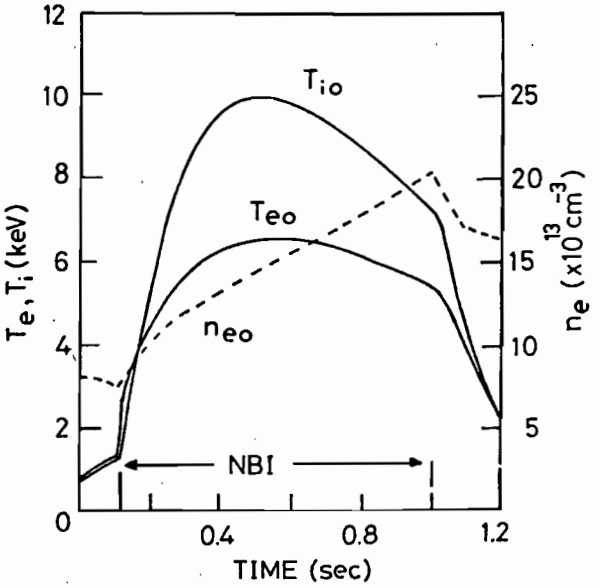
12
10
8
6
4
2
0
25
20
15
10
5
T_{io}
T_{eo}
n_{eo}
NBI
0.4
0.8
1.2
TIME (sec)
T_e, T_i (keV)
n_e ($\times 10^{13}$ cm^{-3})

Fig. 8

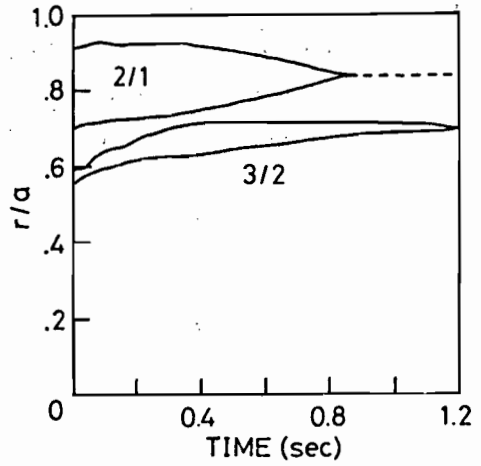
1.0
.8
.6
.4
.2
0
2/1
3/2
r/a
0.4
0.8
1.2
TIME (sec)

Fig. 9

Major Disruption Process in Tokamak

T. Takeda, G. Kurita, M. Azumi, T. Tuda,
T. Takizuka, T. Tsunematsu, S. Tokuda, K. Itoh

Japan Atomic Energy Research Institute
Tokai-mura, Naka-gun, Ibaraki-ken, Japan

The major disruption in a cylindrical tokamak is investigated by using the multi-helicity code, and the destabilization of the 3/2 mode by the mode coupling with the 2/1 mode is confirmed. The evolution of the magnetic field topology caused by the major disruption is studied in detail. The effect of the internal disruption on the 2/1 magnetic island width is also studied. The 2/1 magnetic island is not enhanced by the flattening of the q-profile due to the internal disruption.

§1 Introduction

The major disruption of a tokamak is characterized by rapid release of magnetic and plasma energies within an order of μs followed by reduction of the plasma current with the decay time of several milliseconds, and it is considered to be the main cause of limitation of the plasma current and density. The disruption may bring about a more serious damage to the device as the device becomes larger. It is, therefore, urgently required to clarify the mechanism of the major disruption and to devise methods to control or suppress it.

The m=2 tearing mode plays an important role in the major disruption. The growth of the m=2 magnetic field perturbation is observed as a precursor of the disruption. When the safty factor at plasma boundary, q_a, is less than 2, the major disruption seems to be suppressed. Waddell et al. proposed that a nonlinear interaction between m/n=2/1 and m/n=3/2 tearing modes causes the major disruption[1~4]. The results of their simulation seem to well recover the experimental data. They presented the scaling law of the major disruption time on the basis of the WKB theory. The WKB method, however, is not always applicable to the nonlinear stage of the mode evolution. It is important to establish the theoretical model reliable in this stage. It is also very important to know the mechanism to change the current profile which makes the enhancement of the 2/1 island width.

In this paper we first recover the results of the ORNL group. We find a little disagreement with their results. We also investigate the initiation process of the 2/1 mode assuming that the current density profile is flattened by the 1/1 mode. The 2/1 island obtained in the simulation is compared with those calculated by the Δ' code.

In the next section the basic equations of the present analysis are described. In §3, the results of simulation are presented. Conclusion and discussion are given in §4.

§2 Basic Equations

The reduced set of the resistive magnetohydrodynamic equations of a low β toroidal plasma in the cylindrical coodinate system (R, ϕ, z) is given as

$$\frac{\partial \Psi}{\partial t} + \vec{v} \cdot \vec{\nabla}_{\perp} \Psi = B_0 \frac{\partial \Phi}{\partial \zeta} + \eta J - E_w(t) \tag{1}$$

$$\frac{\partial U}{\partial t} + \vec{v} \cdot \vec{\nabla}_{\perp} U = \vec{\nabla}\zeta \cdot \vec{\nabla} P \times \vec{\nabla}_{\perp} \left(\frac{R}{R_0}\right)^2 + \left(\frac{R}{R_0}\right)^2 \vec{\nabla}\zeta \cdot \vec{\nabla}_{\perp}\Psi \times \vec{\nabla}_{\perp} J + B_0 \frac{\partial J}{\partial \zeta} \tag{2}$$

$$\frac{\partial P_*}{\partial t} + \vec{v} \cdot \vec{\nabla}_{\perp} P_* = 0 \tag{3}$$

$$\vec{B} = B_0 \left(\vec{\nabla}\zeta + \vec{\nabla}\zeta \times \vec{\nabla}_{\perp}\Psi \right) \tag{4}$$

$$\vec{v} = \left(\frac{R}{R_0}\right)^2 \vec{\nabla}\zeta \times \vec{\nabla}_{\perp}\Phi \tag{5}$$

$$\vec{J} = \left(R^2 \vec{\nabla}_{\perp} \cdot \frac{\vec{\nabla}_{\perp}\Psi}{R^2} \right) \vec{\nabla}\zeta \tag{6}$$

$$U = \left(\frac{R}{R_0}\right)^2 \vec{\nabla}_{\perp}^2 \Phi \tag{7}$$

$$P_* = \left(\frac{R}{R_0}\right)^{2\gamma} P \tag{8}$$

where R_0 is the major radius, $\zeta = R_0\phi$, $\vec{\nabla}_{\perp} \equiv \frac{\partial}{\partial R}\vec{\nabla} R + \frac{\partial}{\partial z}\vec{\nabla} z$. The quantities U, Ψ and Φ denote the vorticity, poloidal flux and stream function, respectively. The energy integral of this reduced set of equations is given by

$$\frac{d}{dt}\int d\tau \left[\left(\frac{R}{R_0}\right)^2 |\vec{\nabla}\Phi|^2 + \left(\frac{R}{R_0}\right)^2 |\vec{\nabla}\Psi|^2 + \frac{P}{\gamma - 1} \right]$$
$$= -\int d\tau \left[\left(\frac{R}{R_0}\right)^2 \eta J^2 \right] + 2\pi R_0 E_w(t) I_p \ . \tag{9}$$

The first term in the l.h.s. represents the kinetic energy, the second one the magnetic energy, and the third one the internal energy. The first term in the r.h.s. is the energy dissipation. The electric field at the wall, $E_w(t)$, is obtained from eq.(9) by setting the total plasma current I_p constant.

Now we employ the coordinate system (r, θ, ζ), in which the magnetic lines are straight. The radial coordinate r is defined by

$$r = \left(\frac{R}{R_0}\right)^2 \sqrt{g} \tag{10}$$

where $\sqrt{g}$ is Jacobian. The variables Ψ, J, Φ and P_* are Fourier expanded in θ and ζ directions:

$$\Psi(r,\theta,\zeta) = \sum_{m,n} \Psi_{m/n}(r) \exp i\left(m\theta - \frac{n}{R_0}\zeta \right) \tag{11}$$

where m and n denote the mode numbers in θ and ζ directions, respectively. The Fourier expanded equations are written as follows;

$$\frac{\partial \Psi_{m/n}}{\partial t} = [\,\Psi,\Phi\,]_{m/n} + \frac{B_0}{R_0} n\, \Phi_{m/n} + \eta\, J_{m/n} - E_{m/n} \tag{12}$$

$$\frac{\partial U_{m/n}}{\partial t} = [\,U,\Phi\,]_{m/n} + [\,J,\Psi\,]_{m/n} - \frac{R_0}{B_0} n\, J_{m/n} + [\,F,P\,]_{m/n} \tag{13}$$

$$\frac{\partial P_{*m/n}}{\partial t} = [\,\Phi,P_*\,]_{m/n} \tag{14}$$

where $[\,\Psi,\Phi\,]_{m/n}$ is defined by

$$[\,\Psi,\Phi\,]_{m/n} = \sum_{\substack{m=m'+m'' \\ n=n'+n''}} \frac{m'}{r} \left(\Psi_{m'/n'} \frac{d}{dr} \Phi_{m''/n''} - \Phi_{m'/n'} \frac{d}{dr} \Psi_{m''/n''} \right) . \tag{15}$$

Variables $J_{m/n}$ and $U_{m/n}$ take the form;

$$J_{m/n} = \frac{1}{r} \sum_{m=m'+m''} \Big[\frac{d}{dr}\left(G^{rr}_{m'} \frac{d}{dr} \Psi_{m''/n} \right) - m'' \frac{d}{dr}\left(G^{r\theta}_{m'} \Psi_{m''/n} \right) - m\, G^{r\theta}_{m'} \frac{d}{dr} \Psi_{m''/n} - m\, m''\, G^{\theta\theta}_{m'} \Psi_{m''/n} \Big] \tag{16}$$

$$U_{m/n} = \frac{1}{r} \sum_{m=m'+m''} \Big[\frac{d}{dr}\left(H^{rr}_{m'} \frac{d}{dr} \Phi_{m''/n} \right) - m'' \frac{d}{dr}\left(H^{r\theta}_{m'} \Phi_{m''/n} \right) - m\, H^{r\theta}_{m'} \frac{d}{dr} \Phi_{m''/n} - m\, m''\, H^{\theta\theta}_{m'} \Phi_{m''/n} \Big] . \tag{17}$$

Quantities F_m, G^{ij}_m and H^{ij}_m are defined by

$$\left(\frac{R}{R_0}\right)^2 = \sum_m F_m(r) \exp im\theta \tag{18}$$

$$r\, g^{ij} = \sum_m G^{ij}_m(r) \exp im\theta \tag{19}$$

$$r \left(\frac{R}{R_0}\right)^2 g^{ij} = \sum_m H^{ij}_m(r) \exp im\theta . \tag{20}$$

In this calculation the equation (14) for pressure is neglected because the pressure driven mode is not important in a low β plasma. Morever we neglect the toroidal effects. Even by this simplification, the essential mechanism of the major disruption can be described. We assume the resistivity is constant in time and set it to be

$$\eta(r) = E_w(t=0)/J(r,t=0) \ . \qquad (21)$$

The multi helicity calculation is carried out with up to 29 Fourier components and 200 equal-spacing radial meshes. The equations are solved by both the full-explicit and implicit-explicit predictor-corrector time integration schemes, and a good agreement between both cases is obtained. The time step for the former scheme, however, is restricted to be much small compared with that for the latter scheme.

§3 Computational Results

3.1 Nonlinear Destabilization of 3/2 mode

We choose the q-profile as in Ref.1, $q(r)=1.38[1+(r/0.6)^8]^{1/4}$ and the magnetic Reynolds number $S=2\times10^4$ at q=2 surface. Almost the same behavior of the plasma as that of the ORNL calculation is recoverd, which is presented in the following figures (fig.1-7). Figure 1 (a and b) show the time evolution of magnetic island width obtained by the single-helicity and multi-helicity calculations, respectively. The single helicity calculation shows that the 2/1 and 3/2 modes are both unstable and the widths of the saturated islands are about 0.4 and 0.1, respectively. In contrast with the single-helicity calculation, the multi-helicity calclulation shows the rapid destabilization of 3/2 mode after the island of the 2/1 and 3/2 mode touch each other at $t \simeq 300$, due to the nonlinear interaction between modes with different helicities. The phase of the 5/3 and 7/4 modes are inverted several times at final stage of the disruption. The evolution of the kinetic and magnetic energies are shown in Fig.2 (a and b), respectively. Both the energies rapidly increase from the island-overlapping time ($t \simeq 300$). The time evolution of the growth rate of the magnetic energy is shown in Fig.3. The growth rate of the 2/1 mode is slowly decreasing function of time when the growth rates of the 3/2 and 5/3 modes begin to increase,which means that the 2/1 mode is in the Rutherford regime even after the time of the island overlapping. Figure 4 shows the time evolution of the one turn voltage, $V=[\frac{d}{dt}(E_k + E_M) - Q]/I_p$, where I_p is total plasma current, E_k and E_M are

the kinetic and magnetic energies, and Q is the change in the rate of energy dissipation due to Joule heating. In this figure, V is normalized by $\eta B_t/\mu_0$.. The negative voltage spike is observed is the figure. The order of magnitude of the voltage spike is in good agreement with experimental value. The helical flux contours for several modes with different helicities at the end of the calculation are shown in figure 5. The magnetic islands of the higher harmonics, such as the 8/5 or 13/7 modes, have also fairly large amplitude. In Fig.6, intersections of a single magnetic field line near the separatrix of the 2/1 island at the $\zeta=0$ poloidal plane are plotted. This figure shows that the stochastic region develops during the interval(t= 300∿400) and covers almost the plasma column at the final stage. The stochasticity can be investigated quantitatively by calculating the K-S entropy[5], which is shown in Fig.7. The evolution of the K-S entropy confirms the above result. The stochastic magnetic field in the plasma column enhances the heat loss and causes the rapid cooling of the plasma, which is observed in the soft X ray signals from the plasma center.

3.2 Effect of the Internal Disruption

Next, we calculate the nonlinear evolution of the 2/1 tearing mode in the presence of the 1/1 mode. The purpose of this calculation is to simulate destabilization of the 2/1 mode by the internal disruption through the flattening of the q-profile inside the q=1 surface. The initial q-profile in this case is $q(r)=0.9[1+(r/0.5)^{2\lambda}]^{1/\lambda}$, where $\lambda=2+2r^2$, and $S=2\times10^4$ at the q=1 surface (solid line in Fig.8). In this profile the islands of the 2/1 and 3/2 modes are saturated at relatively narrow width. The saturation width of the 2/1 and 3/2 islands ($W_{2/1}$ and $W_{3/2}$) estimated by using a Δ' code is $W_{2/1}=0.109$ and $W_{3/2}=0.005$ for the initial q-profile, and $W_{2/1}=0.204$, $W_{3/2}=0.062$ for the flattened q-profile (dashed line in Fig.8), respectively. There is no island overlapping between the 2/1 and 3/2 modes for the initial q-profile, while the island overlapping is expected for the flattened q-profile after the internal disruption. In order to investigate this possible enhancement of the 2/1 island width by the flattening of the current profile due to the internal disruption, the calculation is started with only the 2/1 mode, and the 1/1 mode is initiated at t=520 after the 2/1 island is saturated (Fig.9). The saturation width of the the 2/1 island at t=520 is $W_{2/1}=0.07$ which is a little smaller than the expected value. With the growth of the 1/1 mode, the 3/2 mode is produced by the coupling of the 1/1 and 2/1 modes, and the internal disruption occurs at

$t \cong 700$. After the internal disruption the q-profile inside of the q=1 surface is flattened and that outside of it is unchanged, (dotted line in Fig.8). In spite of the change of the q-profile, however, the island evolution of the 2/1 and 3/2 modes seems unchanged, even a long while after the internal disruption, i.e., $W_{2/1}=0.07$ and $W_{3/2}=0.014$ at t=970. These values are about 1/3 - 1/4 of those obtained by using the Δ' code and there is no assurance of island overlapping even if the calculation continues. There are other possibilities to initiate the major disruption. In Ref.6, we have shown that the size of the 2/1 island is strongly enhanced by the internal disruption due to the toroidal coupling. This result suggests that the major disruption is induced by the internal disruption in a toroidal plasma.

§4 Conclusion and Discussion

We have studied the nonlinear evolution of tearing modes with different helicity in a cylindrical plasma and comfirmed that the major disruption is caused by the nonlinear destabilization of the 3/2 mode through the mode coupling with the 2/1 mode. And the evolution of the magnetic field topology has been precisely investigated. All these results support the mechanism of the major disruption, proposed by Waddel et al. The details of our results, however, are different from their results. Especially, in our simulation, the 2/1 mode is deeply in the Rutherford regime and its instantaneous growth rate is not affected even after the 3/2 mode is nonlinearly destabilized. This behavior of the 2/1 mode contradicts with the WKB theory. Therfore, the mechanism of the destabilization of the 3/2 mode remains unsolved

As for the effect of the internal mode on the major disruption, the flattening of the q-profile due to the internal disruption did not cause the enhancement of the 2/1 island width, in spite of the prediction of the major disruption by the Δ' calculation. The flattening occurs only inside of the q=1 surface and the q-profile is not affected near the 2/1 and 3/2 surfaces. Therefore, in order to expect the major disruption by the internal disruption, we have to take into account other effects, such as the toroidicity.

Acknowledgments

The authors would like to thank Dr. M. Tanaka for his helpful discussion and continuing encouragement throughout the whole work. It is also a pleasure to thank Dr. Y. Obata for his encouragement during the whole work.

References

1) B. V. Waddel et al., Phys. Rev. Lett. 41 (1978) 1386.
2) B. V. Waddel et al., Phys. Fluids 22 (1979) 896.
3) B. Carreras et al., Phys. Fluids 23 (1980) 1811.
4) B. Carreras et al., Phys. Fluids 24 (1981) 66.
5) B. V. Chirikov, Phys. Reports 52 (1979) 263.
6) T. Takeda et al., "Internal disruption in high β_p tokamak" in this workshop.

Figure Captions

Fig.1 Time evolutions of the m/n mode magnetic island width for the case of (a) singl-helicity calculation and (b) multi-helicity calculation. The widths for both cases are the same before the island-overlapping time (t=300).

Fig.2 Time evolutions of (a) the kinetic energy and (b) the magnetic energy in the case of multi-helicity calculation. Results of the single-helicity calculation are also shown by dotted lines.

Fig.3 Instantaneous growth rates of the m/n magnetic energy. The growth rates of the 3/2 and 5/3 modes start to increase at the island-overlapping time (t=300), while the 2/1 mode remains in the Rutherford regime.

Fig.4 Time evolution of the one-turn voltage at the limiter.

Fig.5 Helical flux contours of different helicities at the end of the calculation, t=440.

Fig.6 Trajectory of a magnetic field line, starting from a point on the separatrix of the 2/1 island. The cross-section at the poloidal plane $\zeta=0$ is shown. Distinct structure of the 2/1 island is seen at the island-overlapping time t=300, while the trajectory is almost stochastic at t= 440.

Fig.7 Space distributions of the K-S entropy of a magnetic field line at t= 300, 340, 380 and 420. The K-S entropy S is defined by

$$S = \lim_{N=\infty} \frac{1}{N} \sum_{n}^{N} \ln \ell_n$$

where n stands for an iteration serial number and ℓ_n is the distance between two field lines starting from neighbouring positions

Fig.8 Profile of the safety factor q. The solid line denotes the initial q-profile (q_0=0.9 and q_a=3.6). The dotted line is the q-profile changed by the internal disruption. The model q-profile after the internal disruption for the Δ' calculation is shown by the dashed line.

Fig.9 Time evolution of the magnetic island width. The result from t=0 to t=520 is obtained by the single-helicity calculation of the 2/1 mode. The 1/1 perturbation is added at t=520, and the evolution is simulated by the multi-helicity code. The internal disruption, which occurs at t= 690, does not influence the 2/1 mode.

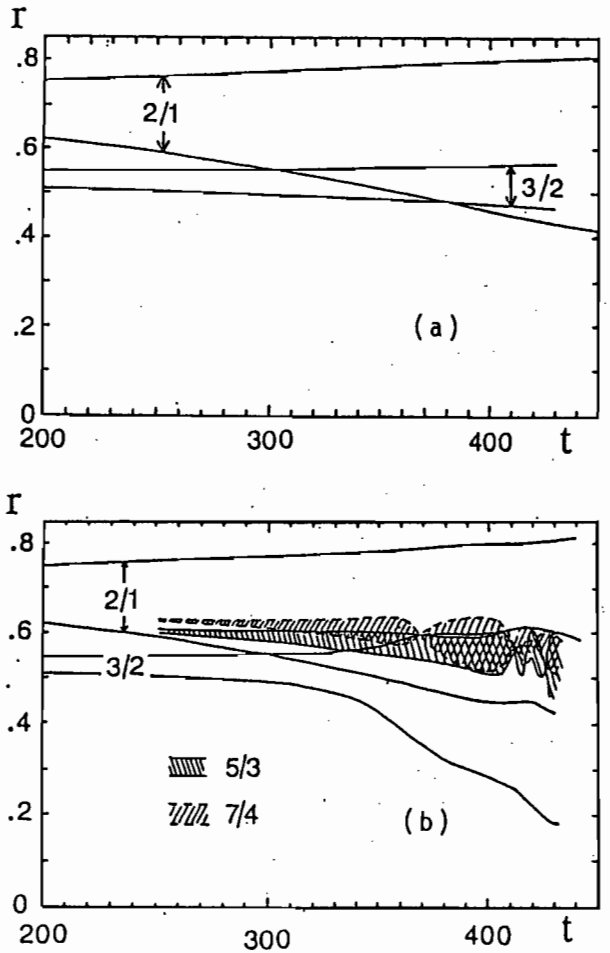

Fig.1

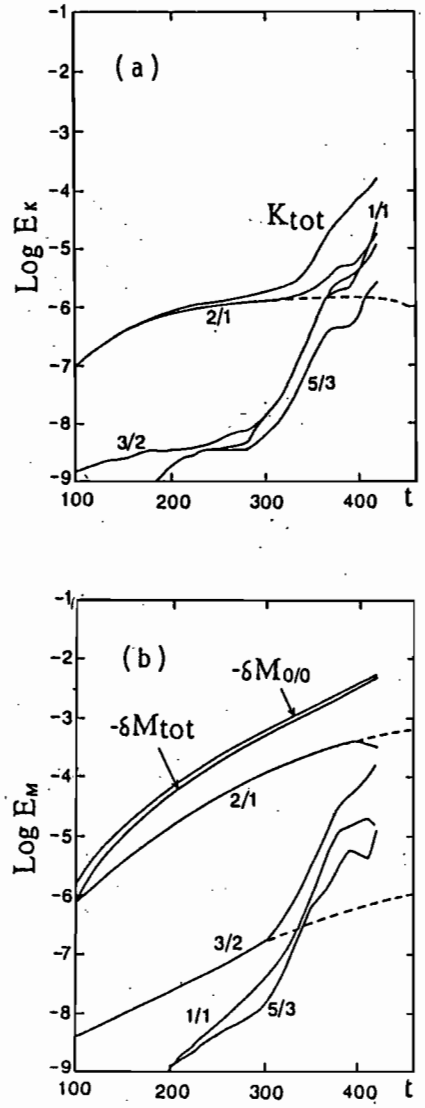

Fig.2

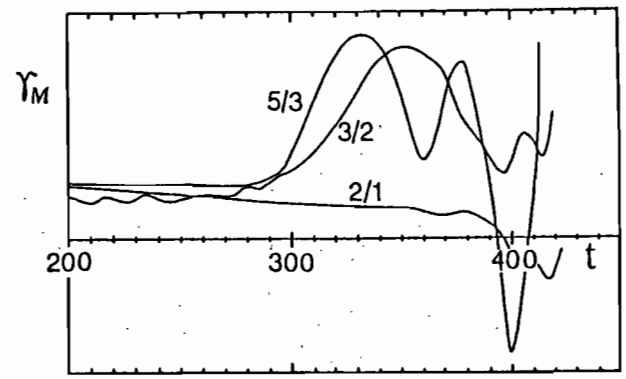

Fig.3

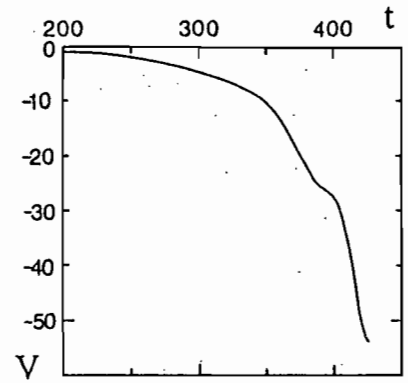

Fig.4

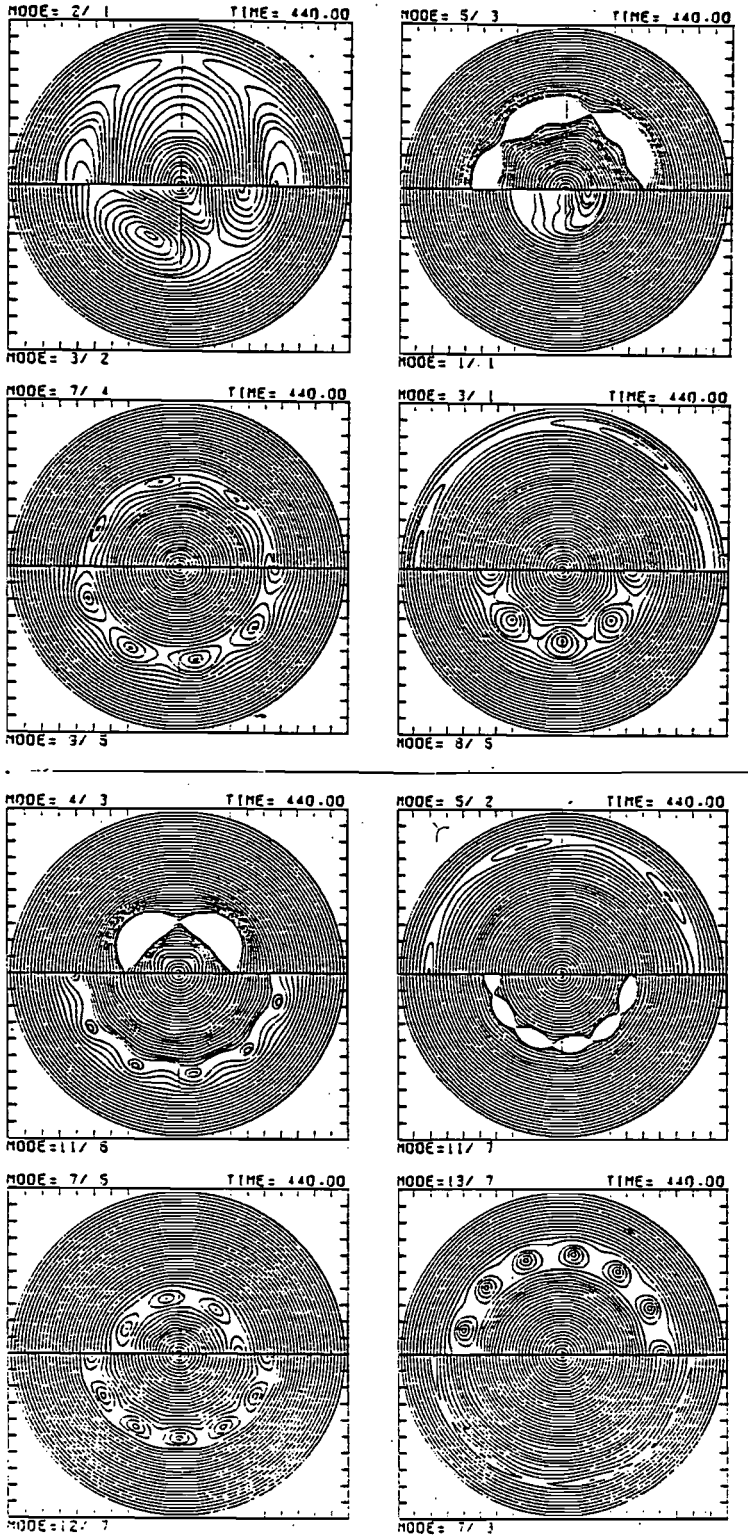
MODE= 2/ 1
TIME= 440.00
MODE= 3/ 2
MODE= 5/ 3
TIME= 440.00
MODE= 1/ 1
MODE= 7/ 4
TIME= 440.00
MODE= 3/ 5
MODE= 3/ 1
TIME= 440.00
MODE= 8/ 5
MODE= 4/ 3
TIME= 440.00
MODE=11/ 6
MODE= 5/ 2
TIME= 440.00
MODE=11/ 7
MODE= 7/ 5
TIME= 440.00
MODE=12/ 7
MODE=13/ 7
TIME= 440.00
MODE= 7/ 3

Fig.5

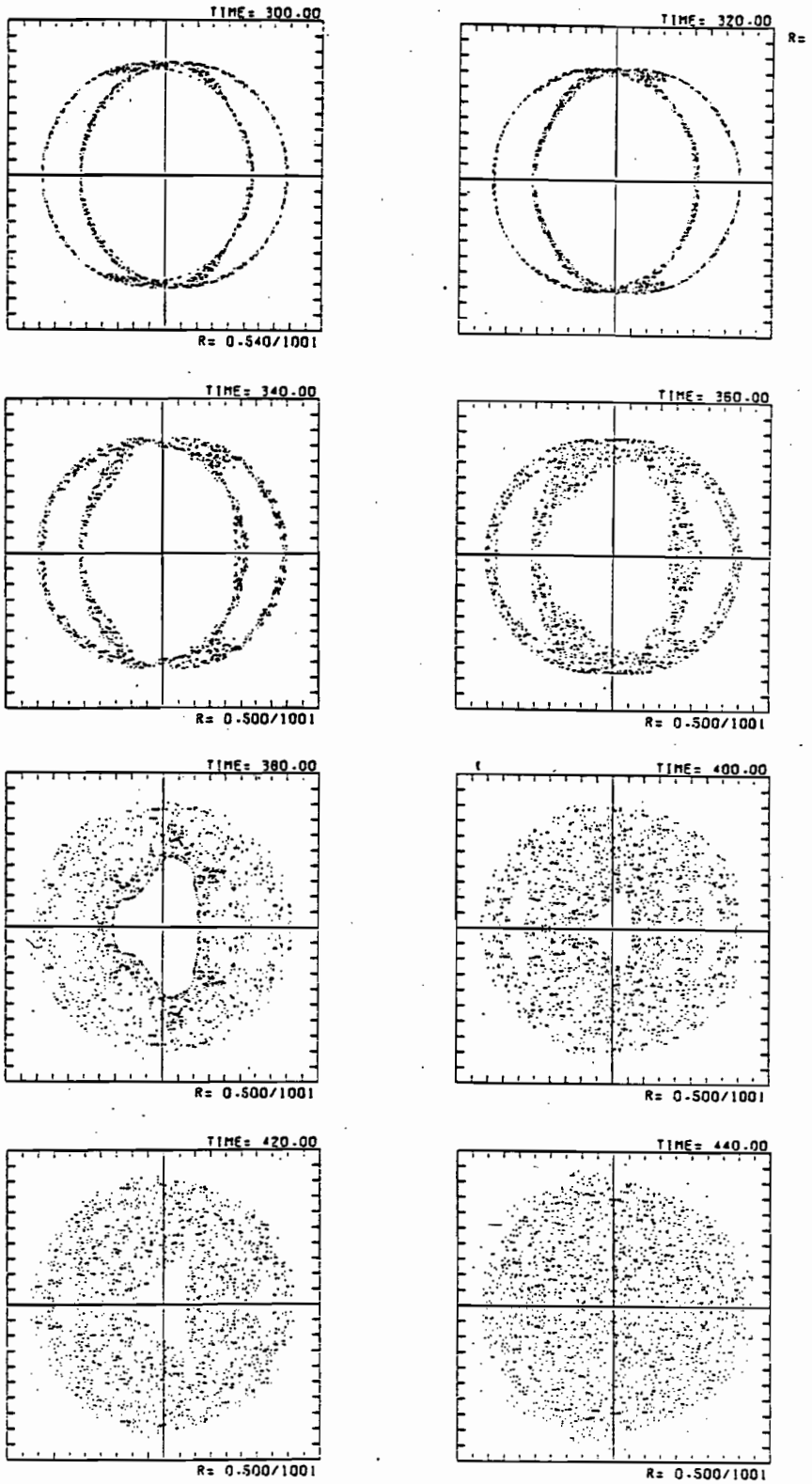
TIME= 300.00
R= 0.540/1001
TIME= 320.00
R=
TIME= 340.00
R= 0.500/1001
TIME= 360.00
R= 0.500/1001
TIME= 380.00
R= 0.500/1001
TIME= 400.00
R= 0.500/1001
TIME= 420.00
R= 0.500/1001
TIME= 440.00
R= 0.500/1001

Fig.6

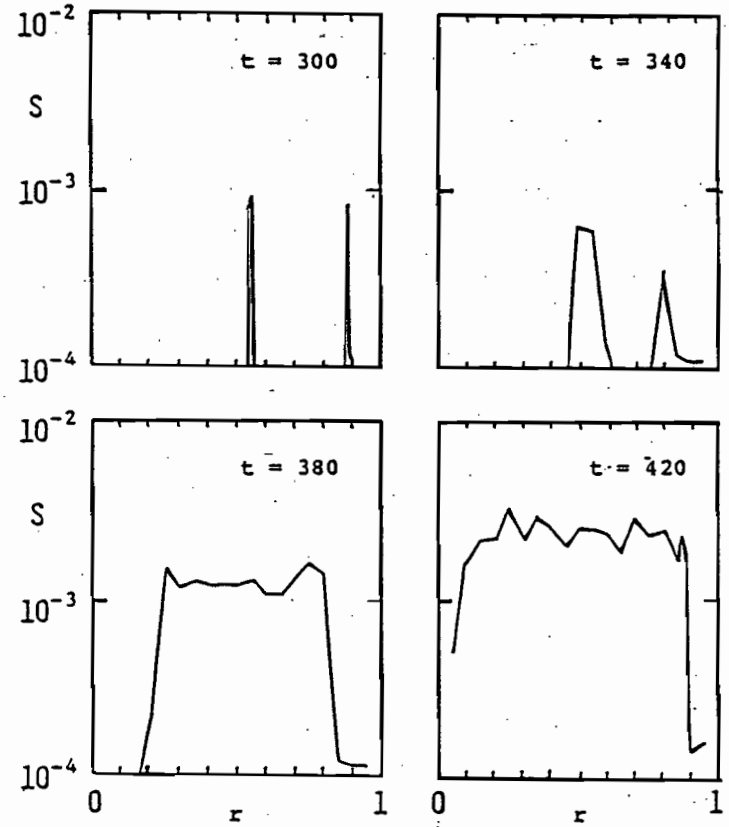

Fig.7

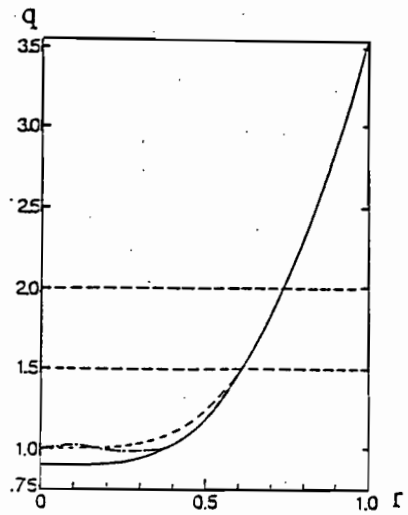

Fig.8

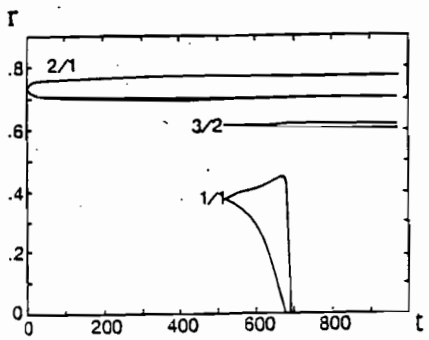

Fig.9

3-D Nonlinear Resistive Studies of High-β PDX Discharges

W. Park, D. A. Monticello, R. B. White, K. McGuire, and M. Reusch
Plasma Physics Laboratory, Princeton University
Princeton, New Jersey 08544 USA

MHD activities of PDX high-β discharges are studied using a 3-D high-β resistive code, HIB. The HIB code solves the high-β reduced tokamak equations finite differenced in r and Fourier decomposed in θ and φ.

The high-β reduced tokamak equations[1] are in (r, θ, φ) coordinates;

$$\frac{d\psi}{dt} = \frac{\partial\psi}{\partial t} + v\cdot\nabla\psi = \frac{\partial u}{\partial\phi} + \eta\nabla^2\psi \quad ,$$

$$\frac{d\nabla^2 u}{dt} = \vec{B}\cdot\nabla\nabla^2 A + \frac{2}{R_o}\left(\frac{\partial P}{\partial r}\sin\theta + \frac{\partial P}{r\partial\theta}\cos\theta\right) \quad ,$$

$$\frac{dP}{dt} = 0 \quad ,$$

where $\vec{v} = \nabla u\times\hat{\phi}$ and $\vec{B} = \nabla\psi\times\hat{\phi} + B_o\hat{\phi}$. Figure 1(a) shows the PDX tokamak geometry and Fig. 1(b) shows our computational modeling. Figure 1(b) also illustrates the position of the plasma-vacuum interface, the placement of the Mirnov magnetic pick-up loops, and the rays used for calculating the soft x-ray signals. The vacuum region is modeled by using a highly resistive plasma.

The equilibrium shown in Fig. 1 has $\langle(a/R)\beta_p\rangle \simeq 0.3$, $q_o = 0.8$, $q_{surface} = 3.2$, and the q = 1 surface at about 1/3 the plasma radius. Figure 2 shows the q profile as a function of the square root of the flux, and the pressure profile as a function of the radius. The abscissa value of 1.0 in Fig. 2(a) corresponds to the flux surface which intersects the M3 detector. In Fig. 3 the n = 1 linear eigenmode of this equilibrium is shown.

We follow the nonlinear development of this linear eigenmode until the amplitude of the Mirnov signal reaches the same level as that found in the experiment. Figure 4 and Fig. 5 show poloidal cross sections of the plasma at φ = 0 and φ = π when ΔB/B at the loop M3 reaches ~ 0.3% which corresponds to the maximum experimental loop signal of the discharge.

Figure 6 compares the experimental Mirnov signal (a) with the

computational results at $\Delta B/B \simeq 0.15\%$ (b) and at $\Delta B/B \simeq 0.3\%$ (c). These show good comparison in both the signal shape and the relative amplitudes. The calculated signals of M6, M7, and M8 are amplified 7 times for the plotting. Signals of M6, M7, and M8, which are on the small major radius side, show fine structure which facilitates a clear comparison between experiment and theory.

Similarly, Fig. 7 compares the soft x-ray signals between experiment (a) and theory at two instants of time; when $\Delta B/B \sim 0.15\%$ (b) and when $\Delta B/B \sim 0.3\%$ (c). Again, both the detailed structures and relative amplitudes agree very well. For good comparison, the incorporation of the nonlinearity of the modes and the vacuum region outside the main plasma were found to be essential. The realistic value of the resistivity $\eta = 10^{-7}$ was also necessary.

Figure 8(a) shows the Fourier components ψ_m in flux coordinates and Fig. 8(b) shows the magnetic topology in the nonlinear state when $\Delta B/B \sim 0.3\%$. From Fig. 8(b), $m > 1$ islands inside the plasma are found to be small. This, together with Fig. 6, then resolves a "puzzling" experimental fact that anomalously large Mirnov signals are detected while $m = 2$ islands inferred from the soft x-ray signals appear to be small. From the simulations, the $m = 2$ island is observed to grow much slower than the $m = 1$ island for small η. This is consistent with our previous 2-D calculations.[2] This is further evident in the large current spike at the $q = 1$ surface compared to the small peak at the $q = 2$ surface in Fig. 4 and Fig. 5, and also in the fact that in Fig. 8(a), $\psi_1(q = 1)/\psi_{1max}$ became larger than that of the linear eigenmode while $\psi_2(q = 2)/\psi_{2max}$ became smaller. On the other hand, the large Mirnov signals are due to the fact that modes whose singular surfaces lie in the vacuum have significant amplitudes at the plasma-vacuum interface as shown in Fig. 8(a).

We have also studied low-β cases for comparison. Figure 9 shows a saturated ohmic state. In this particular case, the $m = 1$ island saturates without sawtooth cycle as shown in Fig. 9(a). Mirnov signals in this case, as shown in Fig. 9(d), are $\Delta B/B \sim 0.005\%$, 1/50 times smaller than the high-β case. This is consistent with the experimental measurements in the low-β discharges.

One of the most important questions to be answered is how these MHD

activities influence the confinement characteristics. Preliminary results show that the Kolmogorov entropy calculated from the state shown in Fig. 8(b) is large enough so that the collisionless diffusion is dominant for about half of the plasma radius. The magnetic diffusion values in this region are found to be comparable to the anomalous experimental diffusion rate.

1. H. R. Strauss, Phys. Fluids 20, 1354 (1977).
2. W. Park, Bull. Am. Phys. Soc. 26, 845 (1981) paper 1A4.

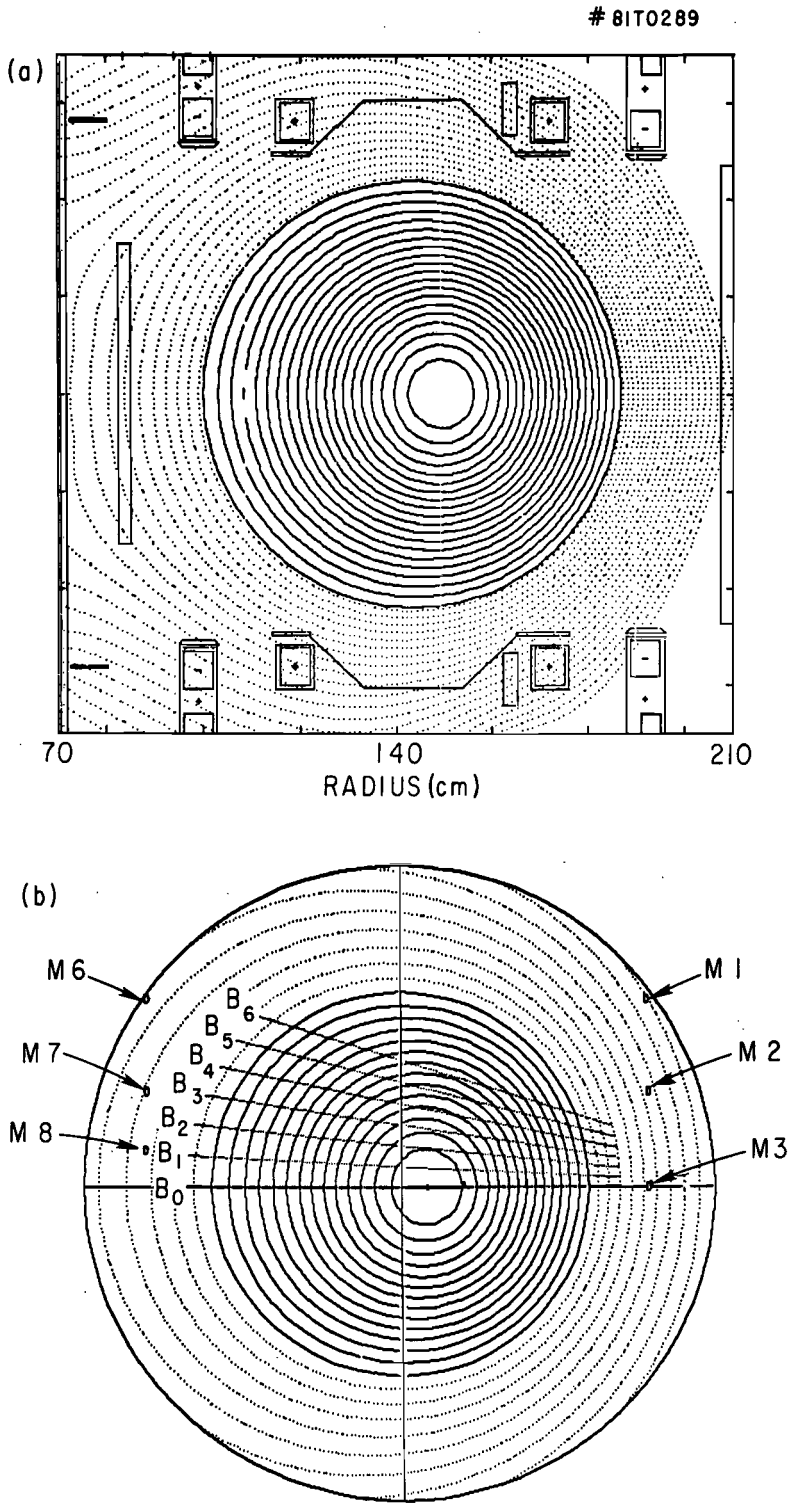
#81T0289
(a)
70
140
210
RADIUS (cm)
(b)
M6
M7
M8
M1
M2
M3
B6
B5
B4
B3
B2
B1
B0

Fig. 1.

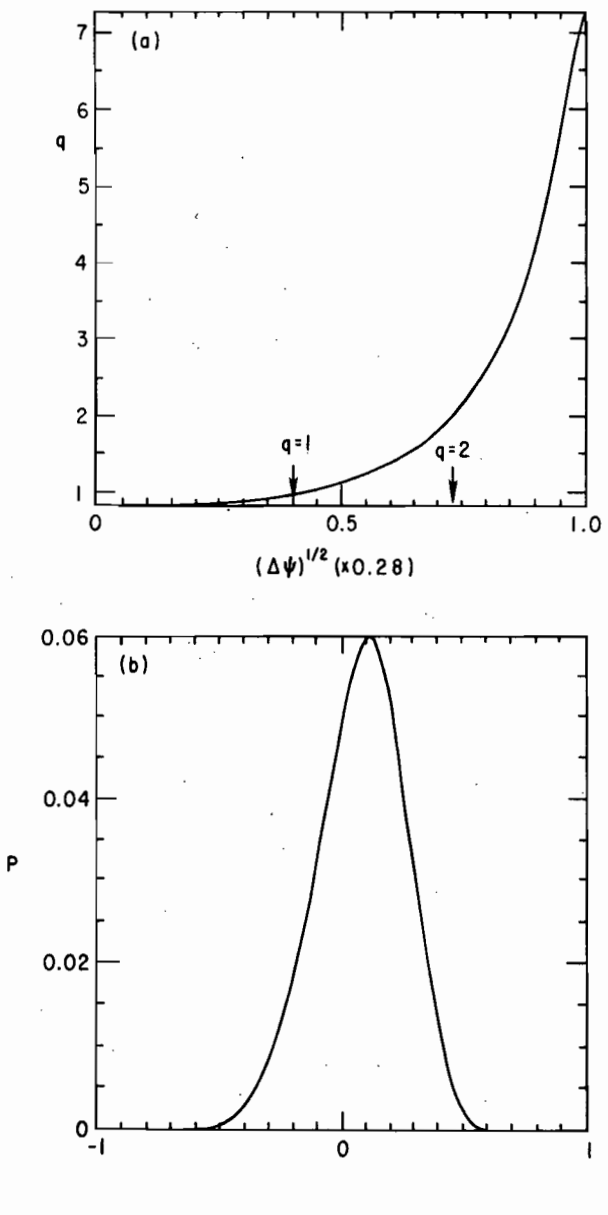
(a)
q
q=1
q=2
$(\Delta\psi)^{1/2}$ (x0.28)
(b)
P

Fig. 2.

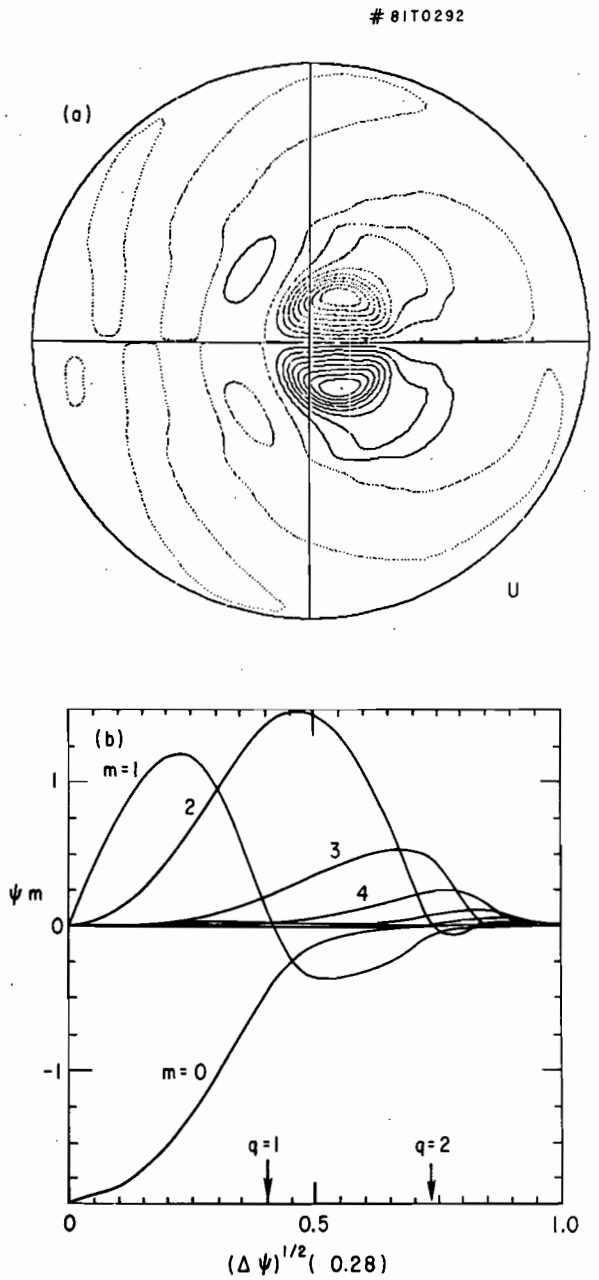
#81T0292
(a)
U
(b)
m=1
2
3
4
m=0
ψm
q=1
q=2
$(\Delta\psi)^{1/2}$(0.28)

Fig. 3.

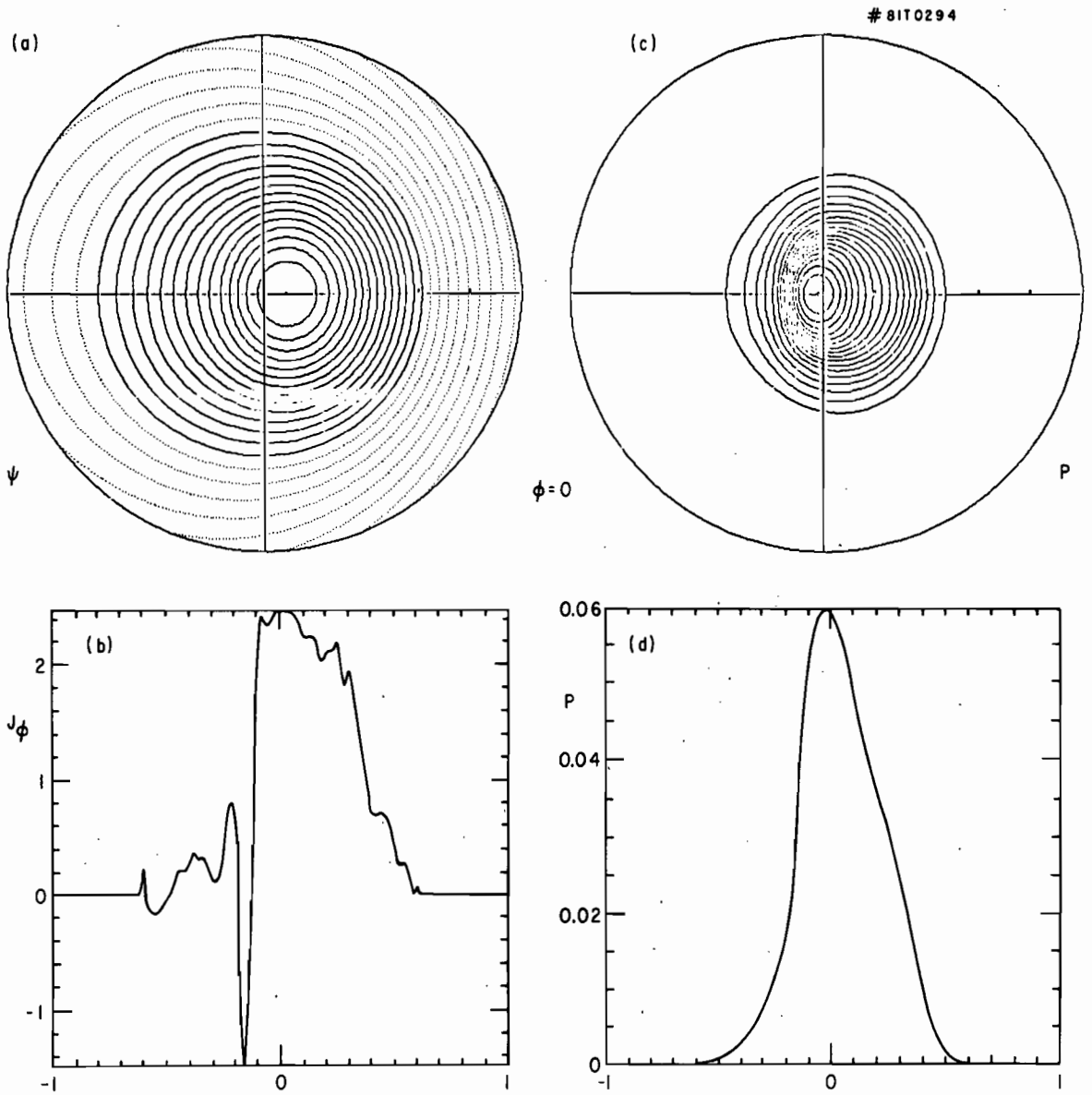

Fig. 4.

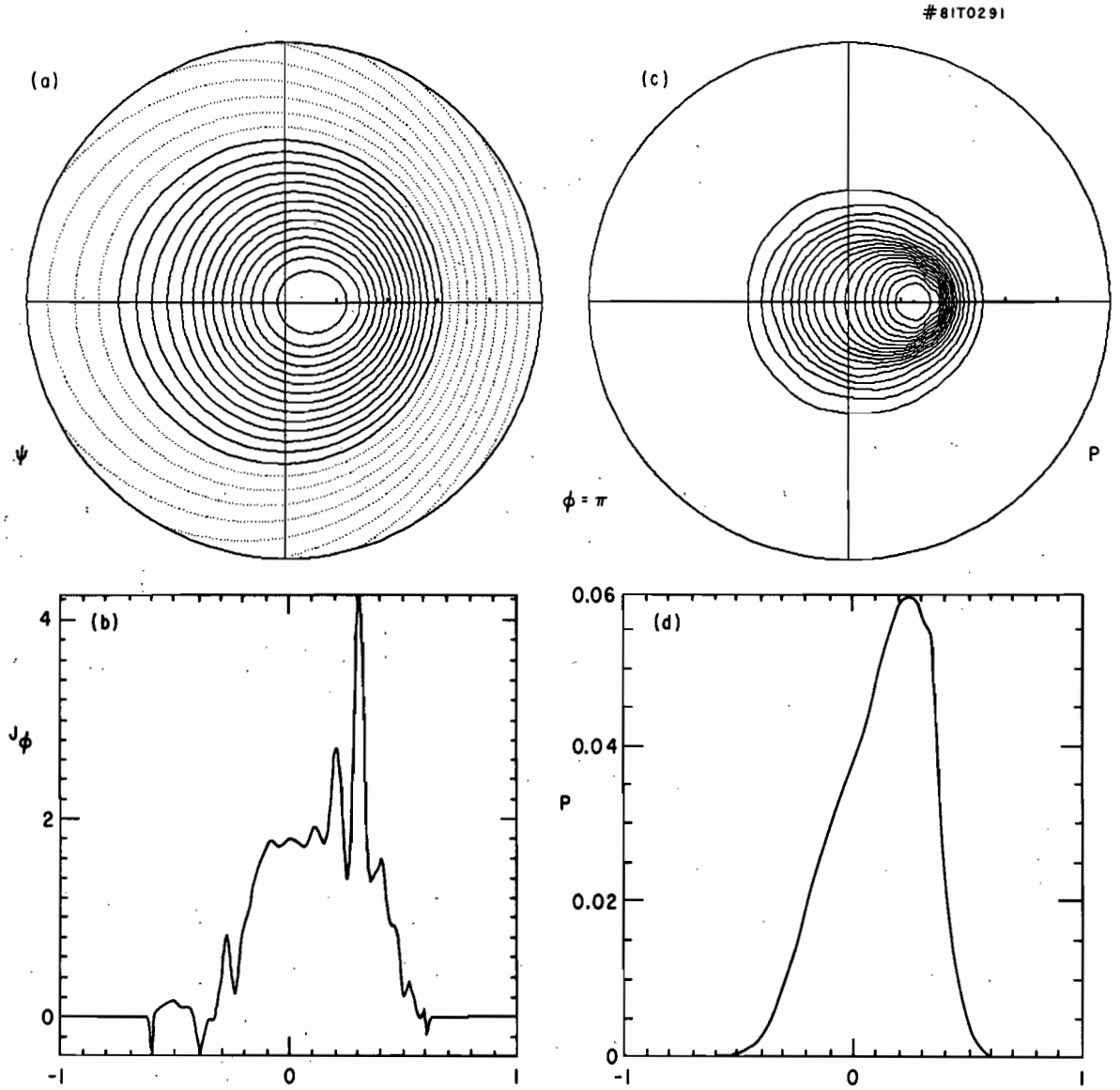

Fig. 5.

81T0287

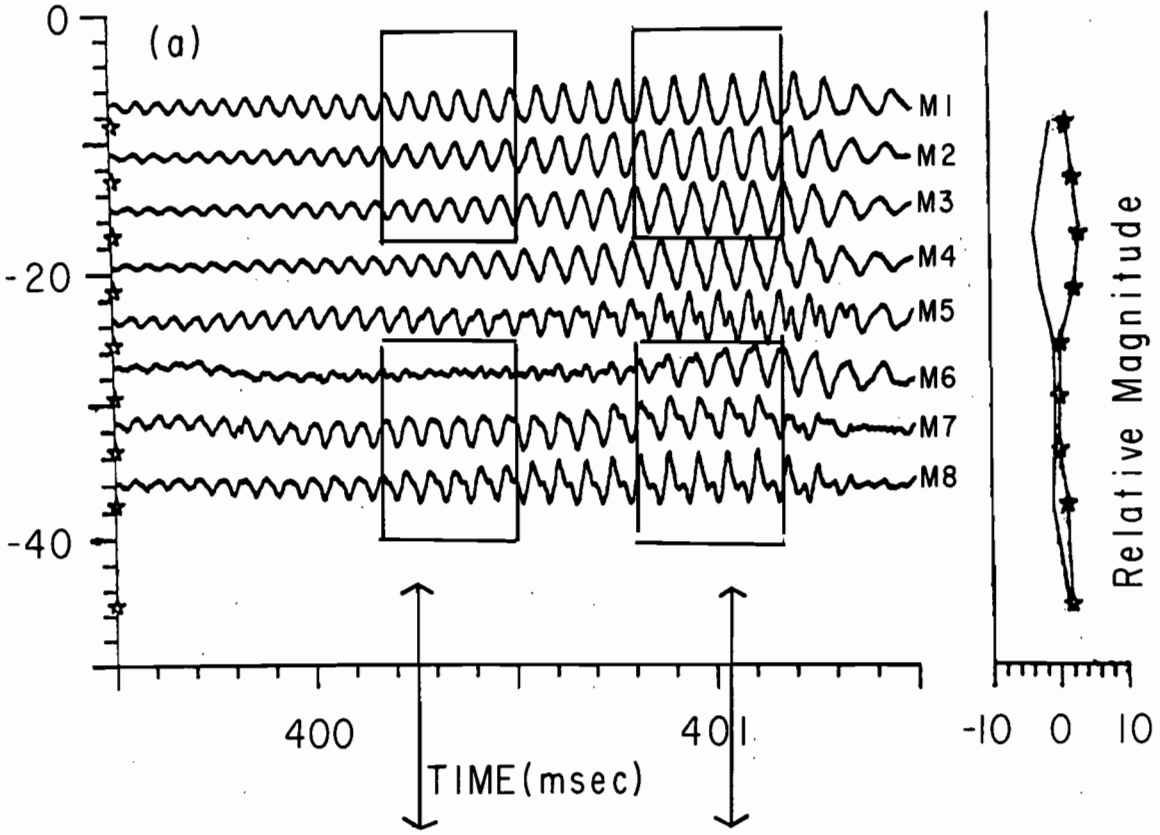

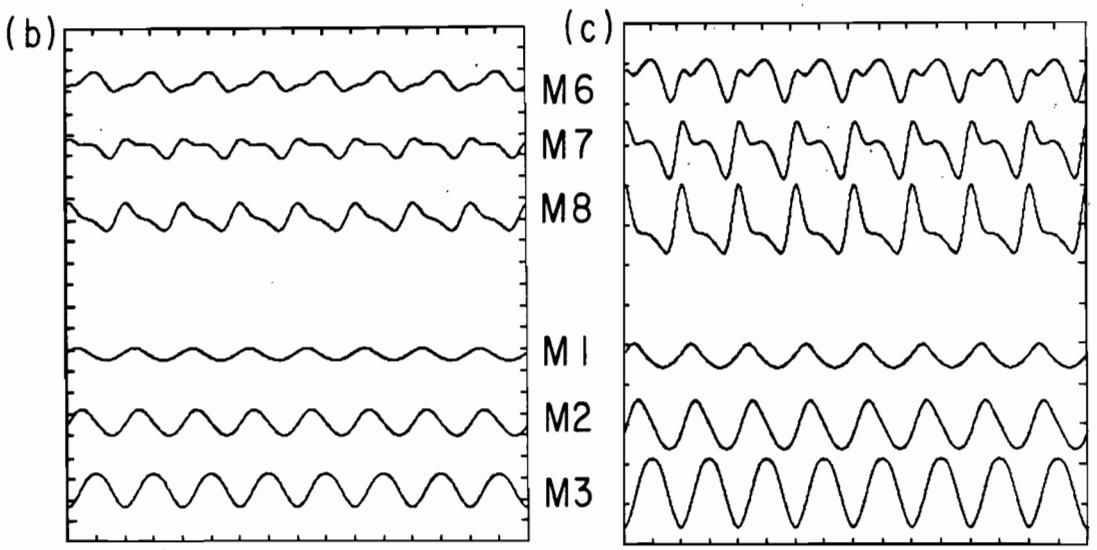

$\Delta B/B \sim 0.15\%$ $\Delta B/B \sim 0.3\%$

Fig. 6.

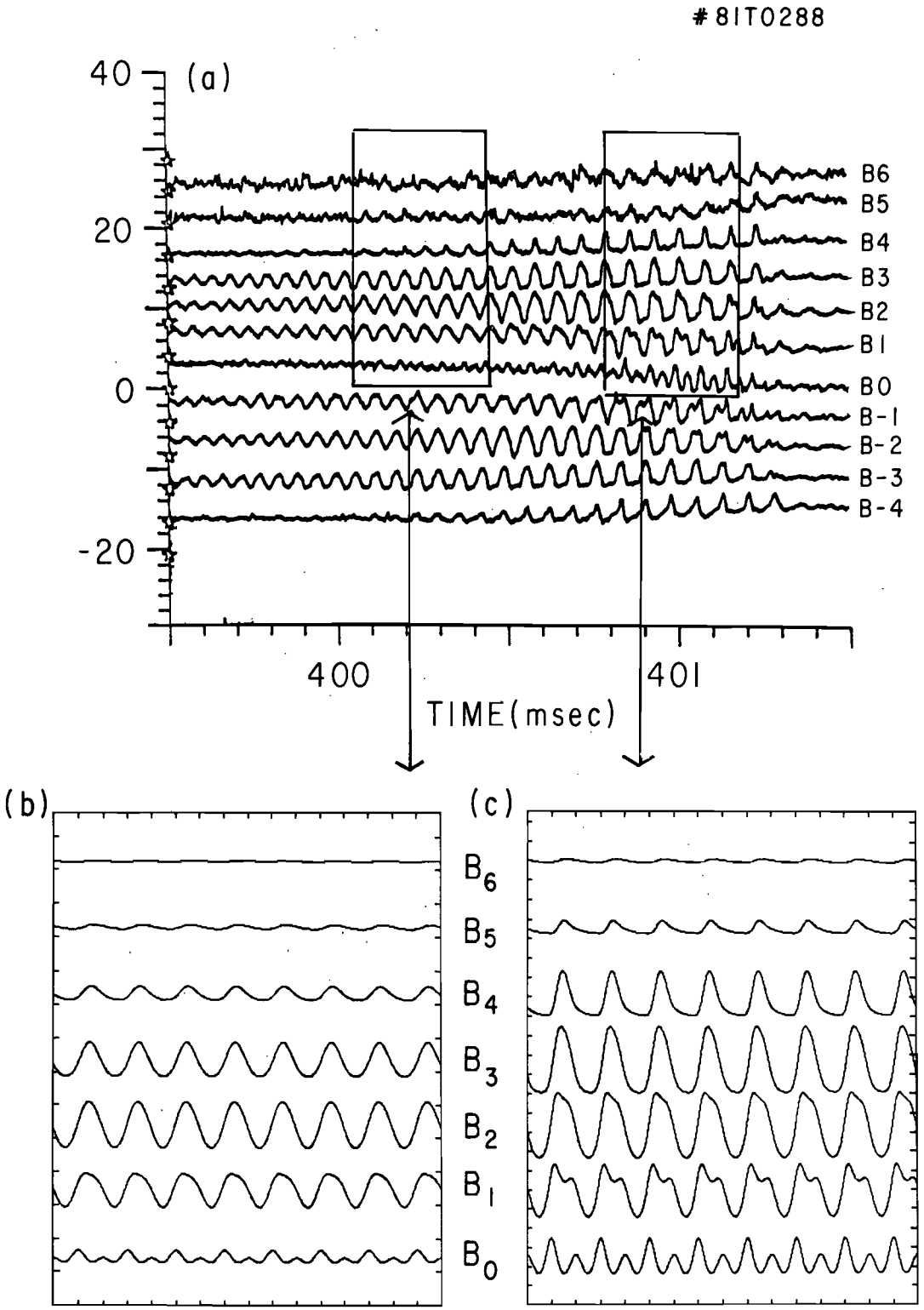

At $\Delta B/B \sim 0.15\%$.

At $\Delta B/B \sim 0.3\%$.

Fig. 7.

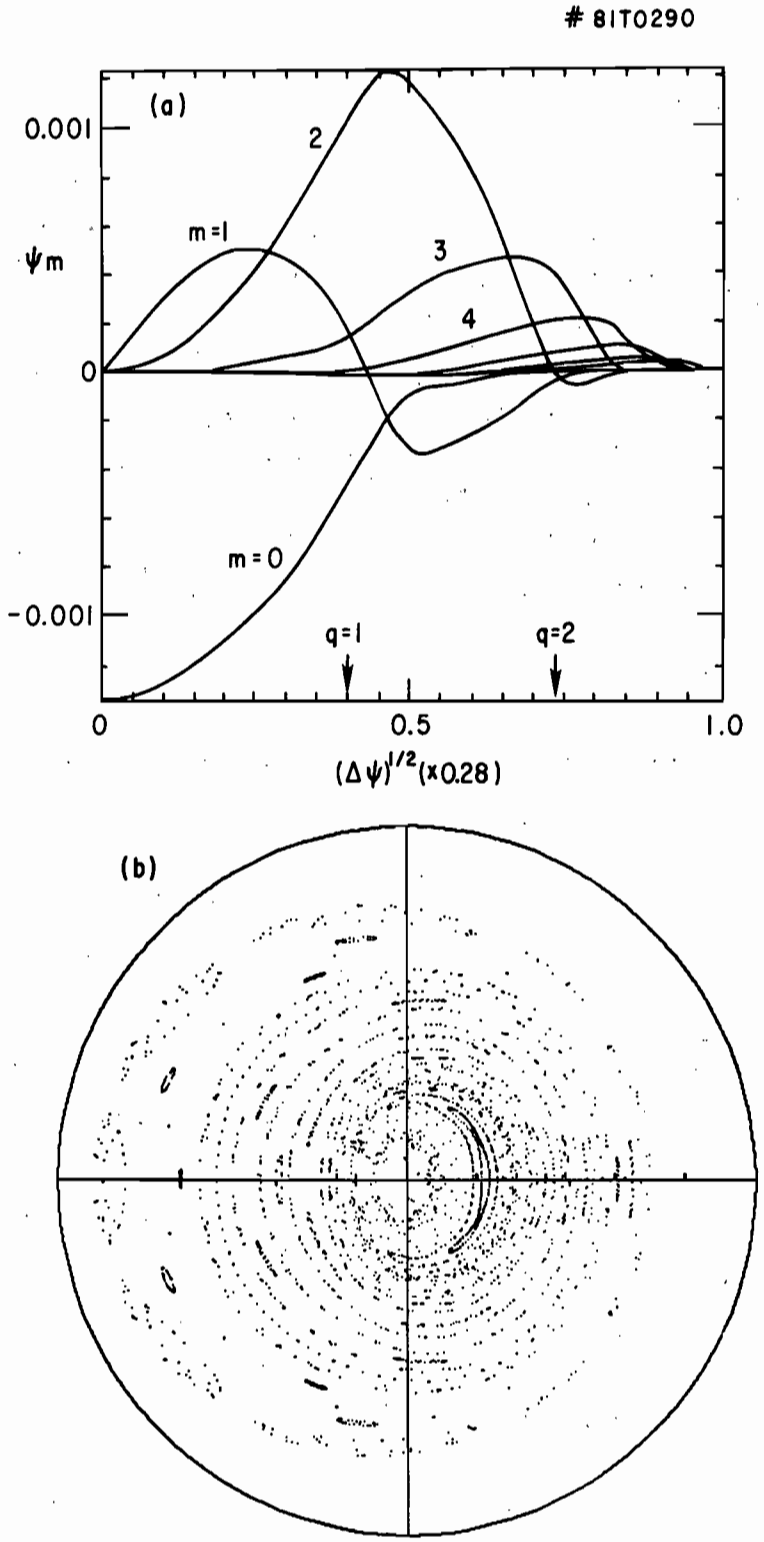

Fig. 8.

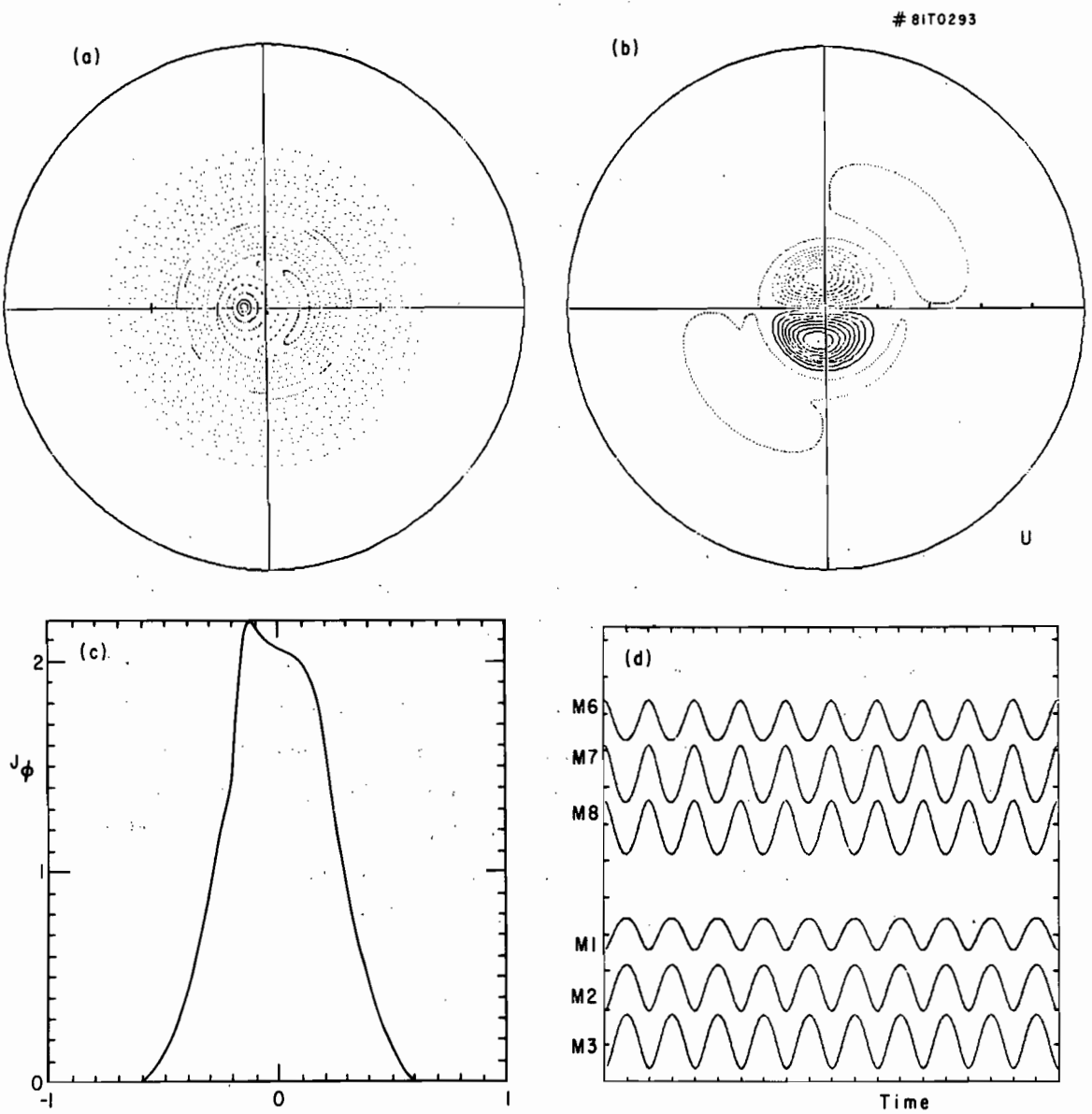

$\Delta B/B \sim 0.005\%$

Fig. 9.

Internal Disruption in High β_p Tokamak

T. Takeda, M. Azumi, S. Tokuda, G. Kurita,
T. Tsunematsu, T. Takizuka, T. Tuda, K. Itoh, Y. Tanaka*

Japan Atomic Energy Research Institute
Tokai-mura, Naka-gun, Ibaraki-ken, Japan

The $m = 1$ MHD activity is investigated from the veiwpoint of the suppression of the internal disruption and the appearance of large amplitude oscillations observed in the recent high β tokamak experiment. The stabilization of the $m = 1$ internal kink mode by the toroidal effect is confirmed by using the revised version of ERATO. The nonlinear evolution of the resistive internal kink mode is investigated and the reasonable saturation of the $m = 1$ magnetic island is obtained by using the new reduced set of equations. The effect of the toroidal coupling between the $m = 1$ and $m = 2$ tearing modes is also studied. The $m = 2$ mode is strongly affected, but the saturation of the $m = 1$ magnetic island is not realized.

* On leave from Fujitsu Ltd.

§1 Introduction

The internal disruption was first observed in the ST tokamak as sawtooth oscillations on soft X-ray signals[1] and, thereafter, it has been commonly observed in tokamaks with the q-value less than unity at the magnetic axis. Since the plasma deformation is restricted within a volume of a critical radius ($\sim \sqrt{2} r_s$, r_s ; the radius of the $q=1$ surface), the effect on the plasma confinement is not serious in high-q discharges. In very low-q discharges, however, the energy confinement time is considerably reduced by the sawtooth oscillations[2]. According to the model by Kadomtsev[3], the unstable $m=1$ tearing mode grows exponentially in time until the current profile becomes flat inside the $q=1$ surface due to the magnetic field reconnection. The disruption process is reproduced in good agreement with the experimental data by a single helicity numerical calculations[4,5]. The sawtooth oscillations are recovered in a result of a tokamak code simulation based on this model modified to include the kinetic effect[6].

In the recent high-power-neutral-beam-injection experiment of the JFT-2 tokamak, it has been observed that the sawtooth oscillations are replaced by large amplitude $m=1$ oscillations[7]. Although Kadomtsev's model has succeeded in the explanation of the sawtooth oscillations, it can not explain the $m=1$ oscillation found in the high β_p experiments. Two possible causes of this new phenomenon are considered: (i) the mode coupling between the $m=1$ and $m=2$ resistive modes due to toroidicity , and (ii) the unstable $m=1$ "resistive internal kink mode". In a toroidal plasma, the $m=1$ and $m=2$ resistive modes are coupled each other due to the outward shift of the magnetic axis. By this coupling, the magnetic energy of the $m=1$ mode can be released through the $m=2$ mode, and the disruption is possibly supressed. This effect becomes larger in a plasma with higher poloidal beta value because of the larger shift of the magnetic axis and of the non-uniformity of the equilibrium current density along the field line.

As for the $m=1$ internal kink mode, it becomes unstable when the poloidal beta value exceeds a critical value[8]. In spite of the large growth rate, the saturation level of the mode is quite low[9,10]. The mode does not develop into the internal disruption but shows finite amplitude saturation, which is smaller than that observed in experiments. Taking into account the resistivity, the "resistive internal kink mode" develops beyond this saturation

level due to the field line reconnection. The evolution of the energy of the toroidal field works as a stabilizing factor to prevent the disruption, and the saturation of the magnetic island is expected.

The purpose of this paper is to study the effects of the toroidicity and ideal mode on the internal disruption, especially in a high beta plasma with the low q-value. In the next section we study the $m=1$ internal kink mode in a tokamak by using the code ERATO and show that the internal mode becomes unstable for increasing the poloidal beta value. The unstable internal resistive mode in a cylindrical plasma is studied in §3 by using the new reduced set of the MHD equation, and the saturation of the magnetic island is shown in a plasma with the high poloidal beta value. The toroidal effects on the nonlinear evolution of the $m=1$ and $m=2$ tearing modes are studied in §4. Summary is given in §5.

§2 Toroidal Effect on the Internal Kink Mode

In this section we study numerically the toroidal effect on the $m=1$ internal kink mode by using the code THALIA[11] and the revised version of ERATO[12] which is incorporated to a high accuracy mapping module and can give accurately a solution with a small growth rate. By the numerical analysis we confirmed that the toroidicity stabilizes the internal kink mode as shown by Bussac et al.[8] and obtained some insights into the resistive internal mode.

Equilibria used in the analyses are as follows. In the toroidal calculations an FCT series of equilibria with a circular cross section and aspect ratio A of 3 is computed for a given pressure profile $p(\psi)$

$$\frac{dp}{d\psi} = p_0 [\, 1 - \alpha\psi - (1-\alpha)\psi^4 \,], \qquad 0 \le \psi \le 1 \tag{2.1}$$

where the parameter p_0 is varied and the safety factor profile, $q(\psi)$, is obtained for a low β and null diamagnetic current ($TdT/d\psi = 0$) equilibrium. The choice of the q-profile gives the ratio $q_a/q_0 = 2.5$. In the cylindrical case the pressure and toroidal field functions are given as

$$\frac{dp}{d\psi} = p_0 (1 - \psi) , \qquad 0 \le \psi \le 1 \tag{2.2}$$

$$B_z \frac{dB_z}{d\psi} = \left(\frac{1}{\beta_p} - 1\right) \frac{dp}{d\psi} . \tag{2.3}$$

This profile gives the ratio $q_a/q_0 \cong 2.4$, which is the approximately same as that of the toroidal analyses. Figure 2.1 shows the profiles of the safety factor q for a toroidal (a solid line) and cylindrical (a dashed line) equilibria with $\beta_p = 1$ and $q_0 = 0.9$. The difference of the positions of the q = 1 surface is small between these two cases.
The "toroidal" wave number of the cylindrical plasma, $k_z a = na/R$, is chosen as 1/3, which corresponds to the n = 1 mode in our toroidal calculations. In Fig. 2.2 the squared growth rates Γ^2 vs. β_p are shown for $q_0 = 0.9$. The growth rate Γ^2 tends to zero for $\beta_p \to 0$ in the cylindrical model, whereas, the mode becomes stable at a finite β_p in the toroidal case. Figure 2.3 shows the stability diagram in the $q_0 - \beta_p$ plane. The solid line and the dashed line denote the stability limit for the toroidal and cylindrical cases, respectively. The dotted-solid line denotes the cylindrical equilibria where the safety factor at the plasma surface (q_a) is unity, which shows that the stability is almost determined by the existence of the q = 1 surface, in the cylindrical model. In the toroidal case, however, there is a critical β_p ($\beta_p = 0.7$ in our model) below which the internal kink mode is completely stabilized. Figure 2.4 shows the structures of the azimuthal component (ξ_θ) of the plasma displacement. As β_p decreases, ξ_θ becomes steep in the toroidal model. For $\beta_p = 0.75$, the half width of the mode is about 0.05a. When the magnetic Reynols number is $S = 10^6$, the width of the resistive layer is the order of $S^{-1/3} = 0.01$. This means that the resistivity broadens the eigenmode when $\beta_p \lesssim 0.75$. In usual ohmically heated plasmas ($\beta_p < 0.5$), the resistive mode plays a dominant role in the confinement of a plasma. When β_p increases, the width of the eigenmode is much broader than that of the resistive layer (Fig.2.4(a)) and resistive effect is weak in the exponentially growing phase.

§3 Simulation of the Resistive Internal Kink Mode

In this section, we study the linear stability and the nonlinear evolution of the m = 1 "resistive internal kink mode" in a cylindrical plasma. The evolution of the tearing modes has been studied by using the usual reduced set of MHD equations. In this set of equations, however, the m = 1 internal mode is marginally stable because the driving terms of this mode, i.e., the second order terms in the inverse aspect ratio are neglected. In order to

simulate the resistive internal mode, therefore, we have to include these terms correctly.

In the following, we assume the perturbations with a single helicity ($f(\vec{r},t) = f(r,\theta+kz,t)$), the incompressible fluid motion $\nabla\cdot\vec{v} = 0$ and the uniform mass density $\rho(\vec{r},t=0) = 1$. Under these assumptions, the magnetic field $\vec{B}$ and the velocity $\vec{v}$ can be expressed by the helical flux function ψ and the helical stream function Φ as

$$\vec{B} = B_\zeta \vec{e}_h + \vec{e}_h \times \vec{\nabla}\psi \tag{3.1}$$

$$\vec{v} = v_\zeta \vec{e}_h + \vec{e}_h \times \vec{\nabla}\Phi \tag{3.2}$$

where $\vec{e}_h = (\vec{e}_\theta - kr\vec{e}_z)/\sigma$ is the unit vector along the helix and $\sigma = 1+(kr)^2$. Using these expressions, the MHD equations can be rewritten into the following equations:

$$\frac{\partial U}{\partial t} + \vec{v}\cdot\vec{\nabla}(U + \frac{2k}{m\sigma^2} v_\zeta) = \frac{k^2}{m^2\sigma^2}\frac{\partial v_\zeta{}^2}{\partial\theta} + \vec{B}\cdot\vec{\nabla}J - \frac{k^2}{m^2\sigma^2}\frac{\partial B_\zeta{}^2}{\partial\theta} \tag{3.3}$$

$$\frac{\partial v_\zeta}{\partial t} + \vec{v}\cdot\vec{\nabla}v_\zeta = \vec{B}\cdot\vec{\nabla}B_\zeta \tag{3.4}$$

$$\frac{\partial\psi}{\partial t} = \vec{B}\cdot\vec{\nabla}\Phi + \sigma\eta J - E_\zeta(t) \tag{3.5}$$

$$\frac{\partial B_\zeta}{\partial t} = -\sigma\vec{v}\cdot\vec{\nabla}(\frac{B_\zeta}{\sigma}) + \sigma\vec{B}\cdot\vec{\nabla}(\frac{v_\zeta}{\sigma}) - \frac{2k}{m\sigma}\vec{B}\cdot\vec{\nabla}\Phi + \sigma\eta R_\eta \tag{3.6}$$

$$U = \Delta^*\Phi, \quad J = \Delta^*\psi + \frac{2k}{\sigma^2}B_\zeta \text{ and } R = \Delta^*B_\zeta - \frac{2k}{\sigma^2}J,$$

($m = 1$), where E_ζ is the externally induced electric field, which we set such that the total plasma current is constant. The energy integral of these equations is written as

$$\frac{d}{dt}(K + M) + Q = 0 \tag{3.7}$$

where K, M and Q denote the kinetic energy, magnetic energy and the rate of the energy dissipation, respectively,

$$K = \frac{1}{2}\int [\frac{1}{\sigma}(\frac{\partial\Phi}{\partial r})^2 + (\frac{1}{r}\frac{\partial\Phi}{\partial\theta})^2 + \frac{1}{\sigma}v_\zeta{}^2]rdrd\theta \tag{3.8}$$

$$M = \frac{1}{2} \int [\frac{1}{\sigma} (\frac{\partial\psi}{\partial r})^2 + (\frac{1}{r} \frac{\partial\psi}{\partial\theta})^2 + \frac{1}{\sigma} B_\zeta{}^2] r dr d\theta \tag{3.9}$$

$$Q = \int \eta [\sigma J^2 + \frac{1}{\sigma} (\frac{\partial B_\zeta}{\partial r})^2 + (\frac{1}{r} \frac{\partial B_\zeta}{\partial\theta})^2] r dr d\theta$$

$$- \frac{r}{\sigma} [(\frac{\partial\psi}{\partial t} - E_\zeta) \frac{\partial\psi}{\partial r} + \eta B_\zeta \frac{\partial B_\zeta}{\partial r}]_{r=a} . \tag{3.10}$$

This set of equations reduces to the conventional one when the longitudinal wave number k goes to zero with keeping kB_ζ constant. Thus, the set of equations can express three different modes; i.e., the internal mode ($\eta = 0$, $k \neq 0$), tearing mode ($\eta \neq 0$, $k = 0$) and resistive internal kink mode ($\eta \neq 0$, $k \neq 0$).

Before studying the nonlinear evolution of the resistive internal kink mode, we study the parameter dependence of the linear growth rate of this mode by linearizing the equations and deriving a generalized matrix eigenvalue equation on the basis of the finite element formulation. Figure 3.1 shows the dependence of the growth rate on the longitudinal wave number k and the resistivity η, where the q profile is chosen as $q(r) = 0.9 + 0.2r^2$ and the radial mesh number N_r is $50 \sim 100$ with mesh accumulation near the q = 1 surface. In a cylindrical plasma, the internal mode is always unstable, except $k = 0$. When k is small and the growth rate of the tearing mode γ_η is much larger than that of the ideal mode γ_I, the localization width of the vorticity near the $q = 1$ surface is determined by the tearing mode. As k increases, the mode becomes essentially the ideal one ($\gamma_I >> \gamma_\eta$). The transition of the mode from the resistive one to the internal one is consistent with the analysis by Coppi et al.[13)]

Now we study the nonlinear evolution of the resistive internal kink mode. We Fourier-expand Eqs.(3.3) to (3.6) with respect to θ+kz. The Fourier-decomposed equations are solved by the predictor-corrector explicit time integration scheme. The evolutions of the three modes, i.e., the internal kink mode, tearing mode, and resistive internal kink mode, are studied for the same q-profile ($q(r) = 0.8(1+r^2)$) and pressure profile ($p(r) = 2(1-r^2)$). The maximum Fourier mode number is 20, and the radial mesh number is 201 with accumulation near the singular point. Figure 3.2

shows the temporal change of the position of the magnetic axis r_a for three cases. When $k=0$ and $\eta = 10^{-4}$, the internal kink mode is marginally stable and the magnetic axis shifts outward exponentially in time due to the resistive mode, and the internal disruption occurs when the magnetic axis touches the critical surface $r=r_c$ as predicted by Kadomtsev[3]. When $k = 1/3$ and $\eta=0$, the internal kink mode causes the shift of the magnetic axis, but this shift saturates at low level due to the development of the skin current. The saturation level of the shift $r_a \simeq 0.1$ is slightly larger than the analytic value[9]. This difference is due to the formation of a thin magnetic island caused by the numerical reason in the saturation stage.

When we take into account the finite resistivity $\eta=10^{-4}$(the resistive internal kink mode), the magnetic axis shifts beyond the saturation level of the internal mode due to the magnetic field line reconnection. Unlike the resistive mode, the longitudinal field B_ζ forms the island structure and the development of the large diamagnetic current prevents the further shift of the magnetic axis before it reaches the critical surface $r=r_c$. In this way, the resistive internal kink mode forms the large, saturated magnetic island. Figure 3.3 shows the ψ and B_ζ contours in the saturation stage. These results shows that the resistive internal kink mode is a candidate of the experimentally observed large amplitude $m=1$ oscillations.

§4 Simulation of the Tearing Modes in a Toroidal Plasma

In this section we study the nonlinear evolution of the $m=1$ mode in a low β_p toroidal plasma. In order to understand the evolution of the $m=1$ mode in a tokamak with high poloidal beta values, we have to take into account correctly both of the mode coupling due to the toroidicity and the unstable internal kink mode. The latter effect can be neglected in a low β_p toroidal plasma. The unstable modes are only the resistive ones and it is relevant to study their evolution using the conventional set of reduced equations[14].

We consider a tokamak with circular cross section and employ the coordinates (r,θ,ϕ), where field lines are straight and $r = \sqrt{g}\, R_0/R^2$. Assuming the smallness of the inverse aspect ratio, $\varepsilon = r/R$, the reciprocal metric tensor is approximated as

$$g^{rr} = 1 + 2\frac{d\Delta}{dr}\cos\theta ; \quad g^{r\theta} = -\left(\frac{d^2\Delta}{dr^2} + \frac{1}{r}\frac{d\Delta}{dr} - \frac{1}{R_0}\right)\sin\theta ;$$

$$g^{\theta\theta} = \frac{1}{r^2}\{1 - 2(\frac{d\Delta}{dr} - \frac{r}{R})\cos\theta\}; \quad g^{\phi\phi} = R_0^2(1 + 2\frac{r}{R_0}\cos\theta), \tag{4.1}$$

where Δ is the shift of the magnetic axis defined by

$$\Delta(r) = \frac{1}{R_0}\int_r^a \frac{dr}{rB_\theta^2}\int_0^r (B_\theta^2 - 2r\frac{dp}{dr})rdr. \tag{4.2}$$

The safety factor and pressure profiles used in the following simulations are; $q(r) = 0.9\{1-(r/r_0)^{2\lambda}\}^{1/\lambda}$ with $r_0 = 0.5$ and $\lambda = 2 + 2r^2$, and $p(r) = p_0(1-r^2)^2$. We employ the equal spacing radial meshes ($N_r = 201$), the maximum mode number $M_m = 31$ and the implicit-explicit time integration scheme.

Figure 4.1 shows the temporal evolution of the magnetic islands with different helicity for the aspect ratio $R_0/a = 10$, the poloidal beta value $\beta_p = 0$ and the resistivity $\eta = 10^{-4}$. The phase of the initial perturbation of the m=2/n=1 mode is chosen to be the same as that of the m = 1 mode for the case (a) and opposite for the case (b). For the comparison, the cylindrical case ($R_0/a = \infty$) is also subject to the simulation (case (c)). The behavior of the m = 1 mode in a toroidal plasma is essentially the same as in the cylindrical plasma. Untill the m = 1 mode grows to a finite level ($t < 50$), the m = 2 magnetic island also grows independently of the m = 1 mode as in the cylindrical plasma. Thereafter, the m = 2 mode is strongly affected by the m = 1 mode through the toroidal coupling. For the case (a), the m = 2 island shrinks and finally changes its phase. On the other hand, the island width for the case (b) is widened by the toroidal effect. This can be seen more remarkably in Fig. 4.2, where the evolution of the magnetic energies with the different helicity is plotted. The energy of the m = 2 mode with the initially opposite phase grows exponentially with the growth rate of about half of that of the m = 1 mode without entering the Rutherford regime, while the energy of the m = 2 mode for the case (a) decreases from the one for the cylindrical case.

Now we consider the difference of the toroidal effect on the m = 2 modes of the in-phase and opposite-phase cases. The total energy of the reduced set of MHD equations in a toroidal plasma is given by

$$E = \frac{1}{2}\int_0^a [\ (\frac{R}{R_0})^2 |\nabla\Phi|^2 + (\frac{R_0}{R})^2 |\nabla\psi|^2\ ]\ d\tau \tag{4.3}$$

This energy can be devided into two parts; the cylindrical energy, E_{cyl}, and

the toroidal one, E_{tor}. When we divide the reciprocal metric g^{ij} into the cylindrical one $\bar{g}^{ij}$ and the toroidal one $\tilde{g}^{ij}(\theta)$, then E_{tor} is expressed, up to the first order of ε, as

$$E_{tor} = \int_0^a [\{\tilde{g}^{ij}(\theta) + \tilde{g}^{ij}(-\theta)\}\left(\frac{\partial\Phi_1}{\partial x^i}\frac{\partial\Phi_2}{\partial x^j} + \frac{\partial\psi_1}{\partial x^i}\frac{\partial\psi_2}{\partial x^j}\right) - \frac{4r}{R_0}\bar{g}^{ii}\frac{\partial\Phi_1}{\partial x^i}\frac{\partial\Phi_2}{\partial x^i}]d\tau \quad (4.4)$$

where we take into account only the toroidal coupling between the $m=1$ (the suffix "1") and $m=2$ (the suffix "2") modes. We approximate Φ_1 and Φ_2 as $\Phi_1 \simeq \hat{\Phi}_1 r/r_s|_{m=1}$ and $\Phi_2 \simeq \hat{\Phi}_2\{r/r_s|_{m=1}\}^2$ in the region $r \leq r_s|_{m=1}$. Then using the relation $\psi_m = -F_m\Phi_m/\gamma_m$, we have

$$E_{tor} \simeq \frac{4}{R_0}\int_0^{r_s|_{m=1}} dr(\psi_1\psi_2 - 3\Phi_1\Phi_2) \simeq \frac{4}{R_0}\int_0^{r_s|_{m=1}} dr\ \psi_1\psi_2\ , \quad (4.5)$$

where γ_m is the growth rate of each mode and $F_m = mB_\theta/r + nB_z/R_0$. This expression shows that the sign of the toroidal coupling energy E_{tor} depends on the phase between the $m=1$ and $m=2$ modes. Because of the small dissipation, the total energy of the system is almost conserved, so that E_{cyl} becomes smaller (or greater) than that in the cylindrical plasma for $\psi_1\psi_2 > 0$ (or $\psi_1\psi_2 < 0$). Since the $m=1$ mode has the larger growth rate and the larger amplitude than those of the $m=2$ mode, the effect of the toroidal coupling on the $m=1$ mode can be neglected. Therefore, the energy of the $m=2$ mode decreases (or increases) due to the toroidal coupling for $\psi_1\psi_2 > 0$ (or $\psi_1\psi_2 < 0$). From these results we see that the toroidal coupling influences only on the $m=2$ mode; the evolution of the $m=1$ mode is almost unaffected and the disruption occurs after the same development shown in the cylindrical calculations.

§5 Conclusion

In this paper, we have studied the linear stability and the nonlinear evolution of the $m=1$ mode. The results obtained here are summarized as the followings;

1. By using the revised version of the code ERATO, it was confirmed that the toroidicity has the stabilizing effect on the $m=1$ internal kink mode and the mode is unstable only for the polidal beta higher than a critical value in a toroidal plasma.

2. The nonlinear evolution of the resistive internal kink mode in a cylindrical plasma shows that the internal disruption can be suppressed due to the modulation of the longitudinal field.
3. In a low β toroidal plasma with large aspect ratio, the behaviour of the $m = 1$ tearing mode is found to be essentially the same as in a cylindrical plasma. The $m = 2$ tearing mode, however, suffers a strong effect of the $m = 1$ mode through the toroidal coupling and forms the magnetic island with larger width than in a cylindrical case.

All these results show that the Kadomtsev's model of the internal disruption is valid in a toroidal plasma with the low poloidal beta. In a high β plasma,however,the internal kink mode was shown to be unstable and this mode plays an important role on the evolution of the $m = 1$ mode. Although the simulation of the nonlinear evolution of the resistive internal kink mode has been studied only in a cylindrical plasma, we can expect the saturation of the island in a toroidal plasma. As for the simulation of the tearing modes in a toroidal plasma, we could not see the remarkable change of the $m = 1$ mode for $\beta_p = 0$. We also simulated the case with $\beta_p = 1$, and the result is the same as for $\beta_p = 0$. The reason is considered to be that the pressure driven term was dropped in the simulation. The effect of this term is now under investigation.

In order to extend these results and to understand the saturation of the $m = 1$ mode observed in the high β tokamk experiments, we are preparing the simulation which includes both effects of the unstable internal kink mode and the toroidicity.

Acknowledgments

The authors would like to thank Dr. M. Tanaka for his helpful discussion and continuing encouragement throughout the whole work. It is also a pleasure to thank Dr. Y. Obata for his encouragement during the whole work. They are grateful to Dr. T. Matsuura for the collaboration concerning vectorization of the numerical codes. Members of the experiment group are greatly acknowledged for the fruitful discussion about the results of the high-power-neutral-beam-injection experiment in the JFT-2 tokamak.

References

1) S. von Goeler, W. Stodiek and N. Sauthoff, Phys. Rev. Lett. 33 (1974) 1201.
2) DIVA Group, Nucl. Fusion 20 (1980) 271.
3) B. B. Kadomtsev, Fizika Plasmy 1 (1975) 710.
4) B.V.Waddel et al., Nucl. Fusion 16 (1976) 528.
5) A.F.Danilov et al., Fizika Plasmy 2 (1976) 167.
6) M. Okamoto, private communication.
7) S. Yamamoto et al., Nucl. Fusion 21 (1981) 993.
8) M. N. Bussac et al., Phys. Rev. Lett. 35 (1975) 1638
9) M. N. Rosenbluth, R. Y. Dagazian and P. H. Rutherford, Phys. Fluids 16 (1973) 1894.
10) W. Park et al., Nucl Fusion 20 (1980) 1181.
11) K. Appart et al., Comput. Phys. Commn. 10 (1975) 11.
12) S. Tokuda et al., in preparation. The original version of ERATO is published by R. Gruber et al. in Compt. Phys. Commn. 21 (1981) 323.
13) B. Coppi et al., Sov. J. Plasma Phys. 2 (1976) 533.
14) T. Takeda et al., "Major disruption process in a tokamak" in this workshop.

Figure Captions

Fig.2.1 Profiles of safety factor q(s) ($s = \sqrt{\psi/\psi_s}$) for $\beta_p = 1$ and $q_0 = 0.9$. The solid and dashed lines denote the toroidal and cylindrical cases, respectively. The q = 1 surfaceses lie at s = 0.45 (the toroidal case) and s = 0.4 (the cylindrical case).

Fig.2.2 Squared growth rate Γ^2.vs. β_p for $q_0 = 0.9$. The growth rate tends to zero for $\beta_p \to 0$ in the cylindrical case (dotted line),whereas the mode becomes stable at a finite β_p ($\beta_p = 0.7$) in the toroidal case (solid line).

Fig.2.3 Stability diagram in the q_0- β_p plane. The stability limit for the cylindrical case (dashed line) is almost determined by the existence of the q = 1 surface (dotted-solid line). In the toroidal case, there is a critical β_p ($\beta_p = 0.7$) in the stability limit (solid line) below which the internal kink mode is stabilized.

Fig.2.4 Structures of the azimuthal component (ξ_θ) of the plasma displacement for (a) $\beta_p = 1.25$ and (b) $\beta_p = 0.75$. The solid line denotes the toroidal case and the dashed line the cylindrical case. As β_p decreases, ξ_θ becomes steep for the toroidal case and the half width of the mode at q = 1 surface for $\beta_p = 0.75$ is comparable to that of the resistive layer $S^{-1/3} \simeq 0.01$ for $S = 10^6$.

Fig.3.1 Dependence of the linear growth rate Γ of the resistive internal kink mode on the longitudinal wave number k . The safety factor profile is $q(r) = 0.9 + 0.2r^2$.

Fig.3.2 Evolution of the magnetic axis due to (a) the tearing mode ($\eta = 10^{-4}$,k = 0), (b) the internal kink mode ($\eta = 0$, k = 1/3), and (c) the resistive internal kink mode ($\eta = 10^{-4}$, k = 1/3). The profiles of the safety factor and the pressure are $q(r) = 0.8(1 + r^2)$ and $p(r) = 2(1 - r^2)$, respectively. The positions of the rational surface and of the critical surface for the disruption are denoted by 'r_s' and 'r_c', respectively.

Fig.3.3 Contour of ψ and B_ζ at the saturation stage of the resistive internal kink mode.

Fig.4.1 Evolution of the magnetic islands with different helicity m/n , where m is the poloidal mode number and n is the toroidal one. The safety factor is $q(r) = 0.9(1 - (r/0.5)^{2\lambda})^{1/\lambda}$ with $\lambda = 2 + 2r^2$ and aspect ratio is 10. The initial phase of the m = 2 mode is the same as that of the m = 1 mode in the case (a) and is opposite in the case (b). The case (c) shows the results in the cylindrical plasma. In all case, the internal disruption occurs at $t \simeq 160$.

Fig.4.2 Evolution of the magnetic energy defined by

$$M_{m/n} = \frac{1}{2} \int \left[\left(\frac{\partial \psi_{m/n}}{\partial r} \right)^2 + \left(\frac{m}{r} \psi_{m/n} \right)^2 \right] r\, dr$$

with different helicity (m/n = 1/1,2/1 and 3/2). Other parameters are the same as in Fig.4.1. The toroidal effect on energy of the m = 2 appears earlier than that on the magnetic island. The width of the island is determined by the perturbation at the rational surface. The m = 1 perturbation is restricted within it's critical radius $r_c \simeq \sqrt{2}\, r_{s|m=1}$, so that the toroidal effect of this mode on the m = 2 mode is also restricted within this radius. The m = 2 perturbation in $r < r_c$ propagates to the rational surface $r_{s|m=2}$ after a while.

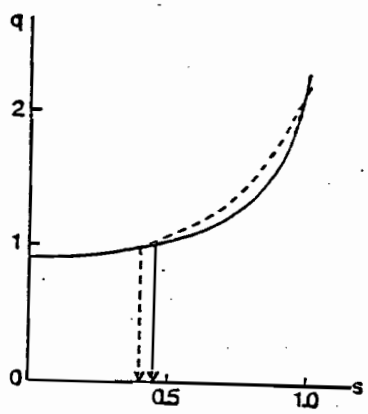

Fig.2.1

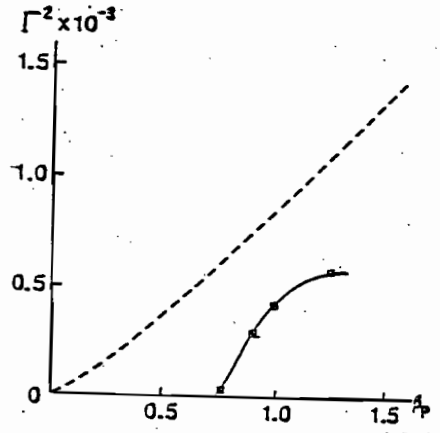

Fig.2.2

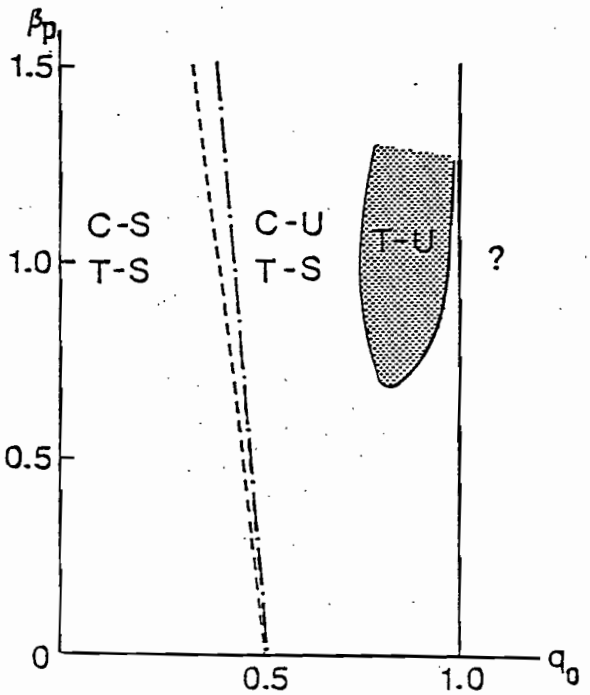

Fig.2.3

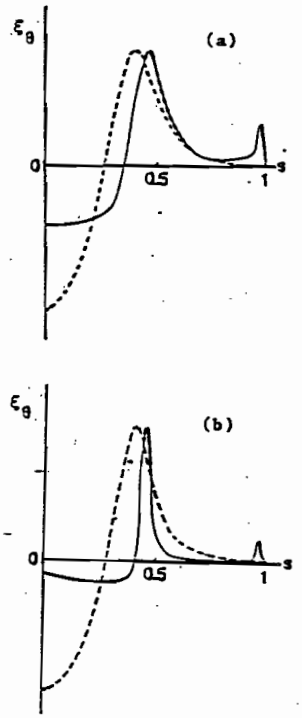

Fig.2.4

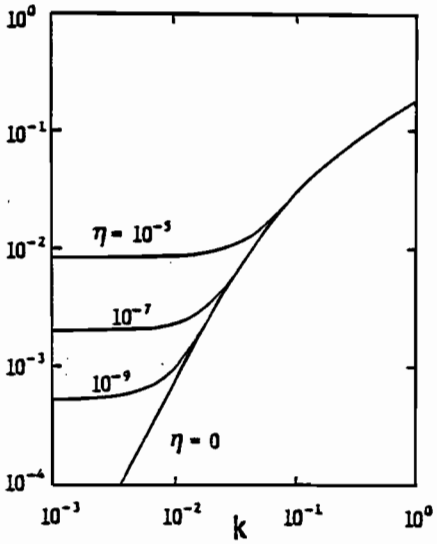

Fig.3.1

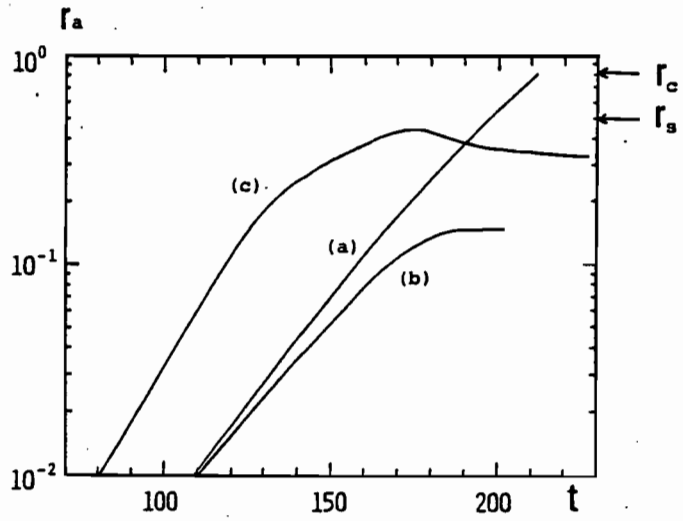

Fig.3.2

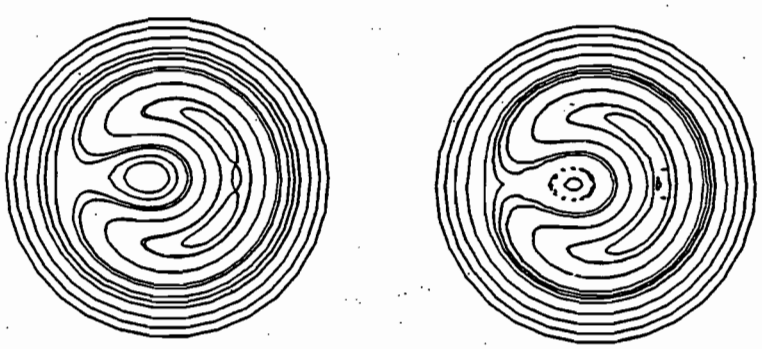

ψ-contour B_ζ-contour

Fig.3.3

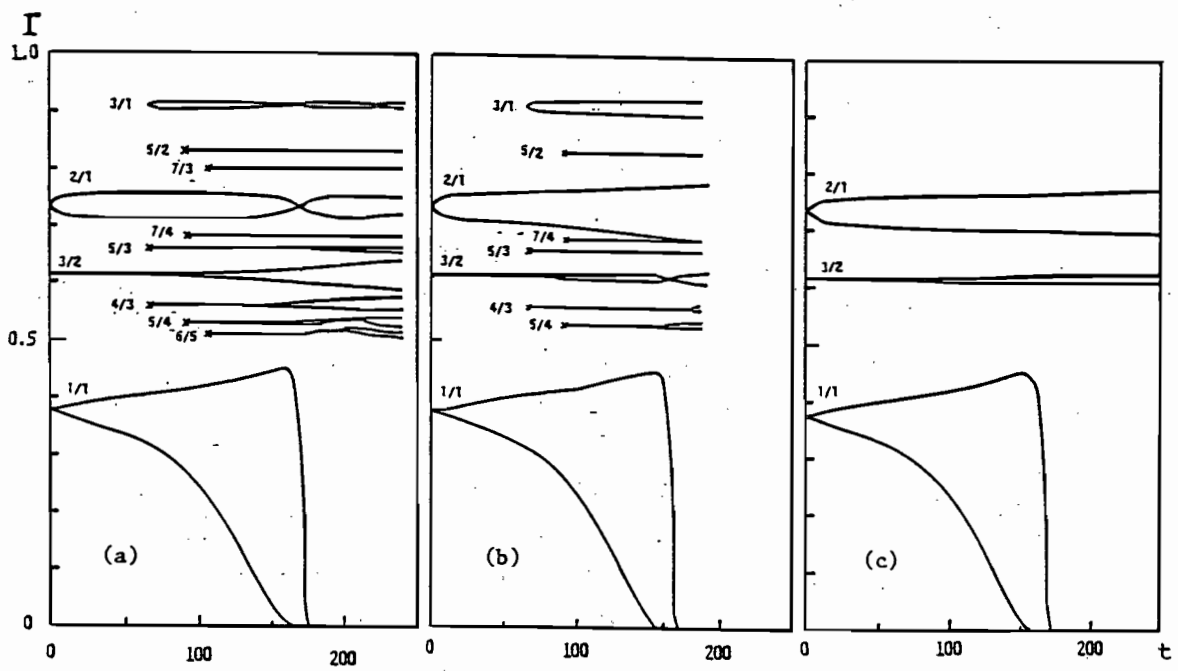
Γ
1.0
0.5
0
3/1
5/2
7/3
2/1
7/4
5/3
3/2
4/3
5/4
6/5
1/1
(a)
(b)
(c)
0
100
200
t

Fig.4.1

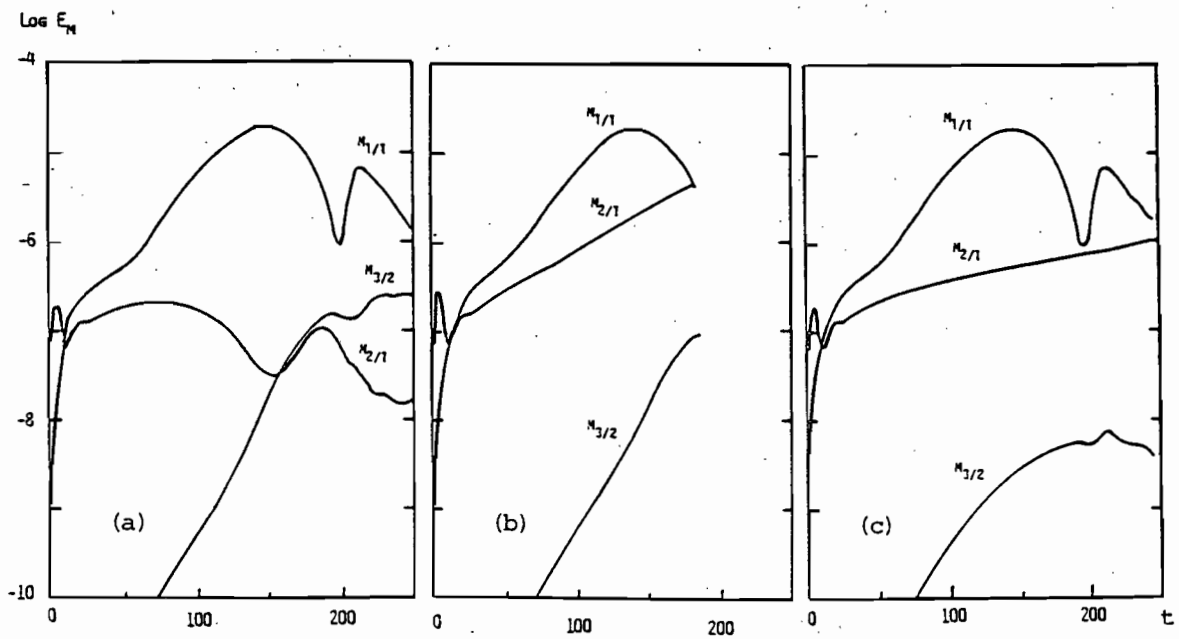
Log E_M
-4
-6
-8
-10
$M_{1/1}$
$M_{3/2}$
$M_{2/1}$
(a)
(b)
(c)
0
100
200
t

Fig.4.2

RESISTIVE MODES IN A HIGH β TOKAMAK*

J. A. Holmes, B. A. Carreras,** L. A. Charlton,
H. R. Hicks, and V. E. Lynch

Computer Sciences at
Oak Ridge National Laboratory
Oak Ridge, Tennessee 37830 USA

ABSTRACT

The stability and evolution of the (m = 1;n = 1) mode in tokamaks having finite β are studied numerically using a reduced set of resistive MHD equations. Particular attention is given to the effects of β, q-profile, and plasma cross-section shape. The results of these studies agree with the systematics of the observed MHD activity in ISX-B [1-6]. Detailed comparison of theoretical and experimental x-ray and magnetic loop signals shows excellent agreement [3-5].

INTRODUCTION

With the success of neutral beam heating, tokamak operation at nonnegligible β has become a reality. In order to study MHD activity at finite β, a 3-D computer code, RST, has been written. RST solves a reduced set of resistive MHD equations as an initial value problem. These equations were first derived by Strauss [7] under the assumptions of large aspect ratio ($\varepsilon \equiv a/R \ll 1$), moderate β ($\beta \sim \varepsilon$), and approximate force balance.

In dimensionless form these equations are

$$\frac{\partial \Psi}{\partial t} = \vec{B} \cdot \vec{\nabla}\Phi + \eta J \tag{1}$$

$$\frac{\partial U}{\partial t} + \vec{v} \cdot \vec{\nabla} U = S^2\left\{\vec{B} \cdot \vec{\nabla} J + \frac{\beta_o}{\varepsilon}\frac{\partial p}{\partial Z}\right\} \tag{2}$$

*Research sponsored by the Office of Fusion Energy, U.S. Department of Energy under contract W-7405-eng-26 with the Union Carbide Corporation.

**Fusion Energy Division.

$$\frac{\partial p}{\partial t} + \vec{v} \cdot \vec{\nabla} p = 0 \tag{3}$$

where $\vec{B} = \frac{\varepsilon}{R} \hat{\zeta} \times \vec{\nabla}\Psi + \hat{\zeta}$, $J = \Delta^*\Psi$, $U = \nabla_\perp^2 \Phi$, and $\vec{v} = \vec{\nabla}\Phi \times \hat{\zeta}$. All lengths are normalized to a generalized minor radius a, and all times to the resistive time $\tau_r = a^2\mu_o/\eta_o$. The quantity S is the magnetic Reynolds number, defined by $S \equiv \tau_r/\tau_{Hp}$ where $\tau_{Hp} = R_o(\mu_o\rho_m)^{1/2}/B_{\zeta o}$ is the poloidal Alfvén time. These high β reduced equations contain both current and pressure driving forces.

In order to consider high β plasmas having circular or noncircular cross-section shape, a flux coordinate system based on the initial equilibrium is adopted. This system is the same as that defined by Grimm, Green, and Johnson [8]. Even though Eqs. (1)-(3) are lowest order in ε, geometric terms are retained such that the axisymmetric toroidal Grad-Shafranov equation

$$\Delta^*\Psi = -\frac{\beta_o}{2\varepsilon^2} R^2 \frac{dp}{d\Psi} - \frac{1}{\varepsilon^2} F \frac{dF}{d\Psi} \quad , \tag{4}$$

exact to all orders in ε, is an equilibrium solution. By considering flux-conserving sequences of equilibria for several plasma shapes and q-profiles, it is possible to study β effects, q-profile effects, and plasma shape effects independently. Since the present study focuses on the (m = 1;n = 1) mode, q-profiles are chosen such that this mode is the dominant instability in the low β cylindrical limit. The calculations are carried out using a finite difference representation in the generalized radial coordinate ρ, and a Fourier series expansion in the poloidal and toroidal angles θ and ζ, respectively. In this representation equilibrium effects such as toroidicity, $\varepsilon\beta_p$, and cross-section shape linearly couple components of different poloidal number m for each toroidal number n. This coupling has observable consequences, as will be shown later. Further details on the assumptions, equations, and numerical techniques used in RST are contained in Refs. 2 and 9.

LINEAR RESULTS

In order to understand the structure and stability properties of the fastest growing eigenfunction for each n, it is possible to run RST in a linearized fashion. For a particular flux-conserving sequence of equilibria the effect of increasing β upon the $n = 1$ linear eigenfunction can be understood as a transition from current-driven to pressure-driven dominance. As β_p is increased, the toroidal current distribution shifts relative to the flux coordinate system which tends to reduce the average current gradient at the $q = 1$ surface. The overall effect is to stabilize the current-driven part of the mode. When pressure forces are taken into account, three regimes emerge: a low β regime in which the mode is mainly current-driven and the effect of pressure is an additional stabilization, probably due to increased couplings between the $m = 1$ and more stable components; a high β regime in which the mode is mainly pressure-driven; and a transition region in which both current and pressure effects are apparent.

For several flux-conserving sequences of equilibria satisfying the constraint of $(m = 1; n = 1)$ dominance in the low β cylindrical limit, the above behavior is observed [Fig. 1a]. In the high β regime ($\beta_p \gtrsim 1.0$) the growth rates are rather insensitive to the q-profile. However, in the low β and transition regions, where current driving terms are important, linear growth rates are sensitive to q with larger (smaller) growth rates corresponding to q-profiles having more (less) shear. For another flux-conserving sequence in which an elliptical cross-section ($e = 1.5$) and circular cross-section are compared, the effect of elongation upon growth rate is minor with a slight uniform (as a function of $\varepsilon\beta_p$) stabilization observed [Fig. 1b].

NONLINEAR RESULTS

When full nonlinear simulations are carried out for a flux-conserving sequence of equilibria, increasing β_p causes a slowing down in time of the growth of the $(m = 1; n = 1)$ mode. For high enough β_p the 1/1 magnetic island saturates at finite width and remains in the plasma. Equilibrium effects induce strong couplings between the $(m = 1; n = 1)$ and other components such as the $(m = 2; n = 1)$ giving rise to a strong poloidal field at the plasma edge in the driven

components. Associating the growth of the 1/1 magnetic island with the observed m = 1 x-ray signal in the ISX-B plasma, and the poloidal magnetic fields at the plasma edge with the observed Mirnov loop signals, the experimental behavior as a function of beam power is the same. Detailed discussions and comparison of calculated and experimental results are given in Refs. [2] and [3].

In ISX-B it has been observed that increasing q_a for fixed β_p leads to a return to "classic" sawtooth behavior: a decrease in the duration of precursor activity, and a decoupling and reduction of the m = 2 magnetic signal. This behavior is also observed in the calculations [Fig. 2a] and is due to the increase in shear as q_a is raised.

The effects of plasma cross-section shaping upon the (m = 1;n = 1) evolution are presently being explored. Plasma elongation does not greatly modify the evolution [Fig. 3], but triangularity causes the 1/1 magnetic island to saturate at a finite width for values of $\varepsilon\beta_p$ at which the circular and elliptical cases undergo full reconnection [Fig. 3].

The interpretation of ISX-B experimental data requires a reliable parameterization of the equilibrium. One equilibrium parameter which is not well known is q_o, but the shear and consequently the type of MHD activity observed are quite sensitive to this parameter [Fig. 2b]. The RST code can be used to help determine q_o by making runs with several test equilibria differing only in q_o and then comparing the calculated MHD activity for each case to that observed experimentally.

COMPARISON WITH EXPERIMENT

Detailed comparison with experimental x-ray and magnetic fluctuation data is carried out through the use of several diagnostic computer codes which analyze RST results [9]. Equilibria which match the actual experimental parameters are used in the RST calculations. Theoretical x-ray data is calculated by assuming that the emissivity is proportional to a power of the pressure p^α where $\alpha = 2$ is normally taken. Then, assuming either toroidal or poloidal rotation, an x-ray signal is calculated by evaluating line integrals across the emissivity profile along the actual x-ray chords. These signals are then compared

with the experimental data [Fig. 4]. With toroidal rotation the agreement between theory and experiment is remarkably good, showing chord by chord agreement on the structure, including interference effects, and relative amplitudes of the signals. With poloidal rotation the comparison is good inside the q = 1 surface, but outside q = 1 where the (m = 1;n = 1) component is small, the results do not agree. This is consistent with the fact that ISX-B has a large toroidal rotation velocity due to the coinjection angle of the neutral beams.

A detailed comparison of magnetic fluctuations with those in ISX-B has not been attempted since RST does not include the actual vessel geometry or loop positions. Theoretical poloidal magnetic field fluctuations are calculated by evaluating $\tilde{B}_\Theta/B_\Theta\big|_{\rho=1}$ and assuming either toroidal or poloidal rotation of the field. Even so, the calculated and experimental fluctuation amplitudes agree well both in magnitude (~1% peak) and in angular dependence, being large toward the outside major radius of the torus and small toward the inside major radius [Fig. 5]. In the region of large amplitude toward the toroidal outside, several different equilibria of various β, q-profile, and shape all show magnetic fluctuation phase behavior in poloidal angle which looks like pure m = 2 [Fig. 5]. The presence of other prominent components, such as (m = 3;n = 1) and (m = 4;n = 1), is revealed by rapid phase changes toward the inside of the torus, where the fluctuation signal is small. This situation accentuates the presence of the (m = 2;n = 1) mode and makes the experimental observation of other modes difficult.

ACKNOWLEDGMENT

It is a pleasure to thank the members of the ISX-B experimental team, especially Julian Dunlap, for their hearty collaboration in this work and for permission to reproduce the data shown in Fig. 4.

REFERENCES

1. J. A. Holmes, B. A. Carreras, H. R. Hicks, K. E. Rothe, "Finite Beta Effects on the Nonlinear Evolution of the (m = 1;n = 1) Tearing Mode in Tokamaks," Sherwood Theory Meeting (Austin, TX, 1981).

2. J. A. Holmes, B. A. Carreras, H. R. Hicks, V. E. Lynch, K. E. Rothe, submitted to Physics of Fluids.

3. J. L. Dunlap, B. A. Carreras, V. K. Pare, J. A. Holmes, S. C. Bates, J. D. Bell, H. R. Hicks, V. E. Lynch, A. P. Navarro, submitted to Phys. Rev. Lett.

4. L. A. Charlton, R. A. Dory, J. A. Holmes, G. H. Neilson, J. L. Dunlap, E. A. Lazarus, R. M. Wieland, D. K. Lee, Bull. APS 26 (1981) 879.

5. B. A. Carreras, Bull. APS 26 (1981) 917.

6. J. A. Holmes, B. A. Carreras, H. R. Hicks, V. E. Lynch, K. E. Rothe, Bull. APS 26 (1981) 961.

7. H. R. Strauss, Phys. Fluids 20 (1977) 1354.

8. R. C. Grimm, J. M. Green, J. L. Johnson, in Methods of Computational Physics, Vol. 16, Academic Press, New York (1976) 253.

9. V. E. Lynch, B. A. Carreras, H. R. Hicks, J. A. Holmes, L. Garcia, to appear in Computer Physics Communications.

FIGURE CAPTIONS

Fig. 1a. $n = 1$ linear growth rate ($\sim \tau_{Hp}^{-1}$) vs $\varepsilon\beta_p$ for three flux-conserving sequences of equilibria. The solid curve is for $q_o = 0.9$, $q_a = 2.3$; the long dashed curve is for $q_o = 0.9$, $q_a = 3.3$; and the short dashed curve is for $q_o = 0.8$, $q_a = 2.3$.

Fig. 1b. $n = 1$ linear growth rate ($\sim \tau_{Hp}^{-1}$) vs $\varepsilon\beta_p$ for elliptical ($e = 1.5$) and circular flux-conserving sequences of equilibria. Both sequences have the same q-profile given by $q_o = 0.9$, $q_a = 3.6$.

Fig. 2a. $m = 1/n = 1$ magnetic island width vs time for $\beta_p = 0.38$ ($q_o = 0.9$, $q_a = 2.3$) and $\beta_p = 0.34$ ($q_o = 0.9$, $q_a = 3.3$) equilibria.

Fig. 2b. $m = 1/n = 1$ magnetic island width vs time for $\beta_p = 0.59$ ($q_o = 0.9$, $q_a = 2.3$) and $\beta_p = 0.57$ ($q_o = 0.8$, $q_a = 2.3$) equilibria.

Fig. 3. $m = 1/n = 1$ magnetic island width for circular ($\varepsilon\beta_p = 0.17$), elliptical ($\varepsilon\beta_p = 0.20$, $e = 1.5$), and D-shaped ($\varepsilon\beta_p = 0.16$, $\delta = 0.5$) plasmas. All cases have identical q-profile parameters $q_o = 0.9$, $q_a = 3.6$.

Fig. 4. Experimental (left-hand side) ISX-B and theoretical (right-hand side) x-ray signals. The equilibrium simulates the actual experimental shot: $q_a = 4.15$, $\beta_p = 1.05$, $\langle\beta\rangle = 1\%$, $e = 1.3$, $\delta = 0.12$.

Fig. 5. Phase and amplitude of calculated poloidal magnetic fluctuation signal at plasma edge as a function of poloidal angle Θ for circular plasmas having $q_o = 0.9$, $q_a = 2.3$ and $q_o = 0.9$, $q_a = 3.6$ and D-shaped plasma having $q_o = 0.9$, $q_a = 3.6$.

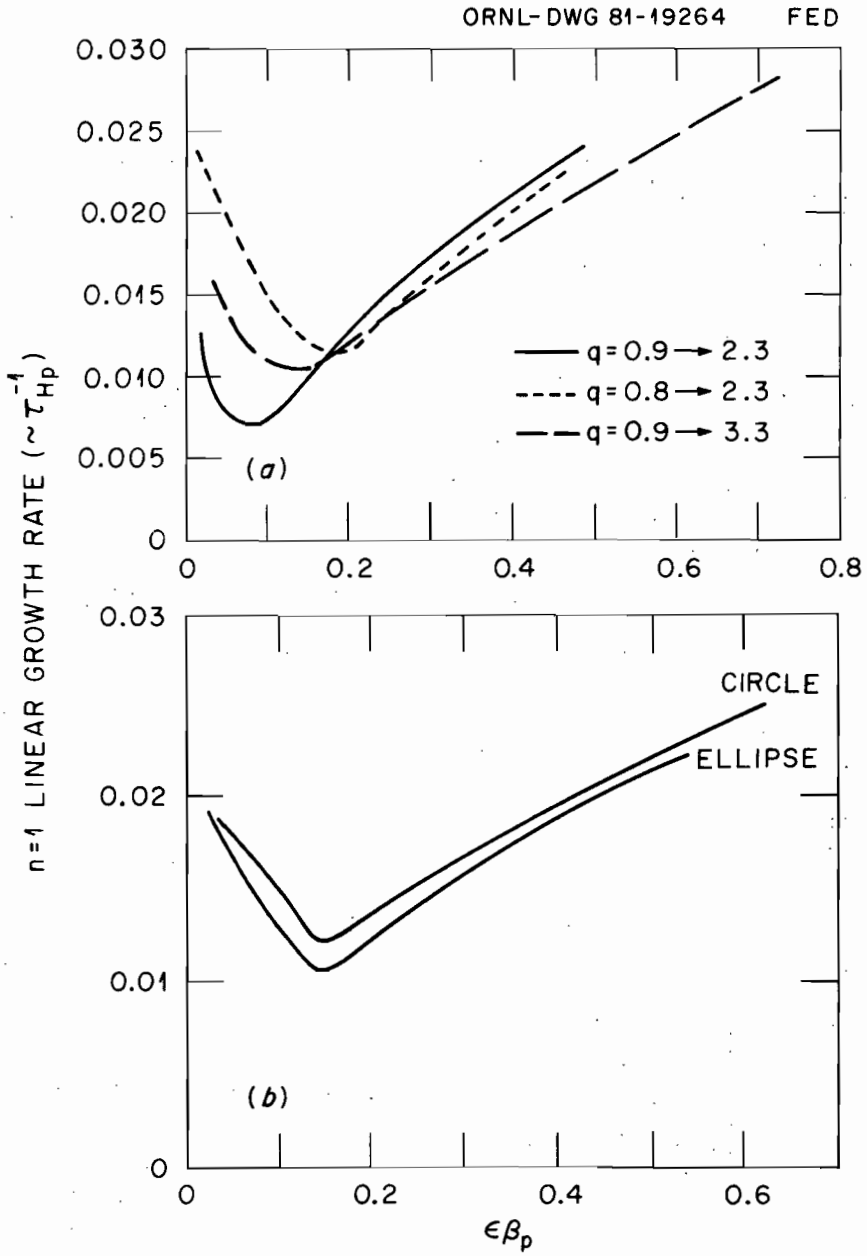
ORNL-DWG 81-19264 FED
n=1 LINEAR GROWTH RATE ($\sim \tau_{Hp}^{-1}$)
0.030
0.025
0.020
0.015
0.010
0.005
0
0
0.2
0.4
0.6
0.8
q=0.9 → 2.3
q=0.8 → 2.3
q=0.9 → 3.3
(a)
0.03
0.02
0.01
0
0
0.2
0.4
0.6
CIRCLE
ELLIPSE
(b)
$\epsilon\beta_p$

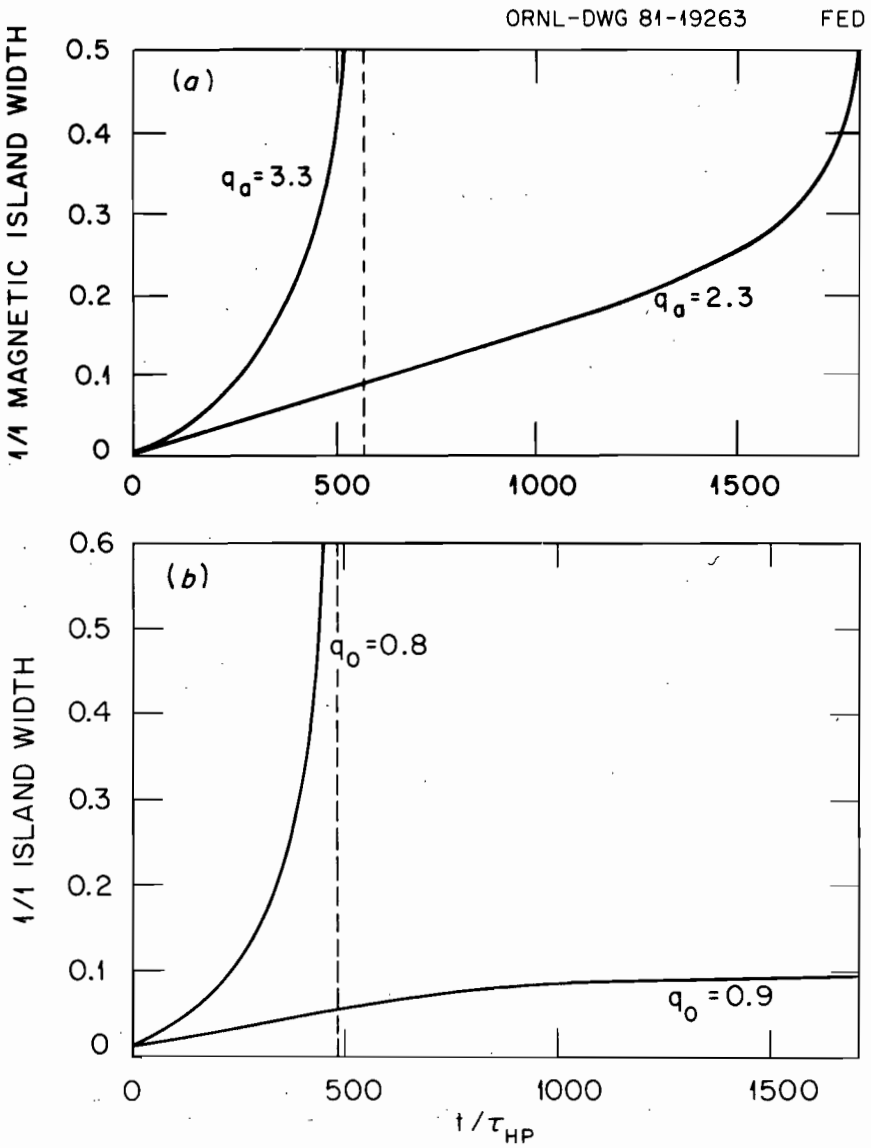
ORNL-DWG 81-19263 FED
1/1 MAGNETIC ISLAND WIDTH
(a)
q_a=3.3
q_a=2.3
0.5
0.4
0.3
0.2
0.1
0
0
500
1000
1500
1/1 ISLAND WIDTH
(b)
q_0=0.8
q_0=0.9
0.6
0.5
0.4
0.3
0.2
0.1
0
0
500
1000
1500
t/τ_{HP}

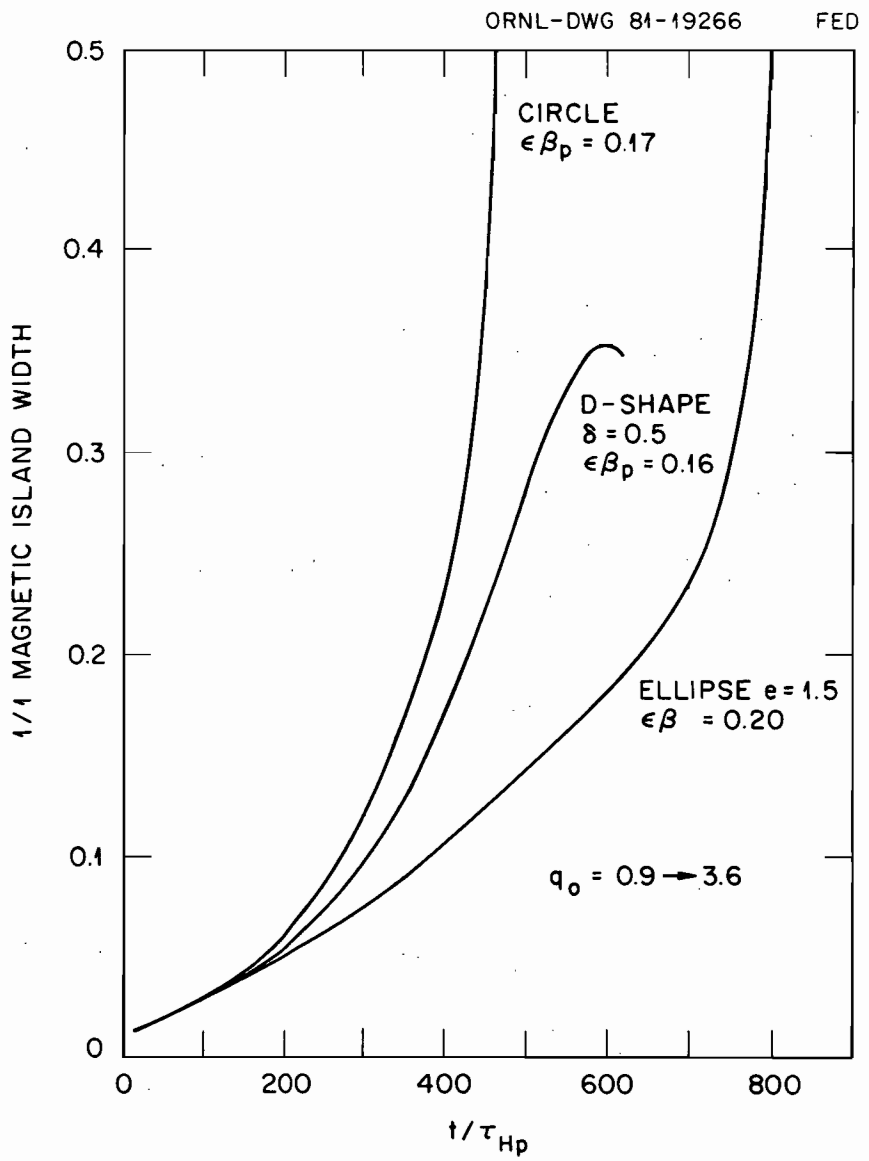
ORNL-DWG 81-19266 FED
CIRCLE
$\epsilon\beta_p = 0.17$
D-SHAPE
$\delta = 0.5$
$\epsilon\beta_p = 0.16$
ELLIPSE e = 1.5
$\epsilon\beta = 0.20$
$q_o = 0.9 \rightarrow 3.6$
1/1 MAGNETIC ISLAND WIDTH
0.5
0.4
0.3
0.2
0.1
0
0
200
400
600
800
t/τ_{Hp}

ORNL-DWG81-19351 FED

ISX-B SHOT 34572 t = 223-224 ms

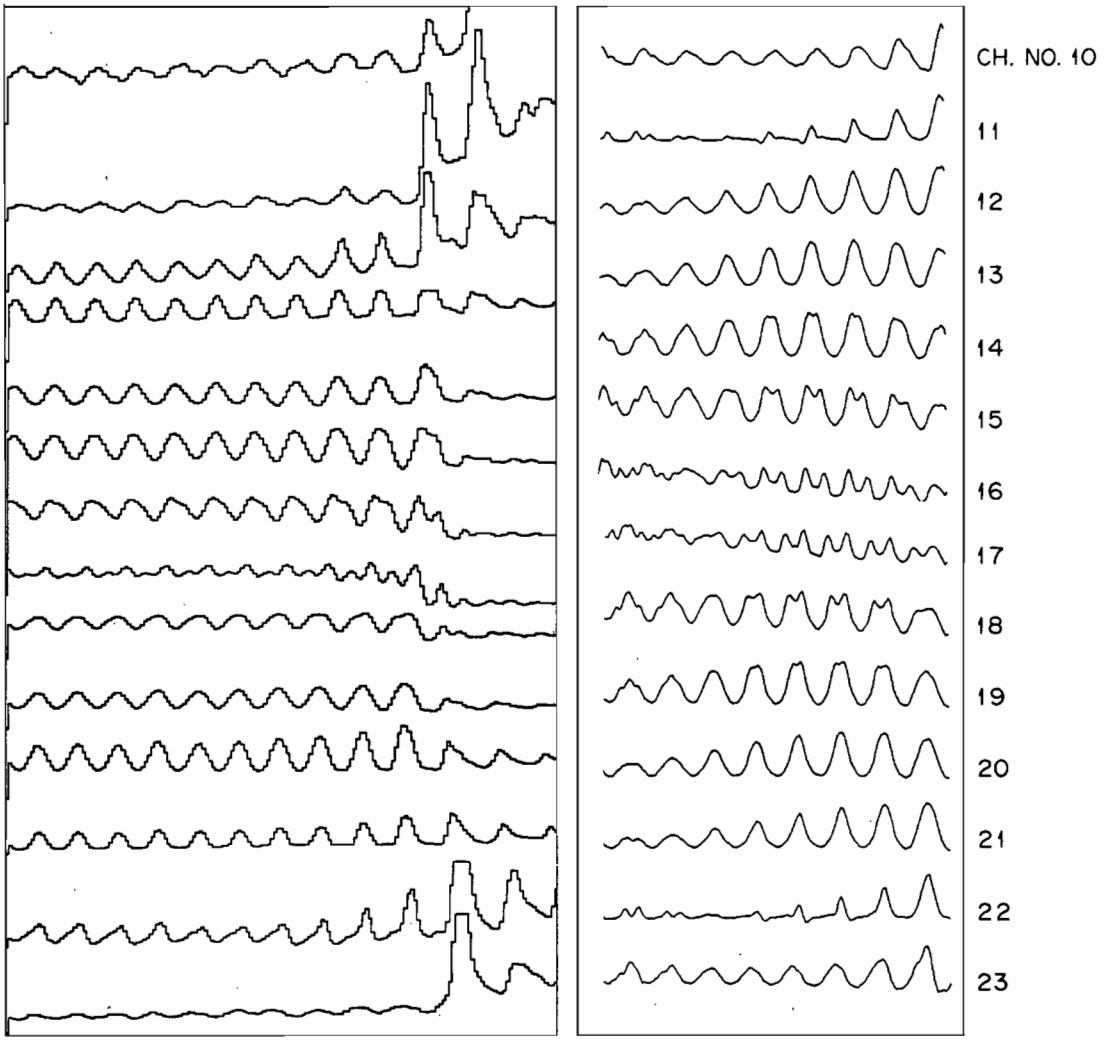

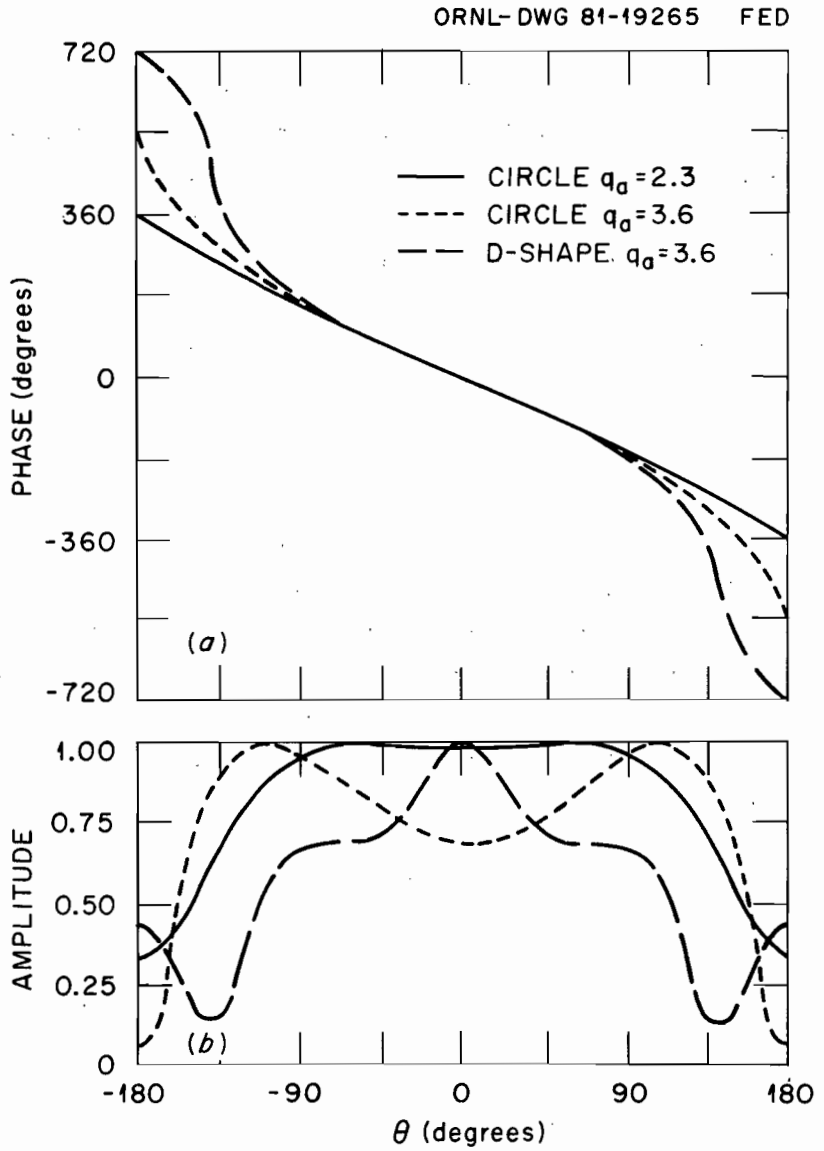
ORNL-DWG 81-19265 FED
720
360
0
-360
-720
PHASE (degrees)
CIRCLE q_a=2.3
CIRCLE q_a=3.6
D-SHAPE q_a=3.6
(a)
1.00
0.75
0.50
0.25
0
AMPLITUDE
(b)
-180
-90
0
90
180
θ (degrees)

PROPERTIES OF THE IDEAL-MHD m=1 MODE IN TOKAMAKS

J. J. Ramos and G. B. Crew
Massachusetts Institute of Technology. Cambridge MA 02139. USA.

Large aspect ratio asymptotic expansions about circular cylinder solutions [1] are used to investigate the ideal-MHD structure of m=1 modes in current carrying axisymmetric toroidal plasmas. The linear eigenfunctions are assumed to be dominated by an m=1 poloidal harmonic, which couples to small amplitude m=0 and m=2 sidebands through the poloidal modulation of the equilibrium functions. The radially dependent Fourier coefficients exhibit discontinuities at the resonant surface r_1, where $n\, q(r_1) = 1$. The behaviour of the m=1 coefficient of the radial plasma displacement, ξ_1, can be described in terms of the parameter

$$\lambda_H \equiv \lim_{r \to r_1} -\pi \frac{(r-r_1)^2}{r_1} \frac{d\,\xi_1}{d\,r} .$$

It is shown that λ_H has the same value at both sides of the mode resonant surface, thus making it possible a symmetric matching through the singular layer where non-ideal effects should be included. By an appropriate choice of gauge, a perturbed magnetic potential can be defined in such a way that its parallel component is related to the radial component of the perturbed magnetic field through

$$\tilde{B}_r = -\frac{1}{r\,R} \frac{\partial(R\,\tilde{A}_{||})}{\partial\theta} .$$

The discontinuity of the m=1 Fourier coefficient of $\tilde{A}_{||}$ is then shown to be

$$\Delta' \equiv \left.\frac{d\,\ln \tilde{A}_{||1}}{d\,\ln r}\right|_{r_1-0}^{r_1+0} = -\frac{\pi}{\lambda_H} .$$

These relationships provide a straightforward generalization of the results in cylindrical geometry.

The parameter λ_H is evaluated analytically in the limit $r_1 \to 0$. Numerically obtained values of λ_H are also presented for several choices of pressure and rotational transform profiles.

---

[1] M. N. Bussac, R. Pellat, D. Edery and J. L. Soule, Phys. Rev. Lett. 35, 1638 (1975).

3-D Simulation of Spheromak Formation

Tetsuya Sato

Institute for Fusion Theory
Hiroshima University, Hiroshima 730, Japan

Three-dimensional magnetohydrodynamic (MHD) code "MAGIC 3" is developed based on the two-step Lax-Wendroff scheme. In the first part, simulation results of the Princeton spheromac formation and the merging of two spheromaks obtained by using the two-dimensional MHD simulation code[1] are briefly reviewed. Then, the result of a preliminary run done by MAGIC 3 is presented.

Two-Dimensional Spheromak Formation

It is already shown by simulations[2,3] that the Princeton formation scheme can soundly produce spheromaks. In this paper, a new aspect of spheromak formation is emphasized. The previous simulation[2] assumed that the shape of the spheromak plasma would be independent of the formation speed. The present simulation, however, has shown that the shape of the spheromak is largely dependent upon the formation speed. Figs.1~3 show the spheromak shapes for three different formation speeds, namely, τ_f/τ_A=68.6, 21.7 and 4.35. As can be clearly seen, the size of the spheromak becomes smaller and smaller as the formation speed increases.

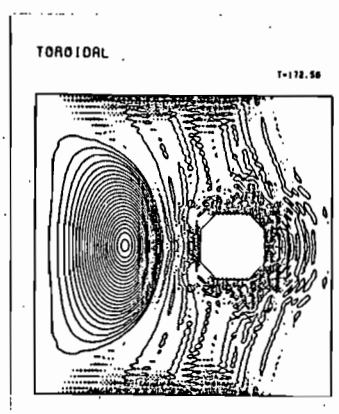

Fig.1

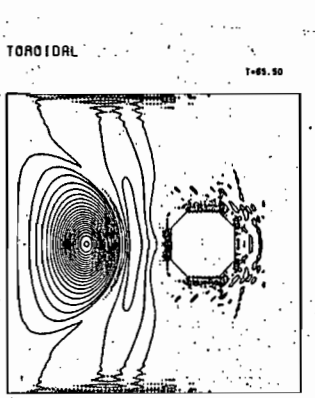

Fig.2

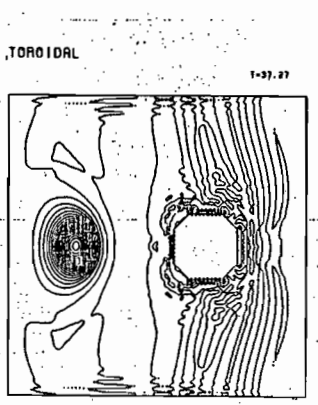

Fig.3

Merging of Two Spheromaks

By using the same code the merging process of two spheromaks is performed. Two spheromaks are generated from two identical flux cores placed with a certain distance by the Princeton method and let them approach to each other to merge into one.

Fig.4 shows an example of such runs. It is seen that two almost identical spheromaks are spontaneously merged. The following flux relation is obtained:

$$\Phi_p \approx \Phi_{p1} \approx \Phi_{p2}$$

$$\Phi_T \approx \Phi_{T1} + \Phi_{T2}$$

where Φ_p and Φ_T are the poloidal and toroidal fluxes, respectively, after merging and the subscripts "1" and "2" correspond to those before merging.

Three-Dimensional Simulation

Three-dimensional MHD simulation code based on the Lax-Wendroff method is developed. As the first application of this code, the formation of the Princeton Spheromak is simulated.

A preliminary run with 31×31×10 (r,z,θ) grid points has shown that the spheromak tends to shift vertically, shifting instability, as shown in Fig.5a,6. These figures correspond to the toroidal field intensity contours (left) and the vertical (z) flow (right) at two cross sections with 90 degrees difference in the azimuthal direction. Fig. 6 shows another example where the formation speed is lower than the other case. Note that in this case shifting instability is weak.

1. T.Sato and T.Hayashi, Phys. Fluids 22, 1189, 1979: T.Sato, JGR 84, 7177, 1979.
2. S.C.Jardin and W.Park, Phys. Fluids 24, 679, 1981.
3. H.C.Lui, C.K.Chu, and A.Aydemir, Phys. Fluids 24, 673, 1981.

Initial Poloidal Field

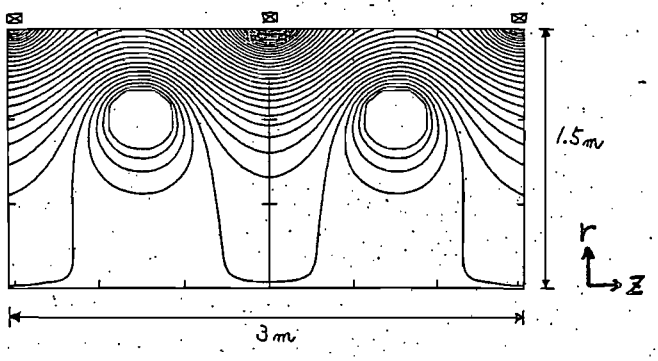

Toroidal

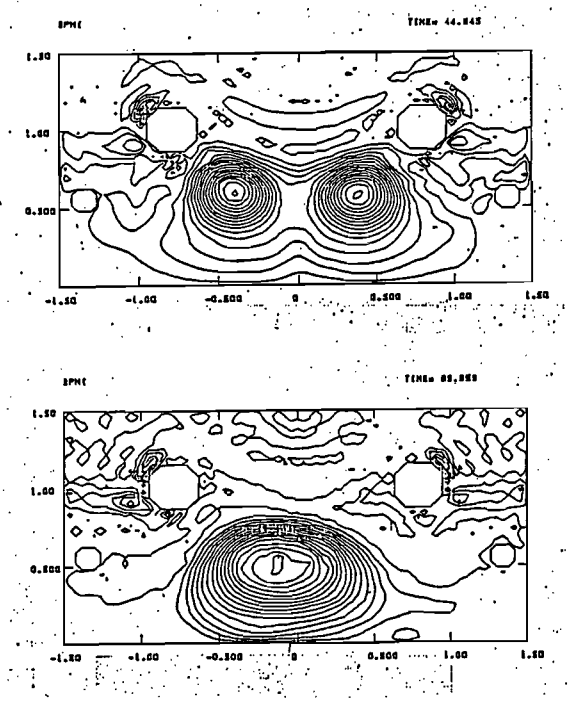

Fig.4

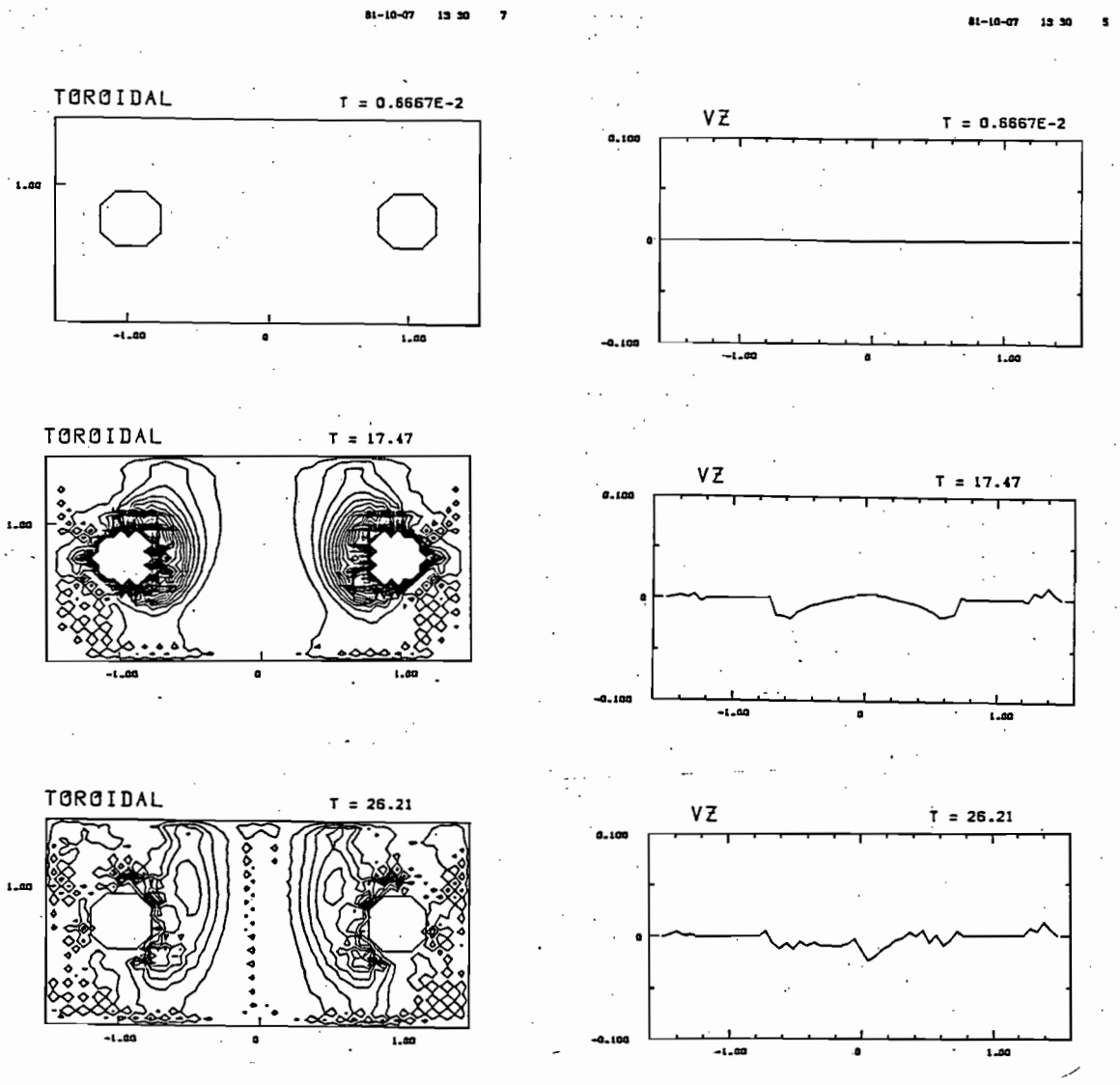

Fig.5a 3-D simulation of spheromak formation ($\theta^{\zeta}=0$).

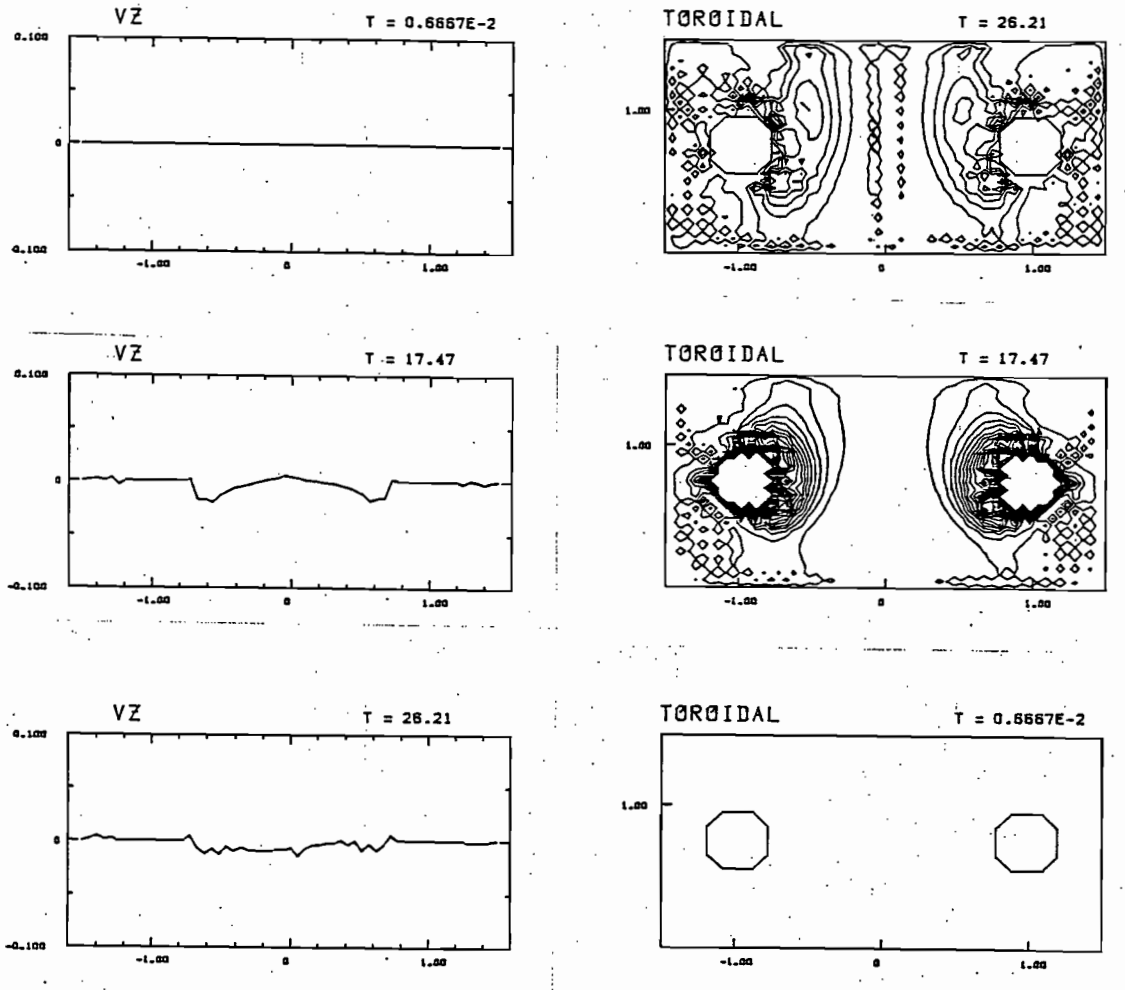

Fig.5b 3-D simulation of spheromak formation(θ=90).

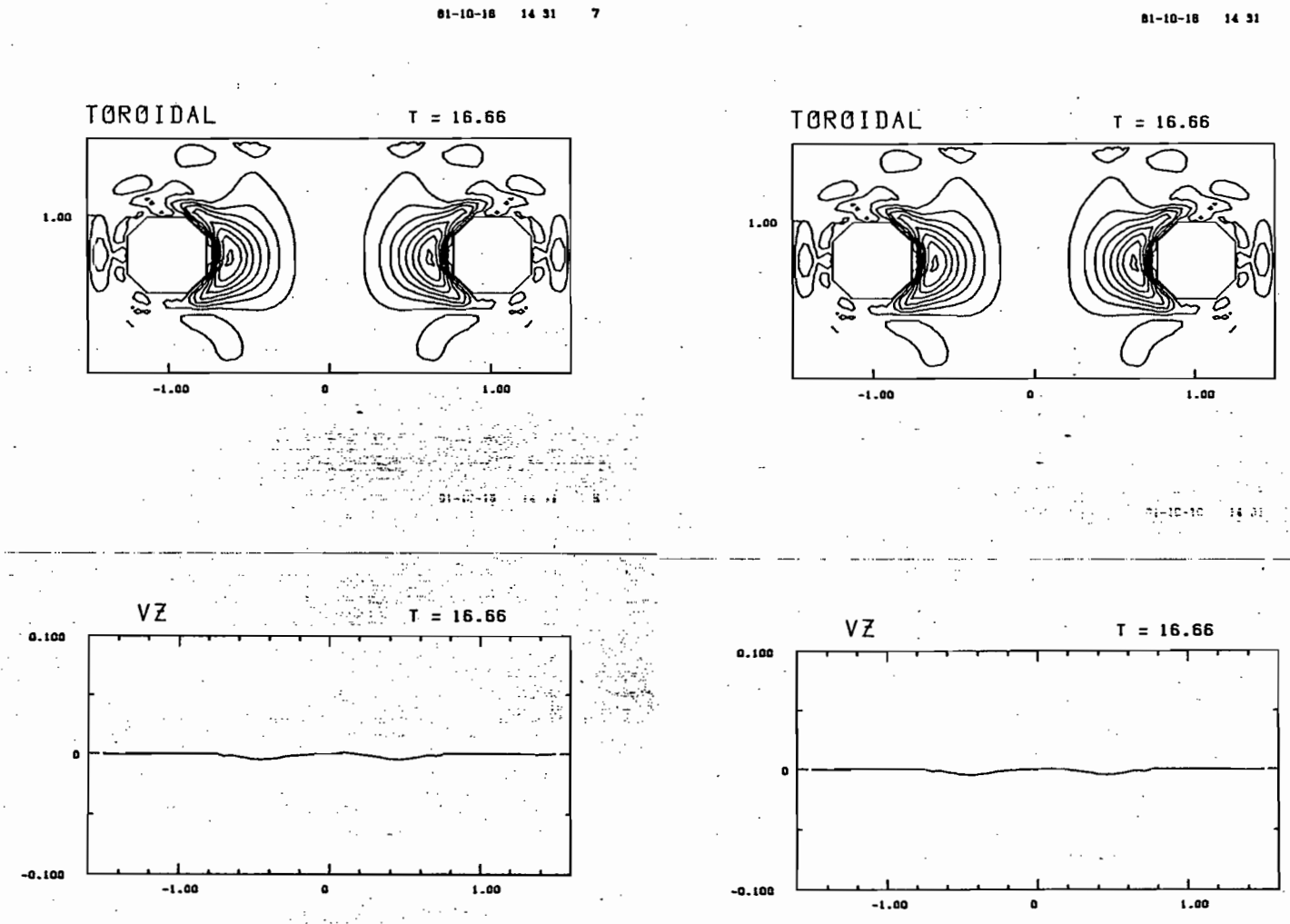
81-10-18 14 31 7
TØRØIDAL
T = 16.66
1.00
-1.00
0
1.00
81-10-18 14 31 15
TØRØIDAL
T = 16.66
1.00
-1.00
0
1.00
VZ
T = 16.66
0.100
0
-0.100
-1.00
0
1.00
VZ
T = 16.66
0.100
0
-0.100
-1.00
0
1.00

Fig. 6

MULTIDIMENSIONAL MHD COMPUTATIONS FOR THE FIELD-REVERSED THETA PINCH AND THE REVERSED-FIELD PINCH

D. D. Schnack
Los Alamos National Laboratory
Los Alamos, New Mexico 87545

I. INTRODUCTION

The study of alternative approaches to the tokamak for the design of a magnetic fusion reactor is an area of active research in both the United States and Japan. Among the most promising of these concepts are the Field-Reversed Theta Pinch (FRTP) and the Reversed-Field Pinch (RFP). This paper briefly describes some recent large-scale numerical MHD simulations of these devices.

The FRTP is one of a class of Field-Reversed Configurations (FRCs) that are characterized by the presence of a separatrix that extends to the major axis. Unlike the spheromak, the FRTP is highly prolate (elongations of 4 to 1 or more are typical) and contains no toroidal field. A field null thus exists. Additionally, both the safety factor and the shear vanish everywhere. The validity of the MHD model in such devices may thus be questioned. However, such calculations are known to give a pessimistic view of stability, and certainly become more valid for larger devices where kinetic effects may become less important. Examples of these calculations and their relevance to particular experiments are given in Sec. II.

Like the tokamak, the RFP is a toroidal pinch that contains both poloidal and toroidal fields. The tokamak attains stability against large-scale ideal MHD modes by satisfying the Kruskal-Shafranov condition. This requires the imposition of a strong toroidal magnetic field such that $B_p/B_T \sim \varepsilon << 1$, where ε is the inverse aspect ratio. The resulting safety factor profile $q(r)$ is greater than unity and monotone increasing. The RFP, on the other hand, is characterized by fields such that $B_p/B_T \sim 1$, and a profile $q(r) << 1$, which is monotone decreasing and changes sign in the outer regions of the plasma. The resulting shear grossly stabilizes the pinch. Thus, high values of β may be attainable. Also, since the toroidal current is not

limited by the Kruskal-Shafranov condition, significant ohmic heating may occur.

It is now accepted that much of the characteristic behavior of tokamak plasmas can be described in terms of the 3-D nonlinear evolution of resistive MHD instabilities. However, as yet the fundamental MHD processes that occur in the RFP remain unknown. Such processes are probably responsible for attainment and maintenance of field reversal. In particular, simple estimates of the resistive diffusion time in the ZT-40M device at Los Alamos indicate loss of field reversal in a time short compared to the observed lifetime. This dynamo effect may result from the turbulent generation of mean magnetic field, or from large scale modes. Accurate simulations of these 3-D nonlinear processes are vital to understanding the basic physics of the RFP.

The advances in 3-D calculations for tokamaks depend crucially on expanding the primitive MHD equations

$$\frac{\partial \underset{\sim}{B}}{\partial t} = \nabla\times(\underset{\sim}{v}\times\underset{\sim}{B} - \frac{\eta}{S}\nabla\times\underset{\sim}{B}) \tag{1a}$$

$$\frac{\partial(\rho\underset{\sim}{v})}{\partial t} = -\nabla\cdot\left[\rho\underset{\sim}{v}\underset{\sim}{v} - \underset{\sim}{B}\underset{\sim}{B} + \frac{1}{2}(p+B^2)\underset{\sim}{I}\right] \tag{1b}$$

$$\frac{\partial\rho}{\partial t} = -\nabla\cdot(\rho\underset{\sim}{v}) \tag{1c}$$

$$\frac{\partial}{\partial t}\left(\frac{p}{\gamma-1}\right) = -p\nabla\cdot\underset{\sim}{v} - \nabla\cdot\left(\frac{p\underset{\sim}{v}}{\gamma-1}\right) + \frac{2\eta}{S}(\nabla\times\underset{\sim}{B})^2 \tag{1d}$$

in the small parameter $\varepsilon = B_p/B_T$, discussed earlier, to obtain the reduced set of equations

$$\frac{\partial A}{\partial t} + \underset{\sim}{v}\cdot\nabla_\perp A - \frac{\eta}{S}\nabla_\perp^2 A = B_0 \frac{\partial v}{\partial z} \tag{2a}$$

$$\frac{\partial \omega}{\partial t} + \underset{\sim}{v}\cdot\nabla_\perp \omega - \underset{\sim}{B}\cdot\nabla_\perp j = B_0 \frac{\partial j}{\partial z} \tag{2b}$$

where $\underset{\sim}{B} = \nabla_\perp \times \hat{e}_z A$, $\underset{\sim}{v} = \nabla_\perp \times \hat{e}_z v$, $\nabla_\perp^2 v = -\omega$, and $\nabla_\perp^2 A = -j$. However, since the field components in the RFP are all of the same order, and since these devices may possess finite β, no universally small expansion parameter exists for this device. Thus, instead of solving the two scalar equations (2) as is the case for the tokamak, computations for the RFP require the solution of the eight primitive equations (1).

Additionally, the computational speed of codes based on the tokamak reduced equations (2) is greatly enhanced by the fact that in this ordering, the plasma is incompressible. This eliminates the fast compressional wave from the calculation. This wave evolves on a time scale that is on the order of the minor radius divided by the Alfvén velocity. The remaining time scale is defined by the shear Alfvén wave that, because of the strong toroidal field, evolves on a time scale that is on the order of the major radius divided by the Alfvén velocity. This time scale may be more than an order of magnitude longer than that of the compressional Alfvén wave. In the RFP, on the other hand, even the (unjustified) assumption of incompressibility does not eliminate the fast time scale, since now a shear Alfvén wave traveling near the field reversal surface evolves on a time scale that is on the order of the minor radius divided by the Alfvén velocity, i.e., the same order as that of the compressional wave.

To summarize the above remarks, calculations for the tokamak require the advancement of two equations that evolve on a slow time scale, while those for the RFP require the advancement of eight equations that evolve on a fast time scale. Because such calculations are difficult and time consuming, most simulations of the RFP have been in two dimensions or have assumed helical symmetry. A recent example of such a calculation is discussed in Sec. III. There we also speculate on a possible dynamo mechanism involving the

interaction of a few large scale resistive modes, and briefly describe a 3-D code that is presently under development.

II. FIELD-REVERSED THETA PINCH

The MHD stability of compact toroids was first investigated analytically by Rosenbluth and Bussac[1] who used a modified energy principle to determine marginal stability to all ideal modes and most tearing modes. They found stability against magnetically driven modes for all toroidal mode numbers $n > 1$, but found an unstable $n = 1$ mode for prolate spheroidal plasmas. This mode, which is characterized by a rotation of the major axis inside the separatrix, is termed the tilting mode. Highly elongated configurations characteristic of FRTP plasmas were investigated by Barnes[2] who found instabilities for all n if the flux surfaces where elliptical. In this case the unstable $n = 1$ displacements are more axial than rotational.

Computationally, these predictions have been investigated in a numerically generated equilibrium that includes plasma on open field lines and closely resembles the FRX-B experiment at Los Alamos.[3,4] These studies have employed the linearized code RIPPLE VI[5] and the nonlinear ideal 3-D code MALICE.[6] Both solve the primitive MHD equations and are initialized with perturbations characterized by $n = 1$ and $k = 1$ for the toroidal and axial mode numbers. They both develop unstable tilting instabilities and the growth rates are in good agreement when the codes use comparable grids.

Using the MALICE code in the pure Lagrangian mode, the instability has been followed into the nonlinear regime. When the tilt has proceeded about 20° a damping of growth and a corresponding increase in internal energy produced by compressive heating effects are observed. At this point the shortened grid spacings of the Lagrangian mesh produces unacceptably small time steps. Attempts to remedy this by increasing the amount of rezoning have lead to numerical diffusion of the magnetic field, which causes much of the reversed-field region to be lost.

The results of the nonlinear simulation are shown in Fig. 1 where contours of constant plasma density, both initially and at the end of the run, are shown. Note that the displacement is primarily axial, in agreement with the theory of Barnes.[2]

The growth rate $\omega t_H \approx 0.5$ as determined numerically corresponds to an e-folding time of ~2 μs. However, experimental results indicate that such configurations can persist in a stable state for times approaching 30 μs, the discharge being lost due to a rotational n = 2 interchange instability. Recently Schwarzmeier,[7] using the Vlasov-fluid kinetic model, has shown that parallel kinetic effects can stabilize the tilting mode. Additionally, he has shown that shaping the flux surfaces in a racetrack manner can significantly reduce the MHD growth rate. Both effects are probably important experimentally, perhaps accounting for the lack of observation of the tilting mode in FRTP devices.

The n = 2 rotational instability has also been simulated with the MALICE code. The results are detailed elsewhere.[8]

III. REVERSED-FIELD PINCH

For the reasons cited in Sec. I, studies of global MHD activity in the RFP are in approximately the same state as similar studies for tokamak plasmas about five years ago. Much of the activity currently underway is limited to the case of helical symmetry. The thrust of these studies is as follows.

1. Classify Possible Modes. Indications are that the RFP does not simply behave as a modified tokamak, but rather exhibits MHD behavior uniquely its own.

2. Can MHD Activity be Induced by Transport and How Does MHD Activity Affect Transport? Studies with transport codes have shown that initially stable profiles will naturally evolve to unstable states. The major question is: how does the nonlinear evolution of these destabilized modes modify the profiles, and can these effects be modeled in transport calculations?

3. Is Self-healing of Profiles Possible? In tokamaks, sawtooth oscillations result when a profile that is destabilized by transport is stabilized by nonlinear MHD activity. There is evidence that analogous activity can occur in the RFP.

4. Can Dynamo Action Result From Large Scale Modes? The usual theories relate dynamo action to small scale turbulence. In either case, fully 3-D simulations are necessary.

An example[9] that addresses part or all of the above questions will now be given.

A stabilized tokamak profile typically has $q > 1$ on axis. Transport processes peak the current on the axis thus lowering q and eventually introduce the $q = 1$ resonance into the plasma. The nonlinear evolution of the resulting $m = 1/n = 1$ mode (which does not enter the Rutherford regime and saturate at a low level) flattens the current outward, raises q on axis, and removes the $q = 1$ resonance. This self-healed profile then evolves again due to transport process leading the familiar sawtooth oscillation.

In the RFP, on the other hand, since $q \ll 1$ many $m = 1/n \gg 1$ resonances exist even in the stable state (they are shear stabilized, for example). Transport processes again peak the current on the axis causing a decrease in q there and a loss of shear stabilization. This process has been observed in 1-D transport studies, and the nonlinear evolution of the resulting $m = 1/n = 10$ tearing mode has been followed with a 2-D helical resistive MHD code that solves the primitive equations.[10] It is found that the mode undergoes two successive reconnections resulting in a stabilized profile. Like the tokamak, the first reconnection removes the $q = 1/10$ rational surface from the plasma. However, since in this case q is monotone decreasing, this must decrease q on axis. Thus, instead of flattening the current, the first reconnection enhances the overpeaking. The plasma then undergoes a second reconnection that flattens the current, increases q_{axis}, and restores the original resonance to an axisymmetric profile that is stable to the original mode.

The sequence of double reconnection is shown in Fig. 2, where we plot the helical flux surfaces and flow patterns at various times during the evolution of the mode. Time is measured in units of Alfvén transit times. The first reconnection is completed by t = 37, and the second reconnection results in an axisymetric state. This convoluted, unlocalized, nonsymmetric tearing has been independently verified by another code.[11]

One can now envision the self-healed profile again evolving due to transport, resulting in relaxation oscillations reminiscent of the tokamak sawtooth behavior. Indeed, bursts of m = 1 activity lasting for tens of microseconds separated by periods on the order of 100 microseconds have been observed in the density signals from ZT-40M. These time scales are consistent with the time scales of the MHD and transport calculations described above.[9]

In light of these results, one can now speculate as to a possible mechanism for the maintenance of field reversal due to large scale modes.[9] It is likely that more than one $m = 1/n \gg 1$ mode will be unstable simultaneously due to the close proximity of the rational surfaces in the RFP. (In the tokamak, the only m = 1 mode allowed corresponds to n = 1 since $q \gtrsim 1$ everywhere.) It is also likely that these m = 1 modes will be preferred over other poloidal mode numbers because they do not enter the Rutherford regime. These modes will interact nonlinearly. For example, the m = 1/n = 10 and m = 1/n = 11 modes will interact as follows:

0th interaction	1/11	1/10			
1st interaction	0/1	2/21			
2nd interaction	1/12	1/10	1/11	1/9	from 0/1
	3/32	1/10	3/31	1/11	from 2/21

It is likely that the 2/21 mode will be stabilized by FLR effects due to its large toroidal mode number. Thus, the only avenue to the nonlinear generation of m = 1 modes (they are "preferred") is by the presence of an active m = 0/n = 1 mode that requires a reversal of the toroidal field for

resonance. We hypothesize that the q = 0 rational surface may be necessary for the "preferred" spectrum and may be created and maintained by the nonlinear interaction of m = 1 modes.

It is interesting to note that the observed m = 1 density oscillations mentioned previously are accompanied by m = 0 oscillations, and that m = 0/n = 1 flux loop signals are characteristic of the latter stages of the ZT-40M discharge.

To either refute or verify the above hypothesis requires an accurate 3-D resistive MHD code in realistic geometry. Such a code must solve the primitive equations, and must include the effects of compressibility since density fluctuations are observed to be large experimentally. To handle a large number of modes accurately and efficiently, spectral or pseudospectral techniques should be employed. This is crucial since one cannot rule out the importance of small scale turbulence. With the advent of vector computers, and for ease of debugging, such a code should be explicit. Additionally, unconditionally stable explicit pseudospectral numerical algorithms can be constructed.[12] Such a code is currently being written at Los Alamos.

IV. ACKNOWLEDGEMENT

Section III is written in conjunction with E. J. Caramana and R. A. Nebel.

REFERENCES

1. M. N. Rosenbluth and M. N. Bussac, Nucl. Fusion 19, 489 (1979).

2. D. C. Barnes, C. E. Seyler, and D. V. Anderson, in Proc. of the US-Japan Joint Symposium on Compact Toruses and Energetic Particle Injection, Princeton Univ., p. 110 (1979).

3. A. I. Shestakov, D. D. Schnack, and J. Killeen, in Proc. of the US-Japan Joint Symposium on Compact Toruses and Energetic Particle Injection, Princeton Univ., p. 126 (1979).

4. D. C. Barnes, A. Y. Aydemir, D. V. Anderson, A. I. Shestakov, and D. D. Schnack, in Proc. of the Third Symposium on the Physics and Technology of Compact Toroids in the Magnetic Fusion Energy Program, LA-8700-C, Los Alamos, p. 134 (1980).

5. A. I. Shestakov, J. Killeen, and D. D. Schnack, UCRL-86493, submitted to J. Comp. Phys. (1981).

6. J. U. Brackbill, in Methods in Computational Physics, Vol. 16, pp. 1 (1976).

7. J. L. Schwarzmeier, C. E. Seyler, and D. C. Barnes, in Proc. Fourth Symposium on the Physics and Technology of Compact Toroids, Livermore, paper B16 (1981).

8. D. C. Barnes and D. V. Anderson, Phys. Rev. Lett. 46, 1337 (1981).

9. E. J. Caramana, R. A. Nebel, D. D. Schnack, and W. Park, Bull. Am. Phys. Soc. 26, 960 (1981).

10. D. Schnack and J. Killeen, J. Comp. Phys. 35, 110 (1980).

11. W. Park, D. A. Monticello, R. B. White, and A. M. M. Todd, Bull. Am. Phys. Soc. 23, 779 (1978).

12. D. Gottlieb and E. Turkel, Studies in App. Math. 63, 67 (1980).

NONLINEAR TILTING MODE IN THE FIELD REVERSED THETA PINCH

T = 0

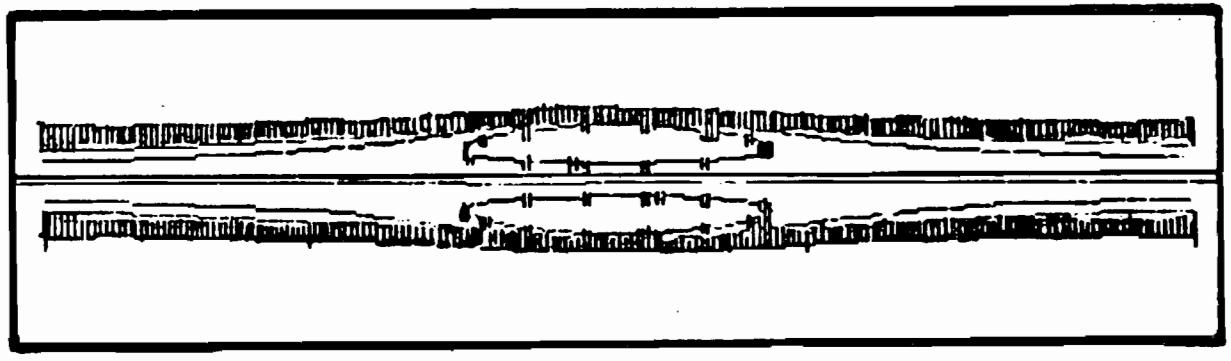

T = 170

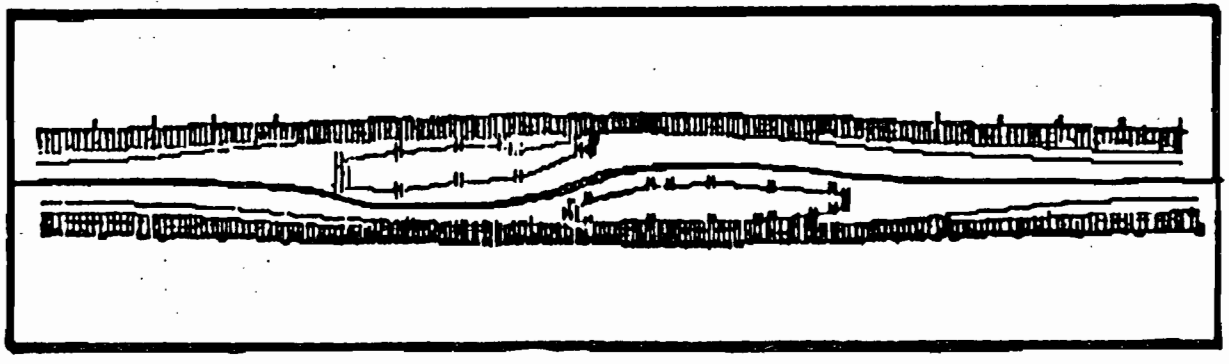

2-D COMPRESSIBLE MHD CODE (D. SCHNACK)[8]

m=1, n=10

Helical Flux and Flow Patterns

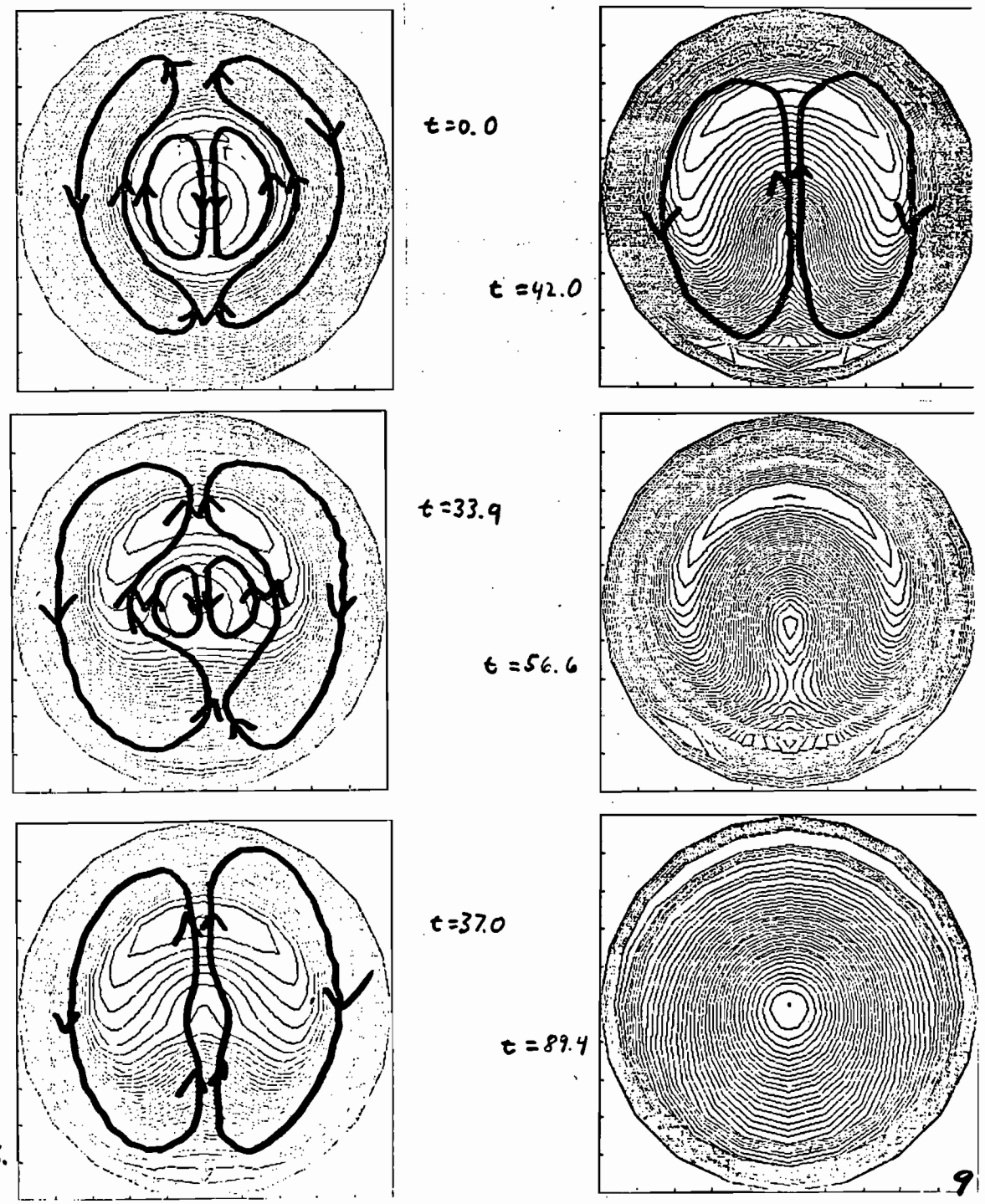

FIG. 4.

A Spectral-Finite Difference Algorithm for Three Dimensional Incompressible MHD

A. Aydemir and D.C. Barnes
The Institute for Fusion Studies, The University of Texas at Austin

I- Introduction

We have developed a code that solves the three dimensional incompressible magnetohydrodynamics equations in a cylindrical geometry. Our algorithm differs from those used in some of the existing 3D codes[1,2] in that no assumption is made about ordering of various quantities; thus, it is applicable for arbitrary beta and aspect ratios. However, we have retained the incompressibility condition in order to eliminate the fast Alfven time scale.

Variables are expanded in Fourier series in the azimuthal and axial coordinates, which reduces the three dimensional MHD equations to one dimensional equations in the radial coordinate for each of the Fourier harmonics. These resulting equations are integrated using a finite-difference scheme in the radial direction.

II- The Equations

We use the usual set of incompressible MHD equations written in the following normalized form:

$$\frac{\partial \underline{u}}{\partial t} = \nabla \cdot (-\underline{u}\underline{u} + \underline{B}\underline{B}) - \nabla p^* \qquad (1)$$

$$\frac{\partial \underline{B}}{\partial t} = -\nabla \times \underline{E} \qquad (2)$$

$$\underline{E} = -\underline{u} \times \underline{B} + \frac{1}{S}\underline{J} \qquad (3)$$

$$\underline{J} = \nabla \times \underline{B} \qquad (4)$$

$$p^* = p + \frac{1}{2}B^2 \qquad (5)$$

$$\rho = 1 \qquad (6)$$

$$\nabla \cdot \underline{u} = 0 \qquad (7)$$

$$\nabla \cdot \underline{B} = 0 \qquad (8)$$

The symbols have their usual meanings. The density is assumed to be constant (unity), which is consistent with Eq. 7 and a uniform initial state.

III- Numerical Scheme

A simple leap-frog scheme is used to time-advance the variables:

$$\underline{u}^{n+1} = \underline{u}^{n-1} + 2\delta t \left\{ \nabla\cdot(-\underline{u}\underline{u} + \underline{B}\underline{B})^{n} - \nabla p^{*n} \right\} \qquad (9)$$

$$\underline{B}^{n+1} = \underline{B}^{n-1} + 2\delta t\, \nabla\times\left[(\underline{u}\times\underline{B})^{n} - \frac{1}{S}\underline{J}^{n-1} \right] \qquad (10)$$

In order to ensure that the flow is divergence-free, we take the divergence of Eq. 9 and set $\nabla\cdot\underline{u}^{n+1} = 0$ to obtain,

$$\nabla^2 p^{*n} = \frac{1}{2\delta t}\nabla\cdot\underline{u}^{n-1} + \nabla : (-\underline{u}\underline{u} + \underline{B}\underline{B})^{n} \qquad (11)$$

which is then inverted to obtain p^{*n} that goes into Eq. 9.[3] Thus, the velocity field $\underline{u}^{n+1}$ given by Eq. 9 satisfies the condition $\nabla\cdot\underline{u}^{n+1} = 0$ identically, even if $\nabla\cdot\underline{u}^{n-1} \neq 0$.

The curl operator in Eq. 10 satisfies the finite-difference form of the vector identity $\nabla\cdot\nabla\times\underline{A} = 0$, for any $\underline{A}$, so that $\nabla\cdot\underline{B}^{n+1} = \nabla\cdot\underline{B}^{n-1}$ identically. Thus, if the initial magnetic field is divergence-free, then

$\nabla\cdot\underline{B}^{n+1} = 0 +$ (accumulated truncation errors).

In our tests until now, the velocity and the magnetic fields have always satisfied the conditions

$$\| \nabla\cdot\underline{u} \| \leq \sum_{m,n} \| (\nabla\cdot\underline{u})_{mn} \| \leq 10^{-10}$$

$$\| \nabla\cdot\underline{B} \| \leq \sum_{m,n} \| (\nabla\cdot\underline{B})_{mn} \| \leq 10^{-10}$$

IV- Stability Criteria

It is difficult to derive necessary stability criteria for the full set of equations used in the code, but one can use

the following conditions obtained from simple model equations as guidelines:

i) $\left| \delta t\,(\underline{k}\cdot\underline{B}_0) \right| < 1$ (12)

ii) $\frac{1}{S}\,\frac{\delta t}{\delta r^2} < \min\left\{\frac{1}{2}, \frac{1}{2M^2}\right\}$ for stability (13)

where $k = \frac{m}{r}\hat{\theta} + \frac{n}{R_0}\hat{\zeta}$

M : maximum poloidal mode number

S : magnetic Reynolds number

Near the axis, Eq. 12 implies $\frac{\delta t\, M B_{\theta_0}}{r} < 1$, or

$$\delta t < \frac{1}{M} \qquad (14)$$

since $B_{\theta_0} \sim r$ for $r \to 0$.

To be able to resolve such fine scale structures as tearing layers, etc., one needs to have the mesh size δr small enough so that $S\delta r^2 \sim O(1)$. Setting $S\delta r^2 = 1$, Eq. 13 imlies

$$\delta t < 1/2M^2 \qquad (15)$$

which is more stringent than Eq. 14. If the resistive terms are treated implicitly, then the time steps that are larger by a factor of 2M can be used. However, in an implicit calculation it would be very difficult, if not impossible, to ensure that $\nabla\cdot\underline{B}^{n+1} = \nabla\cdot\underline{B}^{n-1}$, thus, resulting in large errors in $\nabla\cdot\underline{B}$.

V- Checks on the Code and Some Preliminary Results

a) Dispersion Relation Check.

The frequency of induced shear-Alfven waves is checked by perturbing a uniform axial field equilibrium with a $v_\theta(r;m=0,n=1)$ perturbation. For $B_{\zeta_0} = 1$, the period of the oscillations is found to be 6.28 ± 0.01 in a cylinder of minor and major radii equal to 1, which agrees well with the expected result of 2π. The oscillations were followed for eight periods, during which time the ratio of the change in total energy to the change in kinetic energy, $\Delta E_{TOT}/\Delta E_{KIN}$ was less than 0.2 percent.

b) m=1 Ideal Internal Kink.

Starting with the same equilibrium as in W. Park, et. al.,[4] we calculated linear growth rates for various aspect ratios. The values we obtained were in agreement with theirs to within a few percent.

We also did a non-linear calculation with four harmonics,(0/0, 1/1, 2/2, 3/3) for an aspect ratio of one (Fig. 1). We do see a current

sheet developing at the singular surface; however, without the addition of "artificial field" as in Ref. 4, we are not able to follow the evolution of the instability all the way to saturation.

c) m=2 Resistive Tearing Mode

We did a series of calculations with the following square safety profile[5]:

$$q(r) = 2\left[\frac{1+(r/r_0)^8}{1+(r_{s2}/r_0)^8}\right]^{1/4}$$

where the current channel width $r_0 = 0.6$, and the radius of the q=2 surface $r_{s2} = 0.7$ (Minor radius is equal to one.). Fig. 2a shows the contours of m/n = 2/1 helical flux obtained by integrating the fields, for an aspect ratio of five. Fig. 2b shows the m/n = 2/1 harmonic of the radial field for the same case.

Figs. 3 and 4 show $B_z(r;m/n=2/1)$ for different aspect ratios. As expected from low-β MHD ordering[6], the axial field perturbation tends to zero with increasing aspect ratio for most of the plasma column. However, in the tearing layer around the q=2 surface, a strong perturbation remains, even with the relatively high aspect ratio of twenty (Figs. 4a,b). The runs with aspect ratios of five and twenty were made with 1024 radial mesh points, and as shown in the blow-up of the tearing layer in Fig. 4b, the oscillatory behavior is resolved with approximately 50 mesh points and does not seem to be numerical. The axial velocity displays a similar behavior in the tearing layer. Fig. 5a shows the m=2 island from an incomplete non-linear run with 3 harmonics (0/0, 2/1, and 4/2). The axial current density altered by a current sheet developing at the q=2 singular surface is shown in Fig. 5b.

REFERENCES:

(1) W. Park, D.A. Monticello, R.B. White, Bull. Am. Phys. Soc., 22, 779 (1978).

(2) H.R. Hicks, B. Carreras, J.A. Holmes, D.K. Lee, B.V. Waddell, ORNL Report No. ORNL/PN-7132.

(3) F.H. Harlow, J.E. Welch, Phys. Fluids, 8, 2182 (1965).

(4) W. Park, D.A. Monticello, R.B. White, S.C. Jardin, Nucl. Fusion, 20, 1181 (1980).

(5) B.V. Waddell, B. Carreras, H.R. Hicks, and J.A. Holmes, Phys. Fluids, 22, 896(1979).

(6) H.R. Strauss, Phys. Fluids, 19, 134 (1976).

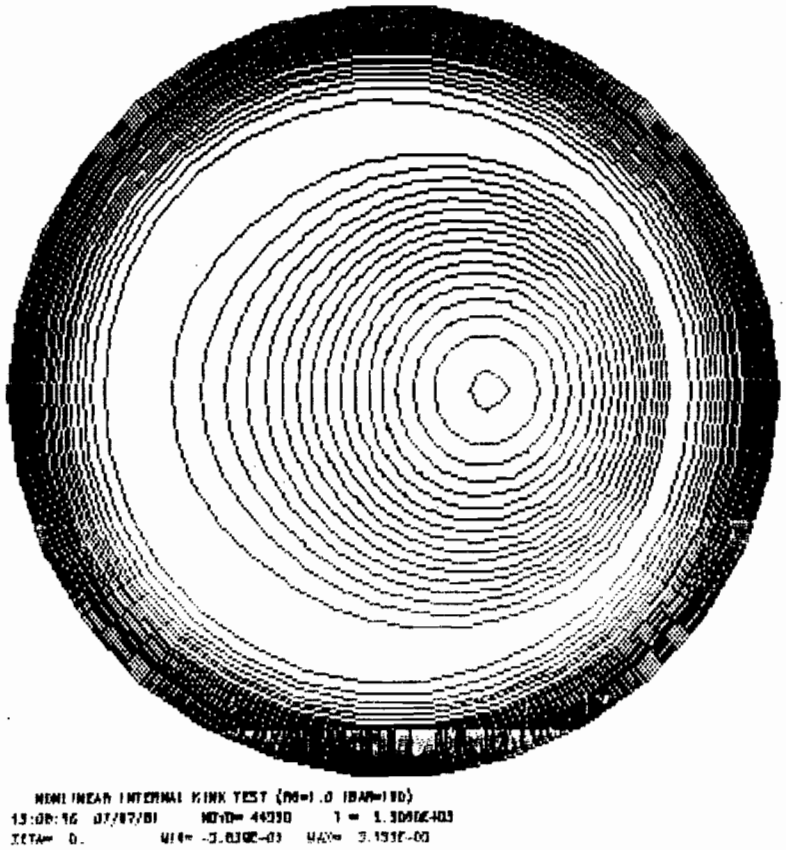

FIG. 1a. HELICAL FLUX CONTOURS (INTERNAL KINK)

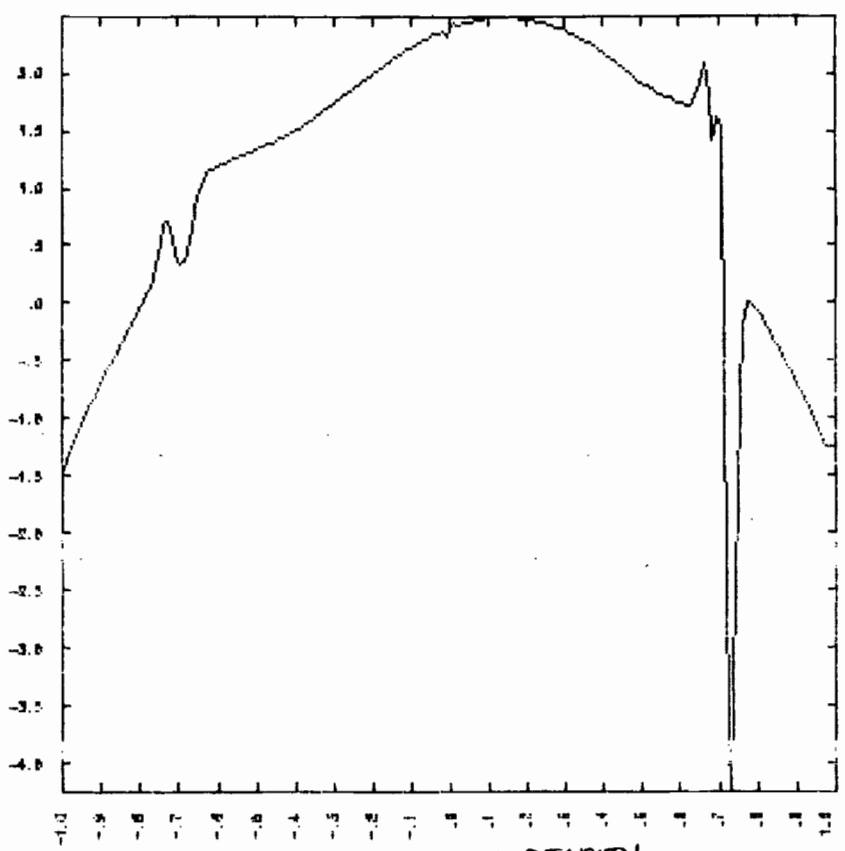

FIG. 1b. HELICAL CURRENT DENSITY

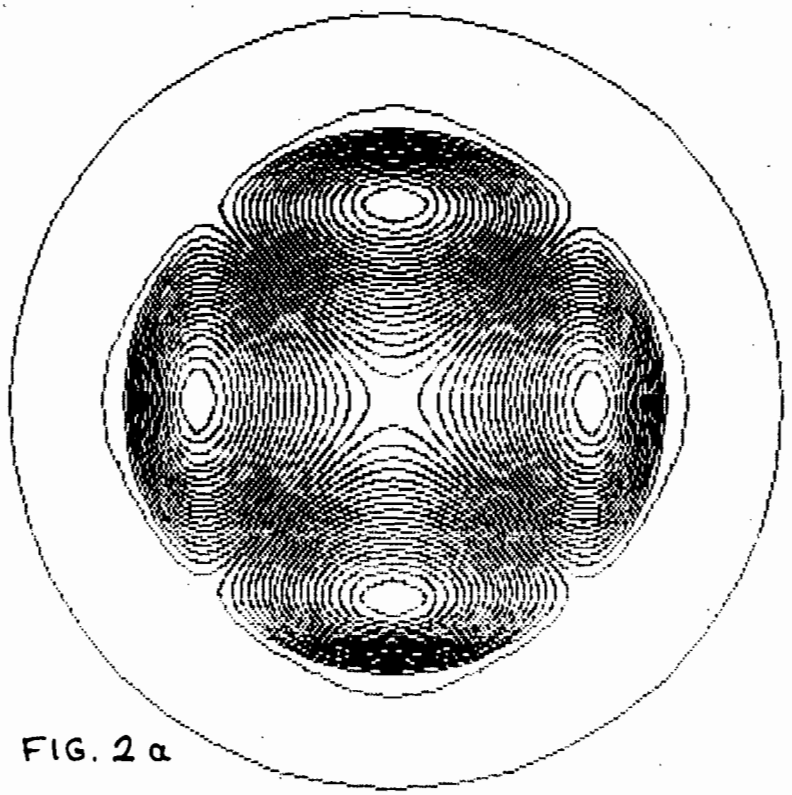

FIG. 2 a

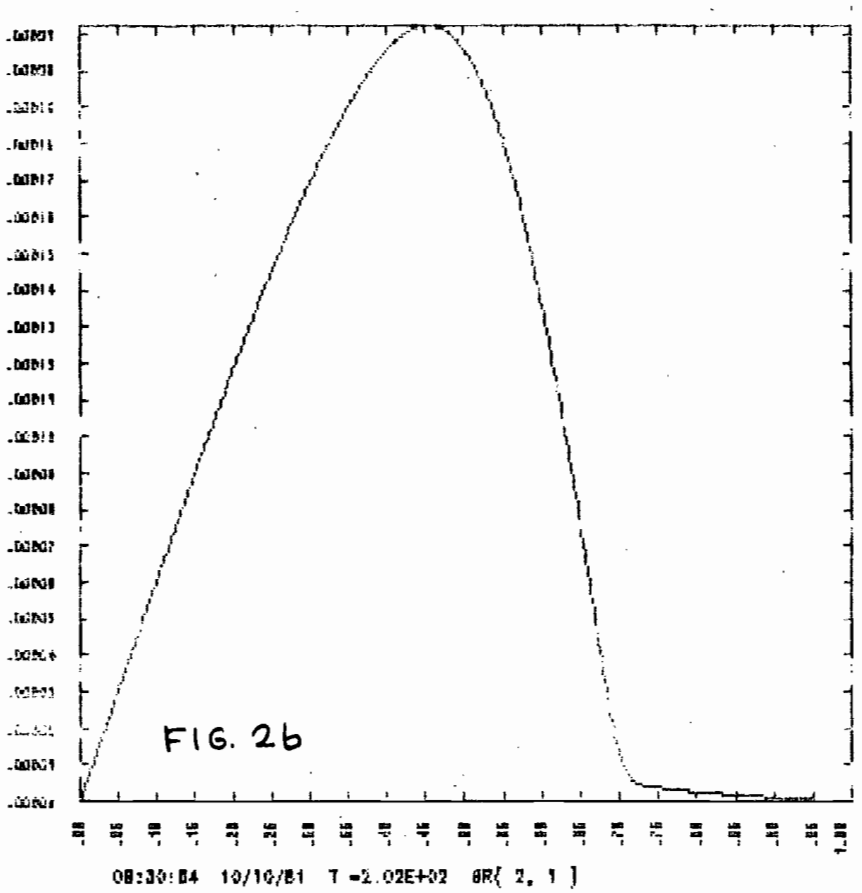

FIG. 2b

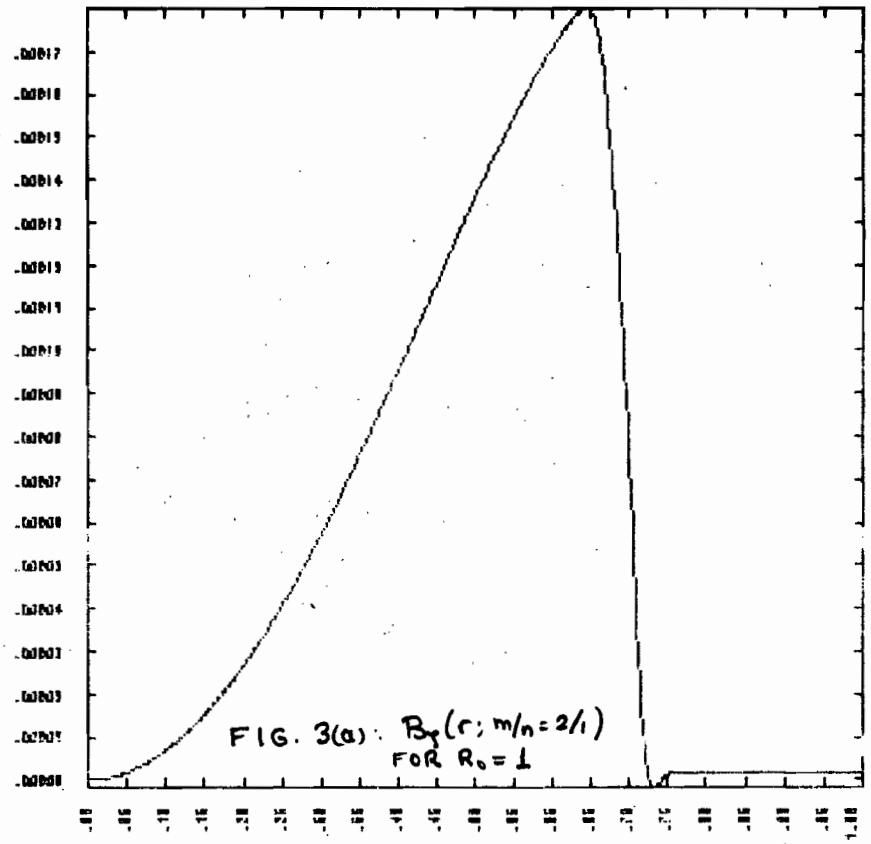

FIG. 3(a): $B_\zeta(r; m/n = 2/1)$ FOR $R_0 = 1$

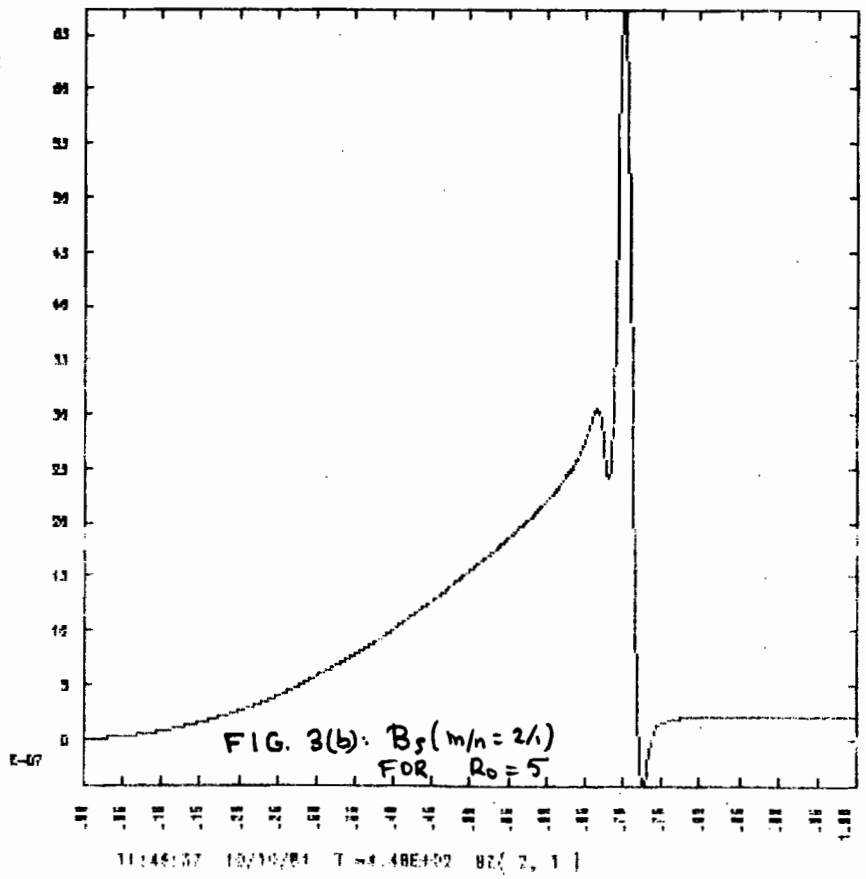

FIG. 3(b): $B_\zeta(m/n = 2/1)$ FOR $R_0 = 5$

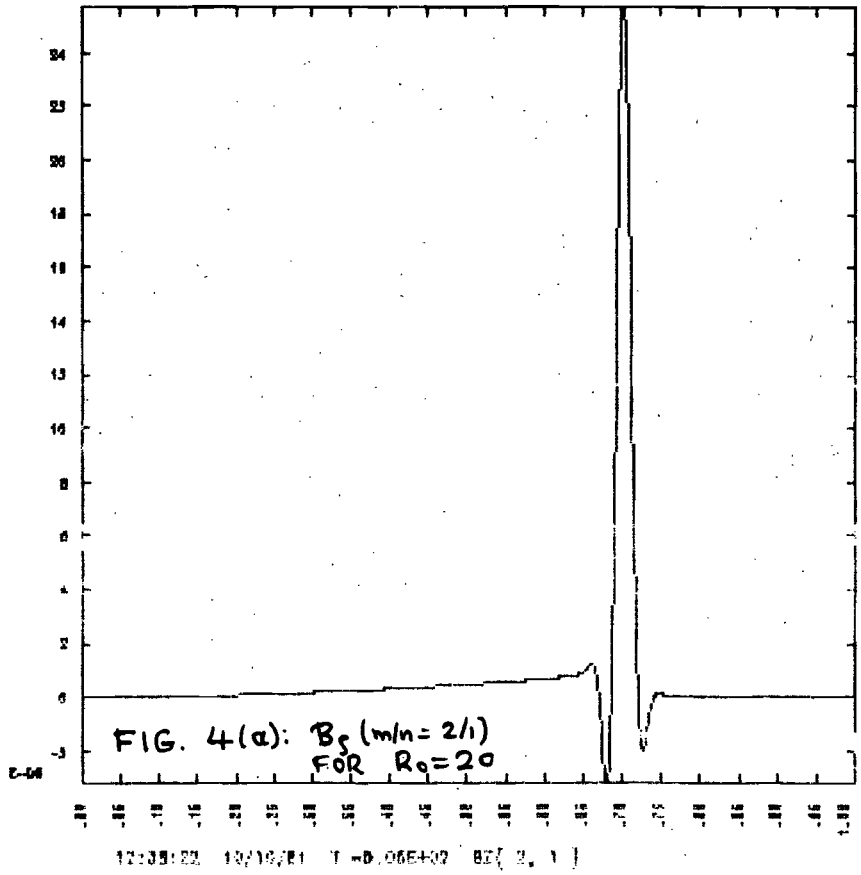
FIG. 4(a): B_ρ (m/n = 2/1)
FOR R_0 = 20
12:38:22 10/10/81 T =0.06E+02 BZ(2, 1)

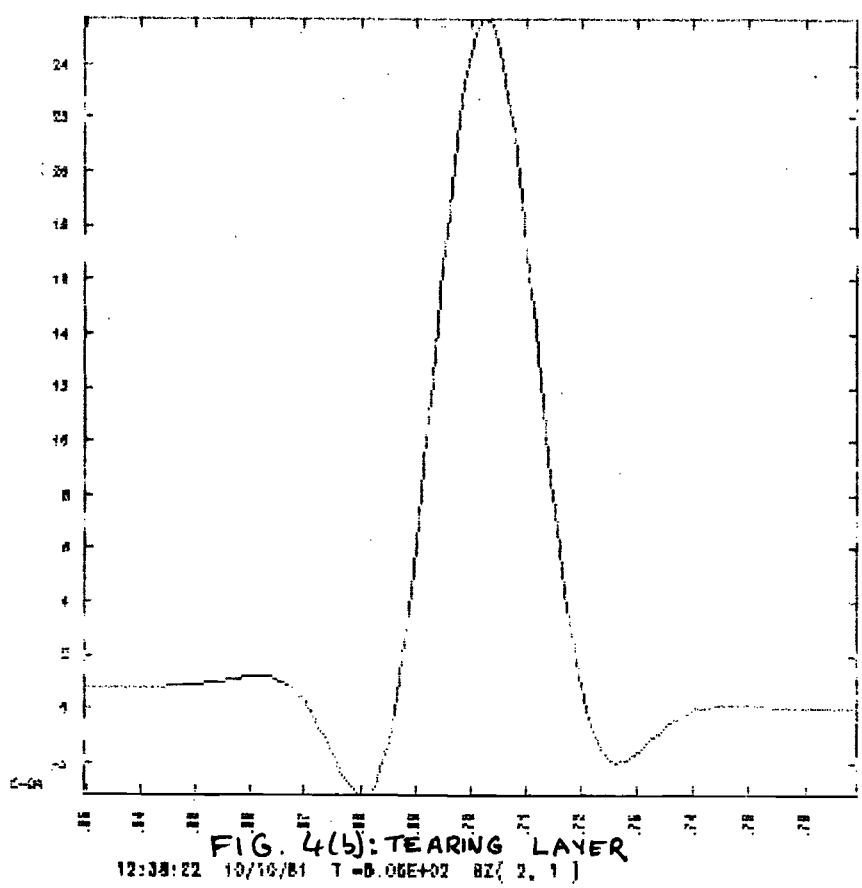
FIG. 4(b): TEARING LAYER
12:38:22 10/10/81 T =0.06E+02 BZ(2, 1)

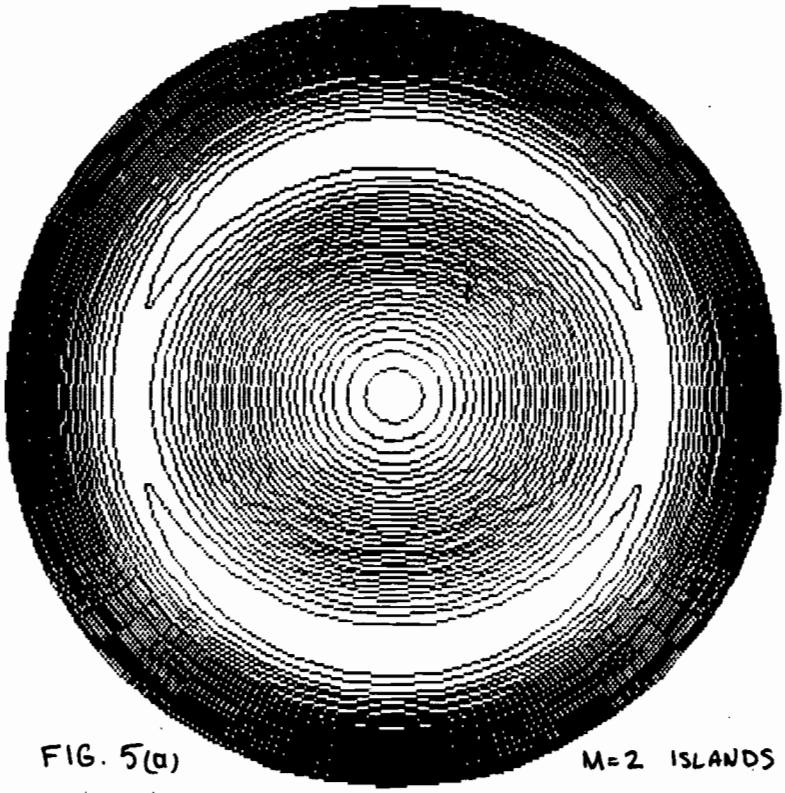

FIG. 5(a) M=2 ISLANDS

NON-LINEAR M=3,N=1 TEARING MODE (IBAR=319,NB=20,S=1.0E4)

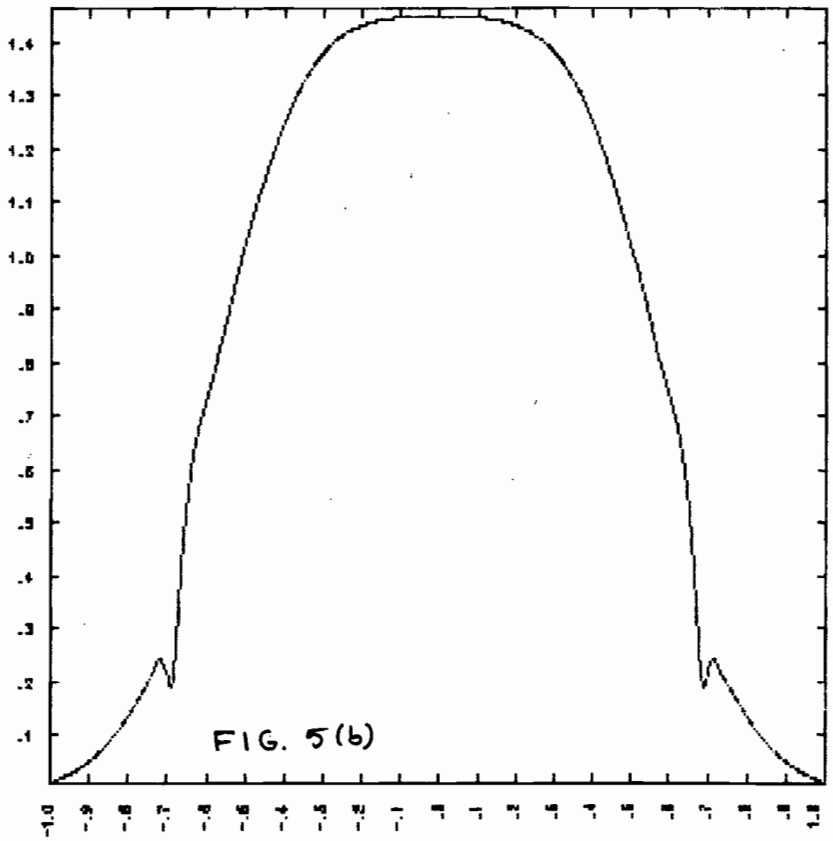

FIG. 5(b)

12:42:48 10/08/81 T =1.62E+03 AXIAL CURRENT DENSITY

3-D TENSOR PRESSURE EQUILIBRIA FOR EBT*

L. W. Owen
Computer Sciences at
Oak Ridge National Laboratory
Oak Ridge, Tennessee

C. L. Hedrick
Fusion Energy Division
Oak Ridge National Laboratory
Oak Ridge, Tennessee

ABSTRACT

Techniques for calculating magnetohydrostatic equilibria with tensor pressure are reviewed. Algorithms for computing 3-D hot electron ring equilibria for the Elmo Bumpy Torus (EBT) with a separable model for the pressure tensor are discussed, as are the numerical methods used in the implementation of those algorithms in a computer code. Some typical results of 3-D equilibrium calculations for EBT-I/S and an EBT reactor conceptual design illustrate the effects of the relativistic electron annuli on the magnetic field. Two significant additions to the 3-D code are planned for the near-term and discussed in this paper. This first concerns the addition of an isotropic pressure component to model the core plasma in EBT. The second is the inclusion of the flow and electric field terms in the momentum balance equation. A straightforward method of including mass flow due to the $\vec{E}\times\vec{B}$ plasma rotation and a discussion of its possible importance for 3-D equilibria in EBT are presented.

*Research sponsored by the Office of Fusion Energy, U.S. Department of Energy, under contract W-7405-eng-26 with the Union Carbide Corporation.

In this paper we discuss methods for computing three-dimensional finite-beta equilibria for the anisotropic electron ring plasma in the Elmo Bumpy Torus (EBT). Typical results of some 3-D tensor pressure equilibrium calculations for EBT-I/S and an EBT reactor conceptual design illustrate the effects of the electron ring diamagnetic currents on the magnetic field. (Space limitations do not permit a discussion of all the topics mentioned in the abstract and covered in the oral presentation; however, a complete report[1] of this work is forthcoming.)

Techniques for determining tensor pressure equilibria, presented in a review by Hedrick, et al.,[2] are briefly outlined for a ring pressure model which is a separable function of the magnetic field B and flux coordinates (α,β). The fundamental magnetostatic equilibrium equations are Maxwell's equations

$$\nabla \times \vec{B} = \mu_o \vec{J}$$
$$\nabla \cdot \vec{B} = 0 \ , \tag{1}$$

and a momentum balance equation

$$\vec{J} \times \vec{B} = \nabla \cdot \underset{\sim}{P} \ , \tag{2}$$

where $\vec{J}$ is the plasma current and $\underset{\sim}{P}$ is the pressure tensor, given by

$$\underset{\sim}{P} = p_\perp \underset{\sim}{I} + (p_\parallel - p_\perp)\hat{b}\hat{b} \ . \tag{3}$$

$(\nabla \cdot \underset{\sim}{P})$ can be resolved into components parallel and perpendicular to $\vec{B}$, with $(\nabla \cdot \underset{\sim}{P})_\parallel = 0$ yielding the useful relation

$$\frac{\partial p_\parallel}{\partial B} - \frac{(p_\parallel - p_\perp)}{B} = 0 \ , \tag{4}$$

and

$$(\nabla\cdot\underset{\sim}{P})_\perp = \vec{\nabla}_\perp p_\perp + (p_\parallel - p_\perp)\vec{\kappa} \ . \tag{5}$$

Consider a coordinate system in which field lines are labeled by (α,β) and $\vec{B}$ is written in the Clebsch representation $\vec{B} = \vec{\nabla}\alpha \times \vec{\nabla}\beta$. For $p_\parallel = p_\parallel(\alpha,\beta,B)$ and $p_\perp = p_\perp(\alpha,\beta,B)$, (5) becomes

$$[\nabla\times(\sigma\vec{B})]\times\vec{B} = \frac{\partial p_\parallel}{\partial\alpha}\vec{\nabla}\alpha + \frac{\partial p_\parallel}{\partial\beta}\vec{\nabla}\beta \ , \tag{6}$$

where we have defined the inverse of the permeability

$$\sigma = \frac{1}{\mu_o} - \left(\frac{p_\parallel - p_\perp}{B}\right) \tag{7}$$

and used (1) and (4). The form of (6) suggests that we define a current-like quantity $\vec{K} = \nabla\times(\sigma\vec{B})$; then

$$\vec{K} \times \vec{B} = \frac{\partial p_\parallel}{\partial\alpha}\vec{\nabla}\alpha + \frac{\partial p_\parallel}{\partial\beta}\vec{\nabla}\beta \ . \tag{8}$$

Since $\nabla\cdot\vec{K} = 0$, $\vec{K}$ can be described by a Clebsch representation,

$$\vec{K} = \vec{\nabla}\phi_1 \times \vec{\nabla}\phi_2 = \nabla\times(\phi_1\vec{\nabla}\phi_2) = \nabla\times(\sigma\vec{B}) \ . \tag{9}$$

Hence $\nabla\times(\sigma\vec{B} - \phi_1\vec{\nabla}\phi_2) = 0$ has solutions of the form

$$\sigma\vec{B} = \phi_1\vec{\nabla}\phi_2 + \vec{\nabla}\phi_3 \ . \tag{10}$$

In order to determine ϕ_1 and ϕ_2, use (10) to form

$$\vec{K}\times\vec{B} = \vec{\nabla}\phi_2(\vec{B}\cdot\vec{\nabla}\phi_1) - \vec{\nabla}\phi_1(\vec{B}\cdot\vec{\nabla}\phi_2) \ . \tag{11}$$

It is assumed in our 3-D code that

$$\begin{aligned} P_{\parallel}(\alpha,\beta,B) &= \hat{P}_{\parallel}(B)g(U) \\ P_{\perp}(\alpha,\beta,B) &= \hat{P}_{\perp}(B)g(U) \ , \end{aligned} \tag{12}$$

where U is a slowly varying function of (α,β). The distribution functions $\hat{p}_{\parallel}$ and $\hat{p}_{\perp}$ are given in Reference (2) and plotted as functions of B in Fig. 1. If we substitute (12) into (8), we find that

$$\vec{K}\times\vec{B} = \hat{p}_{\parallel}(B)\vec{\nabla}g \ , \tag{13}$$

where

$$\vec{\nabla}g = g'(U)\left\{\frac{\partial U}{\partial\alpha}\vec{\nabla}\alpha + \frac{\partial U}{\partial\beta}\vec{\nabla}\beta\right\} \ . \tag{14}$$

Comparing (11) and (13) suggests the choice $\phi_2 = g(U)$. Then $\vec{K}\times\vec{B} = \vec{\nabla}g(\vec{B}\cdot\vec{\nabla}\phi_1) = \hat{p}_{\parallel}(B)\vec{\nabla}g$, provided $(\vec{B}\cdot\vec{\nabla}\phi_1) = \hat{p}_{\parallel}(B)$, or

$$\phi_1(\alpha,\beta,\ell) = \int_0^{\ell}\frac{d\ell'}{B}\,\hat{p}_{\parallel}(B) \ . \tag{15}$$

The system of equations is complete if we substitute (10) into $\nabla\cdot\vec{B} = 0$ to obtain a Poisson's equation for ϕ_3

$$\nabla^2\phi_3 = -\nabla\cdot(\phi_1\vec{\nabla}g) + \vec{B}\cdot\vec{\nabla}\sigma \ . \tag{16}$$

The pressure surfaces are determined in 3-D by requiring that the parallel component of $\vec{J}$ vanish at symmetry planes. In (15) let $\ell=0$ and

and $\ell=\ell_c$ correspond to a sector midplane and adjacent coil plane, respectively. Define $\overline{\phi}_1 = \phi_1(\alpha,\beta,\ell_c)$ and notice that the current

$$\sigma\mu_o\vec{J} = \sigma(\nabla x\vec{B}) = \vec{\nabla}\phi_1 x\vec{\nabla}g + \vec{B}x\vec{\nabla}\sigma ,$$

has the parallel component (at $\ell=\ell_c$)

$$\sigma\mu_o\vec{J}_{\parallel} = \sigma\mu_o\hat{b}\cdot\vec{J} = \vec{\nabla}\overline{\phi}_1 \times \vec{\nabla}g = 0 . \qquad (17)$$

Hence $\vec{\nabla}\overline{\phi}_1$ is parallel to $\vec{\nabla}g$ and contours of constant g (or U) must coincide with contours of constant $\overline{\phi}_1$. This result is the tensor pressure analog of the fact that for scalar pressure the isobaric surfaces must coincide with surfaces of constant $\oint d\ell/B$.

In the calculations discussed below, the choice of ring pressure parameters is based on present understanding of ring formation, location, size, shape, etc. In EBT-I/S the annuli form at the position at which the second harmonic of the electron cyclotron frequency is resonant with the applied microwave frequency. The axial length of the rings is thought to be approximately equal to their radius, and the radial thickness is a few thermal gyroradii.

With reasonable pressure anisotropy it is found that (17) can be satisfied with pressure surfaces that are concentric circles in the midplane, centered roughly at the location of the peak of mod-B, e.g., approximately 3 cm inside the minor axis for EBT-I/S. A comparison of contours of constant U and $\overline{\phi}_1$ is shown in Fig. 2 for an annulus pressure profile having a radius of about 12 cm. The only significant differences in the contours are in regions in which the pressure is less than 10% of its peak value. This difference is to be expected from the behavior of the vacuum magnetic field and can be easily eliminated by spreading out the U contours on the outside (where $R-R_T > 0$) so that they more closely resemble the contours of vacuum mod-B in the midplane.

Figure 3 shows the effects of finite-beta on mod-B in the midplane for two pressure profiles in EBT-I/S; $\beta_\perp$ as a function of minor radius is also shown. Figure 3a probably represents the more realistic annulus, with the peak $\beta_\perp \simeq 27\%$ and the radial thickness of the annulus $\simeq$2.25 cm. In Fig. 4a, mod-B contours and magnetic field lines in the equatorial plane are shown for the vacuum field and for the $\beta_\perp \simeq 40\%$ equilibrium field displayed in Fig. 3b. In Fig. 4b, are shown isometric plots of mod-B in the equatorial plane corresponding to the curves in Fig. 3b.

Figure 5 shows the results of two equilibrium calculations for an EBT reactor conceptual design with and without symmetrizing coils.[3] In each case the annulus radius is chosen to give the largest possible plasma volume (dotted region) subject to constraints imposed by the heating geometry and by the location of the first wall of the reactor chamber.

REFERENCES

1. L. W. Owen and C. L. Hedrick, "Tensor Pressure Equilibria and Particle Orbits in EBT," to be published as ORNL/TM-7388.

2. C. L. Hedrick, G. E. Guest, and D. B. Nelson, "Some Techniques for Determining Tensor Pressure Equilibria," ORNL/TM-4076 (1973).

3. L. W. Owen and N. A. Uckan, "Optimization of EBT Reactor Magnetics," ORNL/TM-7729 (1981).

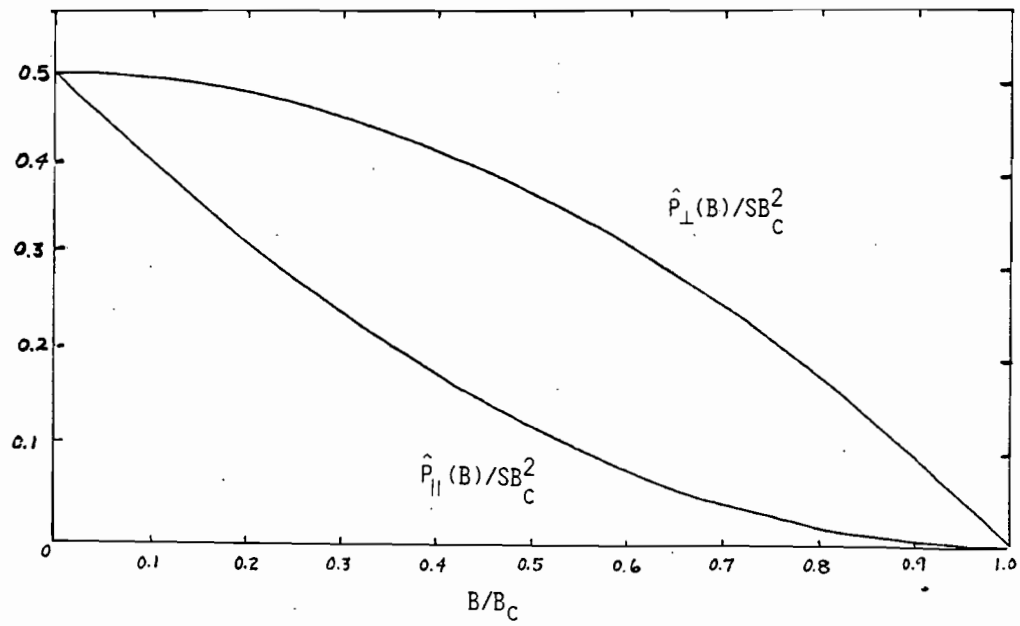

Figure 1. $\hat{p}_{||}(B)$ and $\hat{p}_\perp(B)$ for the "constant-τ" pressure model.

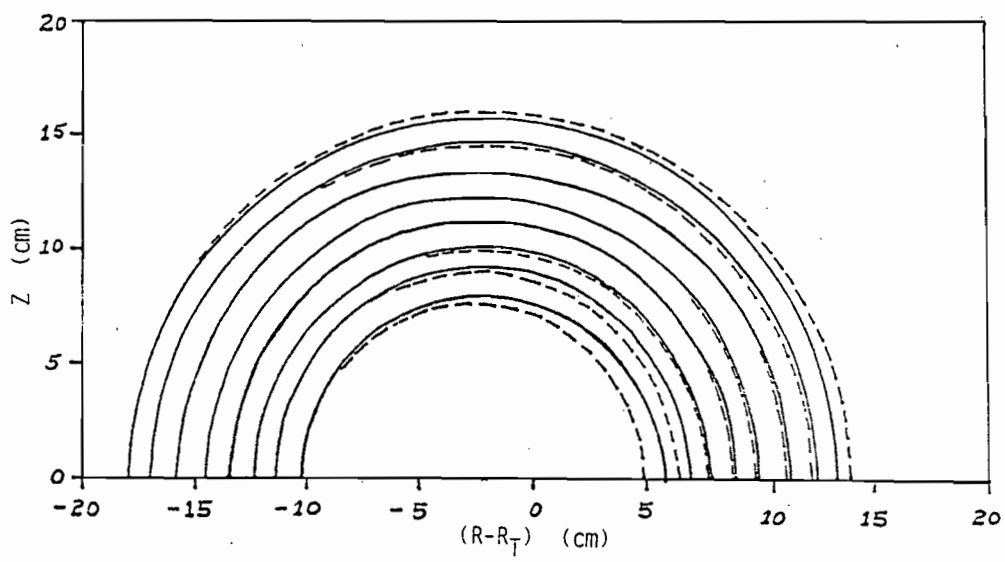

Figure 2. Contours of constant U (solid) and $\overline{\varphi}_1$ (dashed) in the region occupied by the high-beta electron ring plasma.

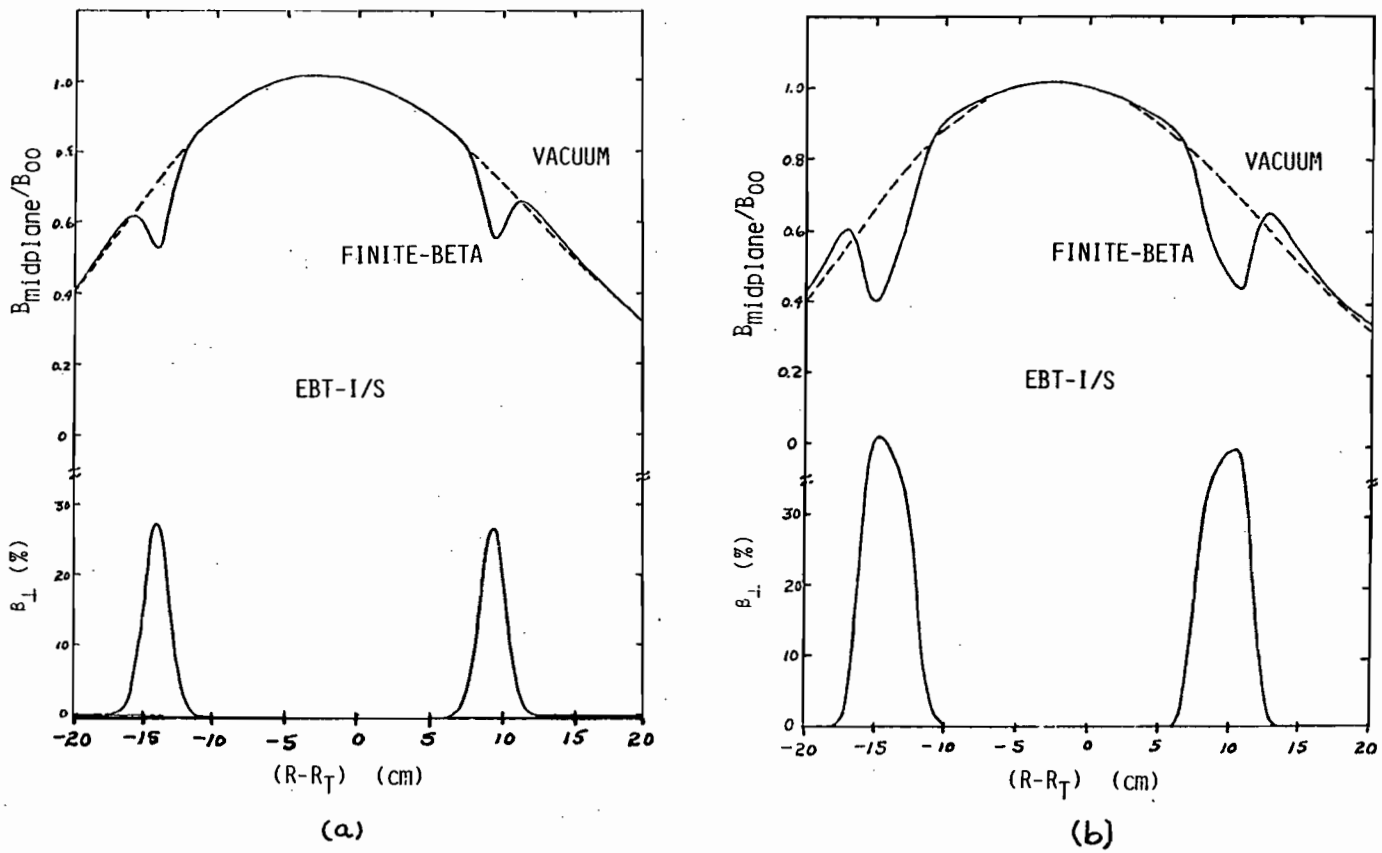

Figure 3. Vacuum and 3-D equilibrium magnetic fields and $\beta_\perp$ as functions of radius in the midplane (a) $\beta_\perp^{peak} \simeq 27\%$, (b) $\beta_\perp^{peak} \simeq 40\%$.

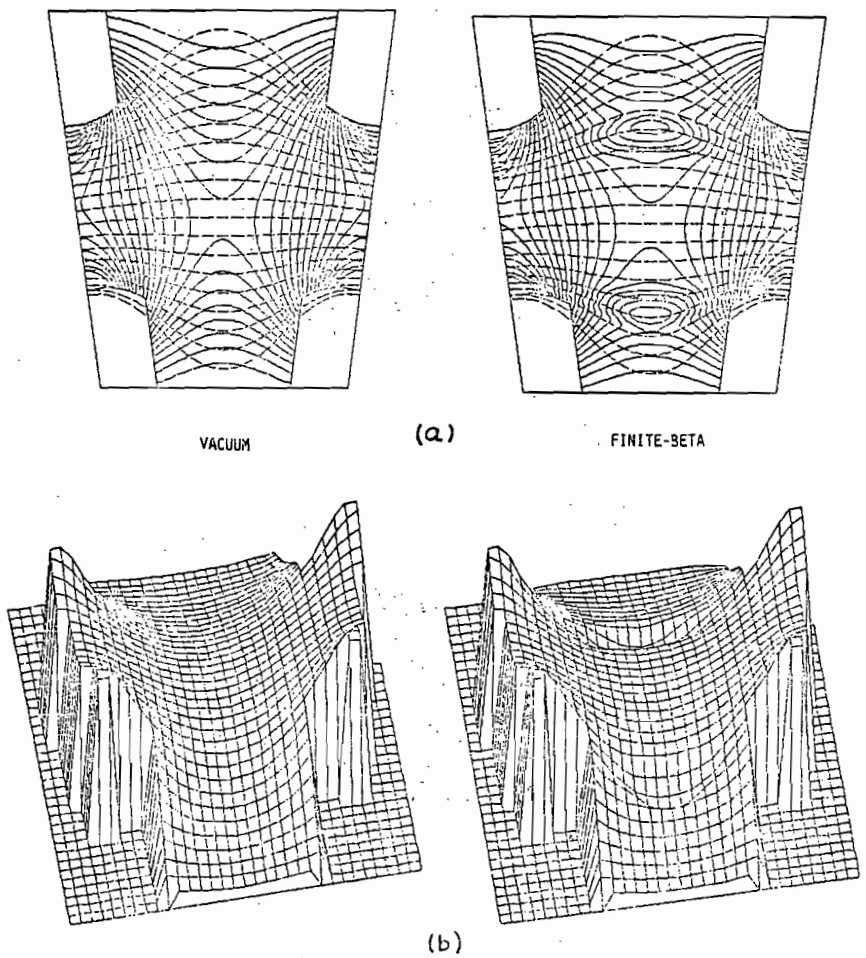

Figure 4. (a) Magnetic field lines (dashed) and mod-B contours (solid) in the equatorial plane of EBT-I/S, (b) Isometric plots of mod-B in the equatorial plane. The finite-beta results correspond to the equilibrium shown in Fig. 3b.

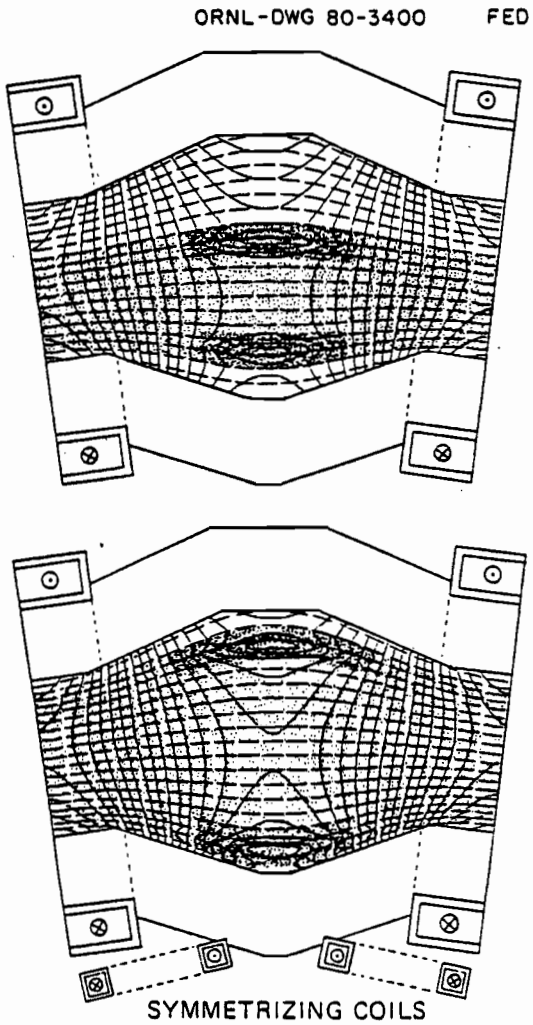

Figure 5. Results of 3-D equilibrium calculations for an EBT reactor conceptual design without (top) and with (bottom) symmetrizing coils. These results illustrate the importance of 3-D equilibria in ascertaining reactor volume utilization efficiency.

Finite Element Method for 3D MHD Simulations

Ichiro Kawakami
Atomic Energy Research Institute
College of Science and Technology, Nihon University

Presented the US-Japan Workshop on "The 3D MHD Studies for Toroidal Devices", Oct. 19-21, 1981, at Oak Ridge National Laboratory

§1. Introduction

For MHD simulations of plasmas confined in fusion devices, finite difference methods (FDM) have been used, and among them, the two step Lax-Wendroff method, the Crank-Nicholson method, the leap from method and doner cell are prevailingly used. Recently, the other types of methods along the line of FDM are available. They are FCT (Flux Corrected Transport), ICE (Implicit Continuous fluids-Eulerian), LINC (Lagrangian technique for incompressible fluid), GALE (Generalized Arbitrary Lagrangian and Eulerian) and FIC (Fluid In Cell). ICED ALE uses moving grids (Arbitrary Lagrangian and Eulerian) to improve accuracy.

In this report, we propose another way of numerical method than FDM. We call this method as FEMALE (Finite Element Method for Arbitrary Lagrangian and Eulerian elements), which may be regarded as a member of finite element method (FEM). In many cases, FDM can be regarded as a special case of FEM. ICED ALE is a special case of FEMALE where the shape function is constant in element (cell). FEMALE makes use of grids which move arbitrarily, as the ICED ALE does. To achieve this, FEMALE uses the shape function which moves with the grids, so the shape function

is time dependent. This show FEMALE is an extention of usual FEM where the shape function is constant in time.

§2. Formulation of FEMALE

2. 1 Basic Equation - differential form

As an example, the following set of differential equations are employed,

$$\frac{\partial n}{\partial t} + \mathrm{div}(n\vec{v}) = 0 \ , \tag{2. 1}$$

$$\frac{\partial \rho\vec{v}}{\partial t} + \mathrm{div}\,\overleftrightarrow{P} = 0 \ , \tag{2. 2}$$

$$\frac{\partial u}{\partial t} + \mathrm{div}\,\vec{g} = 0 \ , \tag{2. 3}$$

$$\frac{\partial \vec{B}}{\partial t} + \mathrm{curl}\ E = 0 \ . \tag{2. 4}$$

Here

$$\overleftrightarrow{P} = (p + \frac{1}{2\mu_o} B^2)\overleftrightarrow{I} + \rho\vec{v}\vec{v} - \frac{1}{\mu_o}\vec{B}\vec{B} \ , \tag{2. 5}$$

$$u = \frac{1}{2}\rho v^2 + \frac{3}{2} p + \frac{1}{2\mu_o} B^2 \ , \tag{2. 6}$$

$$\vec{g} = (p + u)\vec{v} + \frac{1}{\mu_o}(\vec{E}\times\vec{B}) - \kappa\,\mathrm{grad}\ T. \tag{2. 7}$$

The following relations complete the system of MHD equations,

$$\vec{E} + \vec{v} \times \vec{B} = \overleftrightarrow{\eta}\,\vec{j} \ , \tag{2. 8}$$

$$\vec{j} = \frac{1}{\mu_o}\,\mathrm{curl}\ \vec{B} \ , \tag{2. 9}$$

$$\rho = mn, \quad T = p/n \ , \tag{2. 10}$$

where n = number density, $\vec{v}$ = velocity, p = pressure, $\vec{B}$ = magnetic field, $\vec{E}$ = electric field, and the other quantities

may be clear. Dependent variables are n, $\rho\vec{v}$, u and $\vec{B}$.

These equations are to be expressed in specific coordinate system for each space component. For 1D and 2D cases, the coordinates system may be cartesian, cylindrical, toroidal or helical, depending plasma geometries. For 3D case, the coordinates system can be cartesian for all plasma geometries.

2.2 Shape Functions

Let Ω be a space occupied by plasma. Ω is divided into finite elements, Re (e = 1, 2, $\cdots$E):

$$\Omega = \bigcup_{e=1}^{E} Re \quad , \tag{2. 11}$$

$$Re \cap R_f = \phi \quad \text{for } e \neq f \ . \tag{2. 12}$$

E is total number of elements. Let Ne and N be numbers of nodes (verteces) in Re, and number of nodes in Ω , respectively. For simplex element, Ne = 4 (tetrahedron) for 3D, Ne = 3 (triangle) for 2D, Ne = 2 (line) for 1D.

A set of N shape functions $\{\phi^1, \phi^2, \cdots\cdots \phi^N\}$ is introduced as follows:

(i) $$\sum_{\mu=1}^{N} \phi^{\mu}(\vec{\xi}) = 1 \qquad \vec{\xi} \in \Omega \tag{2. 13}$$

(ii) ϕ^{μ} is localized in the elements which include the node μ, and

$$\phi^{\mu}(\vec{\xi}^{\nu}) = \delta^{\mu\nu} \quad , \tag{2. 14}$$

where $\vec{\xi}^{\nu}$ is the position of the node μ .

(iii) $$(\frac{\partial}{\partial t} + \vec{v}_g \cdot \text{grad})\phi^{\mu} = 0 \quad , \tag{2. 15}$$

where $\vec{v}_g$ is the grid velocity.

We define a basic matrix in terms of shape function ϕ^{μ}:

$$A = [\alpha^{\mu\nu}] \ , \tag{2. 16}$$

$$\alpha^{\mu\nu} \equiv \int_{\Omega} d\Omega \phi^{\mu}\phi^{\nu} = \sum_{e=1}^{E} \int_{Re} d\Omega \phi^{\mu}\phi^{\nu} \ .$$

A is positive definite and symmetric. Note that A is a band matrix because ϕ^{μ}'s are localized. Even in the band, A is sparse.

Associated matrix with the basic matrix is defined as

$$A^{-1} \equiv [\alpha_{\mu\nu}] \tag{2. 18}$$

where

$$\sum_{\rho=1}^{N} \alpha_{\mu\rho}\alpha^{\rho\nu} = \delta^{\mu\nu} \ , \tag{2. 19}$$

so that the associated matrix is a inverse of the basic matrix A. In terms of A^{-1}, we introduce a set of conjugate shape functions $\{\phi_1, \phi_2, \cdots\cdots \phi_N\}$
as

$$\phi_{\mu} \equiv \sum_{\rho=1}^{N} \alpha_{\mu\rho}\phi^{\rho} \ . \tag{2. 20}$$

ϕ_{μ} is no more localized around the node μ . The ϕ_{μ}'s play a important role in evaluation of derivatives.

2. 3 Basic Equations - discretized form

For the continuity equation (2. 1),

$$\frac{\partial}{\partial t} \int_{\Omega} d\Omega \phi^{\mu} n = \int_{\Omega} d\Omega \left(\frac{\partial \phi^{\mu}}{\partial t} n + \phi^{\mu} \frac{\partial n}{\partial t}\right) + \int d\Omega \ \mathrm{div}(\phi^{\mu} n \vec{v}_g).$$

The last term comes from the fact that the boundary of the plasma moves with the velocity $\vec{v}_g$. Substituting (2. 1) and (2. 15), we obtain

$$\frac{\partial}{\partial t}\int_{\Omega} d\Omega\phi^{\mu} n = -\int_{\Omega} d\Omega\phi^{\mu} \mathrm{div}\, n(\vec{v} - \vec{v}_g) \qquad (2.\ 21)$$

where ϕ^{μ} is constant in a cell. Eq. (2. 2) is reduced to the basic equation of integral form of ICED ALE method. In a similar way, eqs. (2. 2 - (2. 4) yield the following equations:

$$\frac{\partial}{\partial t}\int_{\Omega} d\Omega\phi^{\mu}\rho v_i = -\int_{\Omega} d\Omega\phi^{\mu} \sum_{j=1}^{3}\frac{\partial}{\partial\xi_j}(P_{ij} - \rho v_i v_{gj}) , \qquad (2.\ 22)$$

$$\frac{\partial}{\partial t}\int_{\Omega} d\Omega\phi^{\mu} u = -\int_{\Omega} d\phi^{\mu}\ \mathrm{div}[\vec{g} - u\vec{v}_g] , \qquad (2.\ 23)$$

$$\frac{\partial}{\partial t}\int_{\Omega} d\Omega\phi^{\mu} B_i = \int_{\Omega} d\Omega\phi^{\mu}\mathrm{div}(B_i\vec{v}_g) - \int_{\Omega} d\Omega\phi^{\mu}(\frac{\partial}{\partial\xi_j} E_k - \frac{\partial}{\partial\xi_k} E_j). \qquad (2.\ 24)$$

Additional term may appear in eq. (2. 22) originating from coliolis force in the noncartesian coordinates system, which is ignored because we are concerned with 3D problems and then only the cartesian coordinates system is concerned.

We expand the quantity f in Galerkin series,

$$f = \sum_{\mu=1}^{N} f_{\mu}\phi^{\mu} , \qquad (2.\ 25)$$

where f_{μ} is the value of f at the node μ . Then, eqs. (2. 21) - (2. 24) can be written as

$$\frac{\partial}{\partial t}\alpha^{\mu\nu} n_{\nu} = - D_1^{i,\mu\nu} n_{\nu}(v_{i,\nu} - v_{gi,\nu}) , \qquad (2.\ 26)$$

$$\frac{\partial}{\partial t}\alpha^{\mu\nu}(\rho v_i)_{\nu} = - D_1^{j,\mu\nu}(P_{ij,\nu} - (\rho v_i)_{\nu} v_{gj,\nu}) , \qquad (2.\ 27)$$

$$\frac{\partial}{\partial t}\alpha^{\mu\nu} u_{\nu} = - D_1^{j,\mu\nu}(g_{j,\nu} - u_{\nu} v_{gj,\nu}), \qquad (2.\ 28)$$

$$\frac{\partial}{\partial t}\alpha^{\mu\nu} B_{i,\nu} = - D_1^{j,\mu\nu} E_{k,\nu} + D_1^{k,\mu\nu} E_{j,\nu} + D_1^{\ell,\mu\nu} B_{i,\nu} v_{g\ell,\nu}, \qquad (2.\ 29)$$

where the summation convention is used for repeated indices. In eq. (2. 29), (i, j, k) is cyclic permutation of (x, y, z).

Eqs. (2. 26) - (2. 29) are our basic equations corresponding to eqs. (2. 1) - (2. 4). The coefficients, $\alpha^{\mu\nu}$ and $D_1^{i,\mu\nu}$, are geometrical factors which do not depend on the physical quantities. They depend on the position of the nodes and time. We shall solve these equations under prescribed intial and boundary conditions.

§3. Numerical Methods

3. 1 Evaluation of Coefficients

For general shape functions, α and D have to be obtained by numerical integration. Gauss's integration formula may be recommended because it is available with small number of evaluation points. However, we can obtain these coefficients by direct and analytic method for the simplex elements. For 3D tetrahedron,

$$\left.\begin{aligned} \alpha^{\mu\nu} &= \frac{6V}{60} \qquad \mu = \nu \\ &= \frac{6V}{120} \qquad \mu \neq \nu \end{aligned}\right\} \tag{3. 1}$$

$$D_1^{i,\mu\nu} = \frac{1}{24}\, a_\mu^i \quad , \tag{3. 2}$$

for each tetrahedron. Here V is the volume of the tetrahedron,

$$6V = \det \begin{bmatrix} 1 & x_1 & y_1 & z_1 \\ 1 & x_2 & y_2 & z_2 \\ 1 & x_3 & y_3 & z_3 \\ 1 & x_4 & y_4 & z_4 \end{bmatrix} \tag{3. 3}$$

and a_μ^i's are minus of the determinant of matrix obtained by replacing the i-th column of the matrix

$$\begin{bmatrix} x_\nu & y_\nu & z_\nu \\ x_\rho & y_\rho & z_\rho \\ x_\omega & y_\omega & z_\omega \end{bmatrix} \tag{3. 4}$$

by unity, where (μ , ν , ρ , ω) is cyclic permutation of node number (1, 2, 3, 4) of tetrahedron.

3. 2 Evaluation of Derivatives

Eqs. (2. 27) - (2. 29) include derivatives, $\vec{j}$, grad T, and div $\vec{v}$, which have to be evaluated at the nodes. We investigate here how derivative can be evaluated at nodes. As simple example, we look into 1D derivative of f,

$$d = \frac{df}{dx} \quad . \tag{3. 5}$$

When we substitute Galerkin series (2. 25) for f into eq. (3. 5), d is reduced by one order. In stead of eq. (2. 25), we use the Galerkin expansion

$$f = \sum_{\mu=1}^{N} \phi_\mu f_\mu \quad , \tag{3. 6}$$

in terms ϕ_μ introduced in eq. (2. 20). This improve the accuracy because f is interpolated in terms of the value f_μ at all nodes (note that ϕ_μ is not localized). Unfortunately, interpolation (3. 6) requires large computing time, and is actually impossible. Equivalent approximation can be obtained by d expanded as

$$d = \sum_{\nu=1}^{N} d_\nu \phi^\nu \tag{3. 7}$$

where d_ν is derivative at the node ν . Then eq. (3. 5) is

$$\sum_{\nu=1}^{N} d_\nu \phi^\nu = \sum_{\nu=1}^{N} f_\nu \frac{d\phi^\nu}{dx} \quad ,$$

$$\alpha^{\mu\nu} d_\nu = D_1^{x,\mu\nu} f_\nu \ . \tag{3. 8}$$

For the linear shape function, and equal grid spacing Δx,

$$\frac{1}{6}\,\Delta x(d_{\mu-1} + 4d_\mu + d_{\mu+1}) = \frac{1}{2}\,(f_{\mu+1} - f_{\mu-1}) \ . \tag{3. 9}$$

This is the equation for d_μ's. The Taylor expansion shows the solution d_μ is accurate up to the order of magnitude $(\Delta x)^4$. When the grid spacings are not equal, error (difference of the left and the right hand sides of eq. (3. 9)) is

$$e = -\frac{1}{12}\,\delta[(\Delta x)^2]\frac{d^2 f}{dx^2}\bigg|_{x=x_\mu} - \frac{1}{144}\,\delta[(\Delta x)^4]\,\frac{d^4 f}{dx^4}\bigg|_{x=x_\mu}$$
$$+ \frac{1}{360}\,[(\Delta x^{\mu+1})^5 + (\Delta x^\mu)^5]\,\frac{d^5 f}{dx^5}\bigg|_{x=x_\mu} + \cdots\cdots \ , \tag{3. 10}$$

where

$$\delta[(\Delta x)^2] = (\Delta x^{\mu+1})^2 - (\Delta x^\mu)^2 \ ,$$

$$\delta[(\Delta x)^4] = (\Delta x^{\mu+1})^4 - (\Delta x^\mu)^4 \ ,$$

$$\Delta x^\mu = x^{\mu+1} - x^\mu \ .$$

Note that when $\alpha^{\mu\nu}$ is lumped, eq. (3. 9) is reduced to

$$\Delta x d_\mu = \frac{1}{2}\,(f_{\mu+1} - f_{\mu-1}) \ . \tag{3. 11}$$

and d_μ is centered difference.

Then we evaluate derivatives by solution of equations of the form (3. 8) at each time step.

3. 3 Method of solution of FEMALE equations

Eqs. (2. 26) - (2. 29) have the form

$$\frac{\partial}{\partial t}\,AU = C(U) \ , \tag{3. 12}$$

which is non-linear, simultaneous, ordinary equation for U. To avoid numerical instabilities, we assume fully implicit scheme:

$$A^{n+1}U^{N+1} = A^{n}U^{n} + C(U^{n+1})\ t\ . \tag{3. 13}$$

At each iteration step, this takes the form,

$$AU = B\ , \tag{3. 14}$$

where B is assumed to be known. A is the basic matrix.

Let us introduce the lumped matrix element,

$$\bar{\alpha}^{\mu\nu} \equiv (\sum_{\rho=1}^{N} \alpha^{\mu\rho})\delta^{\mu\nu}\ , \tag{3. 15}$$

which is diagonal. From $\bar{\alpha}$, define the diagonal matrix,

$$\bar{D} \equiv [\sqrt{\bar{\alpha}^{\mu\nu}}]\ . \tag{3. 16}$$

And then define

$$\bar{A} \equiv \bar{D}^{-1} A\ \bar{D}^{-1}\ , \tag{3. 17}$$

and

$$\bar{B} \equiv \bar{D}^{-1} B\ . \tag{3. 18}$$

Then eq. (3. 14) can be written as

$$\bar{A}\ \bar{U} = \bar{B}\ , \tag{3. 19}$$

where $\bar{U} = \bar{D}\ U$. $\bar{A}$ is symmetric and positive definite. Eigen values of $\bar{A}$ are nearly unity. So eq. (3. 19) can be solved by conjugate gradient method. In this case, $\bar{B}$ is good initial guess for $\bar{U}$. This method is a special case of ICCG (Incomplete Cholesky-Conjugate Gradient method), and is called LMCG (Lumped Matrix-Conjugate Gradient method). We have tested, and found

that LMCG is more efficient than ICCG for the basic matrix A, since $A \cong \bar{D}\bar{D}$.

3. 4 Further Improvements

(i) For saving the computing time and storage, we took $\bar{U} = \bar{B}$ or $U = D^{-1}D^{-1}B$. We compared the 2D results with the results by the ICED ALE, and found qualitatively good agreement.

(ii) Coefficients described in section 3. 3 sometimes yield the computed results depending on the shape of element. We do not know the reason. However, our conjecture is that the shape of control volume depends on that of element, and we have found the control volume less dependent on the shape of element.

Setting Up Phase of Reversed Field Pinch

H. Matsuda, S. Ido* and I. Kawakami
Department of Physics
College of Science and Technology
and
Atomic Energy Research Institute
Nihon University, Tokyo, Japan

Presented at the Workshop on "3D MHD Studies on Toroidal Devices", Oct. 19-21, 1981, Oak Ridge National Laboratory

§1. Introduction

This report summarized the computational studies on reversed field pinch. Main effort in this report concentrates on the setting up phase of the reversed field pinch of TPE 1R of Electrotechnical Laboratory, Tanashi, Tokyo, which is one of the programmed (aided) and fast reversal of toroidal field, time scale being the order of Alfvén time scale. Non-linear evolution of high n mode is also described.

---

* Present Address, Institute for Laser Engineering, Osaka University, Osaka, Japan

§2. Models

The model of computation is described by a set of non-linear MHD equations. The plasma is a single fluid. The electric field, $\vec{E}$, is given by simple Ohm's law, $\vec{E} + \vec{V} \times \vec{B} = \overleftrightarrow{\eta}\vec{j}$. The thermal conduction, $\vec{q} = - k \text{ grad } T$, and the energy loss term, $L = - p(r/a)^2/T_L$, where $\tau_L \approx 1$ μsec, are included.

The numerical method is somehow modified ICED ALE, where the position, $\vec{x}$, the velocity, $\vec{V}$, and the magnetic field, $\vec{B}$, are defined at the vertices of quadrilateral mesh, while the density, n , the temperature, T , the pressure, p , the electric field, $\vec{E}$, and the current, $\vec{j}$, are defiend at the center of the quadrilateral. The plasma is bounded by the cylindrical conducting shell.

In 2D simulation, initially, the plasma has constant density and temperature, confined by the toroidal magnetic field, and at rest. The plasma at the wall is at rest throughout computation. The toroidal field at the wall begin to decrease at some instant (~ 2 μsec), and finally reversed. The poloidal field, which is initially vanishing, start increasing because of increasing of the toroidal plasma current, which reaches the maximum value at some instant (- 4 μsec), and then crowbered.

For the 3D simulation, we start computation from the state with the Bessel function model for the magnetic field, and with non-vanishing pressure, on which some perturbations of m = 1 and n > 0 modes are imposed.

§3. The 2D simulation

We investigate the setting up of the reversed field configurations by the F-θ diagram and the profiles of magnetic fields and of currents.

For general references, we first consider the case where the resistivity, $\overleftrightarrow{\eta}$, is classical. Results are shown in Fig. 1. The fields are flat around axis, so that the currents are peaked near the wall. These show the diffusion is poor in this case, suggesting η must be anomalous. The F-θ diagram is shown in Fig. 2. Simulation points go down along the Bessel function model line. After the reversal of field, the θ values stay near $\theta \simeq 1.2$.

The result of computation with the pure classical resistivity showed that the plasma profiles are not in agreement with the experimental ones, and the plasma must be more resistive. We examined the resistivity which is anomalous and isotropic. The profiles of the magnetic fields are also shown in Fig. 1. The diffusion of the magnetic fields are observed. However, the F-θ diagram shows the failure of setting up of equilibrium of reversed field configuration for this case. The θ values grows indefinitely.

These two cases of computation suggest that the resistivity is anomalous at the setting up phase. However, the anomalous resistivity fails to sustain reversed field configuration. We note that at the setting up phase, the current has a large perpendicular component to the magnetic field, while the current is almost parallel to the magnetic field (force free configuration). We conjectured that the $\overleftrightarrow{\eta}$ is not isotropic, and the $\eta_{/\!/}$

is classical and the $\eta_\perp$ is anomalous. The conjecture is confiemed as shown Figs. 1-4. The plasma is almost force free and the θ value remains at $1 \lesssim \theta \lesssim 2$ for long time.

We have assumed that the anomaly is of the Chodura type. We examined the other type of anomaly, such as the Bohm anomaly, and found that the anomaly has little effect on the diffusion. We must note that we are investigating the fast MHD processes.

The anomaly we have assumed is not used in the joule heating, but is included in the diffusion term of the magnetic field. When we included the anomaly in the joule heating, an anomalous heating of the plasma near the wall was found, and the resistivity became so small and the diffusion was also small. The resulting profiles are not in agreement with the force free configuration. Thus, we are thinking that the anomaly do not come from collisions. The anomalous diffusion may be some 2D projections of 3D MHD activity.

§4. The 3D simulation

In the 3D simulation, the periodic boundary condition along the axis is assumed. The pressure is initially assumed to be sinusoidal, $p = p_o \cos(\pi r/2a)$. Upon this quasi-equilibrium, small perturbations of (m, n) mode are imposed. The resistivity is constant throughout computation and over whole plasma region. The parameters given in this way correspond to the magnetic Reynolds number, $S \cong 5 \times 10^{3}$ and the safety factor, $q \cong 0.154$ to -0.042.

The evolution of kinetic energy is shown in Fig. 5. The

vorteces are formed corresponding to the (m, n) values. For $m = 1$ and $n \lesssim 5$, we could not observe the growth of kinetic energy, showing non-linear stability. For high n modes, $n \geqq 10$, the plasma is initially stable, showing the decrease of kinetic energy. However, it suddenly shows rapid growth of kinetic energy. For intermediate values of n , we have not yet analysed complicated behaviors of perturbations.

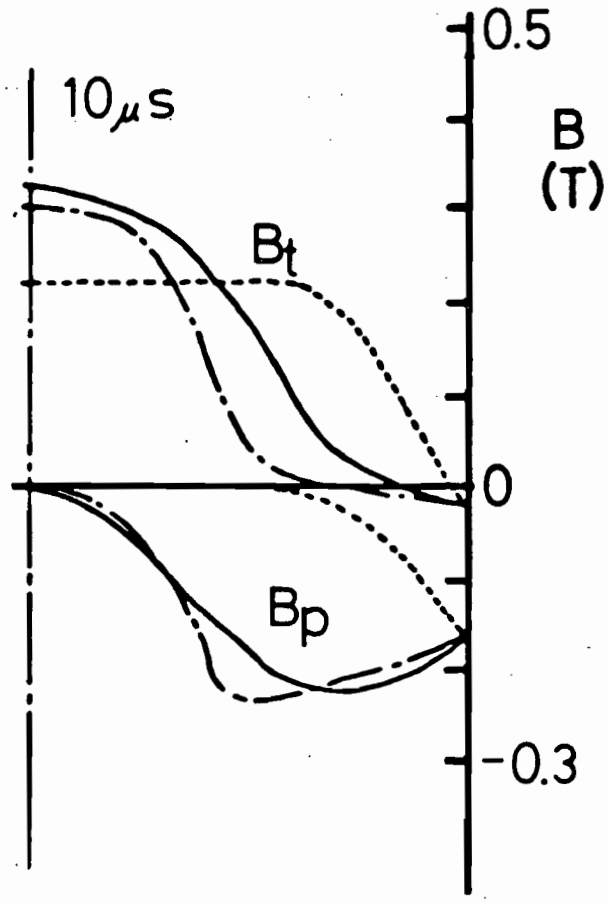

FIG. 1 PROFILES OF TOROIDAL FIELD, B_T, AND POLOIDAL FIELD, B_P, AT 10 μS FOR CLASSICAL η (----), ANOMALOUS η (-·-·-), AND CLASSICAL $\eta_{//}$ AND ANOMALOUS $\eta_{\perp}$ (——).

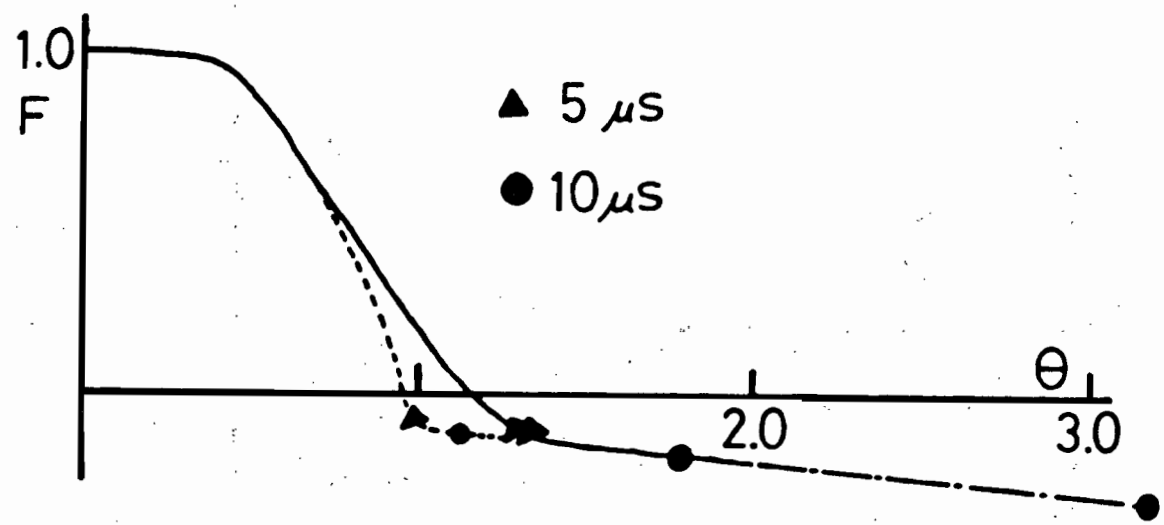

FIG. 2 F-θ DIAGRAM FOR CLASSICAL η (----), ANOMALOUS η (-·-·-), AND CLASSICAL $\eta_{//}$ AND ANOMALOUS $\eta_{\perp}$ (———) .

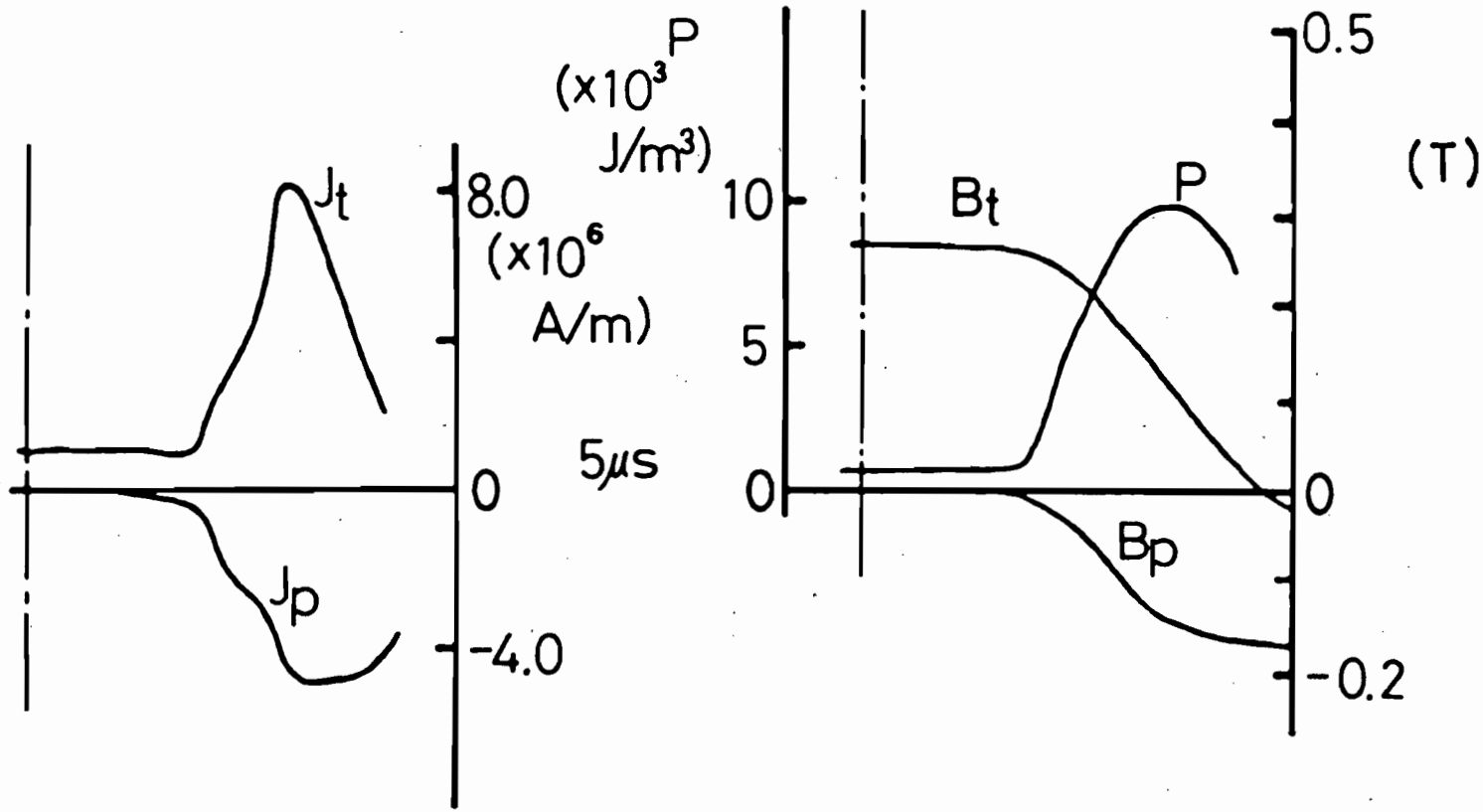

FIG. 3 PROFILES OF PRESSURE, TOROIDAL AND POLOIDAL FIELDS, AND TOROIDAL AND POLOIDAL CURRENTS AT 5 μs

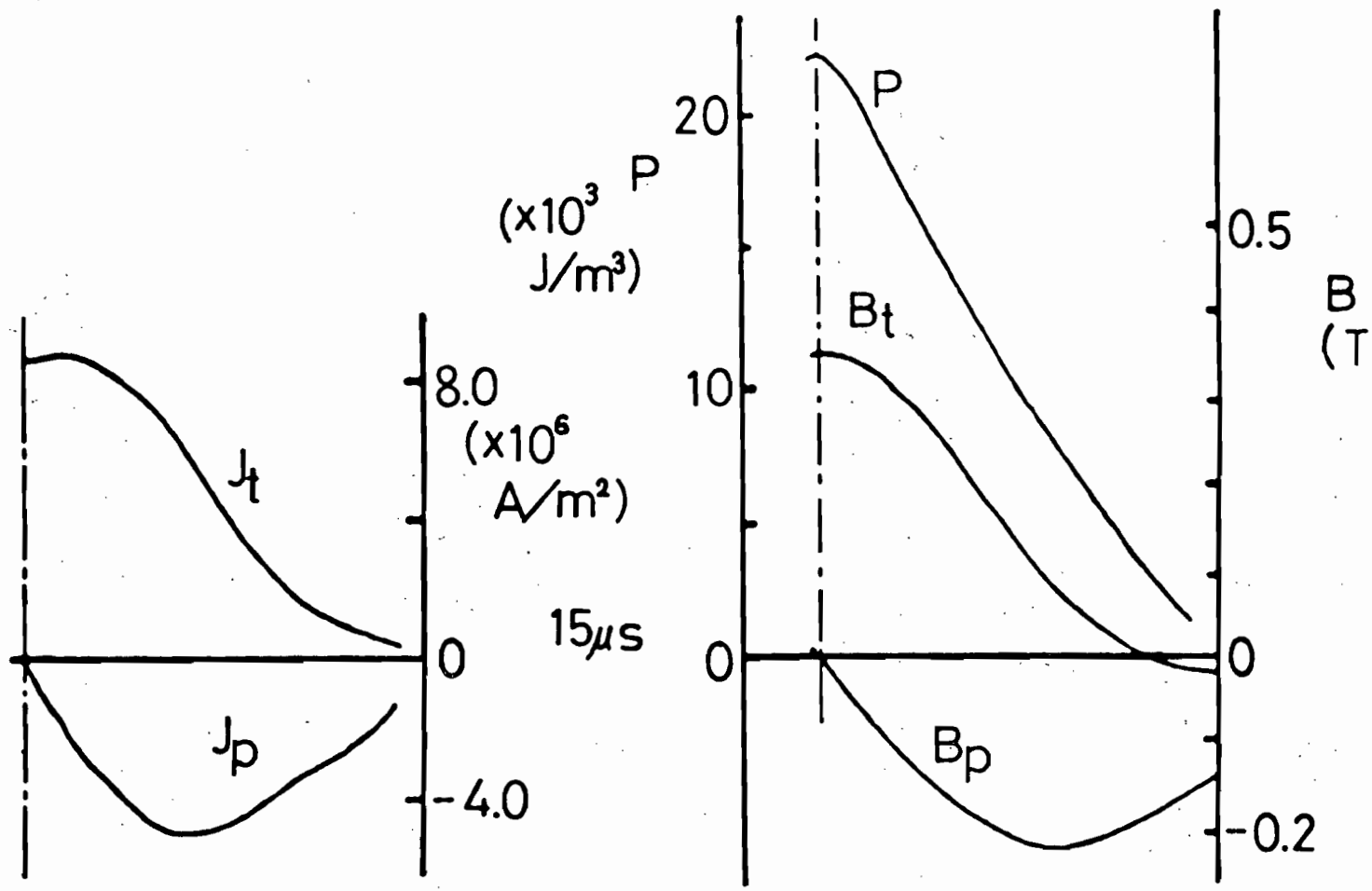

FIG. 4 PROFILES OF PRESSURE, TOROIDAL AND POLOIDAL FIELDS, AND TOROIDAL AND POLOIDAL CURRENTS AT 15 μs

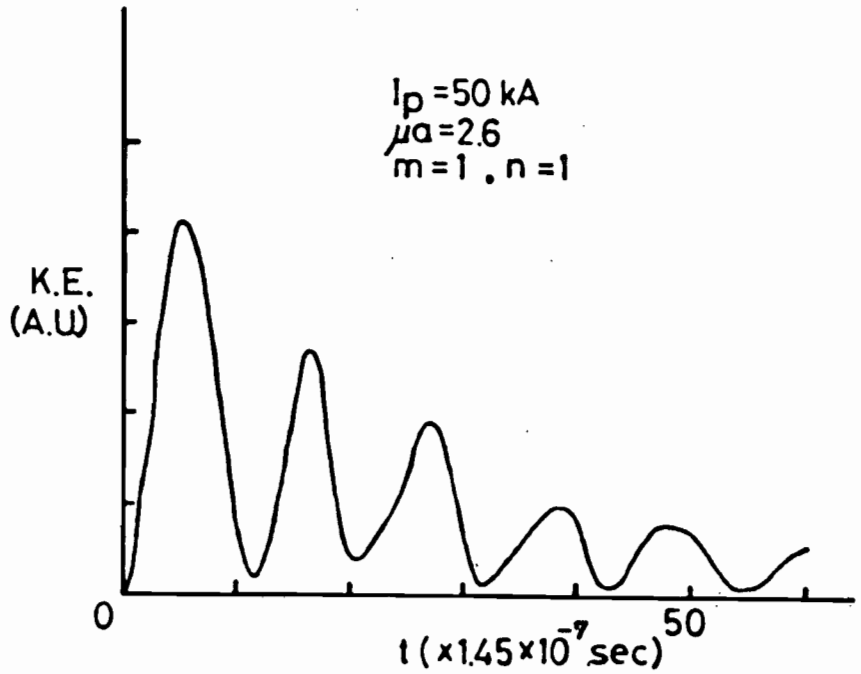

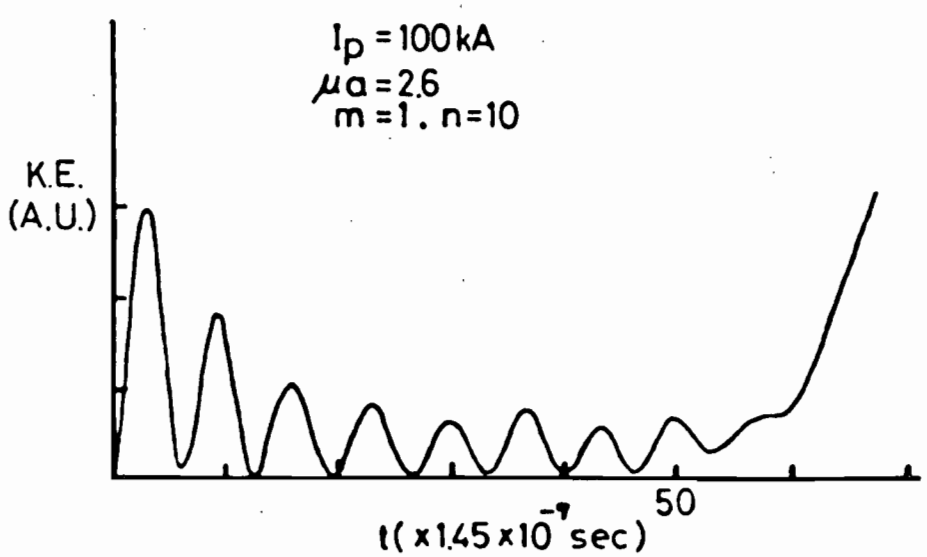

FIG. 5 NONLINEAR EVOLUTION OF KINETIC ENERGY

Abstract of presentation at the US-Japan Theory Workshop on 3D-MHD Studies to be held in Oak Ridge, Tennessee on October 19-21-, 1981.

A 3D MHD ALGORITHM FOR SIMULATION*

by

Torkil H. Jensen and Ming S. Chu

General Atomic Company

San Diego, California

Computer simulation of plasma dynamics has become important since it has been realized that strict stability of simple MHD equilibria against instabilities in the resistive MHD model may not be required for fusion plasmas. Simple axisymmetric tokamak plasmas for example, which are unstable to tearing modes, have shown an ability to relax to nearby, nonaxisymmetric equilibria which are more stable than the original axisymmetric plasmas. One role of computer simulation is therefore to search for such more stable equilibria; another is to assess if these more stable configurations are stable enough to be of interest for fusion reactors. Since such configurations presently appear too complicated for analytical treatment, the numerical approach seems necessary.

A fusion reactor plasma may, in the approximation of resistive MHD, exhibit dynamical behavior with timescales ranging from the Alfvén time scale ($\sim 10^{-7}$ sec) to the resistive time scale ($\sim 10^{3}$ sec). Classical transport phenomena, which here are assumed not included in the resistive MHD description, may give rise to dynamical phenomena on the time scale of the necessary energy confinement time (~ 1 sec). Therefore, in the simple resistive MHD description, phenomena of interest have timescales from 10^{-7} to 1 sec.

In the common approach to the simulation problem the finite mass density of the plasma is taken into account. Such simulation codes have been able successfully to exhibit phenomena similar to those observed experimentally[1]. Dynamical phenomena such as sawtooth oscillations and disruptions appear similar in experiments and in simulations, and almost stationary (but rotating) equilibria with complicated configurations found in experiments show striking similarities to those found using simulation codes. This suggests that the MHD model is reasonably realistic.

One limitation in the usefulness of existing simulation codes stems from the finite computer time available. Therefore, there is a need for a search for alternative approaches. We are suggesting an approach in which inertial forces are neglected entirely, i.e. the ratio between the resistive and the Alfvén time scale, S, is infinite instead of $S \sim 10^{10}$ for a fusion reactor. With this assumption, the linear growth, of for example a tearing mode, cannot be simulated since the growth rate is infinite. Very similar phenomena may, however, be simulated with growth rates of $a/\Delta\ \tau_R^{-1}$ or $(a/\Delta)^2 \tau_R^{-1}$, where a is a characteristic dimension of the plasma, Δ is the grid distance and τ_R the resistive time, $\tau_R \equiv a^2/\eta$ where η is the plasma resistivity. The slower growth rate may correspond to the case of a singular surface, the faster to that of a singular line (hyperbolic axis). This approach, where inertial forces are neglected may be considered an extension to three dimensions of the two dimensional code of Grad[2].

The basic idea of the suggested approach is given elsewhere[3]. The numerical advance of a state is done in two steps; one step may be termed an ideal MHD step, the other a resistive step. For the ideal MHD step, the ideal MHD constraints are observed, i.e. the change of the vector potential is everywhere perpendicular to the magnetic field, the number of particles in a fluxtube is conserved, and the pressure follows the adiabatic law. Within these constraints

one seeks the state of lowest energy. This state of lowest energy is an MHD equilibrium and it can be shown that the suggested algorithm (which is similar to the one used in the Chodura code[4]) always converges exponentially toward a stable MHD equilibrium (in the ideal MHD sense). The resistive step consists of changing everywhere the component of the vector potential parallel to the magnetic field whereby the ideal MHD constraints are changed. This change is proportional to the component of the current density in the direction of the magnetic field, to the plasma restivity and to the length of the time step. The state after this resistive step is not an MHD equilibrium, but the subsequent ideal MHD step will find a (the) nearby (stable) MHD equilibrium with the same constraints.

One may expect (hope) that a simulation in this ($S = \infty$) approximation will carry the plasma through similar configurations as those found from a simulation in which inertial forces are taken into account. The main difference may be that fast dynamics are not accounted for accurately in the $S = \infty$ simulation, since slow dynamics are independent of inertial forces. One may expect that a simulation code in which the effects of inertial forces are neglected may require only a relatively coarse grid and relatively little computer time. It appears difficult to test the validity of these expectations by other means than direct comparison of code results.

References

(1) B. V. Waddell, B. Carreras, H. R. Hicks, J. A. Holmes, D. L. Lee, Phys. Rev. Letters, 41, 1386, (1978)

D. Biskamp and H. Welter; Plasma Physics and Controlled Nuc. Fusion Res. (IAEA Vienna 1977, Vol. I, p. 579)

D. Edery, R. Pellat, J. L. Soule, M. Frey, J. P. Somon, IAEA CN-38/J4, Brussels, July, 1980

R. B. White, D. A. Monticello, and M. N. Rosenbluth, Phys. Rev. Letters, 39, 1618 (1977)

(2) H. Grad and J. Hogan, Phys. Rev. Letters, 24, p. 1337 (1970)
H. Grad, P. N. Hu and D. C. Stevens, Proc. Nat. Acad. Sci. U. S. A. p. 3789 (1975)

(3) M. S. Chu, T. H. Jensen, and B. Dy, GA-A16367, "A Method for Finding Minimum Energy Three Dimensional Magnetohydrodynamic Equilibria with Given Constraints", Aug. 1981. GA-A16367. Submitted for publication to Physics of Fluids.

(4) R. Chodura and A. Schlüter, JCP, 41, p. 68 (1981)

*Supported by U. S. Department of Energy Contract No. DE-AT03-76ET51011

AUTHOR INDEX

T. Amano, 21, 104
A. Aydemir, 187
M. Azumi, 116, 140
D. C. Barnes, 187
O. Betancourt, 10
A. Bhattacharjee, 82
B. A. Carreras, 59, 156
L. A. Charlton, 156
R. Chodura, 51
M. S. Chu, 227
G. B. Crew, 168
W. Dommaschk, 51
L. Garcia, 59
S. Hamada, 21
K. Hanatani, 21
C. L. Hedrick, 197
F. Herrnegger, 51
H. R. Hicks, 59, 156
N. Hodoshima, 21
J. A. Holmes, 59, 156
S. Ido, 217
K. Itoh, 116, 140
T. H. Jensen, 227
I. Kawakami, 207, 217
J. Killeen, 98
G. Kurita, 116, 140
W. Lotz, 51
V. E. Lynch, 59, 156
H. Matsuda, 217
K. McGuire, 129
D. Montgomery, 32
D. A. Monticello, 70, 129
J. Nührenberg, 51
L. W. Owen, 197
W. Park, 129
J. J. Ramos, 168
M. Reusch, 129
T. Sato, 170
A. Schlüter, 51
D. Schnack, 176
K. Shimizu, 104
H. R. Strauss, 70
T. Takeda, 116, 140
T. Takizuka, 116, 140
Y. Tanaka, 140
S. Tokuda, 116, 140
T. Tsunematsu, 116, 140
T. Tuda, 116, 140
K. Uo, 21
M. Wakatani, 21
H. Weitzner, 1
R. B. White, 129

LIST OF ATTENDEES

US-JAPAN THEORY WORKSHOP ON 3-D MHD STUDIES FOR TOROIDAL DEVICES

Oak Ridge, Tennessee

October 19-21- 1981

Dr. Hirotada Abe
Department of Electronics
Kyoto University
Kyoto, JAPAN

Professor Tsuneo Amano
Institute of Plasma Physics
Nagoya University
Nagoya, JAPAN

Dr. A. Aydemir
Institute for Fusion Studies
University of Texas
Austin, TX 78712

Dr. O. Betancourt
Courant Institute
New York University
251 Mercer Street
New York, NY 10012

Dr. Amitava Bhattacharjee
Institute for Fusion Studies
R. L. Moore Hall 11.310
University of Texas
Austin, TX 78712

Dr. A. Bondeson
Physics Department
University of Maryland
College Park, MD 20742

Dr. Francoise Brunel
Institute for Fusion Studies
University of Texas
Austin, TX 78712

Dr. B. A. Carreras
Oak Ridge National Laboratory
P. O. Box Y
Oak Ridge, TN 37830

Dr. L. A. Charlton
Oak Ridge National Laboratory
P. O. Box Y
Oak Ridge, TN 37830

Dr. M. S. Chu
General Atomic Company
P. O. Box 81608
San Diego, CA 92138

Dr. W. A. Cooper
Oak Ridge National Laboratory
P. O. Box Y
Oak Ridge, TN 37830

Dr. R. A. Dory
Oak Ridge National Laboratory
P. O. Box Y
Oak Ridge, TN 37830

Dr. L. Garcia
Oak Ridge National Laboratory
P. O. Box Y
Oak Ridge, TN 37830

Professor K. Hanatani
Plasma Physics Laboratory
Kyoto University
Jukasho, Ugi
Kyoto, JAPAN

Dr. C. L. Hedrick
Oak Ridge National Laboratory
P. O. Box Y
Oak Ridge, TN 37830

Dr. H. R. Hicks
Oak Ridge National Laboratory
P. O. Box Y
Oak Ridge, TN 37830

Dr. S. P. Hirshman
Oak Ridge National Laboratory
P. O. Box Y
Oak Ridge, TN 37830

Dr. J. T. Hogan
Oak Ridge National Laboratory
P. O. Box Y
Oak Ridge, TN 37830

Dr. J. A. Holmes
Oak Ridge National Laboratory
P. O. Box Y
Oak Ridge, TN 37830

Dr. T. H. Jensen
General Atomic Company
P. O. Box 81608
San Diego, CA 92138

Professor Ichiro Kawakami
Atomic Energy Research Institute
& College of Science and Technology
Nihon University
Tokyo, JAPAN

Dr. John Killeen
Lawrence Livermore National Laboratory
National Magnetic Fusion Energy
Computer Center, L-561
P. O. Box 5509
Livermore, CA 94550

Ms. Vickie E. Lynch
Oak Ridge National Laboratory
P. O. Box Y
Oak Ridge, Tennessee 37830

Dr. J. F. Lyon
Oak Ridge National Laboratory
P. O. Box Y
Oak Ridge, TN 37830

Dr. M. A. Marçal
Courant Institute
New York University
251 Mercer Street
New York, NY 10012

Dr. David Montgomery
William & Mary College
Physics Department
Williamsburg, VA 23185

Dr. D. A. Monticello
Princeton Plasma Physics Laboratory
Princeton University
P. O. Box 451
Princeton, NJ 08544

Dr. R. W. Moore
General Atomic Company
P. O. Box 81608
San Diego, CA 92138

Dr. J. Nührenberg
Max-Planck Institut fur Plasmaphysik
D-8046 Garching
Federal Republic of Germany

Dr. L. W. Owen
Oak Ridge National Laboratory
P. O. Box Y
Oak Ridge, TN 37830

Dr. W. Park
Princeton Plasma Physics Laboratory
Princeton University
P. O. Box 451
Princeton, NJ 08544

Dr. J. Ramos
Massachusetts Institute of Technology
Cambridge, MA 02139

Dr. J. A. Rome
Oak Ridge National Laboratory
P. O. Box Y
Oak Ridge, TN 37830

Dr. Tetsuya Sato
Institute for Fusion Theory
Hiroshima University
Hiroshima, JAPAN

Dr. D. Schnack, CTR-6, MS-642
Los Alamos National Laboratory
P.O. Box 1663
Los Alamos, NM 87544

Dr. Tatsuoki Takeda
Japan Atomic Energy Research Institute
Tokai-Mura, Naka-Gun, Ibaraki-Ken
JAPAN 319-11

Dr. Harold Weitzner
Courant Institute
New York University
251 Mercer Street
New York, NY 10012

Dr. J. A. Wesson
Culham Laboratory
Abingdon, Oxfordshire, 3DB OX14
ENGLAND

AGENDA

US-JAPAN THEORY WORKSHOP ON

3-D MHD STUDIES FOR TOROIDAL DEVICES

OCTOBER 19-21, 1981

Oak Ridge, Tennessee

Monday, October 19, 1981

8:00 - 9:00	Registration, Ridge Room, Holiday Inn
9:00 - 10:15	Welcome
	"3-D MHD Equilibrium," H. Weitzner
10:15 - 10:30	COFFEE BREAK
10:30 - 12:00	"Beta Limits for Torsatrons," O. Betancourt
	"MHD Equilibrium and Stability of Straight Helical Systems," K. Hanatani
12:00 - 1:00	LUNCH
1:00 - 3:15	"Computation of Inverse Magnetic Cascades," D. Montgomery
	"Theoretical Optimization of Stellarators," J. Nürenberg
	"Resistive Modes in Stellarator-Tokamak Configurations," H. R. Hicks
3:15 - 3:30	COFFEE BREAK
3:30 - 5:00	"Limiting Beta of Stellarators with No Net Current," D. Monticello
	"Variational Solutions to the Three-Dimensional Inverse Equilibrium Problem in Toroids," A. Bhattacharjee
6:30 - 7:30	RECEPTION

Tuesday, October 20, 1981

8:00 - 9:15	Registration
9:15 - 10:15	"A Review of Three Dimensional Resistive Magnetohydrodynamic Calculations," J. Killeen
10:15 - 10:30	COFFEE BREAK
10:30 - 12:00	"MHD Calculations for Toroidal Devices - Aims and Methods," J. Wesson
	"Tokamak Current Disruptions Due to Impurity Radiation Cooling," T. Amano
	"Major Disruption Process in Tokamak," T. Takeda
12:00 - 1:00	LUNCH
1:00 - 3:15	"3-D Nonlinear Resistive Studies of High Beta PDX Discharges," W. Park
	"Internal Disruption in High β_p Tokamak," T. Takeda
	"Resistive Modes in a High Beta Tokamak," J. A. Holmes

Tuesday, October 20, 1981 (Contd.)

3:15 - 3:30	COFFEE BREAK
3:30 - 5:00	"Particle MHD Code Applied to Compressible High Beta Plasma and Fast Magnetic Reconnection," F. Brunel
	"Properties of the Ideal MHD m = 1 Mode in Tokamaks," J. Ramos

Wednesday, October 21, 1981

8:00 - 9:15	Registration
9:15 - 10:15	"3D MHD Simulations of Spheromak Formation," T. Sato
10:15 - 10:30	COFFEE BREAK
10:30 - 12:00	"Three-Dimensional MHD Computations for RFP and FRC Plasmas," D. D. Schnack
	"A Spectral-Finite Difference Algorithm for Three Dimensional Incompressible MHD," A. Aydemir
12:00 - 1:00	LUNCH
1:00 - 3:15	"3-D Finite Beta Equilibria for EBT," L. W. Owen
	"Finite Element Method for 3-D MHD Simulation," I. Kawakami
	"Setting up Phase of Reversed Field Pinch," I. Kawakami
	"A 3-D MHD Algorithm," T. H. Jensen
3:15 - 3:30	COFFEE BREAK
3:30 - 4:30	"Particle Simulation of Ion Heating and Current Generation due to the Localized Lower Hybrid Waves," H. Abe
4:30 - 5:00	Discuss Next Workshop